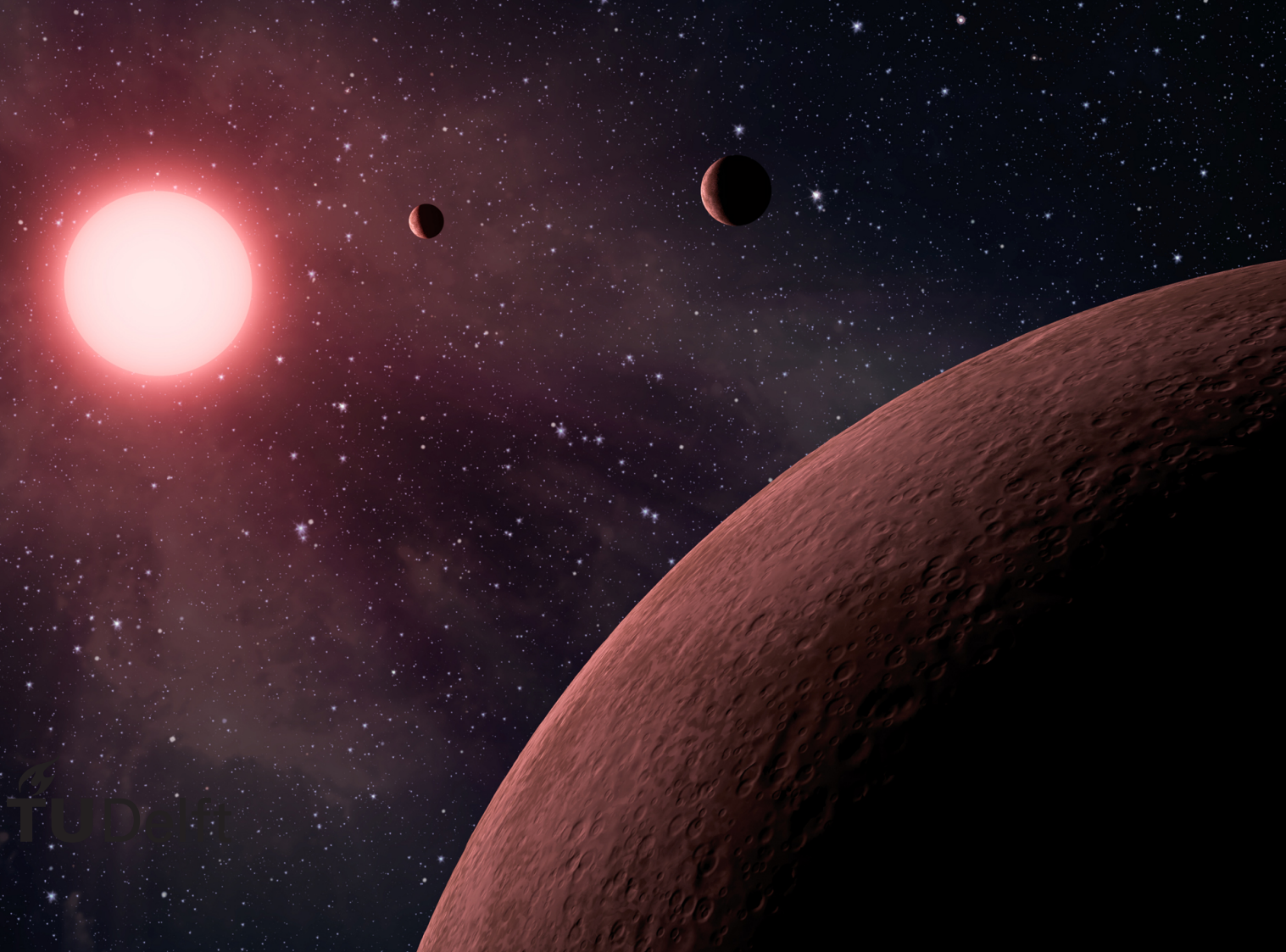


Reflected signals of extrasolar systems

Detectability of lunar companions

J. Berzosa Molina



Reflected signals of extrasolar systems

Detectability of lunar companions

by

J. Berzosa Molina

to obtain the degree of Master of Science in Aerospace Engineering
at the Delft University of Technology,
to be defended publicly on Tuesday January 29, 2017 at 2:00 PM.

Student number: 4416848

Project duration: October, 2016 – August, 2017

Thesis committee: Prof. dr. Bert Vermeersen, TU Delft, chairman of the committee
Dr. Daphne Stam, TU Delft, supervisor
Dr. Loïc Rossi, TU Delft, co-supervisor
Dr. Alessandra Menicucci TU Delft

An electronic version of this thesis is available at <http://repository.tudelft.nl/>.



Preface and Acknowledgements

Three years ago, I proposed the field of exoplanets as suggested thesis research topic as I would fill in the application form for TU Delft. At present, I am very happy to conclude my master studies by presenting this novel research work on exoplanet and exomoons. These three years, which I have spent in the Netherlands and Germany, have been a burst of new experiences, learnings, and challenges along which I have shared with people I will never forget. All together made me a better professional and a better person.

During my internship at OHB in Germany, I had the opportunity to work on the PLATO project and get to meet the technical and research teams of people behind it. It was not until I travelled to Leuven to participate on a PLATO workshop, and had a chat with Dr. René Heller from MPS, that my interest for research and extrasolar systems sparked again. I was immediately astonished by his work on exomoons and, after considering the possibilities, he offered me the possibility of doing my thesis at MPS. However, the project timing didn't match my academic schedule and thus could not be materialized. Aware of the exoplanet research work developed in the Astrodynamics and Space Missions department at the Aerospace Faculty of TU Delft, I had a Skype chat with Daphne Stam evaluating possible master thesis topics. I just couldn't get over it when she mentioned the opportunity of doing a thesis on exomoon modelling in reflected starlight signals. I accepted the proposal right away.

I would like to express my gratitude to Daphne Stam and Loïc Rossi for giving me the opportunity to carry out a cutting-edge research on exomoons, and for their supervision and valuable feedback in the past year. I would like to thank Chris Möckel and Ventsislav Pazhev for their support and help with reviewing the thesis report. Special thanks go to Ventsislav and Pablo Vizcaíno, for sharing with me these months of hard work and help me make the difficult moments a bit easier. Finally, I am particularly grateful to my family, who always supported me and gave me the opportunity of being who I am.

*J. Berzosa Molina
Delft, August 2017*

Summary

The detection of moons around extrasolar planets is one of the main foci of current and future observatories. These silent companions contribute to the planets' observed signals but are barely detectable with current methods. Numerous gaseous exoplanets are known to orbit in the habitable zones of stars and the expected abundance of natural satellites, and their diversity in composition, make them ideal targets in the search for habitable celestial bodies.

Current instruments such as Spectro-Polarimetric High-contrast Exoplanet Research (SPHERE) and Gemini Planet Imager (GPI) have capabilities to perform high-contrast, direct imaging and characterization of exoplanets, both through spectroscopy and polarimetry. Previous modelling of light curves and polarization signals [see e.g. Karalidi, T. et al., 2012, Seager et al., 2000, Stam, 2008, Stam et al., 2004] shows that polarimetry not only increases the contrast between the exoplanet and its star, but can also unveil the structure and composition of the atmosphere and surface.

In this work we took one step further by analysing how the presence of a Moon-like companion influences the flux and polarization signals of an Earth-like exoplanet. The influence is two-fold: 1. the flux reflected by the planet-moon system increases according to the moon's reflection properties, and 2. the transits and eclipses between the moon, planet, and star modulate the observable signal.

We described the flux and polarization of starlight that is reflected by a spatially unresolved planet-moon system by a Stokes vector [Hansen and Travis, 1974] computed using and adding-doubling radiative transfer model [de Haan et al., 1987], assuming the starlight is unpolarized [Kemp et al., 1987]. Our model planet has a Lambertian surface with horizontally homogeneous atmospheric layers filled with gas particles, and our model moon has a Lambertian surface without atmosphere.

The observable Stokes vectors at a certain epoch are a function of the illumination and viewing geometries of each body, which depend on the bodies' phase angle α (the angle between the direction to the star and the observer measured from the centre of the body), and on the orbital geometry of the bodies involved, which can lead to partial or total blockage of any of these bodies. In particular, we have modelled the following interferences:

- A transit: the interposition of a body between the observed target and the observer, partially (or totally) blocking the light that is reflected by the target while adding reflected light from the body.
- An eclipse: the interposition of a body between the star and the observed target, casting a shadow on (part of) the reflecting target.

We computed the orbital dynamics and geometries using the 'nested two-body' model introduced in Kipping [2010b, 2011]. This builds upon the assumption that the motion of the planet and moon around the planet-moon system barycentre, as well as the motion of this barycentre around the star, can be described by Keplerian orbits.

The traces of exomoons that we found in our numerical simulations emerge as remarkable signatures in the signal of the spatially unresolved planetary system. The flux and polarization variations due to eclipses and transits are of the same order of magnitude as the overall signal and can span several hours. The analysis of these curves, together with the sensitivity analysis carried out with respect to the lunar parameters, allowed us to relate the shape of the recorded features to the reflection properties of the planet and moon, as well as their orbit geometry.

Moreover, we studied the probability of exomoon detection via polarization, for direct and indirect methods. We suggested the use of frequency analysis techniques as a potential tools for satellite detection and concluded that, in the event of existing an orbiting edge-on satellite around an Earth-like exoplanet, mutual events are likely to be detected within short observation periods.

Contents

Nomenclature	ix
List of Figures	xv
List of Tables	xix
1 Introduction	1
1.1 Why study exomoons?	2
1.2 On the trail of exomoons	4
1.3 Direct Imaging of extrasolar systems	5
1.4 Polarimetry as a next-generation tool	7
1.5 Problem Statement.	8
1.6 Research Methodology.	10
1.7 Thesis Outline	11
2 Computing reflected starlight	13
2.1 Stokes vectors and polarization	13
2.2 Computing disk–integrated Stokes vectors	14
2.3 Selection of scattering plane	17
2.4 Atmosphere and surface models	18
2.5 Computational steps	19
3 Geometry of the Extrasolar System	21
3.1 Generic formulation of the point-masses motion	21
3.2 The Nested Two Body Problem	22
3.2.1 Assumptions and range of application.	22
3.2.2 Framework and model parameters	23
3.2.3 Mathematical elaboration	26
3.3 Varying the observer position	29
3.4 Three-dimensional description of the system.	30
3.4.1 Pixel position vector	31
3.4.2 Angular geometry of the planet–moon–star–observer system	32
3.4.3 Flux incidence along the grid	36
4 Mutual events	39
4.1 Definition of mutual events.	39
4.2 Mutual photometric phenomena	40
4.3 Mutual events model assumptions.	41
4.4 Computing eclipses	42
4.4.1 Types of eclipses	42
4.4.2 Computing the magnitude of an eclipse	43
4.4.3 Occurrence of eclipses	46
4.4.4 Umbra nodes	46
4.4.5 Antumbra nodes	47
4.4.6 Penumbra nodes	48
4.4.7 Computational steps	49
4.5 Mathematical description of transit events calculation	50
5 Results: reflected starlight by edge-on unresolved Earth–Moon planetary system	53
5.1 Earth–Moon system set-up	53
5.1.1 Orbital geometry	53
5.1.2 Modelling the reflection properties of the bodies	54

5.2	Starlight reflected by the individual planet & moon bodies	55
5.3	Baseline reflected starlight by the planet–moon system	57
5.4	Characterization of planet–moon events	59
5.4.1	General characteristics	59
5.4.2	Analysis of transit events	62
5.4.3	Analysis of eclipse events	66
5.5	On the detection of mutual events	70
5.5.1	Geometrical probability of mutual event direct observation in an edge-on Earth–Moon system	71
5.5.2	Different observer position in coplanar Earth–Moon system	72
5.5.3	Study of the frequency of mutual events	75
6	Results: variation of reflected signal with lunar parameters	79
6.1	Variation with lunar period	79
6.2	Variation with lunar albedo	81
6.3	Variation with lunar radius	82
6.4	Variation with lunar eccentricity	88
6.5	Variation with lunar inclination	91
6.6	Summary of results	98
7	Conclusions and recommendations	101
A	Models verification	105
A.1	Radiance disk integration	105
A.2	Transits model	106
A.3	Eclipses model	107
B	Trade–off analyses	109
B.1	Cloudy–clear sky models trade–off	109
B.2	Number of pixels along the equator trade–off	111
B.3	Number of Gauss points trade–off	111
C	Extra figures	115
D	ExoPy introduction manual	135
E	Reproduction of EPSC 2017 abstract	147
	Bibliography	151

Nomenclature

Abbreviations

ADI	Angular Differential Imaging
AU	Astronomical Unit
CHEOPS	CHaracterising ExOPlanets Satellite
CoRoT	Convection, Rotation and planetary Transits
E-ELT	European Extremely Large Telescope
EPICS	Exoplanet Imaging Camera and Spectrograph
ESA	European Space Agency
ExoPy	Exo-planets and Exo-moons Python
GPI	Gemini Planet Imager
HEK	Hunt for Exomoons with Kepler
HZ	Habitable Zone
JWST	James Webb Space Telescope
NASA	National Aeronautics and Space Administration
PLATO	Planetary Transits and Oscillations of stars
PyMieDAP	Python Mie Doubling-Adding Program
SPHERE	Spectro-Polarimetric High-contrast Exoplanet Research
TDV	Transit Duration Variation
TESS	CHaracterising ExOPlanets Satellite
TPF	Terrestrial Planetary Finder
TTV	Transit Timing Variation
VLT	Very Large Telescope
XAO	eXtreme Adaptive Optics

Astronomical Constants

a_m	Semi-major axis of the Moon orbit around the Earth	384 748 km
AU	Astronomical Unit	149 597 870 700 m
G	Universal gravitational constant	$6.697\,408(31) \times 10^{-11} \text{ m}^3 \cdot \text{kg}^{-2} \cdot \text{s}^{-1}$
M_{J}	Mass of Jupiter	$1.898 \times 10^{27} \text{ kg}$
pc	Parsec	3.26 light years

Greek Symbols

$\alpha, \alpha_m, \alpha_p$	Phase angle: angle between the star and the observer as seen from the observed moon/planet
α_A	Angular radius of body A as seen from a pixel on body B during an eclipse event
α_i	Planet azimuthal angle: angle between the star and the observer as seen from pixel i on the planet/moon disk
β, β_i, β_j	Angle between the local meridian plane and the local scattering plane as seen from a pixel on the planet (β_i) or moon (β_j)
β_i	Angle between the position of pixel i on body B and the body A (or star S) as measured from point O_1 during an eclipse event
χ	Direction of polarization
Δt	Time interval between observations
δ	Angular distance between the body A and the star S as seen from a pixel on body B during an eclipse event
δ	Particle depolarization factor
$\delta, \delta_i, \delta_j$	Angle between the star-to-body vector and the pixel–zenith direction, centre at a planet pixel i /lunar pixel j
η	Angle between the position of body B and the star S as measured from auxiliary point O_3 during an eclipse event
v_{bs}	True anomaly of the planet–moon system barycentre position along its orbit around the star
v_{eff}	Second of the two–parameters defining the Gamma cloud particle size distribution in the planetary atmosphere
v_{mb}	True anomaly of the moon position along its orbit around the planet–moon system barycentre
Ω	Semi-aperture of the penumbral cone
ω_i	Angle between the position of pixel i on body B and the body A as measured from point O_2 during an eclipse event
Ω_{bs}	Right ascension of the ascending node of the planet–moon system barycentre orbit around the star
ω_{bs}	Argument of perihelion of the planet–moon system barycentre orbit around the star
Ω_{mb}	Right ascension of the ascending node of the lunar orbit around the planet–moon system barycentre
ω_{mb}	Argument of perihelion of the lunar orbit around the planet–moon system barycentre
$\phi - \phi_0, \phi_i - \phi_{0,i}$	Azimuthal difference angle: angle between the plane containing the local zenith direction and the direction towards observer and the plane containing the local zenith direction and the direction towards the star ass seen from pixel i
Ψ	Semi-aperture of the umbral and antumbral cones
ψ	Angle between the lunar scattering plane and the planet–moon system scattering plane
ρ	Angle between the position of body B and body A as measured from auxiliary point O_4 during an eclipse event
τ_c	Cloud particles' optical thickness

θ	Angle between the position of body B and the body A (or star S) as measured from point O_5 during an eclipse event
θ, θ_i	Observer–zenith angle: angle between the local zenith direction and the direction towards observer as seen from pixel i
$\theta_0, \theta_{0,i}$	Solar–zenith angle: angle between the local zenith direction and the direction towards the star as seen from pixel i
φ_{ob}	Observer azimuthal angle
ϑ_{ob}	Observer polar angle
ζ_p	Planet azimuthal angle: angle between the x_0-z_0 plane and the planet scattering plane

Roman Symbols

α_S	Angular radius of the star S as seen from a pixel on body B during an eclipse event
\mathbb{T}_x	Three-dimensional clockwise elemental rotation around the x -axis
\mathbb{T}_y	Three-dimensional clockwise elemental rotation around the y -axis
\mathbb{T}_z	Three-dimensional clockwise elemental rotation around the z -axis
\mathbb{T}_{01}	Three-dimensional rotation matrix from reference frame S_1 to S_0
\mathbb{T}_{0r}	Three-dimensional rotation matrix from reference frame S_r to S_0
\mathbb{T}_{12}	Three-dimensional rotation matrix from reference frame S_2 to S_1
\mathbb{T}_{23}	Three-dimensional rotation matrix from reference frame S_3 to S_2
$\mathbb{T}_{r'r}$	Three-dimensional rotation matrix from reference frame S_r to S'_r
\mathfrak{D}	Moon–planet separation in units of the planet's Hill sphere radius
\mathbf{F}	Stokes vector
$\mathbf{F}_i, \mathbf{F}_j^m, \mathbf{F}_i^p$	Stokes vector of reflected light by lunar pixel j and planetary pixel i
\mathbf{L}	Stokes vector rotation matrix
\mathbf{R}_1	First column of the local planetary reflection matrix
\vec{r}_m	Moon position vector with respect to the planet–moon–star three–body system barycentre
\vec{r}_p	Planet position vector with respect to the planet–moon–star three–body system barycentre
\vec{r}_s	Star position vector with respect to the planet–moon–star three–body system barycentre
\vec{r}_{AB}	Position vector of body B on with respect to body A during an eclipse/transit event
\vec{r}_{Ai}	Position vector of pixel i with respect to body A during an eclipse/transit event
\vec{r}_{AS}	Position vector of the star S with respect to body A during an eclipse/transit event
\vec{r}_{bs}	Planet–moon system barycentre's position vector with respect to the star
\vec{r}_{ip}	Position vector of pixel i on the planet with respect to the planet centre
\vec{r}_{is}	Position vector of pixel i on the planet with respect to the star centre
\vec{r}_{jm}	Position vector of pixel j on the moon with respect to the moon centre
\vec{r}_{js}	Position vector of pixel i on the moon with respect to the star centre
\vec{r}_{mp}	Moon position vector with respect to the planet

\vec{r}_{ms}	Moon position vector with respect to the star
\vec{r}_{pb}	Moon position vector with respect to the planet–moon system barycentre
\vec{r}_{pb}	Planet position vector with respect to the planet–moon system barycentre
\vec{r}_{ps}	Planet position vector with respect to the star
A	Eclipsing/transiting body centre label during eclipse/transit event
A_o	Overlapping area between the body A and the star S as observed from a specific pixel on body B during an eclipse event
A_S	Total stellar bright area observed from a specific pixel on body B during an eclipse event
a_{bs}	Semi-major axis of the planet–moon system barycentre orbit around the star
a_{mb}	Semi-major axis of the lunar orbit around the planet–moon system barycentre
a_{surf}	Surface albedo
B	Shadowed body centre label during eclipse/transit event
b	Planet–moon system barycentre position label
b, b_i, b_j	Weighting factor for the blocking of a pixel from sight due to mutual transits events at a specific planetary/lunar pixel
$b(R)$	Stellar brightness at distance R from the centre of body A as viewed projected onto the sky plane from a point on the shadowed body B during an eclipse event
c, c_i, c_j	Weighting factor for the dimming of stellar flux due to mutual eclipses at a specific planetary/lunar pixel
d, d_i, d_j	Weighting factor for the dependence of the stellar flux that is incident on a planetary/lunar pixel to distance.
dq	Differential of stellar flux along an elementary ring on the stellar disk
E	Eccentric anomaly
e'_i	Expected flux hitting pixel i on the planet/moon in the absence of eclipse events
e_i	Flux hitting pixel i on the planet/moon
e_{bs}	Eccentricity of the planet–moon system barycentre orbit around the star
e_{mb}	Eccentricity of the lunar orbit around the planet–moon system barycentre
F	Total flux. First Stokes vector component
i	Index matching a specific pixel across the planetary disk
i_{bs}	Inclination of the planet–moon system barycentre orbit around the star
i_{mb}	Inclination of the lunar around the planet–moon system barycentre
j	Index matching a specific pixel across the lunar disk
M	Mean anomaly
m	Moon position label
m_g	Molecular mass of Earth–like gas mixture
m_m	Mass of the moon

m_p	Mass of the planet
m_s	Mass of the star
n	Number of bodies in the system ($n = 3$)
N^{eq} , N_p^{eq} , N_m^{eq}	Number of pixels along the equator of a planet/moon body
N_m	Number of pixels on the disk of the moon
N_p	Number of pixels on the disk of the planet
n_r	Cloud particles' refractive index
O_1	Apex position of the umbral and antumbral cones
O_2	Apex position of the penumbral cone
O_3	Auxiliar point along the star–body A line delimiting the region of full umbral eclipse during an eclipse event
O_4	Auxiliar point along the star–body A line delimiting the region of no–eclipse during an eclipse event
O_5	Auxiliar point along the star–body A line delimiting the region of no–umbral eclipse during an eclipse event
P	Degree of polarization
p	Planet position label
p_1	Reference plane for the definition of the barycentre's orbit. For $\theta_{ob} = 0^\circ$ and $\phi_{ob} = 0^\circ$ p_1 coincides with the plane of sky
p_2	Plane defined by the barycentre's orbit around the star
p_3	Plane defined by the moon's orbit around the planet–moon system barycentre
p_c	Pressure at the cloud top level
p_{surf}	Air pressure at the surface level
Q	Linearly polarized flux (horizontal–vertical direction). Second Stokes vector component
R_A	Radius of eclipsing body A during eclipse/transit event
R_B	Radius of shadowed body B during eclipse/transit event
R_m	Radius of the moon
R_p	Radius of the planet
R_S	Radius of star
r_{eff}	First of the two–parameters defining the Gamma cloud particle size distribution in the planetary atmosphere
S	Star centre label
s	Star position label
S'_r	Rotating reference frame centre at the star, with the z'_r –axis directed towards the observer and the plane x'_r – z'_r passing through the moon centre
S_0	Observer's reference frame

S_1	Reference frame for the definition of the planet–moon system barycentre’s orbit around the star
S_2	Reference frame for the definition of the lunar orbit around the planet–moon system barycentre
S_3	Reference frame for the definition of the two-dimensional orbit of the moon around the planet–moon system barycentre
S_r	Rotating reference frame centre at the star, with the z_r -axis directed towards the observer and the plane x_r – z_r passing through the planet centre
$T(h_o)$	Transmission of rays passing at a distance h_o from the centre of body B during an eclipse event
t_f	Final simulation time
T_{bs}	Orbital period of the planet–moon system barycentre trajectory around the star
T_{mb}	Orbital period of the lunar trajectory around the planet–moon system barycentre
U	Linearly polarized flux ($\pm 45^\circ$ direction). Third Stokes vector component
V	Circularly polarized flux. Fourth Stokes vector component

List of Figures

1.1	Artist impression of an extrasolar moon–planet system	2
1.2	Cumulative number of exoplanet detections with time per detection method	4
1.3	Examples of directly imaged planetary systems around stars 2M1207 and HR8799	6
1.4	Illustration of the definition of direction of polarization and generation of polarization by molecular scattering	7
1.5	High level flow diagram for a standard simulation with <i>ExoPy</i>	10
2.1	Graphical representation of polarization states and correlation with the Stokes vector	13
2.2	Three-dimensional view and projection onto the x_0 – y_0 plane of a discretized planet or moon	14
2.3	Graphical definition of phase angle α and its influence on the observed exoplanet and exomoon disks	15
2.4	Three-dimensional sketch and simulation results of mutual events between bodies	16
2.5	Graphical illustration of the planetary and lunar scattering planes, as well as the angle ψ	17
3.1	Sketch of the three-dimensional Keplerian orbit of the planet–moon system barycentre around the parent star	23
3.2	Sketch of the two-dimensional Keplerian orbit of the planet–moon system barycentre around the parent star	24
3.3	Sketch of the three-dimensional Keplerian orbit of the moon around the planet–moon system barycentre	24
3.4	Sketch of the two-dimensional Keplerian orbit of the moon around the planet–moon system barycentre	25
3.5	Sketch of the reference frames and orbital geometry of an edge-on planet–moon system and a face-on planet–moon system	26
3.6	Geometry involved in the rotation of the observer coordinate system, S_0	30
3.7	Graphical definition of the rotating reference frame S_r	31
3.8	Angular geometry of the spherical triangle centred at pixel i and defined by the zenith direction unit vector, the observer’s direction unit vector, and the star direction unit vector	33
3.9	Graphical definition of the β angle between the pixel-based local meridian plane and the scattering plane	35
3.10	Graphical interpretation of the inverse-square law	36
3.11	Geometry involved in the determination of the night side of the planetary disk	37
4.1	Sketch illustrating the modelled mutual events between bodies	40
4.2	Graphical representation of a stellar eclipse modelled by a parallel and conical rays approach	43
4.3	Illustration of a differential elementary ring for the integration of the total stellar flux hitting a specific pixel	44
4.4	Geometrical description of a generic eclipse scenario	45
4.5	Stellar and eclipsing body disks as seen from a pixel on the shadowed body	48
4.6	Stellar and eclipsing body disks as seen from a pixel on the shadowed body	49
4.7	Geometrical description of a generic transit scenario	51
5.1	Sketch illustrating the orbital geometry of the edge-on planetary system	54
5.2	Pixel distribution of the three first Stokes parameters and the direction of polarization for the planet and moon at phase angle $\alpha = 0^\circ, 50^\circ$	56
5.3	Total flux, linearly polarized fluxes and degree of linear polarization results as a function of phase angle for an edge on system	58

5.4 Sketch illustrating the sequence of planetary and lunar transits, as well as planetary and lunar eclipses for a fraction of the barycentre's orbit on an edge-on system	59
5.5 Flux relative difference between the baseline and the continuum results	61
5.6 Degree of polarization absolute difference between the baseline and the continuum results	61
5.7 Ingress transit direction during lunar and planetary transits	62
5.8 ΔF results during lunar transits as a function of lunar true anomaly and relative time . .	63
5.9 Illustration of lunar transit duration variations with phase angle	63
5.10 ΔP results during lunar transits as a function of lunar true anomaly and relative time . .	64
5.11 ΔF results during planetary transits as a function of lunar true anomaly and time . . .	65
5.12 Illustration of planetary transit duration variations with phase angle	65
5.13 ΔP results during planetary transits as a function of lunar true anomaly and time . . .	66
5.14 Geometrical definition of the φ_{ms} angle between the star and the moon as measured from the planet position	66
5.15 ΔF results during planetary eclipses as a function of angle φ_{ms} and time	67
5.16 ΔP results during planetary eclipses as a function of angle φ_{ms} and time	68
5.17 ΔF results during lunar eclipses as a function of angle φ_{ps} and time	68
5.18 ΔP results during lunar eclipses as a function of angle φ_{ps} and time	69
5.19 Probability of mutual event observation as a function of sampling time and total observation time	71
5.20 Maximum probability of mutual events observation as a function of the total duration of the observation	72
5.21 Maximum $ \Delta P $ and $ \Delta F $ results maps as a function of observer azimuth angle and polar angle	73
5.22 Phase angle for maximum $ \Delta P $ and $ \Delta F $ maps as a function of observer azimuth angle and polar angle	74
5.23 Graphical definition of the sidereal, T_{mb} , and lunar synodic periods, T'_{mb}	75
5.24 Power Spectral Density of the unresolved planet–moon system polarization signal for an edge–on system	76
5.25 Power Spectral Density of the unresolved planet–moon system polarization signal for a face–on system	77
 6.1 $ \Delta F_{\max} $ and $\Delta F_{\text{alb max}}$ as a function of lunar semi-major axis	80
6.2 ΔP_{\max} as a function of lunar semi-major axis	80
6.3 ΔF and ΔP as a function of time for varying lunar surface albedo during a lunar eclipse at $\alpha = 87.1^\circ$	81
6.4 ΔF and ΔP as a function of time for varying lunar surface albedo during a planetary eclipse at $\alpha = 72.5^\circ$	82
6.5 F and P as a function of phase angle for varying lunar radius	83
6.6 Flux and degree of polarization curves during lunar transit at $\alpha = 67.2^\circ$ and planetary eclipse at $\alpha = 72.5^\circ$ for varying lunar radius	84
6.7 $ \Delta F_{\max} $ results as a function of moon–to–planet radius ratio for planetary darkening events	85
6.8 $ \Delta P_{\max} $ results as a function of moon–to–planet radius ratio for planetary darkening events	85
6.9 $ \Delta F_{\max} $ results as a function of moon–to–planet radius ratio for lunar darkening events .	86
6.10 Flux and degree of polarization curves during planetary transit at $\alpha = 80.6^\circ$ and lunar eclipse at $\alpha = 87.1^\circ$ for varying lunar radius	87
6.11 $ \Delta P_{\max} $ results as a function of moon–to–planet radius ratio for lunar darkening events .	88
6.12 ΔF results during the lunar transit at $\alpha = 67.2^\circ$ and subsequent planetary eclipse, and the planetary transit at $\alpha = 80.6^\circ$ and subsequent lunar eclipse, as a function of time for increasing lunar eccentricity	89
6.13 Generic edge–on eccentric lunar orbit configuration around the planet	90
6.14 Flux and degree of polarization curves during lunar transit at $\alpha = 67.2^\circ$ for varying lunar eccentricity	90
6.15 Sketch of maximum lunar inclination for transits occurrence	91
6.16 Sketch of maximum lunar inclination for lunar eclipses occurrence	92
6.17 Sketch of various transit and eclipse scenarios with varying lunar impact parameter, inclination, and line of nodes orientation	93

6.18 Flux and degree of polarization curves during lunar transits at $\alpha = 0^\circ, 90^\circ$ for varying lunar impact parameter	94
6.19 Flux and degree of polarization curves during lunar eclipses at $\alpha = 0^\circ, 90^\circ$ for varying lunar impact parameter	95
6.20 ΔF and ΔP results during lunar and planetary transit at $\alpha = 67.2^\circ, 80.6^\circ$ as a function of time for varying orbital inclination and lunar line of nodes aligned with the planet–observer line	96
6.21 $ \Delta P $ results as a function of time and lunar orbit inclination for $\Omega_{bm} = 330^\circ$	97
A.1 Absolute error in the disk integrated flux of a Lambertian reflecting body	105
A.2 Simulation results for the blocked planetary reflected light during lunar transit	106
A.3 Predicted eclipse path for three different solar eclipses at Earth	108
B.1 Planetary reflected flux phase curves for varying cloud particle size	109
B.2 Degree of polarization phase curves for varying cloud particle size	110
B.3 Trade-off analysis on number of pixels along the equator	112
B.4 ΔF_n and ΔP_n as a function of phase angle	113
B.5 Trade-off analysis on number Gauss points n_{mug}	114
C.1 Maximum $ \Delta P $ and $ \Delta F $ interpolated maps as a function of observer azimuth angle and polar angle	116
C.2 Phase angle for maximum $ \Delta P $ and $ \Delta F $ interpolated maps as a function of observer azimuth angle and polar angle	117
C.3 Continuum F and P as a function of phase angle for varying lunar albedo	118
C.4 $\Delta F_{\text{continuum}}$ as a function of relative time for increasing lunar albedo	119
C.5 F and P as a function of relative time for increasing lunar albedo during transit events .	120
C.6 F and P as a function of relative time for increasing lunar albedo during eclipse events .	121
C.7 ΔF and ΔP as a function of relative time for increasing lunar albedo during transit events	122
C.8 ΔF and ΔP as a function of relative time for increasing lunar albedo during eclipses events	123
C.9 $\Delta F_{\text{alb max}}$ results as a function of moon-to-planet radius ratio for planetary and lunar darkening events	124
C.10 $\Delta F_{\text{continuum}}$ as a function of relative time for increasing lunar radius	125
C.11 F and P as a function of relative time for increasing lunar radius during transit events .	126
C.12 F and P as a function of relative time for increasing lunar radius during eclipse events .	127
C.13 ΔF and ΔP as a function of relative time for increasing lunar radius during transit events	128
C.14 ΔF and ΔP as a function of relative time for increasing lunar radius during eclipses events	129
C.15 ΔF results during a series of lunar transits and subsequent planetary eclipses, and plan- etary transits and subsequent lunar eclipses, as a function of time for increasing lunar eccentricity.	130
C.16 ΔP results during a series of lunar transits and subsequent planetary eclipses, and plan- etary transits and subsequent lunar eclipses, as a function of time for increasing lunar eccentricity.	131
C.17 ΔF and ΔP as a function of relative time for increasing lunar orbit eccentricity during transit events	132
C.18 F and P as a function of relative time for increasing lunar orbit eccentricity during transit events	133
C.19 ΔF and ΔP as a function of relative time for increasing moon orbit inclination during transit events, being the lunar line of nodes aligned with the planet–observer line	134

List of Tables

2.1	Parameters of the planet and moon models	18
3.1	Parameters of the barycentre and lunar orbits describing the edge-on and face-on reference systems	27
5.1	Planet-moon system barycentre and moon's orbital elements for the edge-on extrasolar system	54
5.2	Relation of parameters defining the planet and moon reflection properties	55
5.3	Timing variations during planetary transits with increasing phase angle	69
5.4	Timing variations during lunar eclipses with increasing phase angle	69
A.1	Results of the transits model verification	107
A.2	Modified lunar orbital elements for the verification of the eclipses model	107
A.3	Results of the eclipses model verification	108
B.1	Phase curve computation time for clear and cloudy atmosphere models	110

Introduction

As I stand out here in the wonders of the unknown at Hadley, I sort of realize there's a fundamental truth to our nature, Man must explore... and this is exploration at its greatest.

Dave Scott, Commander Apollo 15, 31 July 1971

The calling of exploration has led humankind to the far corners of this planet. Humans for centuries have explored out of scientific curiosity or to improve their current standings. With limited possibilities in the solar system, humankind is turning their focus beyond the limits of our solar system. The study of the stars and the solar system is as old as civilization and continues to inspire generation of scientists. As of 2015, human-kind have visited all eight planets in the solar system, have landed on Near-Earth Objects and explored the Pluto-Charon system in the Kuiper Belt. On the verge of searching for signs of life among the Jovian moons and starting the human colonization of Mars, new technology allows for finding new prospects of exploration.

In this way, the stars that once guided our early explorers throughout their sailing expeditions are today subjected to a constant monitoring. These stars are now the target for space exploration, as exemplified by the ambitious proposed Breakthrough Starshot mission¹.

Since the detection of the first substellar mass objects beyond our Solar System [Campbell et al., 1988, Wolszczan and Frail, 1992], the number of exoplanets discovered breaks records each year², resulting in a total of over 3600 confirmed discoveries [Schneider et al., 2011] and almost 2500 unconfirmed candidates to this day [Han et al., 2014]. Conservative estimates foresee the existence of at least 100 billion planets in the Milky Way [Cassan et al., 2012] and at least 2 trillion galaxies in the observable universe [Conselice et al., 2016]. The forthcoming space observatories, such as Characterising ExOPlanet Satellite (CHEOPS), PLAnetary Transits and Oscillations of stars (PLATO), Transiting Exoplanet Survey Satellite (TESS), and (to an extent) James Webb Space Telescope (JWST), aim at continuing the trend in exoplanet discoveries. The upgraded sensitivity of these missions even allow for the search to lunar companions and planetary rings.

The continuous increase in instrument precision and spatial resolution has made possible the debut of a new generation of ground instruments, such as the Gemini Planet Imager (GPI) instrument [see Macintosh et al., 2014] on the Gemini North telescope, the Spectro-Polarimetric High-contrast Exo-planet Research (SPHERE) instrument [see Beuzit et al., 2006] used on the Very Large Telescope (VLT) and the proposed Exoplanet Imaging Camera and Spectrograph (EPICS) [see Gratton et al., 2010, Keller et al., 2010] on the under construction European Extremely Large Telescope (E-ELT). These have the capability to perform high contrast direct imaging and characterization of extrasolar systems through spectroscopy and polarimetry techniques.

Direct detection of extrasolar bodies presents a major challenge as their observed radiation, both emitted and reflected, is very weak compared to the hosting star. In addition, the angular distance from

¹Breakthrough Starshot project overview available at <https://breakthroughinitiatives.org/Initiative/3>

²Updated databases of proposed and confirmed exoplanet discoveries are provided by the Extrasolar Planets Encyclopaedia at <http://exoplanet.eu/>, the NASA Exoplanet Archive at <http://exoplanetarchive.ipac.caltech.edu/> and the Exoplanets Data Explorer at <http://exoplanets.org/>.

the planet to the star is extremely small. Consequently, the vast majority of exoplanets have only been detected indirectly. In contrast, direct imaging of the planet can reveal a wealth of information of the planet properties. One of the main metrics of interest for direct imaging is the flux and polarization.

In this work, we analyse how the presence of an orbiting Moon-sized Lambertian exomoon influences the flux and degree of polarization of the starlight reflected by an Earth-like exoplanet. It is shown that, under favourable orbital configurations and directions of observation, the occurrence of mutual shadowing events may lead to the detection and, ultimately, characterization of the exomoon. We study the shape of the expected variations of flux and degree of polarization during mutual events as well as the likelihood of such events to be detected, in an attempt to find an answer to the research questions posed in Section 1.5.

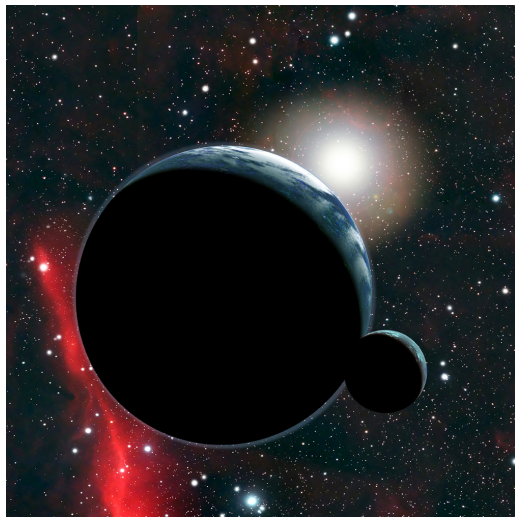


Figure 1.1: Artist impression of an extrasolar moon-planet system (credit D. Aguilar, CfA).

This introductory chapter aims at providing an introduction to the exomoon exploration field in Section 1.1, followed by a analysis of the state of the art on exomoon detection techniques in Section 1.2. Right after, Section 1.3 provides a closer look at direct imaging of extrasolar systems and Section 1.4 introduces the reader into the concept of polarimetry and analyses its current uses in extra-solar exploration and potential use in exomoon detection. The research goal, research questions and research objectives are posed in Section 1.5, while the research methodology is described in Section 1.6. Finally, we provide an overview of the thesis outline in Section 1.7.

1.1. Why study exomoons?

The Solar System hosts 8 planets and 149 known natural satellites³, 19 of which are large enough to be gravitationally rounded. Six of the eight planets in our Solar System are orbited by moons, which vary greatly in size, structure, and atmosphere, and with many secrets to be unveiled. Titan and Io are prime example for geological processes and Europa and Enceladus have proven to be the most promising targets for the search of extraterrestrial life. It is without doubt, that the moons in our solar system are very interesting targets.

Unfortunately, no moons have been detected beyond the limits of our solar system. The best candidate so far comes from the ring system around J1407b [Kenworthy and Mamajek, 2015]. However, this does not allow for claiming the first discovery. The lack of exomoons, in combination of the unexpected abundance of close-in planet orbiting close to the parent star [Heller et al., 2016a], raises the question how special our solar system. Are the gas giants with their moon system an outlier in the universe?

The discovery of the first exomoons will constitute a major milestone in exoplanet research and will help us further develop our understanding in, at least, three different directions.

³Data retrieved from <https://solarsystem.nasa.gov/planets/>.

1. Exomoon habitability

The increasing discovery of exoplanets has further intensified interest in the search for extraterrestrial life. Planets that traverse their Habitable Zone (HZ), i.e. the distance from a star in which a planetary surface may pertain some degree of liquid water (ultimately subjected to the presence of an atmosphere capable of holding the surface gases) [Hinkel and Kane, 2013], are candidates for supporting life. This search has been extended to exomoons, and studies on extrasolar satellite habitability have been carried out during the last decade. Giant gaseous planets within the stellar HZ are predicted to host habitable environments on hypothetical Earth-sized satellites [Canup and Ward, 2006]. In such case, Reynolds et al. [1987] and Heller and Barnes [2015] point out the importance of the moon's orbital history on the possible surface water content, potentially creating conditions that could support the existence of life in particular cases. In this direction, Scharf [2006] concluded that tidal heating could maintain surface temperatures compatible with life for large moons around cold giant planets. However, excessive tidal and planetary emitted radiation might turn the lunar surface completely sterile and eclipse times might produce enormous climate variations thus threatening their habitability [Forgan and Yotov, 2014, Heller, 2012, Heller and Barnes, 2013].

Recent research by Lehmer et al. [2017] shows that even small moons would be able to retain their atmosphere for a limited period of time, while Ganymede-sized moons falling into the stellar HZ could hold an atmosphere and surface water indefinitely. Thus, everything suggests natural satellites are potential candidates for hosting extraterrestrial life. This puts satellites in the spotlight of the scientific community.

2. Extra-solar system characterization

Detection and characterization of exomoons and their interaction with their hosting planet will not only provide information on lunar orbit and physical properties (e.g. mass, density, surface and atmosphere composition), but will allow for constraining some of the planetary characteristics. Among others, the planetary mass [Kipping et al., 2009, Schneider et al., 2015], planetary oblateness, and rotation axis [Barnes and Fortney, 2003, Schneider et al., 2015] are expected to be derived by comparing future observations with orbit dynamics models.

The signal from a planet-moon system could easily be observed as that of a single planet. For big moons, the impact on planetary characteristics would involve an overestimation of the planetary mass and effective temperature [see Williams and Knacke, 2004]. Moreover, when performing spectral studies of the target for composition analysis, the identified planetary and lunar components would be thought to be present at one unique body. As claimed by Schneider et al. [2015], the simultaneous detection of water (H_2O), oxygen (O_2), ozone (O_3), methane (CH_4), and carbon dioxide (CO_2) on a planet would suggest possible biological activity, while this argument does not stand if any of these compounds are not found on the planet but its orbiting moon instead. In fact, an accurate characterization of an extra-solar system would require exhaustive analysis on all potential existing elements, i.e. star, planets, moons, ring particles.

3. Planetary formation theories

The study of moons in our solar system have yielded essential insight on the formation mechanism and evolution of our solar system [see Heller, 2017, and references therein]. While some of the satellites are thought to be formed from early circumplanetary debris, e.g. the major moon of Neptune, Uranus and Saturn, other such as our Moon [Rufu et al., 2017] and the small Martian satellites Phobos and Deimos [Rosenblatt et al., 2016] suggest a cumulative bombardment as the most probable theory. Moreover, the existence of Neptune's Triton moon is probably explained by the capture of a minor planet [Agnor and Hamilton, 2006], while collisions are thought to have altered the relative alignment between Uranus and its moons [Morbidelli et al., 2012].

The examples provided above illustrate the invaluable importance of exomoon research as a means to further understand and refine current planetary formation theories in a way that could not be achieved by mere observation of exoplanets.

To this day, exomoons remain as silent planetary companions. Mars-sized (and even probably Ganymede-sized) satellites are thought to be traceable in current archived Kepler data [Heller et al., 2014]. Consequently, increasing effort is being placed on the development of techniques for exomoon detection. These are detailed below.

1.2. On the trail of exomoons

Exoplanets are extremely faint light bodies compared to their parent star. Their proximity to the star (in the order of astronomical units (AU)) together with the great distance of the stellar light spot to the observer (in the order of light years) implies an extremely small observed angular separation between the bodies. This problem is specially acute when looking for extra-solar satellites given their smaller size and proximity to the planet. Consequently, only a reduced number of exoplanets (1.2% of total discoveries to this day [NASA's Jet Propulsion Laboratory]) have been directly imaged (see Figure 1.2), while indirect detection techniques have granted an increasing number of discoveries.

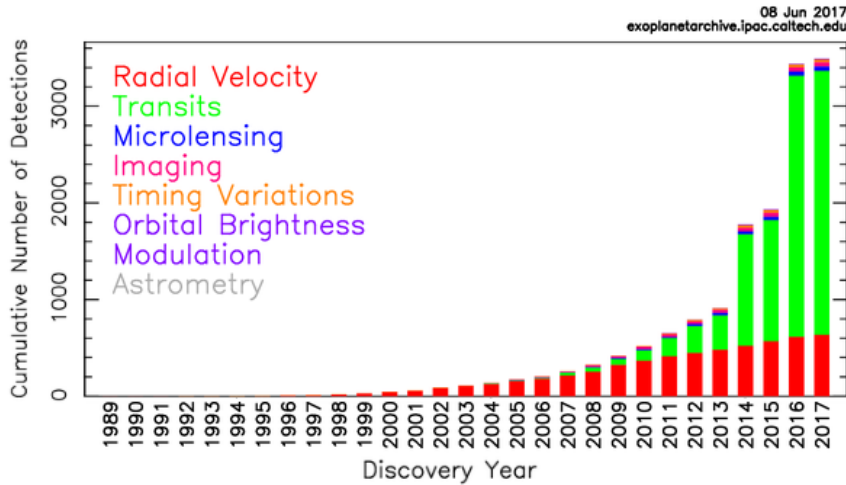


Figure 1.2: Cumulative number of exoplanet detections with time per detection method. Distinction is made between direct detections (imaging) and indirect detections (radial velocity, transits, microlensing, timing variations, orbital brightness, modulation, and astrometry). Resource available at <http://exoplanetarchive.ipac.caltech.edu/>.

With the discoveries of the first exoplanets, Sartoretti and Schneider [1999] envisaged that exomoons could be detected using the well-known method of transit photometry. In a nutshell, bodies interposing between a distant star and our position as observers exhibit as a drop in stellar brightness which is proportional to the radius of the body squared and repeats every orbital period [see e.g. Winn, 2010a]. NASA's Kepler space observatory has been continually monitoring the brightness of 145000 stars yielding an incommensurable amount of light curves from which thousands of exoplanets have been discovered.

Sartoretti and Schneider [1999] suggested that the exomoon contribution to the stellar dimming could yield key information on the lunar properties and orbit. Almost two decades later, more than a dozen indirect methods for exomoon detection have been developed. According to the classification presented by Heller [2017], we can distinguish between three types of indirect exomoon detection methods: (1) direct photometric transits signatures of exomoons, (2) dynamical effects of planetary transits, and (3) other methods. We will discuss these three types below.

1. Direct photometric transits signatures of exomoons

Exomoons are expected to contribute to the stellar dimming in case of transiting the star together with the planet, bringing forward (delaying) the start of the transit event in the case of leading (trailing) satellites. Complex configurations involving multiple planets and moons transiting each other have been studied by Pál [2012], Sato and Asada [2009], obtaining fluctuating light curves from which the radii, distance, masses, and system configuration (i.e. binary system or planet–satellite system) could be retrieved.

Unfortunately, the lunar contribution is very small compared to the planetary one and, thus, it could be easily hidden in the light curves noise resulting from the intrinsic stellar activity [see e.g. Gilliland et al., 2011] if the lunar size was not large enough [Tusnski and Valio, 2011]. In order to increase the signal-to-noise ratio, Heller [2014], Heller et al. [2016a] propose to combine big amounts of light curves into one single superstack curve which can then be used to search for moon traces [Hippke, 2015] on a method known as the Orbital Sampling Effect.

2. Dynamical effects of planetary transits

Alternatively to observing the faint contribution of lunar transits, the presence of exomoons can be indirectly inferred by observing the planet–moon dynamics effect on the planetary transits. Two different methods can be differentiated: the study of planet’s Transit Timing Variations (TTVs) and Transit Duration Variations (TDVs).

Opposite to the case of a single planet, in a planet–moon system both bodies orbit around their common center of mass referred to as barycentre. Such rotation entails a slightly different time of planetary transit start (TTV), breaking the complete periodicity of the signal [see Kipping, 2009a, Sartoretti and Schneider, 1999, Simon et al., 2007, 2015, Szabó et al., 2006]. Therefore, measuring the ingress, center and/or egress time differences between successive planetary transits may yield TTVs on the order of seconds–minutes which would point out the presence of a lunar companion [Heller, 2017].

As the planet transits its star, the absolute planetary velocity vector is the result of summing the barycentre’s velocity and the relative velocity on its motion around the barycentre. Depending on the planet/moon position along its orbit around the barycentre, the relative speed component can contribute positively or negatively to the total tangential planetary velocity across the star, resulting in a variation of the total transit duration (TDV) between successive light curves [see Kipping, 2009a]. The amplitude of the TDV is augmented if the planet–moon system orbital plane is inclined with respect to the barycentre’s stellar orbit [Kipping, 2009b].

3. Other methods

Alternative exotic detection techniques imply the use of gravitational microlensing [Han and Han, 2002], which led to the discovery of a free-floating exoplanet–exomoon candidate by Bennett et al. [2014], planet pulsar timing variations [Lewis et al., 2008], generation of plasma tori of volcanic active exomoons [Ben-Jaffel and Ballester, 2014], among others [see Simon et al., 2010, 2012, Williams and Knacke, 2004, Zhuang et al., 2012].

From all methods enumerated above, only those employing photometric observations allow to carry out systematic exomoon surveys. The first and only exhaustive search for exomoons is carried out through the project *Hunt for Exomoons with Kepler (HEK)* [Kipping et al., 2012], which makes use of combined photometric transits, TTV, and TDV data. The most recent summary on the exomoon survey does not unveil the detection of any exomoon, even though great hope is placed in upcoming analyses [Kipping et al., 2015].

During the next years, the exomoon search will continue by analysing all archived photometric observations from Kepler and the COnvection ROtation and planetary Transits (CoRoT) space observatory. Alternatively, the combined use of data from the upcoming CHEOPS, TESS, and PLATO would offer a compelling opportunity for exomoon discovery [Heller et al., 2016b].

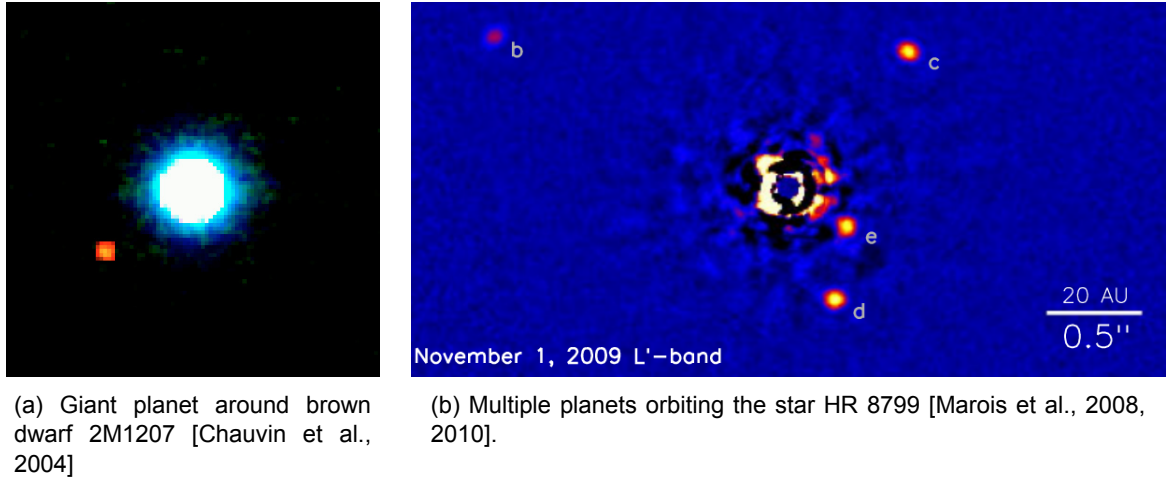
The discovery of the first exomoon would confirm the existence of natural satellites out of the Solar System and would allow a limited characterization of the exomoon properties and its orbit. The use of direct detection techniques is expected to overpass this limitation and bring in-depth lunar details. Hereafter, an overview of the current state of the art on direct imaging of extra-solar bodies is provided.

1.3. Direct Imaging of extrasolar systems

Direct imaging of the emitted and/or reflected radiation by exoplanets is extremely challenging because of the need to overcome three major barriers [Traub and Oppenheimer, 2010a]: (1) the low planet–star contrast, i.e. the ratio of planetary to star flux imposed by astrophysics, (2) light diffraction imposed by physics, and (3) light scattering originated by polishing and/or reflectivity engineering errors which introduce speckles in the final image. Additionally, Earth base telescopes have to deal with wave-front errors originated by the atmospheric turbulences.

Current technology allows to image planetary companions under special circumstances, i.e. young hot giant planets orbiting cold stars or dim brown dwarfs at large distances (10–40 AU). For this, a combination of different techniques such as coronagraphy [Roddier and Roddier, 1997], eXtreme Adaptive Optics (XAO) [Fusco et al., 2006], and Angular Differential Imaging (ADI) [Traub and Oppenheimer, 2010a], together with image post-processing, allow to overcome the effect of optical speckles and increase the effective contrast up to 10^{-6} in the Near Infrared J, H and K bands (1.1 to 2.4 μm) [Hugot et al., 2012].

The first imaged candidate planet came by the hand of Chauvin et al. [2004], who found a $5 \pm 2 M_{\oplus}$ ⁴ companion orbiting the young brown dwarf 2M1207 at 55 AU distance using the NACO adaptive optics instrument of the VLT (see Figure 1.3a). It was not until 2008 when the first exoplanet, Fomalhaut b, was imaged orbiting around a normal star (i.e. not a brown dwarf) at 119 AU using the HST [Kalas et al., 2008]. Since then, multiple exoplanets have been added to the list of discoveries, including highlights such as the (at least) quadruple planetary system around the 40 pc distance HR 8799 star discovered by Marois et al. [2008, 2010] (see Figure 1.3b) and the $4^{+4.5}_{-1.0} M_{\oplus}$ Jovian exoplanet orbiting the Sun-like star GJ 504 by Kuzuhara et al. [2013].



(a) Giant planet around brown dwarf 2M1207 [Chauvin et al., 2004]

(b) Multiple planets orbiting the star HR 8799 [Marois et al., 2008, 2010].

Figure 1.3: Examples of directly imaged planetary systems. Figure 1.3a shows a composite image of the brown dwarf 2M1207 and its giant planet companion in H (blue), K_s (green) and L' (red) bands [Chauvin et al., 2004, Girard et al., 2011]. Figure 1.3b shows a L' band image of the star HR8799 and the four observed companions observed by November 2009 [Marois et al., 2008, 2010].

Besides confirming the existence of an exoplanet, direct imaging of exoplanets allows their characterization through the spectroscopic technique. The study of the planetary spectrum yields fundamental insight on the atmospheric and surface composition [Schneider et al., 2010], as well as the thermal structure of the body [Traub and Oppenheimer, 2010a]. Narrow spectral bands indicate the volatile present in the atmosphere or on the surface. Thus, enhanced radiometric and spectral resolution is required for spectroscopic analysis.

The continuous technological development has lead to GPI in 2014 [see Macintosh et al., 2014] and to SPHERE in 2015 [see Beuzit et al., 2006]. The first direct observations by these instruments have recently come from the hand of Macintosh et al. [2015] and Wagner et al. [2016a], both discovering young Jovian planets whose atmospheric properties and orbit were characterized through near-infrared spectroscopy.

New observational techniques are expected to provide enhanced instrument precision and spatial resolution, which will allow us to point at more mature and bright stars, as well as observe lighter planets in the near-infrared. While currently available data in visible wavelength is often limited to broadband photometry [Snellen et al., 2009], new techniques are becoming increasingly capable of detecting visible light reflected by exoplanetary atmospheres. Moreover, increasing effort has been put on numerical and analytical modelling of directly imaged close-in giant planets which receive very high stellar radiation [Burrows et al., 2008, Cahoy et al., 2010, Madhusudhan and Burrows, 2012, Marley et al., 1999, Seager and Sasselov, 1998, Seager et al., 2000, Sudarsky et al., 2000, 2005], opening the way for the search of cold Earth-like planets. The direct detection and characterization of an Earth-like exoplanet at visible wavelengths would require contrast capabilities of around 1×10^{-10} , while it has been demonstrated that a coronagraphic space-borne telescope could reach the required performance level for achieving such a milestone [Trauger and Traub, 2007]. Attempts to develop such a telescope took place with the cancelled ESA's Darwin mission and NASA's Terrestrial Planetary Finder (TPF) missions [see Henry et al., 2004, Kaltenegger and Fridlund, 2005, Traub et al., 2006].

⁴ M_{\oplus} stands for the mass of Jupiter.

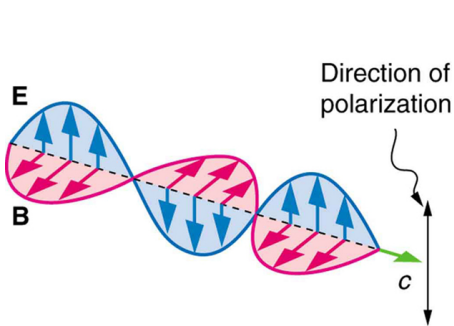
When looking for exomoons, their proximity to the hosting planet would require extremely high angular resolution imaging for which large interferometers with baselines of at least 400 m would be required [see Schneider et al., 2010]. Instead, current and future ground-based telescopes allow to acquire the unresolved planet–moon system as a single light-spot that represents the added signals of both bodies. Cabrera and Schneider [2007], Schneider et al. [2015] suggested that the fingerprint of a lunar companion could be observed as a sudden variation of the observed reflected flux due to mutual events between the two bodies, i.e. mutual transits and eclipses partially or totally shadowing each other.

The analysis developed by Cabrera and Schneider [2007] employed simplified approximated analytical models for the computation of mutual shadows (i.e. the penumbra eclipse region was neglected, occulted surface areas during mutual events were assumed to have constant brightness, and lunar ingress and egress epochs were neglected) and was restricted to a particular orbital configuration prone to displaying such events in which the hosting star, planet, moon and observer lie on a same plane, the so called edge-on configuration. In the absence of a more detailed analysis, it can be affirmed that the proposed indirect technique for exomoon detection constitutes an interesting alternative to the well-known transit photometry technique. Since the method requires to observe at visible reflected light (for which current telescopes provide low planet-star contrast) and the observed events are predicted to be around one order of magnitude lower than the measured flux [Cabrera and Schneider, 2007], the detection of exomoons with this technique would have to wait until future next-generation telescopes.

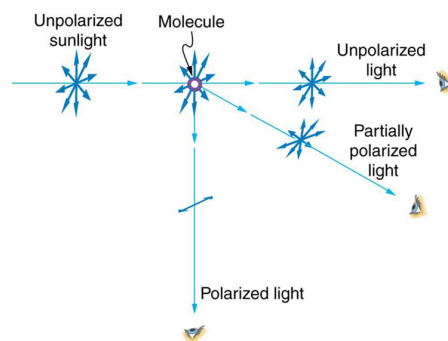
Such waiting time could be considerably cut down if we do not only pay attention to the total flux received from such distant planetary systems, but also to the polarization status of the received light. In next section, the potential of polarimetry for exoplanet characterization is introduced, analysing its prospective use for exomoon detection.

1.4. Polarimetry as a next-generation tool

According to classical physics, light is nothing more than an electromagnetic transverse wave composed of an electrical and magnetic field oscillating perpendicular to the direction of propagation (see Figure 1.4a). We define the irradiance of flux of light as the power received by a surface per unit area. Polarization is then defined as the attribute that a wave's oscillations have a definite direction relative to the direction of propagation of the wave. As a convention, the direction of polarization is taken as the direction of the electric field. The degree of polarization, P , stands for the ratio of polarized to total flux in a specific direction, with $P = 0\%$ for unpolarized, $P = 100\%$ for polarized, and $0\% < P < 100\%$ for partially polarized radiation. When looking at a light source emitting randomly polarized waves, the observed signal is said to be unpolarized, as there is no privileged direction of polarization. This is the case of light emitted by our Sun [Kemp et al., 1987].



(a) Electromagnetic wave.



(b) Polarization by scattering.

Figure 1.4: Illustration of polarized electromagnetic waves [OpenStax College, 2013]. The electric and magnetic fields shown in (a) are perpendicular to the direction of propagation of the transverse wave, the direction of polarization being defined as the direction of the electric field. Unpolarized light scattered from molecules has a polarization perpendicular to the original direction of propagation as seen in (b).

However, such unpolarized light may have its polarization state changed by interaction with matter. As represented in Figure 1.4b, a light wave hitting a particle is scattered in all different directions with

different flux magnitude and direction of polarization. Similar principle applies to light reflected on a different medium, e.g. a solid surface. Hence, starlight being scattered and reflected at the exoplanet is expected to be polarized according to the structure and composition of the atmosphere and surface (and rings). Therefore, measuring the polarization allows to characterize the structure and stratification of an exoplanet atmosphere without optically resolving the planet, providing complementary information to pure imaging and spectroscopy observations [Snik, 2009]. Understanding the polarization patterns of cloudy atmospheres as that of Venus [see e.g. Mahapatra et al., 2017, Rossi et al., 2015a,b, 2016a] is key for carrying out accurate exoplanet characterization.

Despite not having been exploited yet, great hope is placed in the polarimetry capabilities of current and future telescopes as powerful tools for detecting and characterizing exoplanets [see Hough and Lucas, 2003, Hough et al., 2003, Saar and Seager, 2003, Seager et al., 2000, Snik and Keller, 2013, Stam, 2003, 2008, Stam et al., 2004]. Previous works in this field involve the modelling of stellar polarization during planetary transits [Kostogryz et al., 2011, 2015, Sengupta, 2016, Wiktorowicz and Laughlin, 2014], the modelling of light curves and polarization of starlight reflected signals in the visible range of Earth-like planets [Karalidi, T. et al., 2012, Stam, 2008] and [Rossi and Stam, 2017] (in press), and giant Jupiter-like planets [Seager et al., 2000, Stam et al., 2004], as well as the modelling of exoplanetary atmospheres in the infrared [De Kok et al., 2011], which demonstrated the usefulness of direct observations on exoplanet characterization. Recently, Bott et al. [2016] reported linear polarization observations of the hot Jupiter system HD 189733. As a next natural step, the modelling of more complex planetary systems is under the spotlight.

In this direction, Nelk and Stam [2017] (accepted for publication) characterized the reflected signal by a gaseous exoplanet with dusty ring particles. Polarization has also been proposed as a means for exomoon detection. Sengupta and Marley [2016] studied the effect of a satellite transiting its host planet in infrared polarization of thermal radiation for the case of homogeneous spherically symmetric cloudy planets. Given the assumption that the planet emits and scatters thermal radiation in the same way along the observed disk, the interposition of a companion body between the planet and the observer would induce an asymmetry that would be reflected on the measured polarization signal. The expected peak polarization ranges between 0.1 and 0.3 % in the infrared, where current polarimetric accuracies are in the order of magnitude of $10^{-3}\% - 10^{-2}\%$ [van Holstein, 2016]. For a 30% polarized disk the absolute polarimetric accuracy in infrared bands raises up to $\sim 0.3\%$.

The polarization models developed for exoplanets show that polarization observations allow to increase the contrast between the exoplanet and its hosting star, compared to flux observations, as the star can be considered unpolarized [Kemp et al., 1987] while starlight being scattered and reflected at the exoplanet is expected to be polarized according to the structure and composition of the atmosphere and surface. Hence, polarimetry shows as a promising tool for the search of planetary companions when looking at the starlight reflected by a planet–moon system.

1.5. Problem Statement

As illustrated in Sections 1.3 & 1.4, current technology does not allow to perform direct imaging observations of satellites beyond our Solar System. Instead, indirect methods have been proposed and are currently being employed for digging into Kepler archived data without success. Given the rapid escalation of direct imaging and polarimetry technology, great expectation is placed on the characterization of exoplanets by analysis of polarization and flux observations of reflected starlight.

As suggested by Cabrera and Schneider [2007], the orbital motion of a companion satellite around a hosting planet is expected to leave a fingerprint on the observed flux in favourable combinations of orbital geometry and viewing direction. In accordance with the line of work of Rossi and Stam [2017, 2016], Stam [2008], Stam et al. [2004], Stam and Karalidi [2013], the exomoon is expected to be traceable in polarization observations as a function of the planet-moon system orbital geometry, atmospheric, and surface properties. Moreover, most of the exoplanet discovery missions (e.g. PLATO and CHEOPS) look for stellar transits on edge-on planetary systems. These are continuously monitored and their detection is carried out with increasing ease. Thus, we concentrate the study presented in this report on edge-on planet–moon systems.

Based on the motivation detailed in Section 1.1 and in accordance with the state of the art on extra-solar system research in general and exomoon research in particular, the Research Goal, Research Questions and Research Objectives for the current project are described.

Research Goal

The objective of the research project is to characterize the flux and degree of polarization signals of an Earth–Moon-like edge-on system imaged as an unresolved light source as a function of lunar orbital parameters and lunar physical properties, by modelling the orbital evolution of the system, the shadowing interaction between bodies, and the reflection and scattering of light interacting with the bodies.

Research Questions

In order to meet the external goal of the research, a series of research questions and sub-questions which steer the activities to be performed during the research period are here formulated. The answer to this questions logically imply fulfilment of the research objective posed above:

RQ 1 - Which are the flux and polarization curves as a function of phase angle and time for an unresolved coplanar Earth–Moon-like system observed in edge-on configuration?

RQ 1.1 - How can the flux and degree of polarization of starlight reflected by an arbitrary body be modelled?

RQ 1.2 - How can the surface and atmosphere of the Earth and Moon type of bodies be characterized in the visible wavelength range?

RQ 1.3 - Which are the planetary and lunar position as a function of time for an arbitrary set of orbital elements?

RQ 1.4 - Which is the total shadowed area on the planet and moon bodies as seen from a distant observer position as a function of time?

RQ 1.5 - Which is the impact of bodies' shadowing on the flux and polarization curves in an edge-on configuration?

RQ 2 - Which are the main characteristics of the flux and polarization curves obtained that could yield to the detection of a lunar companion?

RQ 2.1 - Which is the magnitude and characteristic duration of the lunar traces found?

RQ 2.2 - Are the observed traces bounded to particular viewing perspectives?

RQ 2.3 - How probable is it to witness lunar traces on flux and/or polarization curves of extra-solar systems?

RQ 2.4 - Which is the sensitivity of the lunar traces found in the flux and polarization curves on lunar model parameters, i.e. lunar orbital and physical parameters?

Research Objectives

Alongside with the research questions, the specific actions that will answer the research questions constitute a set of research objectives which will define the path of the current research:

RO 1 - Model the reflection of light by an arbitrary point on the surface of an arbitrary body.

RO 2 - Model the combined reflected flux and degree of polarization signals by unresolved planet–moon arbitrary system of bodies.

RO 3 - Model the surface and atmosphere reflection properties of an Earth and Moon type of bodies in the visible wavelength range.

RO 4 - Model the orbital motion of the planet and moon around the star.

RO 5 - Model the time dependent shadowed area on the planetary and lunar surfaces as observed from a infinitely distant observer.

RO 6 - Analyse and understand the characteristics and features of flux and polarization curves.

RO 7 - Assess the impact of changing observer position on the flux and polarization curves.

RO 8 - Assess the impact of changing lunar parameters on the flux and polarization curves.

1.6. Research Methodology

As enumerated in the research objectives for the current thesis, fulfilment of the research goal requires to model the reflection and scattering of light by the bodies, the orbital mechanics of the system conformed by the star, planet and moon, as well as the shadowing interaction and transits between the three bodies. The conjunction of these three elements allows to asses the impact of an orbiting moon on the total reflected starlight by the system.

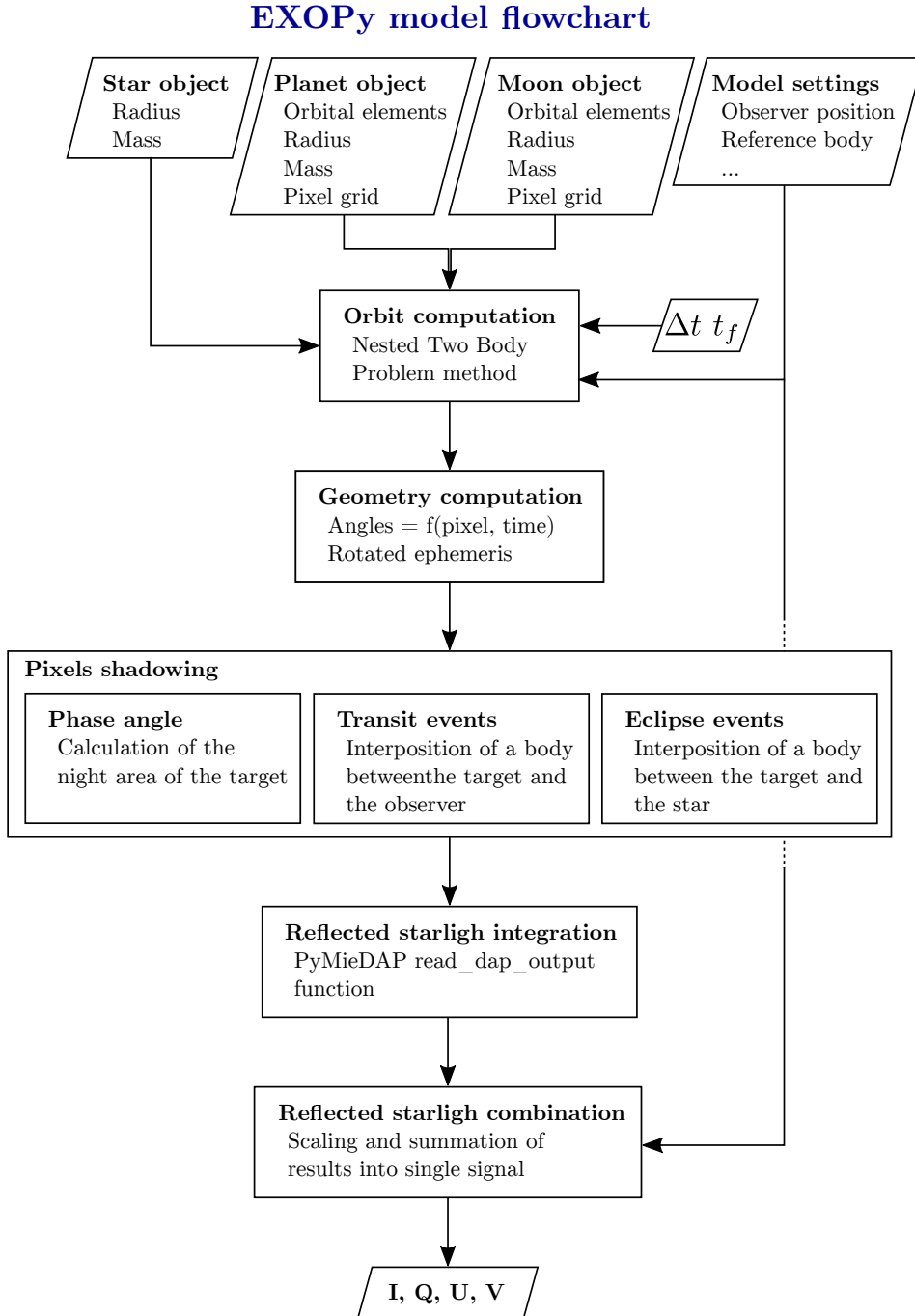


Figure 1.5: High level flow diagram for a standard simulation with *ExoPy* showing the basic tool architecture. *ExoPy* allows the user to define the bodies taking part in the planetary system, as well as a series of model settings. These are used as inputs for the orbit computation, the system's three-dimensional geometry computation, and pixel shadowing modules. After these, reflected light across the planet and moon bodies' disks is integrated and subsequently combined, resulting in the unresolved system's Stokes elements I , Q , U , and V .

During the course of the project, the three models are brought together and constitute a tool named *ExoPy: Exo-planets & Exo-moons Python*, a compact set of Python objects, modules and tools for numerically computing flux and polarization curves of complex arbitrary planet–moon systems. *ExoPy* belongs to the broader Python-based tool *Pymiedap* (*Python Mie Doubling-Adding Program*) [Rossi et al., 2016b] which allows to define a planetary atmosphere and compute the flux and polarization of scattered light using the doubling-adding method [de Haan et al., 1987] (see Chapter 2 for further details). Thus, *ExoPy* feeds itself on *Pymiedap*, standing as a powerful, flexible and generic tool for the study of planet–moon systems and binary systems, and with great potential of expansion to higher number of bodies involved and other structures as exorings.

The tool is implemented utilizing a modular structure. This allows the user to easily switch off/on, replace or upgrade an existing module, substitute part of a model by external input data (e.g. orbital position of bodies), as well as to develop and incorporate new complementary modules which could broaden the scope of use of *ExoPy* beyond the study of exomoons.

As observed in Figure 1.5, *ExoPy* is conformed by three main blocks: (1) orbit and geometry computation, determining the position and angles involved in the radiative transfer problem as a function of time, (2) pixel shadowing, determining which parts of the observed bodies are out of the reach of the stellar radiation, blocked by a transiting body, or shadowed by an eclipsing body, and (3) reflected starlight computation, which makes use of *Pymiedap* to compute the reflected starlight by each body, and combines the signal into one undistinguishable emission source. The binding element for the various blocks (and the modules inside) is the *body*-type of object which serves as a defining element for the lunar, planetary and stellar bodies, as well as container of all the information required and generated by the tool, i.e. inputs, outputs, and intermediate variables. The tool also incorporates dedicated functions for analysing and displaying results.

After implementation, validation, and verification of the tool (see Appendix A), a series of key simulations will be performed in an attempt to address the research questions and meet the research goal. The implemented tool is not bounded to particular physical properties of the bodies nor specific orbital configurations. However, due to time constraints and in an attempt to write a concise thesis report, the simulations have been restricted to reproduce a simplified Earth–Moon system with varying lunar albedo, size and lunar orbital parameters. The reader is directed to Section 7 for an enumeration of recommendations and potential alternative studies to be carried out with *ExoPy*.

A short manual introducing the major functionalities of *ExoPy* and illustrating its use for results retrieval is available in Appendix D. Detailed instructions on how to use *Pymiedap* in general and *ExoPy* in particular are available after installing the software. *ExoPy* can be downloaded and installed together with *Pymiedap* using Git⁵.

1.7. Thesis Outline

The thesis is structured in two major blocks, differentiating between the description of the models developed and the presentation of results and discussion.

The first block introduces the radiative transfer model employed for computing the unresolved planet–moon system reflected starlight in Chapter 2, describes the implemented orbital mechanics model and three-dimensional geometry models in Chapter 3, and delineates the model employed for computing the interaction between bodies, i.e. mutual transits and eclipses, in Chapter 4.

Corresponding to the second block, Chapter 5 shows the computed light curves and polarization signals for a reference edge-on Earth–Moon–like planetary system, analysing and characterizing the possible lunar traces, and assessing the feasibility of lunar detection. To conclude the presentation of results, Chapter 6 presents an analysis of flux and polarization curves’ sensitivity on lunar model parameters.

Finally, the conclusions extracted from the research are summarized and gathered together in Chapter 7, ending with an enumeration of recommendations and further work.

⁵As of yet, the latest version of *Pymiedap* can be found in <https://gitlab.com/loic.cg.rossi/pymiedap>

2

Computing reflected starlight

This chapter provides an overview of the working principles of the radiative transfer model employed, determining which are the parameters that allow computing the reflection and atmospheric scattering of starlight in the planetary and lunar bodies. Section 2.1 introduces the basic terminology employed to describe the flux and polarization state of electromagnetic radiation. Then, Section 2.2 details how the reflected signal is integrated along the observed disks. The selection of reference scattering plane is discussed in Section 2.3 and Section 2.5 enumerates the computations to be performed for obtaining the reflected radiation of the unresolved planet–moon system.

2.1. Stokes vectors and polarization

We describe the flux and polarization of starlight with a Stokes vector [see e.g. Hansen and Travis, 1974]:

$$\mathbf{F} = \begin{bmatrix} F \\ Q \\ U \\ V \end{bmatrix}, \quad (2.1)$$

with F the total flux, Q and U the linearly polarized fluxes, and V the circularly polarized flux, all with dimensions W m^{-2} . Fluxes Q and U are defined with respect to a reference plane, for which we use the scattering plane, which contains the observer and the centres of the body and the star (see Section 2.3). In the following, we do not compute the circularly polarized flux V , because it is usually much smaller than the linearly polarized fluxes [see Hansen and Travis, 1974, Kawata, 1978], and ignoring V does not lead to significant errors in the computation of F , Q , and U [see Stam and Hovenier, 2005]. As Figure 2.1 illustrates, a non-zero contribution of Q introduces a component of horizontal ($Q > 0$) or vertical ($Q < 0$) polarization, while a non-zero U value introduces a diagonal polarization component of $+45$ deg ($U > 0$) or -45 deg ($U < 0$).

$$\mathbf{F}_{\text{hor}} \propto \begin{bmatrix} 1 \\ 1 \\ 0 \\ 0 \end{bmatrix}, \quad \mathbf{F}_{\text{ver}} \propto \begin{bmatrix} 1 \\ -1 \\ 0 \\ 0 \end{bmatrix}, \quad \mathbf{F}_{+45} \propto \begin{bmatrix} 1 \\ 0 \\ 1 \\ 0 \end{bmatrix}, \quad \mathbf{F}_{-45} \propto \begin{bmatrix} 1 \\ 0 \\ -1 \\ 0 \end{bmatrix},$$

Figure 2.1: Graphical representation of polarization states and correlation with the Stokes vector. Positive (negative) Q values introduce horizontal (vertical) polarization, while positive (negative) U values introduce diagonal polarization at 45 deg (-45 deg). The fourth Stokes parameter, V , has been dismissed as its impact is neglected in the current study.

The light of the star is assumed to be unpolarized [see Kemp et al., 1987], and it is described by $\mathbf{F}_0 = F_0 \mathbf{1}$, with $\mathbf{1}$ the unit column vector and πF_0 the flux measured perpendicular to the light's propagation direction. The flux incident on a body depends on the distance. In the most generic case, we assume the lunar and planetary orbits to be eccentric, so that the distance star–planet and star–moon is not necessarily constant. Hence, the stellar standard flux πF_0 is defined with respect to the periapsis of the orbit described by the barycentre of the planet–moon system (see Chapter 3 for further details on the lunar and planetary orbits).

The degree of polarization, P , of the reflected light Stokes vector \mathbf{F} is defined as the portion of flux which is linearly polarized:

$$P = \frac{\sqrt{Q^2 + U^2}}{F}, \quad (2.2)$$

and the direction of polarization, χ , with respect to the chosen reference plane is given by:

$$\tan 2\chi = \frac{U}{Q}, \quad (2.3)$$

where angle χ is chosen such that $0 \leq \chi < \pi$, while $\cos 2\chi$ and Q have the same sign [Hansen and Travis, 1974, Hovenier et al., 2004].

2.2. Computing disk–integrated Stokes vectors

The Stokes vector and degree of polarization defined by Equations 2.1 and 2.2 are integrated along the planetary and lunar disks as described hereafter. We compute the Stokes parameters F , Q , and U and the degree of polarization of a planet and its moon that are observed spatially resolved from the parent star, but spatially unresolved from each other, by integrating the Stokes parameters computed across the illuminated and visible parts of the disks of the planet and the moon.

To enable the integration of locally computed Stokes parameters to obtain disk–integrated Stokes parameters and polarization, we discretize the disks of the planet and the moon according to the observer's perspective. As shown in Figure 2.2, the observed disk of a body is divided into a regular grid of equally sized, square pixels. In the following, we refer to the number of pixels on the disk of the planet as N_p and on the disk of the moon as N_m . Obviously, the smaller the pixels, the better the actual shape of the disk is approached, and (shown in Figure 2.4), the better the approximation of the terminator, the transits and the eclipses.

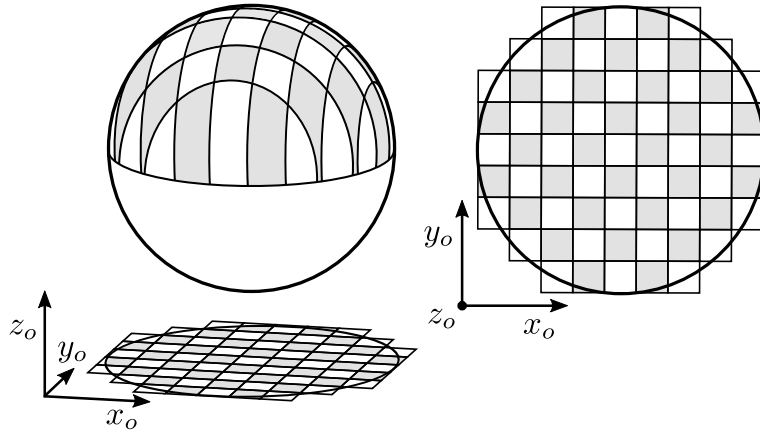


Figure 2.2: Three–dimensional view and projection onto the x_o – y_o plane of a discretized planet or moon. For the figure on the left, the direction towards the observer is along the z_o –axis. The figure on the right shows the observer's view of the planetary disk. The colors have been added to emphasize the division into squares. The orientation of the x_o and y_o axes is arbitrarily defined and not fixed with respect to the orientation of the planet nor moon disk pixel grids due to their motion around the star (more details available in Section 3.4.1).

For each pixel, i , we compute the Stokes vector of the locally reflected starlight using [see Hansen and Travis, 1974]:

$$\mathbf{F}_i(\theta_i, \theta_{0,i}, \phi_i - \phi_{0,i}) = \cos \theta_{0,i} \mathbf{R}_1(\theta_i, \theta_{0,i}, \phi_i - \phi_{0,i}) \mathbf{F}_0 \quad (2.4)$$

with θ the angle between the local zenith direction and the direction towards observer, θ_0 the angle between the local zenith direction and the direction towards the star, and $\phi - \phi_0$ the azimuthal difference angle, i.e. the angle between the plane containing the local zenith direction and the direction towards the observer and the plane containing the local zenith direction and the direction towards the star [see de Haan et al., 1987]. Furthermore, \mathbf{R}_1 is the first column of the local planetary reflection matrix (we only use the first column, because the incident starlight is assumed to be unpolarized).

We use an adding-doubling algorithm based on the method proposed by de Haan et al. [1987], which fully includes polarization for all orders of scattering to compute the coefficients of the Fourier-series expansion of \mathbf{R}_1 for the model bodies. First, the algorithm computes the Fourier coefficients at values of $\cos \theta_0$ and $\cos \theta$ that coincide with an user-defined Gaussian abscissae (see trade of analysis on number of Gaussian points in Appendix B.3). For increased accuracy in the disk-integration, we also compute Fourier coefficients at $\cos \theta_0 = 1$ ($\theta_0 = 0^\circ$) and $\cos \theta = 1$ ($\theta = 0^\circ$). Given the local illumination and viewing angles of a model body at a given time t , we can use the stored Fourier-coefficients to efficiently compute \mathbf{R}_1 and then the Stokes vector of the locally reflected starlight for every pixel, using Equation 2.4. Our radiative transfer algorithm provides parameters I_i , Q_i and U_i of each locally reflected Stokes vector, \mathbf{F}_i , as defined with respect to the local meridian plane: the plane through the local zenith and the local direction towards the observer.

The illumination of each body at a certain epoch depends in the first instance on the phase angle α , i.e. the angle between the direction to the star and the observer as measured from the center of the body, which, as illustrated in Figure 2.3, determines the fraction of a body disk that is illuminated as viewed from the observers perspective. A phase angle of 0° implies a completely illuminated observed body disk as, while 180° entails observing the night side of the body.

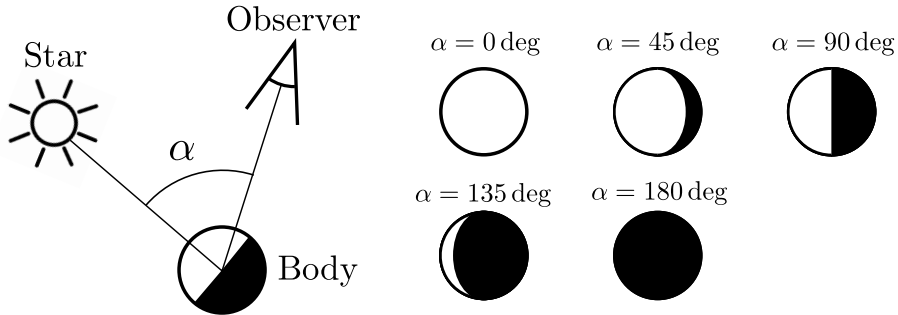


Figure 2.3: Left, graphical definition of phase angle, α . Right, body disk as viewed from the observer position from 0° to 180° phase angle. In our case, the observer position coincides with the planet Earth, while 'body' stands for either the exoplanet or the exomoon. The region in black (white) stands for the night side (illuminated side) of the body.

On top of that, the orbital geometries and size of the bodies involved may lead to situations in which they interfere with each other in what Cabrera and Schneider [2007] denominated mutual events. In particular, we have modelled the following types of interference events (see Figure 2.4):

- A transit: one body is (partially) positioned between the observer and the illuminated and visible disk of the second body, (partially) blocking the light that is reflected by the second body from the observer's field of view.
- An eclipse: one body is (partially) positioned between the star and the second body, casting a (partial) shadow on the illuminated and visible disk of the second body.

Note that the nomenclature employed differs from the established nomenclature for exoplanet transit studies. Details on the nomenclature employed and how we determine the illumination of each body at each time epoch, accounting for the phase angle and these two types of mutual events, are given in Chapter 4.

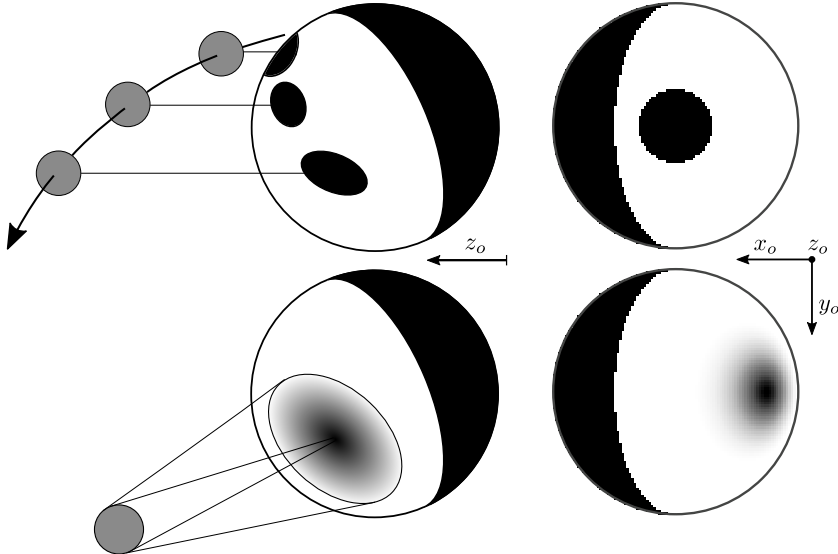


Figure 2.4: Three-dimensional sketch and simulation results of mutual events between bodies. Figures at the top represent a moon transiting in front of a planet (left) and the observed disk as modelled in Chapter 4 (right). Figures at the bottom stand for a three-dimensional planetary eclipse (left) and the observed disk as modelled in Chapter 4 (right). The observer is located towards the positive direction of axis z_o . White-black scale indicates full-null illumination of a body's surface as viewed from the observer's position.

We model the integrated combined starlight reflection by the unresolved planet–moon system as the discrete summation of the contribution of all pixels along the planet and moon. Considering an uniform pixel area of $\pi R^2/N$ for each body, the Stokes vector \mathbf{F} of the planet–moon system at a given time t is thus computed according to:

$$\mathbf{F} = \mathbf{F}^p + \mathbf{L}(\psi) \mathbf{F}^m = \frac{\pi R_p^2}{N_p} \sum_{i=1}^{N_p} b_i c_i d_i \mathbf{L}(\beta_i) \mathbf{F}_i^p + \mathbf{L}(\psi) \frac{\pi R_m^2}{N_m} \sum_{j=1}^{N_m} b_j c_j d_j \mathbf{L}(\beta_j) \mathbf{F}_j^m, \quad (2.5)$$

with N_p the number of pixels on the planetary disk, and N_m the number of pixels on the disk of the moon. The vectors \mathbf{F}_i^p and \mathbf{F}_j^m are the locally reflected Stokes vectors for the i th and j th pixels on the planet and moon, respectively. The factors before the summation symbols guarantee a total disk area of πR^2 , with R the radius of the disk of the planet or the moon, accounting for the signal scaling with bodies' size. Factors c_i and c_j range from 0.0 to 1.0, and are weighting factors for the dimming of stellar flux due to mutual eclipses at each pixel of the planet and moon, respectively. Factors b_i and b_j take values 0 and 1, and account for the blocking of a pixel from sight due to mutual transits. Both factors c and b are further discussed in Section 4. Factors d_i and d_j account for the dependence of the stellar flux that is incident on a pixel to the distance between the pixel and the star (described by the inverse-square law), as further discussed in Section 3. Angles β_i and β_j are used to rotate vectors \mathbf{F}_i^p and \mathbf{F}_j^m from their local meridian planes to the local scattering plane, by applying rotation matrix \mathbf{L} which is given by [see Hovenier and van der Mee, 1983]:

$$\mathbf{L}(\beta) = \begin{bmatrix} 1 & 0 & 0 & 0 \\ 0 & \cos 2\beta & \sin 2\beta & 0 \\ 0 & \sin 2\beta & \cos 2\beta & 0 \\ 0 & 0 & 0 & 1 \end{bmatrix}, \quad (2.6)$$

with β the angle between the pixel local meridian plane and the scattering plane, measured rotating in the clockwise direction from the local meridian to the scattering plane when looking towards the planet ($0^\circ \leq \beta < 180^\circ$)¹. Finally, the angle ψ is introduced for rotating the lunar integrated Stokes vector to

¹Hovenier and van der Mee [1983] write that β is measured rotating in the anti-clockwise direction when looking towards the observer, which of course yields the same angle.

the planet–moon system scattering plane which, as discussed in Section 2.3, is defined to coincide with the planetary scattering plane. Stokes vectors \mathbf{F}^p and \mathbf{F}^m are normalized such that the total flux that the planet and moon reflect at $\alpha = 0^\circ$, equals the planet’s and moon’s geometric albedo, respectively (see Stam et al. [2006]). Furthermore, we normalize the combined Stokes vector \mathbf{F} so that the reflected flux by the planet–moon system at $\alpha = 0^\circ$ equals the unresolved system albedo, taking as a reference the planetary disk area.

In Equation 2.5, the contributions of the planet and the moon are calculated individually and then summed. Given the different sizes of the bodies, the number of pixels used for discretizing them determines the spatial and radiometric resolution of the computed signals. An optimum superposition of the planet and moon signals would require an equal spatial resolution, meaning that a planetary pixel would have the exact same size as a moon pixel. Because N_p and N_m are integers, this is not possible for all planet–moon size combinations: for a given planet grid, it may not be possible to evenly fill the moon disk using the exact same pixel size. Even using equally sized pixels, the planet and moon grids could be displaced with respect to each other yielding a systematic spatial error.

To match the spatial resolutions of the planet’s and the moon’s disks as closely as possible, we select N_m^{eq} , the number of pixels along the moon’s equator, according to the following equation:

$$N_m^{eq} = N_p^{eq} \left\lceil \frac{R_m}{R_p + 0.5} \right\rceil, \quad (2.7)$$

with N_p^{eq} the number of pixels along the equator of the planet, and R_m and R_p the physical radii of, respectively, the moon and the planet. In this way, a moon that is 3 times smaller than its planet with $N_p^{eq} = 100$, would have $N_m^{eq} = 33$. To facilitate the merging of the planet and the moon signals, we align the orientation of both pixel grids with the planet–moon system scattering plane (see Figure 2.5), which is discussed in Section 2.3.

2.3. Selection of scattering plane

As introduced in Section 2.1, the linearly polarized fluxes, Q and U are defined with respect to the scattering plane, containing the observer, the star, and the centre of the modelled body. Previous works using similar methodology [see e.g. Stam, 2008, Stam et al., 2004] study a single body system for which the scattering plane is unambiguously defined. In the present system, the introduction of

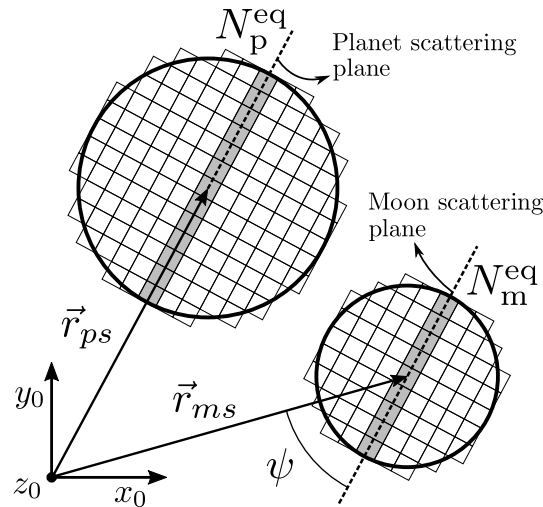


Figure 2.5: Graphical illustration of the planetary and lunar scattering planes, as well as the angle ψ required to combine the individual planet and moon Stokes vectors. The figure also shows the parallel alignment of the planetary and lunar pixel grids. The observer is located towards the positive direction of the z_0 -axis. The coordinate system $S_0 \equiv x_0, y_0, z_0$ is centred at the star position and defined as described in Section 3.3. \vec{r}_{ps} and \vec{r}_{ms} stand for the vector position of the planet and moon with respect to star. N_p^{eq} and N_m^{eq} stand for the total number of pixels along the equator of the planet and moon disks, accordingly. Distances to the star have been diminished in order to emphasize the angular difference between the planetary and lunar scattering planes.

one more body requires to clarify the different existing scattering planes as well as the reference plane employed to compute the combined planet–moon system unresolved signal.

As Equation 2.5 shows, the reflected light contributions of the planet and moon bodies are first separately computed. For each of these, our radiative transfer model provides the individual contributions \mathbf{F}^p and \mathbf{F}^m expressed with respect to the planetary scattering plane and moon scattering plane correspondingly. Expressed with respect to different planes, these results cannot be directly combined. Instead, a common reference plane for both bodies is to be employed. The difference between the two planes (exaggerated in Figure 2.5) is reduced with increasing distance from the star to the planet–moon system. Therefore, the use of a common reference plain guarantees a correct combination of planet and moon signals even for close-in exoplanets.

Our model allows the user to set either the planetary, lunar scattering planes, or a fixed plane with respect to the orbital motion of the bodies (i.e. plane z_0-x_0 in Figure 2.5) as reference scattering plane for the planet-moon system. The results presented in this report make use of the planetary scattering plane as reference planet-moon system reference scattering plane. Thus, the lunar Stokes vector is to be rotated an angle ψ , angle between the planetary and lunar scattering planes (see Figure 2.5), by using the rotation matrix presented in Equation 2.6. Further details on the computation of ψ are available in Chapter 3.

2.4. Atmosphere and surface models

As stated in Section 1.5, the reflected starlight is to be calculated for an Earth–Moon-like planetary system. Increasing complexity of the models employed for the Earth and Moon bodies entails increasing computational time for simulations carried out with our radiative transfer model. Therefore, the models here introduced result as a trade-off between computational effort and level of modelling detail.

Our Earth–like atmosphere-surface model has a flat Lambertian, i.e. isotropically reflecting, depolarizing surface with surface albedo, a_{surf} , of 0.3 and surface pressure, p_{surf} , of 1 bar. On top of it, we place three horizontally homogeneous atmospheric layers filled with gas and/or aerosol particles. We assume an Earth–like gas mixture in each layer, with a molecular mass, m_g , of 29 g/mol and a depolarization factor, δ , of 0.03 [Hansen and Travis, 1974] and [Rossi and Stam, 2017] (in press). Our computations are done at continuum wavelengths, thus ignoring absorption by the gas.

In our model, we have implemented two different variants of planetary atmospheres: a fully clear and a fully cloudy model. While the first one has its layers only filled with gas, the second one has an extra atmospheric layer with gas and liquid water cloud particles. These are characterized by a refractive index $n_r = 1.33 + 10^{-8}i$, particle size distribution following the two-parameters Gamma distribution of Hansen and Travis [1974] with $r_{\text{eff}} = 8.0\mu\text{m}$ and $\nu_{\text{eff}} = 0.1$, and optical thickness, τ_c , of 6.0. Moreover, the clouds span a vertical extend of 100 mb, and have a cloud top pressure, p_c , of 0.7 bar, corresponding to mid-altitude clouds on Earth.

Table 2.1: Parameters of our planet and moon models: a_{surf} is the surface albedo; p_{surf} is the surface pressure; δ is the depolarization factor; m_g is the mean molecular mass; g is the acceleration of gravity (not used in our radiative transfer computations); r_{eff} is the effective radius and ν_{eff} the effective variance of the cloud particle size distribution; τ_c is the cloud optical thickness; p_c is the cloud top pressure.

Parameter	Clear sky planet	Cloudy sky planet	Moon
a_{surf} [-]	0.30	0.30	0.36
p_{surf} [bar]	1.0	1.0	-
δ [-]	0.03	0.03	-
m_g [g/mol]	29	29	-
g [m/s ²]	9.81	9.81	1.625
r_{eff} [μm]	-	8.0	-
ν_{eff} [-]	-	0.1	-
τ_c [-]	-	6.0	-
p_c [bar]	-	0.7	-

Our model moon has Lambertian surface without atmosphere, which stands as an approximation of the Moon. The employed lunar albedo is $a_{surf} = 0.36$, higher than the Moon's albedo ($a_{surf} = 0.10$ [David R. Williams, 2017]), in order to enhance visibility of the flux and polarization features obtained. The impact of varying lunar albedo is evaluated in Chapter 6. The employment of more refined Earth and lunar models e.g. using a patchy clouds Earth model [see Rossi and Stam, 2017] (in press) and/or a lunar regolith surface model fall outside the scope of our investigation.

A summary of the surface and atmospheric parameters is listed in Table 2.1. The results presented in Chapters 5 and 6 correspond to an observed wavelength of 450 nm, corresponding to the blue color at which the uniform Earth assumption stands as a good assumption. Once presented the surface and atmospheric models, a summary of the computational steps to be carried out for computing the planet–moon system Stokes vector is presented below.

2.5. Computational steps

As described in Section 2.2 and illustrated by Equation 2.5, the Stokes vector of a given planet–moon system at a given moment in time requires the computation of a series of intermediate parameters. Summarizing, the following steps are to be performed:

1. Compute the illumination and viewing geometries, i.e. angles θ , θ_0 , and $\phi - \phi_0$, for the N_p and N_m pixels on the disks of, respectively, the planet and the moon at every time epoch (see Chapter 3).
2. Compute the pixel reflected Stokes vectors \mathbf{F}_i along the planet and moon disks at every time epoch using Equation 2.4.
3. Compute the angles β_i for the rotation of the locally reflected Stokes vectors of each pixel on the planetary and lunar disks to each body's scattering plane, as well as the rotation angle ψ for the rotation of the lunar integrated Stokes vector to the planetary scattering plane (see Chapter 3).
4. Compute the star–planet and star–moon distances, and the related factors d_i and d_j , respectively, that account for the incident stellar flux dimming with distance (see Chapter 3).
5. Compute the factors b_i , b_j , c_i and c_j that weigh the contribution of each pixel depending on transits (one body covering the other) and eclipses (the shadow of one body on the other) (see Section 4).
6. Carry out the Stoke vector integration over all pixels on the planet and the moon according to Equation 2.5.

In this chapter, we laid the foundations for the computation of the Stokes parameters describing the reflected starlight by the unresolved planet–moon system. Moreover, the planetary and lunar atmosphere and surface models were presented, and a roadmap towards the computation of the final planetary system Stokes vector was provided. The temporal variations of the angles involved, Stokes vectors and parameters c , b , and d depend on the dynamical evolution of the star–planet–moon–observer system. How we compute this dynamical evolution is described in the next Chapter 3.

3

Geometry of the Extrasolar System

As described in Chapter 2, the starlight reflection by each pixel along the planet and moon disks is a function of the local illumination and observing angles, for given the surface and atmosphere models. Moreover, the occurrence of mutual events depends on the relative position between planet, moon, star, and observer, while their characterization requires thorough description of the three-dimensional geometry of the bodies and their location with respect to others.

For these reasons, we design and describe a three-dimensional geometry model of the planet–moon–star system in this chapter. Firstly, the orbital motion of the bodies considered as point masses is modelled, posing the generic Euler formulation of the problem in Section 3.1 and describing the employed Nested two body problem approximation as solution for the three body problem in Section 3.2. Then, Section 3.3 defines the direction of observation with respect to the orbital system. Finally, the three-dimensional nature of the spherical bodies is described in Section 3.4, taking into account the discretization and the angular geometry of the problem at each pixel.

3.1. Generic formulation of the point-masses motion

Both the motions of the exoplanet and its moon around the star are solely determined by their mutual gravitational interaction. Assuming that the three bodies attract as point masses, such a system constitutes a classical three-body problem described by a set of second-order differential equations in time domain. Denoting the star by s , the orbiting planet by p , and its moon by m , we can be written down the set of equations in their Euler or classical formulation as [Wakker, 2015]:

$$\left\{ \begin{array}{l} \frac{d^2 \vec{r}_p}{dt^2} = G \frac{m_m}{|\vec{r}_{pm}|^3} \vec{r}_{pm} + G \frac{m_s}{|\vec{r}_{ps}|^3} \vec{r}_{ps} \\ \frac{d^2 \vec{r}_m}{dt^2} = G \frac{m_s}{|\vec{r}_{ms}|^3} \vec{r}_{ms} + G \frac{m_p}{|\vec{r}_{mp}|^3} \vec{r}_{mp} \\ \frac{d^2 \vec{r}_s}{dt^2} = G \frac{m_p}{|\vec{r}_{sp}|^3} \vec{r}_{sp} + G \frac{m_m}{|\vec{r}_{sm}|^3} \vec{r}_{sm} \end{array} \right. , \quad (3.1)$$

with G the universal gravitational constant, m_i the mass of body i , \vec{r}_i the position of body i with respect to the three body system's barycentre, $\vec{r}_{ij} = \vec{r}_j - \vec{r}_i$ the position of body j with respect to body i , and t the time.

A breakdown of Equation 3.1 in Cartesian coordinates, $\vec{r} = [x, y, z]^T$, yields a set of first-order non-linear differential equations of the order eighteen. In the absence of an analytical solution, the computation of orbital positions for the planet and moon around the star would require to perform a numerical propagation of a given set of initial conditions for Equation 3.1. The use of reduced time steps in combination with a stable integration scheme leads accurate orbit predictions through the so-called target shooting approach [see Kumar et al., 2012]. Alternatively, analytical methods allow to specify the orbital elements for the motion of the bodies enhancing insight on the solution through the user-specified input parameters.

For the presented work, a analytical simplified version of the three-body problem has been implemented: the nested two-body problem. A complete description of this model is presented in the next section.

3.2. The Nested Two Body Problem

Analytical models are predictable, fast, and easy to implement. With this motivation, Kipping came up with a simplified version of the more generic three-body problem for a planet–moon–star system which he dubbed as the nested two-body problem [Kipping, 2010a, 2011]. This approximation is based on the assumption that the motion of the planet and moon around the planet–moon system barycenter, as well as the motion of this barycenter around its star, can be described by Keplerian orbits. The advantages of using this approximation are:

1. The solution can be analytically described [Kipping, 2010a, 2011].
2. The computational time is significantly reduced (by means of a vectorial implementation of the solution) compared to when numerical integrations are used.
3. Enhanced insight on the computed orbits is guaranteed as the elements of all orbits can be specified.
4. Unlike the circular restricted three–body problem simplification, the nested two–body problem allows the use of complex eccentric orbit geometries.

The model build on a fundamental assumption and has some limitations which limit its range of application. These are discussed in Section 3.2.1. Afterwards, the reference frames and model parameters required for describing the orbits are introduced in Section 3.2.2, followed by the mathematical description of the model in Section 3.2.3.

3.2.1. Assumptions and range of application

The nested two–body model relies on the assumption that the planet and its moon are a binary system orbiting the star at a large distance. Therefore, in the frame of the barycentre of the planet–moon system, also referred to simply as barycentre in this report, the planet and moon orbits around the barycentre are not affected by the star, while their trajectory around the star is defined by the orbital motion of the system’s barycentre. In other words, it is assumed that Kepler’s Third Law is satisfied in these nested frames over the time-scale of the orbital period of the bodies. In such case, Equation 3.1 is rewritten as:

$$\left\{ \begin{array}{l} \frac{d^2\vec{r}_{pb}}{dt^2} = G \frac{m_m}{|\vec{r}_{pb}|^3} \vec{r}_{pb} \\ \frac{d^2\vec{r}_{mb}}{dt^2} = G \frac{m_p}{|\vec{r}_{mb}|^3} \vec{r}_{mb} \\ \frac{d^2\vec{r}_{bs}}{dt^2} = G \frac{m_p + m_m + m_s}{|\vec{r}_{bs}|^3} \vec{r}_{bs} \end{array} \right. . \quad (3.2)$$

In this case, the equations above describe a system of Keplerian orbits which can be analytically solved. As demonstrated by Kipping [2010a], this model is an excellent approximation of the generic three–body problem for $\mathfrak{D} \leq 0.531$ (both for prograde and retrograde moons), where \mathfrak{D} is the moon–planet separation in units of the planet’s Hill’s sphere radius [see De Pater and Lissauer, 2015]. As follows from Domingos et al. [2006], Kipping [2011], stable, prograde orbiting moons are predicted to fulfill $\mathfrak{D} \leq 0.4895$, while retrograde orbiting moons can exist at larger separations, limited by $\mathfrak{D} \leq 0.9309$. Thus, the nested two–body model will reliably describe all cases of prograde orbiting moons, while retrograde orbiting moons are only partially covered, depending on \mathfrak{D} .

In the present work, we focus on the study of prograde moons. The reason for this is that, we do not expect a major influence of the moon rotation direction along its orbit on the obtained flux and degree of polarization phase curves,besides a mirroring effect during mutual events. Prior to the mathematical description of the nested two body problem, the reference frames and model parameters are introduced and defined in Section 3.2.2.

3.2.2. Framework and model parameters

In this section, we provide the basic framework required to describe the formulae behind the nested two body problem, and provide the reader with the three-dimensional visual references required to visualize the results presented in this report. Hereafter, we present the orbital elements and reference frames which define the orbits involved in the nested two body problem: (a) the barycentre's orbit around the star and (b) the moon's orbit around the barycentre.

Barycentre's orbit around the star

The barycentre of the planet–moon system (b) describes a Keplerian orbit around the star (s). The geometry of the system, together with the reference frames required for describing the barycentre's orbit around the star, are illustrated in Figure 3.1.

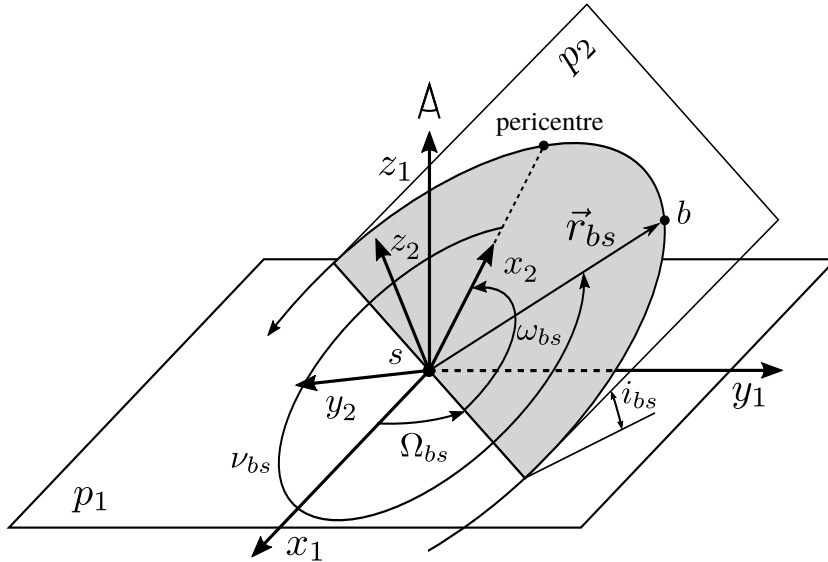


Figure 3.1: Sketch of the three-dimensional Keplerian orbit of the planet–moon system barycentre around the parent star. The drawing shows the reference frames S_1 and S_2 , and orbital elements involved in the description of the orbit orientation with respect to the observer. The plane p_1 corresponds to the plane of the sky as seen by the observer and the plane p_2 is defined as the orbital plane of the barycentre around the star. i is the orbital inclination, ω is the argument of periastron, Ω is the right ascension of the ascending node and ν is the true anomaly. Indices are s for the star and b for the barycentre. \vec{r}_{bs} stands for the position vector of the barycentre with respect to the star.

As can be seen in Figure 3.1, the orthonormal, right-handed coordinate system $S_1 = \{x_1, y_1, z_1\}$ is the reference system for the observation of the planet–moon–star system, with the star at the origin, and the z_1 -axis pointing towards the observer¹. The x_1 - and y_1 -axes have an arbitrary (but fixed) orientation. S_1 serves as reference for the definition of the three-dimensional orbit of the planet–moon barycentre, described through the following set of orbital elements:

a_{bs}	semi-major axis
e_{bs}	eccentricity [0,1]
i_{bs}	inclination [0°, 180°]
ω_{bs}	argument of periastron [0°, 360°]
Ω_{bs}	right ascension of the ascending node [0°, 360°]
ν_{bs}	true anomaly [0°, 360°]

The right ascension of the ascending node, Ω_{bs} , defined with respect to the positive x_1 -axis and contained in the reference plane x_1 – y_1 (here denominated p_1), determines the ascending node of the orbit. Together with the orbital inclination, i_{bs} , these two parameters define the orbital plane of the barycentre (centre of mass of the planet–moon system). Note that the value of Ω_{bs} will not influence

¹The observer direction can be easily modified a posteriori as described in Section 3.3.

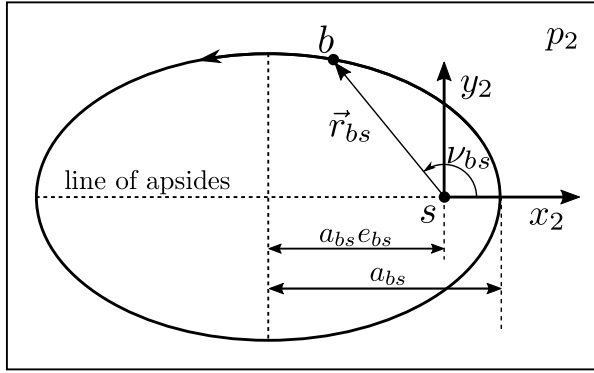


Figure 3.2: Sketch of the two-dimensional Keplerian orbit of the planet–moon system barycentre around the parent star. The drawing shows the reference frame S_2 as well as the orbital elements involved in the description of the barycentre's position along its orbit. The plane p_2 corresponds to the orbital plane of the barycentre around the star. a is the orbital semi-major axis, e is the eccentricity and ν is the true anomaly. Indices are s for the star and b for the barycentre. \vec{r}_{bs} stands for the position vector of the barycentre with respect to the star.

the total reflected flux signal, nor the degree of polarization of the planet–moon system, as it prescribes merely a rotation around the z_1 –axis (observer's axis). However, depending on the choice of the reference scattering plane for the planet–moon system, it could entail a variation of the linearly polarized fluxes Q and U given by the rotation matrix in Equation 2.6. Considering a generic eccentric orbit, the argument of periastron, ω_{bs} , determines the line of apsides by setting the position of the orbital pericentre.

At this point, the second orthonormal, right-handed coordinate system $S_2 = \{x_2, y_2, z_2\}$ can be defined centred at the star, with its x_2 –axis directed towards the barycentre's orbit pericentre and the z_2 –axis perpendicular to the orbital plane. As illustrated in Figure 3.2, the orbit of the barycentre around the star in reference frame S_2 consists of an ellipse of semi-major axis a_{bs} and focal distance $a_{bs}e_{bs}$ product of the semi-major axis and orbital eccentricity. The position of the barycentre along its orbit is given by the true anomaly angle ν_{bs} .

Moon's orbit around the barycentre

The description of the lunar orbit around the barycentre uses as a reference the barycentre's orbit around the star. Hence, we define the reference plane for the lunar orbit as the orbital plane of the

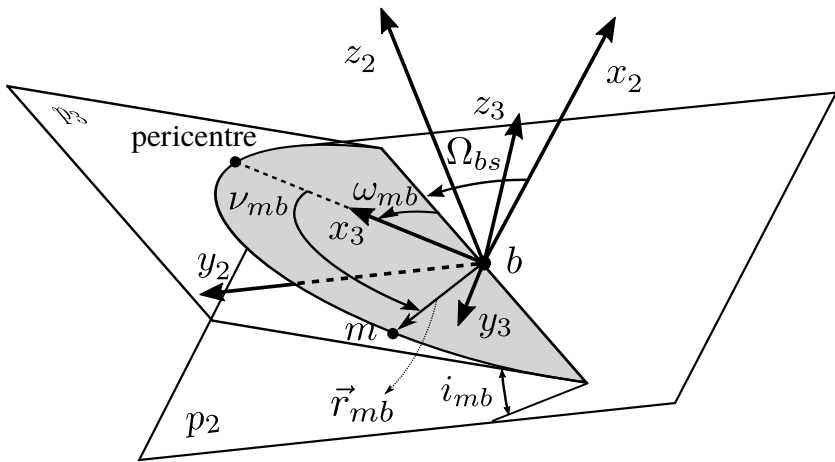


Figure 3.3: Sketch of the three-dimensional Keplerian orbit of the moon around the planet–moon system barycentre. The drawing shows the reference frames S_2 and S_3 , and orbital elements involved in the description of the orbit orientation with respect to the observer. The plane p_2 corresponds to the orbital plane of the barycentre around the star and the plane p_3 is defined as the orbital plane of the moon around the barycentre. i is the orbital inclination, ω is the argument of periastron, Ω is the right ascension of the ascending node and ν is the true anomaly. Indices are s for the star and m for the moon. \vec{r}_{mb} stands for the position vector of the moon with respect to the barycentre.

barycentre, p_2 , and translate the coordinate system S_2 so that it is centred at the barycentre's position at any time (see Figures 3.3 and 3.4). The reference frame S_2 now allows to define the three-dimensional orbit of the satellite, independent of the barycentre's motion, through the following set of orbital elements:

a_{mb}	semi-major axis
e_{mb}	eccentricity [0, 1]
i_{mb}	inclination [0°, 180°]
ω_{mb}	argument of periastron [0°, 360°]
Ω_{mb}	right ascension of the ascending node [0°, 360°]
ν_{mb}	true anomaly [0°, 360°]

In this case, the lunar right ascension of the ascending node, Ω_{mb} , lies on the plane p_2 , defined with respect to the positive x_2 -axis. As explained in the case of the barycentre's orbit, the orbital inclination defines the plane of the orbit, which can be described as a planar ellipse (see Figure 3.4). For this, the orthonormal, right handed coordinate system $S_3 = \{x_3, y_3, z_3\}$ is defined centred at the barycentre's position, with its x_3 -axis directed towards the lunar pericentre (determined by the argument of periastron, ω_{mb}) and the z_3 -axis perpendicular to the orbital plane. Expressed in S_3 , the lunar position with time can be defined through the semi-major axis, a_{bs} , orbital eccentricity, e_{bs} , and true anomaly, ν_{bs} .

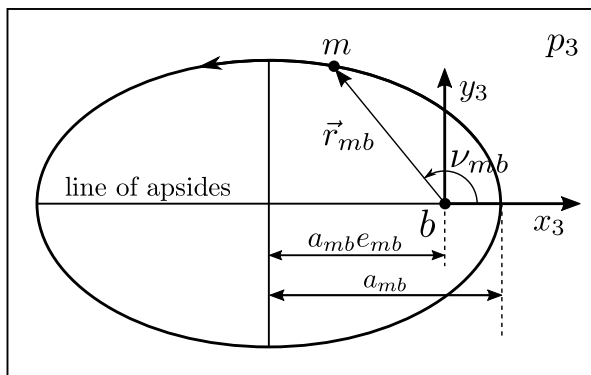


Figure 3.4: Sketch of the two-dimensional Keplerian orbit of the moon around the planet–moon system barycentre. The drawing shows the reference frame S_3 and orbital elements involved in the description of the moon's position along its orbit. The plane p_3 corresponds to the orbital plane of the moon around the barycentre. a is the orbital semi-major axis, e is the eccentricity and ν is the true anomaly. Indices are s for the star and m for the moon. \vec{r}_{mb} stands for the position vector of the moon with respect to the barycentre.

Reference orbit geometry configurations

The orbital composition required for defining the lunar motion complicates the interpretation of the entire three-dimensional system. The results presented in Chapters 5 and 6, are based on two different system configurations which are here described as reference scenarios. These have been illustrated in Figure 3.5. Table 3.1 gathers the main orbital elements which describe the posed geometries.

- Edge-on system: The trajectories of the exoplanet and its satellite (i.e. the barycentre of the system) are confined to a plane perpendicular to the sky plane, reference plane p_1 in Figure 3.5a. According to the reference frames and orbital elements here described, an edge-on system requires the barycentre's orbit to have an orbital inclination of $i_{bs} = 90^\circ$. The lunar orbital plane is coplanar to the barycentre's orbit. Thus, the lunar orbital inclination is set to $i_{mb} = 0^\circ$. In the present work, true anomalies are chosen to align the lunar and barycentre's line of apsides with the direction towards observer, i.e. $\omega_{bs} = 90^\circ$ and $\omega_{mb} = 0^\circ$. Moreover, an arbitrary value of Ω_{mb} is chosen, in this case $\Omega_{mb} = 90^\circ$ ².

²Variations on the barycentre's right ascension of the ascending node constitute a rotation around the observer axis, modifying the obtained linearly polarized fluxes Q and U , but not altering the total observed reflected flux F nor degree of polarization P by the planet–moon system.

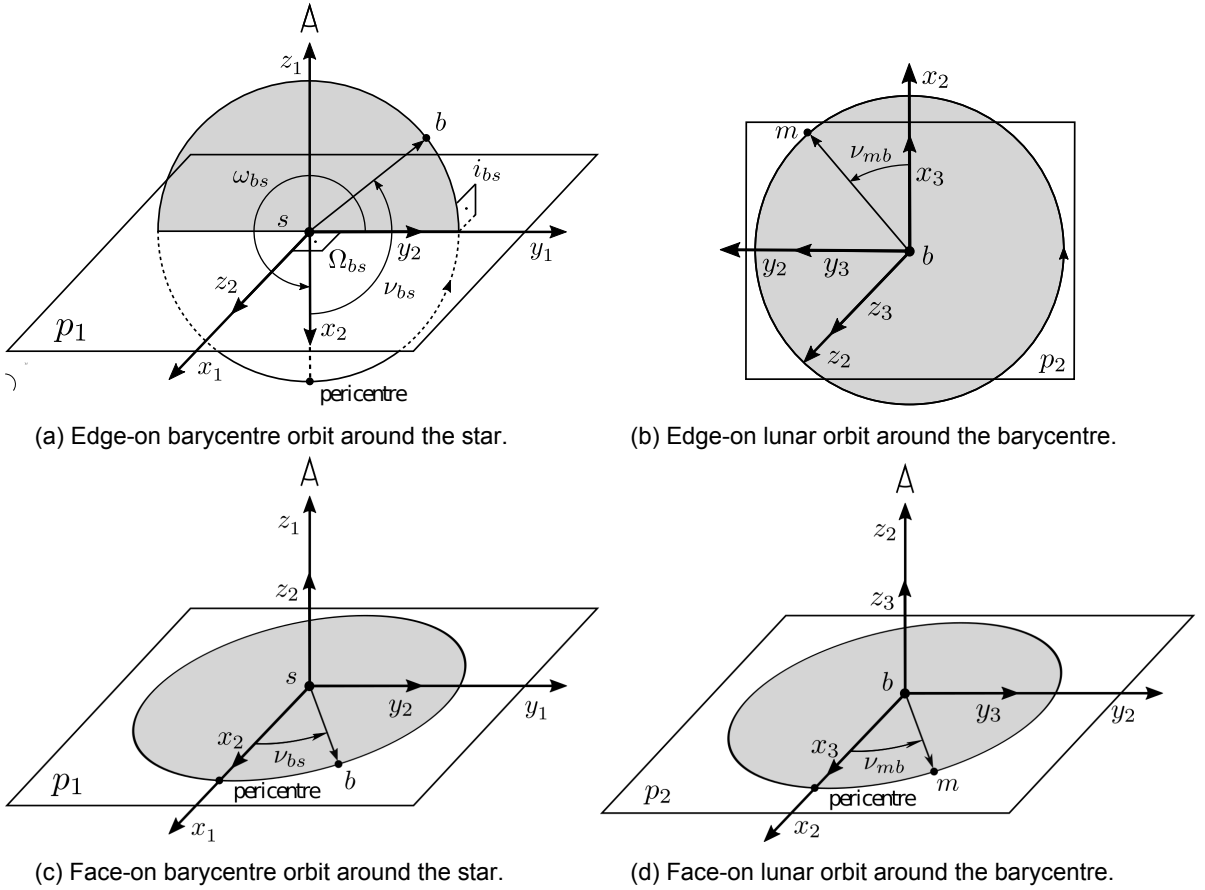


Figure 3.5: Sketch of the reference frames and orbital geometry of two reference systems: an edge-on planet–moon system (a) (b) and a face-on planet–moon system (c) (d). The reference plane p_1 corresponds to the plane of the sky as seen by the observer, while the reference plane p_2 corresponds to the barycentre’s orbital plane. i is the orbital inclination, ω is the argument of periastron, Ω is the right ascension of the ascending node and ν is the true anomaly. Indices are s for the star, p for the planet and m for the moon.

- Face-on system: The trajectories of the planet and moon are contained in the sky plane, reference plane p_1 in Figure 3.5c. In this case, the barycentre and moon orbit inclinations are set to zero degrees, $i_{bs} = 0^\circ$ and $i_{mb} = 0^\circ$. As convention for face-on systems, the true anomalies are selected to align the lunar and barycentre’s line of apsides along the x_1 -axis. The right ascension of the ascending node of the orbits is undefined for planar orbits [Wakker, 2015]. In the present work, Ω_{bs} and Ω_{mb} are set to zero (see Table 3.1).

Once presented the coordinate systems and parameters that constitute the heart of the nested two body problem, the mathematical description of the nested two body problem model is provided in Section 3.2.3.

3.2.3. Mathematical elaboration

As stated in Section 3.2.1 and visualized in 3.2.2, the nested two body problem approximation assumes that the motion of the moon and the planet around their barycentre is independent of the barycentre’s trajectory around the star. Our goal is to compute the three-dimensional position vector of the exoplanet and its satellite at any given time, expressed in the observer’s reference frame S_1 . The absolute position vector of the bodies, $\vec{r}_{ps}|^{S_1}$ and $\vec{r}_{ms}|^{S_1}$, is computed by composition of the position vector of the planet and moon around the barycentre, $\vec{r}_{pb}|^{S_1}$ and $\vec{r}_{mb}|^{S_1}$, with the barycentre’s position vector, $\vec{r}_{bs}|^{S_1}$:

$$\vec{r}_{ps}|^{S_1}(t) = \vec{r}_{pb}|^{S_1}(t) + \vec{r}_{bs}|^{S_1}(t), \quad (3.3)$$

Table 3.1: Parameters of the barycentre and lunar orbits describing the edge-on and face-on reference systems: i is the orbital inclination, ω is the argument of periastron, and Ω is the right ascension of the ascending node.

Orbital parameter	Edge-on system	Face-on system
i_{bs} [deg]	90.0	0.0
ω_{bs} ² [deg]	270.0	0.0
Ω_{bs} ³ [deg]	90.0	0.0
i_{mb} [deg]	0.0	0.0
ω_{mb} ² [deg]	0.0	0.0
Ω_{mb} [deg]	0.0	0.0

$$\vec{r}_{ms}|^{S_1}(t) = \vec{r}_{mb}|^{S_1}(t) + \vec{r}_{bs}|^{S_1}(t). \quad (3.4)$$

The mathematical description of the problem is, therefore, split in three steps: (1) the computation of the barycentre's position vector in coordinate system S_1 , $\vec{r}_{bs}|^{S_1}$, (2) the computation of the planetary and lunar position vectors with respect to the barycentre in coordinate system S_2 , $\vec{r}_{pb}|^{S_2}$ and $\vec{r}_{mb}|^{S_2}$, and (3) the composition of the absolute position vectors for the planet and moon in coordinate system S_1 , $\vec{r}_{ps}|^{S_1}$ and $\vec{r}_{ms}|^{S_1}$.

Position vector of the barycentre with respect to the star in S_1 , $\vec{r}_{bs}|^{S_1}$

Considering the Keplerian motion of the barycentre around the star (see Section 3.2.1), we use the well-known Kepler's orbit equation to compute the radial distance from the star position to the planet–moon system barycenter, r_{bs} , as a function of the orbital elements a_{bs} , e_{bs} and ν_{bs} as follows:

$$r_{bs}(t) = \frac{a_{bs} (1 - e_{bs}^2)}{1 + e_{bs} \cos \nu_{bs}(t)}, \quad (3.5)$$

where the true anomaly ν_{bs} and, thus, the radial distance r_{bs} are a function of time, t .

As follows from Figure 3.2, the coordinates of the barycenter's orbital position in system S_2 , $\vec{r}_{bs}|^{S_2}$, are given by scalar projection of r_{bs} onto the x_1 - and y_1 -axes:

$$\vec{r}_{bs}|^{S_2}(t) = r_{bs}(t) \begin{bmatrix} \cos \nu_{bs}(t) \\ \sin \nu_{bs}(t) \\ 0 \end{bmatrix}. \quad (3.6)$$

As formulated by Murray and Correia [2010], the position vector can then be put through a series of matrix rotations, to yield the position of the barycentre in the observer reference coordinate system S_1 for each value of the true anomaly. The transformation matrix \mathbb{T}_{12} , which accounts for the three-dimensional geometry of the barycentre's orbit and allows us to rotate from coordinate system S_2 to S_1 , can be written as the product of three successive clockwise elemental rotations around the x - and z -axes:

$$\begin{aligned} \mathbb{T}_{12} &= \mathbb{T}_z(\Omega_{bs}) \mathbb{T}_x(i_{bs}) \mathbb{T}_z(\omega_{bs}) = \\ &= \begin{bmatrix} \cos \Omega_{bs} & -\sin \Omega_{bs} & 0 \\ \sin \Omega_{bs} & \cos \Omega_{bs} & 0 \\ 0 & 0 & 1 \end{bmatrix} \begin{bmatrix} 1 & 0 & 0 \\ 0 & \cos i_{bs} & -\sin i_{bs} \\ 0 & \sin i_{bs} & \cos i_{bs} \end{bmatrix} \begin{bmatrix} \cos \omega_{bs} & -\sin \omega_{bs} & 0 \\ \sin \omega_{bs} & \cos \omega_{bs} & 0 \\ 0 & 0 & 1 \end{bmatrix} =, \end{aligned} \quad (3.7)$$

³The edge-on and face-on configurations do not restrict the argument of periastron of the lunar and barycentre's orbits nor the barycentre's right ascension of the ascending node. The given values correspond to the convention used for the present work.

⁴Variations on the barycentre's right ascension of the ascending node constitute a rotation around the observer axis, not altering the observed total reflected flux by the planet–moon system, F .

$$= \begin{bmatrix} \cos \Omega_{bs} \cos \omega_{bs} - \sin \Omega_{bs} \cos i_{bs} \sin \omega_{bs} & -\cos \Omega_{bs} \sin \omega_{bs} - \sin \Omega_{bs} \cos i_{bs} \cos \omega_{bs} & \sin \Omega_{bs} \sin i_{bs} \\ \sin \Omega_{bs} \cos \omega_{bs} + \cos \Omega_{bs} \cos i_{bs} \sin \omega_{bs} & -\sin \Omega_{bs} \sin \omega_{bs} + \cos \Omega_{bs} \cos i_{bs} \cos \omega_{bs} & -\cos \Omega_{bs} \sin i_{bs} \\ \sin i_{bs} \sin \omega_{bs} & \sin i_{bs} \cos \omega_{bs} & \cos i_{bs} \end{bmatrix}.$$

At this point, the coordinates of the barycentre's position along its orbit around the star in the observer coordinate system S_1 , $\vec{r}_{bs}|^{S_1}$, are computed by rotating the $\vec{r}_{bs}|^{S_2}$ vector using transformation matrix \mathbb{T}_{12} as follows:

$$\vec{r}_{bs}|^{S_1}(t) = \mathbb{T}_{12} \vec{r}_{bs}|^{S_2}(t), \quad (3.8)$$

Position vector of the planet and moon with respect to the barycentre in S_2 , $\vec{r}_{pb}|^{S_2}$ and $\vec{r}_{mb}|^{S_2}$

As introduced in Section 3.2.2, the definition of the lunar and planetary motion around their barycentre is defined by the orbital elements of the moon orbit. Thus, following the same rationale as applied in the computation of the barycentre's position, and taking as a reference Figure 3.4, the coordinates of the lunar orbital position in system S_3 , $\vec{r}_{mb}|^{S_3}$ are given by:

$$\vec{r}_{mb}|^{S_3}(t) = r_{mb}(t) \begin{bmatrix} \cos \nu_{mb}(t) \\ \sin \nu_{mb}(t) \\ 0 \end{bmatrix}, \quad (3.9)$$

where the time-dependent radial distance from the barycentre to the moon is given by the Kepler's orbit equation as a function of the orbital elements a_{mb} , e_{mb} and ν_{mb} :

$$r_{mb}(t) = \frac{a_{mb} (1 - e_{mb}^2)}{1 + e_{mb} \cos \nu_{mb}(t)}. \quad (3.10)$$

Thus, the coordinates of the lunar position along its orbit around the barycentre in the system S_2 , $\vec{r}_{mb}|^{S_2}$, are computed as:

$$\vec{r}_{mb}|^{S_2}(t) = \mathbb{T}_{23} \vec{r}_{mb}|^{S_3}(t), \quad (3.11)$$

where the transformation matrix \mathbb{T}_{23} is given as a function of successive clockwise elemental rotation (see Equation 3.7):

$$\mathbb{T}_{23} = \mathbb{T}_z(\Omega_{mb}) \mathbb{T}_x(i_{mb}) \mathbb{T}_z(\omega_{mb}) = \quad (3.12)$$

$$= \begin{bmatrix} \cos \Omega_{mb} \cos \omega_{mb} - \sin \Omega_{mb} \cos i_{mb} \sin \omega_{mb} & -\cos \Omega_{mb} \sin \omega_{mb} - \sin \Omega_{mb} \cos i_{mb} \cos \omega_{mb} & \sin \Omega_{mb} \sin i_{mb} \\ \sin \Omega_{mb} \cos \omega_{mb} + \cos \Omega_{mb} \cos i_{mb} \sin \omega_{mb} & -\sin \Omega_{mb} \sin \omega_{mb} + \cos \Omega_{mb} \cos i_{mb} \cos \omega_{mb} & -\cos \Omega_{mb} \sin i_{mb} \\ \sin i_{mb} \sin \omega_{mb} & \sin i_{mb} \cos \omega_{mb} & \cos i_{mb} \end{bmatrix}.$$

Once we have calculated the position vector of the moon with respect to the barycentre, we can compute $\vec{r}_{pb}|^{S_2}$, the position vector of the planet in reference frame S_2 , using the definition of the barycenter:

$$\vec{r}_{mb}|^{S_2}(t) m_m + \vec{r}_{pb}|^{S_2}(t) m_p = 0, \quad (3.13)$$

$$\vec{r}_{pb}|^{S_2}(t) = -\frac{m_m}{m_p} \vec{r}_{mb}|^{S_2}(t),$$

with m_m the mass of the moon, and m_p the mass of the planet.

Composition of the absolute position vectors for the planet and moon, $\vec{r}_{ps}|^{S_1}$ and $\vec{r}_{ms}|^{S_1}$

Finally, the time-dependent planetary and lunar position vectors with respect to the star, expressed in the observer coordinate system S_1 are obtained by retaking Equations 3.3 and 3.4, and making use of the transformation matrix \mathbb{T}_{12} to convert the bodies' position relative to the barycentre from coordinate system S_2 to S_1 as:

$$\vec{r}_{ps}|^{S_1}(t) = \mathbb{T}_{12} \vec{r}_{pb}|^{S_2}(t) + \vec{r}_{bs}|^{S_1}(t), \quad (3.14)$$

$$\vec{r}_{ms}|^{S_1}(t) = \mathbb{T}_{12} \vec{r}_{mb}|^{S_2}(t) + \vec{r}_{bs}|^{S_1}(t), \quad (3.15)$$

where $\vec{r}_{bs}|^{S_1}$, $\vec{r}_{pb}|^{S_2}$ and $\vec{r}_{mb}|^{S_2}$ are obtained through Equations 3.8, 3.13, 3.11, respectively.

The equations presented above are an explicit function of the true anomaly angle and, therefore, an implicit function of time. While the angular formulation of the problem helps describing the orbit, a true anomaly to time conversion is required for characterizing the time elapsed during observations. For this purpose, we use Kepler's equation for elliptic orbits ($0 \leq e < 1$) applied to both the barycentre and lunar orbits:

$$M(t) = E(t) - e \sin E(t), \quad (3.16)$$

where M is the mean anomaly, defined as $M = n(t - t_0)$, with n the orbital mean motion, $t - t_0$ the time since the last pericentre passage, and E is the eccentric anomaly, that is related to the true anomaly, ν , via:

$$\tan \frac{\nu}{2} = \sqrt{\frac{1+e}{1-e}} \tan \frac{E}{2}. \quad (3.17)$$

Combination of Equations 3.16 and 3.17 yields an implicit function of the time and true anomaly variables, t and ν , $F(t, \nu) = 0$:

$$F(t, \nu) = n(t - t_0) - \arctan\left(\sqrt{\frac{1-e}{1+e}} \tan \frac{\nu}{2}\right) - e \sin\left(2 \arctan\left(\sqrt{\frac{1-e}{1+e}} \tan \frac{\nu}{2}\right)\right) = 0. \quad (3.18)$$

For a given time epoch, the corresponding true anomaly is obtained by finding the root of function F through, for instance, a Newton–Raphson algorithm.

To conclude the section, a summary of the computational steps is as follows:

1. Provided a time, t , orbital parameters, and time of periapsis passage for the barycentre and lunar orbits, $t - t_{0bs}$ and $t - t_{0mb}$, the corresponding true anomalies, ν_{bs} and ν_{mb} are calculated using Equation 3.18.
2. The transformation matrices \mathbb{T}_{12} and \mathbb{T}_{23} are computed using Equations 3.7 and 3.12.
3. The time-dependent position vectors of the barycentre's orbit around the star in coordinate system S_1 , $\vec{r}_{bs}|^{S_1}$, and lunar orbit around the barycentre expressed in S_2 , $\vec{r}_{mb}|^{S_2}$, are computed using Equations 3.8 and 3.11.
4. The time-dependent position vector of the planet with respect to the barycentre, $\vec{r}_{pb}|^{S_2}$, is obtained via Equation 3.13.
5. The three-dimensional time-dependent position vectors of the exoplanet and its satellite, expressed in observer's coordinate system S_1 , $\vec{r}_{ps}|^{S_1}$ and $\vec{r}_{ms}|^{S_1}$, are computed using Equations 3.14 and 3.15.

3.3. Varying the observer position

The position vectors of the planet and moon bodies computed via the nested two body problem approximation (see Equations 3.14 and 3.15) are expressed in coordinate system S_1 , which is employed as reference for the orbital geometry definition. In principle, the z_1 -axis is directed towards the observer, so that the plane x_1-y_1 represents the observed sky plane. Given the large number of parameters defining the orbital geometry of the planet and moon (see Section 3.2.2), modifying the observer position without altering the bodies' relative orbits, i.e. rotating the observer's view of a fixed system, can be challenging for complex moon-barycentre orbit configurations. As an alternative, a new coordinate system, the observer's reference frame, is here defined as $S_0 = \{x_0, y_0, z_0\}$ and illustrated in Figure 3.6.

Our model allows to specify an alternative observer position as a function of the azimuthal angle φ_{ob} and the polar angle θ_{ob} . Therefore, we define the transformation matrix from coordinate system S_1 to S_0 as the product of two elementary rotations around the y - and z -axes:

$$\begin{aligned} \mathbb{T}_{01} = \mathbb{T}_y(\theta_{ob}) \mathbb{T}_z(\varphi_{ob}) &= \begin{bmatrix} \cos \theta_{ob} & 0 & -\sin \theta_{ob} \\ 0 & 1 & 0 \\ \sin \theta_{ob} & 0 & \cos \theta_{ob} \end{bmatrix} \begin{bmatrix} \cos \varphi_{ob} & \sin \varphi_{ob} & 0 \\ -\sin \varphi_{ob} & \cos \varphi_{ob} & 0 \\ 0 & 0 & 1 \end{bmatrix} = & (3.19) \\ &= \begin{bmatrix} \cos \theta_{ob} \cos \varphi_{ob} & \cos \theta_{ob} \sin \varphi_{ob} & -\sin \theta_{ob} \\ -\sin \varphi_{ob} & \cos \varphi_{ob} & 0 \\ \sin \theta_{ob} \cos \varphi_{ob} & \sin \theta_{ob} \sin \varphi_{ob} & \cos \theta_{ob} \end{bmatrix}. \end{aligned}$$

Then, we express the planetary and lunar position vectors in the observer coordinate system as:

$$\vec{r}_{ps}|^{S_0}(t) = \mathbb{T}_{01} \vec{r}_{pb}|^{S_1}(t), \quad (3.20)$$

$$\vec{r}_{ms}|^{S_0}(t) = \mathbb{T}_{01} \vec{r}_{mb}|^{S_1}(t). \quad (3.21)$$

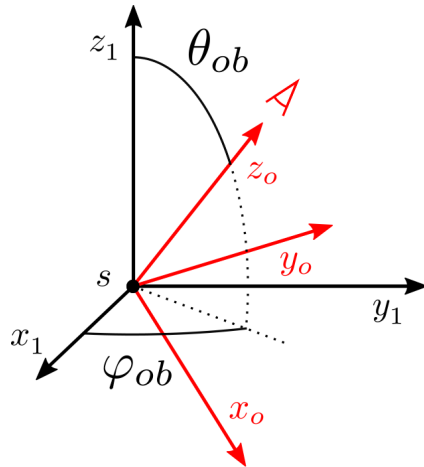


Figure 3.6: Geometry involved in the rotation of the observer coordinate system, S_0 , with respect to the orbital motion coordinate system, S_1 . φ_{ob} stands for the azimuthal angle of rotation, while θ_{ob} is the polar rotation angle. The observer's location is directed towards the positive z_0 -axis. Index s stands for the star position.

In this way, the position vector of planet and moon bodies is concisely described as a function of time, as viewed from an arbitrary external observer position. However, the computation of the pixel contributions to the total reflected starlight by the bodies requires us to describe the planet and moon not only as point masses but as three-dimensional spheres. The three-dimensional nature of the bodies is addressed next.

3.4. Three-dimensional description of the system

The computation of the reflected starlight by the unresolved planet–moon system is carried out by summation of the individual pixel contributions of the bodies (see Equation 2.5). Moreover, as described by Equations 2.5 and 2.4 the reflection properties of each pixel strongly depend on its location on the sphere related to the position of the observer, star and companion body. Hereafter, we grant the planet and moon bodies with a three-dimensional discrete description in Section 3.4.1, calculating the pixel-dependent geometrical factors and angles involved in the aforementioned equations in Sections 3.4.1 and 3.4.2.

3.4.1. Pixel position vector

As introduced in Section 2.3, the planet and moon spherical bodies are discretized through a series of equispaced orthonormal cuts, perpendicular to the sky plane $x_0 - y_0$, resulting in a regular grid of equally sized, square pixels, as seen from the observer's position (see Figure 2.2). As illustrated in Figure 2.5 and argued in Section 2.3, the pixel grids of the planet and moon bodies are defined to be aligned with the planetary scattering plane, i.e. the plane containing the star, planet and observer, at any given time.

We define the rotating orthonormal right-handed coordinate system $S_r = \{x_r, y_r, z_r\}$, centred at the star, with the x_r -axis directed towards the projection of the planet centre onto the sky plane and the z_r -axis directed towards the observer, as seen in Figure 3.7. Translation of S_r to the planet and moon position allows to unequivocally define the vector coordinates of an arbitrary planetary pixel i and lunar pixel j with respect to the planet and moon centres, $\vec{r}_{ip}|^{S_r}$ and $\vec{r}_{jm}|^{S_r}$. Then, the absolute position vector of pixels i and j with respect to the star in S_0 coordinate system is given via vector composition:

$$\vec{r}_{is}|^{S_0}(t) = \vec{r}_{ps}|^{S_0}(t) + \vec{r}_{ip}|^{S_0}(t) = \vec{r}_{ps}|^{S_0}(t) + \mathbb{T}_{0r}(t) \vec{r}_{ip}|^{S_r}, \quad (3.22)$$

$$\vec{r}_{js}|^{S_0}(t) = \vec{r}_{ms}|^{S_0}(t) + \vec{r}_{jm}|^{S_0}(t) = \vec{r}_{ms}|^{S_0}(t) + \mathbb{T}_{0r}(t) \vec{r}_{jm}|^{S_r}, \quad (3.23)$$

where $\vec{r}_{ps}|^{S_0}$ and $\vec{r}_{ms}|^{S_0}$ are obtained through Equations 3.20 and 3.21 respectively, and \mathbb{T}_{0r} is the time dependent coordinate transformation matrix from coordinate system S_r to S_0 , which can be written as an elementary clockwise rotation with respect to the z -axis:

$$\mathbb{T}_{0r}(t) = \mathbb{T}_z(\zeta_p(t)) = \begin{bmatrix} \cos \zeta_p(t) & -\sin \zeta_p(t) & 0 \\ \sin \zeta_p(t) & \cos \zeta_p(t) & 0 \\ 0 & 0 & 1 \end{bmatrix}, \quad (3.24)$$

with ζ_p the time dependent planet azimuthal angle with respect to the observer reference frame S_0 , i.e. the angle between the planes $x_0 - z_0$ and $x_r - z_r$ as seen in Figure 3.7. ζ_p , ranges from 0 to 2π , and is given at any time epoch as a function of the planetary coordinates in S_0 coordinate system as:

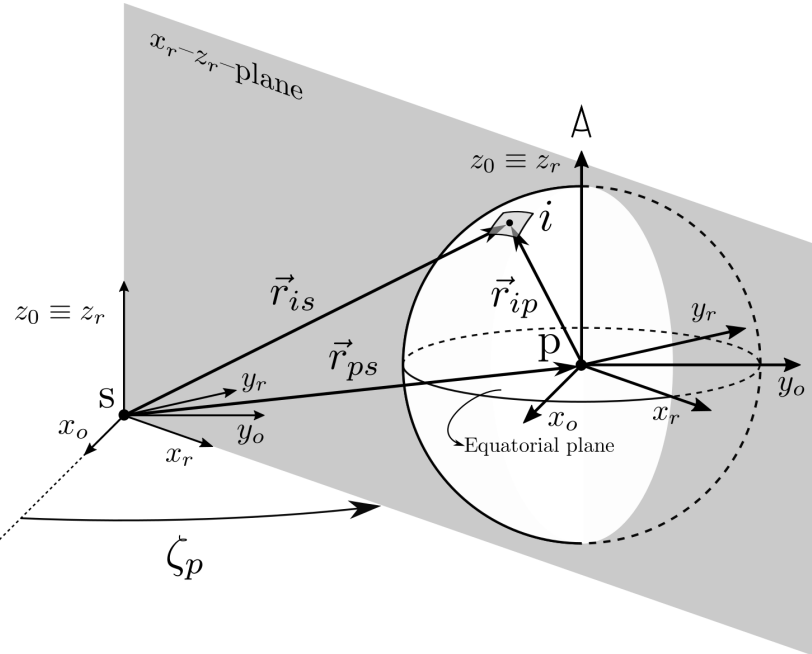


Figure 3.7: Graphical definition of the rotating reference frame S_r and the time dependent position vector of an arbitrary planetary pixel i with respect to the star, \vec{r}_{is} , and with respect to the planet, \vec{r}_{ip} . The planet scattering plane is defined as the $x_r - z_r$ plane. ζ_p is the time dependent planet azimuthal angle with respect to the observer reference frame S_0 , i.e. the angle between planes $x_0 - z_0$ and $x_r - z_r$. The observer's location is directed towards the positive z_0 -axis. Indices are s for the star, p for the planet and i for the planetary pixel.

$$\zeta_p = \arctan 2 \left(\hat{u}_y^T \cdot \vec{r}_{ps}|^{S_0}, \hat{u}_x^T \cdot \vec{r}_{ps}|^{S_0} \right), \quad (3.25)$$

with \hat{u}_x and \hat{u}_y the unity vectors corresponding to the x - and y -axes of reference frame S_0 respectively, and \cdot the inner product between two vectors.

Once determined the position of the N_p planetary pixels and the N_m lunar pixels with respect to the star, we describe the pixel dependent angles taking part in Equations 2.5 and 2.4 as a function of time in Section 3.4.2.

3.4.2. Angular geometry of the planet–moon–star–observer system: angles α , θ , θ_0 , $\phi - \phi_0$, ψ , β

After describing the time dependent position of the planet and moon centre along their orbits, we describe and formulate the angles required to calculate the pixel starlight reflection contribution and to merge the planet–moon signals: the phase angle α , the observer–zenith angle θ , the star–zenith angle θ_0 , the azimuthal difference angle $\phi - \phi_0$, the beta angle β and the scattering plane rotation angle ψ for the planet and the moon.

Phase angle, α

As defined in Section 2.2, the phase angle is the angle between the direction to the star and the observer as measured from the centre of the bodies, ranging from 0 to 180° . The phase angle of the planet and moon, α_p and α_m respectively, are computed at any given time as:

$$\alpha_p(t) = \arccos \left[\hat{u}_z^T \cdot \left(-\frac{\vec{r}_{ps}|^{S_0}(t)}{\|\vec{r}_{ps}|^{S_0}(t)\|} \right) \right], \quad (3.26)$$

$$\alpha_m(t) = \arccos \left[\hat{u}_z^T \cdot \left(-\frac{\vec{r}_{ms}|^{S_0}(t)}{\|\vec{r}_{ms}|^{S_0}(t)\|} \right) \right], \quad (3.27)$$

where $\hat{u}_z = [0 \ 0 \ 1]^T$ is the unitary vector along the z -axis of the S_0 coordinate system.

Given the small separation between the planet and moon compared to their distance to the star, the planetary phase angle is very similar to the lunar phase angle, i.e. $\alpha_p \approx \alpha_m$. Our computations make use of both planetary and lunar phase angles. In the figures presented in this report, the planetary phase angle, α_p , is used as independent variable for the light and polarization curves of the unresolved planet–moon system.

Local observer–zenith angle, θ

The local observer–zenith angle is defined as the angle between the local zenith direction of a certain pixel and the direction towards observer as illustrated in Figure 3.8. Previously described in Section 3.4.1, the pixels' coordinates are steadily defined in the rotating reference frame S_r , which z -axis is directed towards the observer's position. Therefore, the planetary and lunar observer–zenith angles, θ_i and θ_j , are time-invariant and can be computed as:

$$\theta_i = \arccos \left(\hat{u}_z^T \cdot \frac{\vec{r}_{ip}|^{S_r}}{\|\vec{r}_{ip}|^{S_r}\|} \right), \quad (3.28)$$

$$\theta_j = \arccos \left(\hat{u}_z^T \cdot \frac{\vec{r}_{jm}|^{S_r}}{\|\vec{r}_{jm}|^{S_r}\|} \right), \quad (3.29)$$

where θ_i and θ_j take values from 0° (pixels at the sub-observer location) to 90° (limb pixels), $\hat{u}_z = [0 \ 0 \ 1]^T$ is the unitary vector along the z -axis of the S_r coordinate system, and i and j stand for arbitrary planetary and lunar pixels.

Star–zenith angle, θ_0

In parallel to the observer–zenith angle, the star–zenith angle is defined as the angle between the local zenith direction of a pixel and the direction towards the hosting star as illustrated in Figure 3.8. In this

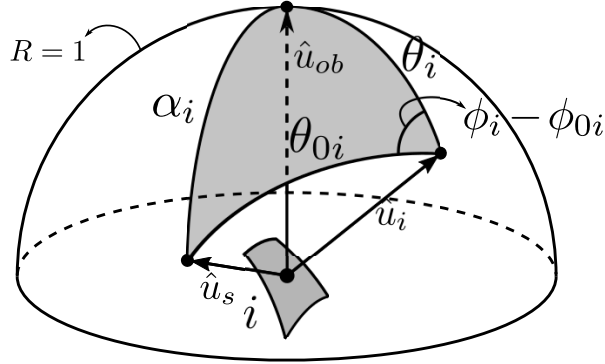


Figure 3.8: Angular geometry of the spherical triangle centred at pixel i and defined by the zenith direction unit vector, \hat{u}_i , the observer's direction unit vector, \hat{u}_{ob} , and the star direction unit vector, \hat{u}_s . The sides of the spherical triangle are: the observer–zenith angle θ_i , the star–zenith angle θ_{0i} , and the pixel-based phase angle α_i , all centred at pixel i . The angle between sides θ_{0i} and θ_i is the azimuthal difference angle $\phi_i - \phi_{0i}$.

case, the star position relative to the grid orientation changes with time, so that the time-dependent planet and moon pixels' star–zenith angles, θ_{0i} and θ_{0j} can be expressed as:

$$\theta_{0i}(t) = \arccos \left[\frac{\vec{r}_{ip}^T |^{S_0}(t)}{\|\vec{r}_{ip} |^{S_0}(t)\|} \cdot \left(-\frac{\vec{r}_{is} |^{S_0}(t)}{\|\vec{r}_{is} |^{S_0}(t)\|} \right) \right], \quad (3.30)$$

$$\theta_{0j}(t) = \arccos \left[\frac{\vec{r}_{jm}^T |^{S_0}(t)}{\|\vec{r}_{jm} |^{S_0}(t)\|} \cdot \left(-\frac{\vec{r}_{js} |^{S_0}(t)}{\|\vec{r}_{js} |^{S_0}(t)\|} \right) \right], \quad (3.31)$$

where θ_{0i} and θ_{0j} take values from 0° (substellar pixels) to 180° ⁵ (pixels in opposite direction to the star). The pixels' position with respect to the bodies in S_0 coordinate system are obtained as done in Equations 3.25 and 3.25, i.e. using the transformation matrix \mathbb{T}_{0r} defined in Equation 3.41, as follows:

$$\vec{r}_{im} |^{S_0}(t) = \mathbb{T}_{0r}(t) \vec{r}_{ip} |^{S_r}, \quad (3.32)$$

$$\vec{r}_{jm} |^{S_0}(t) = \mathbb{T}_{0r}(t) \vec{r}_{jm} |^{S_r}. \quad (3.33)$$

Azimuthal difference angle, $\phi - \phi_0$

The azimuthal difference angle at pixel i is defined as the angle between the planes described by the zenith–observer's directions and the zenith–star directions⁶. As Figure 3.8 shows, placing a unit radius sphere centred at pixel i allows us to describe the relation between angles through the spherical triangle described by the great circles connecting the unit vectors \hat{u}_i , \hat{u}_{ob} and \hat{u}_s , directed towards the pixel zenith, the observer and the star. Then, we make use of the spherical law of cosines relating the sides of the triangle and the $\phi_i - \phi_{0i}$ angle as follows:

$$\cos \alpha_i = \cos \theta_i \cos \theta_{0i} + \sin \theta_i \cos \theta_{0i} \cos (\phi_i - \phi_{0i}), \quad (3.34)$$

$$\phi_i - \phi_{0i} = \arccos \left(\frac{\cos \alpha_i - \cos \theta_i \cos \theta_{0i}}{\sin \theta_i \cos \theta_{0i}} \right).$$

where α_i is the angle between the observer direction and the star direction, measured from the centre of pixel i , i.e. the pixel-based phase angle. Given that $\|\vec{r}_{ip}\| \ll \|\vec{r}_{ps}\|$ and $\|\vec{r}_{jm}\| \ll \|\vec{r}_{ms}\|$, the pixel-based phase angle can be approximated by the body's phase angle α_p and α_m , resulting in:

$$\phi_i - \phi_{0i} = \arccos \left(\frac{\cos \alpha_i - \cos \theta_i \cos \theta_{0i}}{\sin \theta_i \cos \theta_{0i}} \right), \quad (3.35)$$

⁵In practice, pixels with star–zenith angle larger than 90° , $\theta_0 > 90^\circ$ fall at the night side of the body and are skipped in our computations (see Section 3.4.3).

⁶Only the difference between ϕ and ϕ_0 is important, as ϕ is defined with respect to an arbitrarily defined base vector, i.e. ϕ and ϕ_0 can be offset by any value.

$$\phi_j - \phi_{0j} = \arccos \left(\frac{\cos \alpha_m - \cos \theta_j \cos \theta_{0j}}{\sin \theta_j \cos \theta_{0j}} \right). \quad (3.36)$$

Scattering plane rotation angle, ψ

The scattering plane rotation angle stands for the angle between the planet and moon centred at the star and projected onto the sky plane, i.e. the angle between the moon and planet scattering planes measured clockwise from the former (see Figure 3.9b). Ranging from 0 to $2\pi^\circ$, ψ is calculated at any given time as:

$$\psi = \arctan 2 \left(-\hat{u}_y^T \cdot \vec{r}_{ms}|^{S_r}, \hat{u}_x^T \cdot \vec{r}_{ms}|^{S_r} \right), \quad (3.37)$$

where the lunar position with respect to the star in rotating reference frame S_r , $\vec{r}_{ms}|^{S_r}$, is obtained using the transformation matrix \mathbb{T}_{0r} (see Equation 3.41) as:

$$\vec{r}_{ms}|^{S_r}(t) = \mathbb{T}_{0r}^T \vec{r}_{ms}|^{S_0}(t). \quad (3.38)$$

Beta angle, β

Used to rotate vectors F_i^p and F_j^m in Equation 2.5, the angle β is defined as the angle between the body scattering plane and the pixel local meridian plane, i.e. the plane through the pixel position vector from the body and the viewing direction. As Figure 3.9a illustrates, due to the alignment between the planetary grid and the planet scattering plane (see Section 2.2), the beta angle of a planetary pixel i does not vary with time. β_i is, therefore, solely determined by the pixel position vector from the planet in rotating coordinate system S_r as:

$$\beta_i = \arcsin \frac{y_{ip}|^{S_r}}{x_{ip}^2|^{S_r} + y_{ip}^2|^{S_r}}, \quad (3.39)$$

where $\vec{r}_{ip}|_{S_r}$ has been decomposed as:

$$\vec{r}_{ip}|^{S_r} = \begin{bmatrix} x_{ip}|^{S_r} \\ y_{ip}|^{S_r} \\ z_{ip}|^{S_r} \end{bmatrix}.$$

In the case of the lunar pixels, the time-dependent misalignment between the lunar scattering plane and the grid orientation, i.e. the rotating coordinate system S_r , yields a time varying β_j angle. The computation of a lunar pixel's beta angle requires to express \vec{r}_{jm} in an alternative rotating coordinate system $S'_r = \{x'_r, y'_r, z'_r\}$ (see Figure 3.9b):

$$\vec{r}_{jm}|^{S'_r}(t) = \mathbb{T}_{r'r} \vec{r}_{jm}|^{S_r}(t), \quad (3.40)$$

where use is made of the transformation matrix $\mathbb{T}_{r'r}$, elemental clockwise rotation around the z -axis defined as:

$$\mathbb{T}_{r'r}(t) = \mathbb{T}_z(\psi(t)) = \begin{bmatrix} \cos \psi(t) & -\sin \psi(t) & 0 \\ \sin \psi(t) & \cos \psi(t) & 0 \\ 0 & 0 & 1 \end{bmatrix}, \quad (3.41)$$

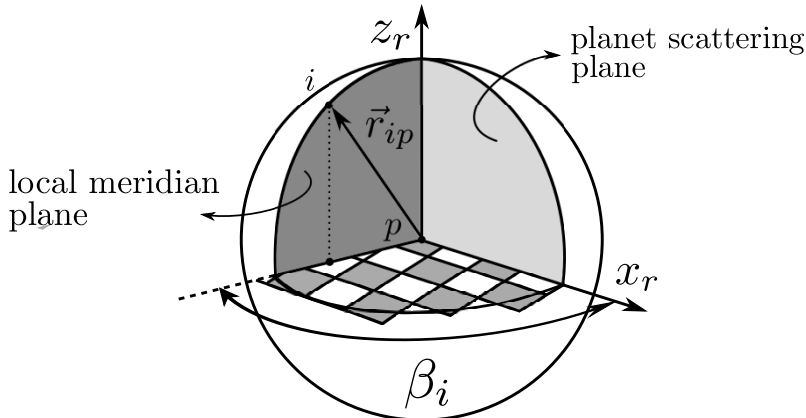
with ψ being the scattering plane rotation angle (see Figure 3.9c).

In the rotating coordinate system S'_r , the angle β_j can be computed as a function of time as:

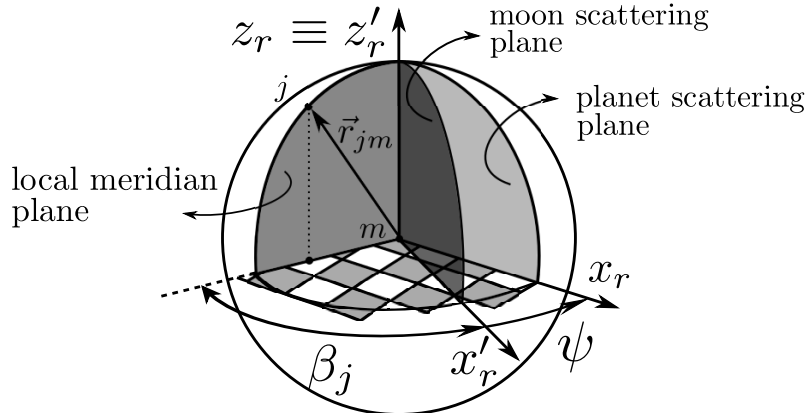
$$\beta_j = \arcsin \frac{y_{jm}|^{S'_r}}{x_{jm}^2|^{S'_r} + y_{jm}^2|^{S'_r}}, \quad (3.42)$$

where $\vec{r}_{jm}|_{S'_r}$ has been decomposed as:

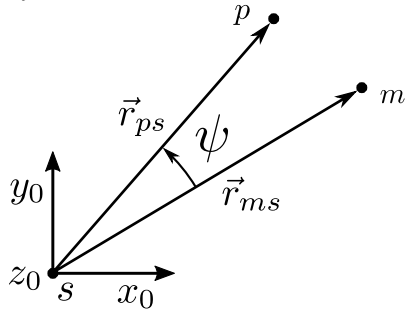
$$\vec{r}_{jm}|_{S'_r} = \begin{bmatrix} x_{jm}|_{S'_r} \\ y_{jm}|_{S'_r} \\ z_{jm}|_{S'_r} \end{bmatrix}. \quad (3.43)$$



(a) Planetary pixel β_i angle.



(b) Lunar pixel β_j angle.



(c) Definition of η angle.

Figure 3.9: Graphical definition of the β angle between the pixel-based local meridian plane and the scattering plane for the case of the planet (a) and moon (b). The rotation angle around the z_0 -axis for coordinates transformation from reference frame S'_r to S_r is graphically defined in (c). The local meridian plane is defined by the position vector of each pixel and the z_r -axis. The planet scattering plane coincides with the x_r-z_r plane, and the moon scattering plane is defined by the $x'_r-z'_r$ plane. The planetary and lunar disk grids are aligned with the x_r and y_r axes. Indices are p for the planet, m for the moon, i for a planetary pixel, and j a lunar pixel.

3.4.3. Flux incidence along the grid: factor d

Light intensity evenly radiated from a point source into three-dimensional space is diluted as we get farther from the emitter. Spread along a total surface area of a sphere, $4\pi r^2$, the flux per area is then inversely proportional to the square of the distance from the source. This is known as the inverse-square law:

$$F \propto \frac{1}{r^2}, \quad (3.44)$$

where F stands for the luminous power at a certain distance r from the source.

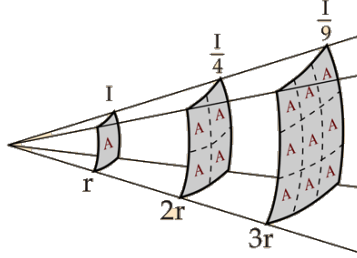


Figure 3.10: Graphical interpretation of the inverse-square law. Light intensity twice as far from the source is spread over four times the area, hence one-fourth the intensity. Figure retrieved from Georgia State University [2016].

The radiative transfer model employed assumes a constant stellar flux πF_0 . In general, the eccentric trajectory of the barycentre, together with the relative motion of the planet and moon around their centre of mass, could yield considerable variations of the actual flux hitting the surface of the bodies. In the present work, the reference stellar flux is chosen to match the flux arriving at the barycentre's periapsis position, i.e. at $a_{bs}(1 - e_{bs})$ distance from the star. Pixel-to-pixel flux variations could be neglected in first instance. However, the pixel absolute position vector computed through Equations 3.25 and 3.23, allows us to easily account for the small pixel-to-pixel variations.

The actual flux arriving at pixels i is thus corrected in Equation 2.5 by introducing the factors d_i and d_j , with $d > 1$ for pixels farther than the barycentre's periastron and $d \in (0, 1)$ for pixels closer than the pericentre. Thus, the incident flux correction factor is computed as:

$$d_i = \left(\frac{a_{bs}(1 - e_{bs})}{\|\vec{r}_{is}\|^{S_0}} \right)^2. \quad (3.45)$$

Equation 3.45 assume that all pixels in the grids are exposed to stellar radiation. However, pixels falling within the dark night region of the bodies receive no radiation, i.e. $d_i = 0$. Assuming a distant point source emitting star, pixels with $\theta_0 > 90^\circ$ fall at the night side, as the parent star falls below the local horizon (see Figure 3.11). However, the three-dimensional nature of the star becomes more relevant when close-in bodies are modelled. In this case, we establish a different criterion for determining black pixels which takes into account the finite radius of the star, based on angle δ : as Figure 3.11 shows, the angle between the star-to-body vector and the pixel-zenith direction, centred at the pixel. Thus, pixels with $\delta < \delta_{max}$ are considered to be black, where the pixel δ angle and δ_{max} for the planet and moon can be expressed as:

$$\delta_i = \arccos \frac{\vec{r}_{ip}^T \cdot \vec{r}_{ps}}{\|\vec{r}_{ip}\| \|\vec{r}_{ps}\|}, \quad (3.46)$$

$$\delta_j = \arccos \frac{\vec{r}_{jm}^T \cdot \vec{r}_{ms}}{\|\vec{r}_{jm}\| \|\vec{r}_{ms}\|}, \quad (3.47)$$

$$\delta_{p\ max} = \arccos \frac{R_s - R_p}{\|\vec{r}_{ps}\|}, \quad (3.48)$$

$$\delta_{m\ max} = \arccos \frac{R_s - R_m}{\|\vec{r}_{ms}\|}. \quad (3.49)$$

Both approaches neglect the existence of sunset pixels, i.e. pixels which receive stellar radiation from only part of the star. This feature could be easily modelled in future versions of the tool by integration of the stellar emitted radiation along the observed star effective area, in combination with a star limb darkening model.

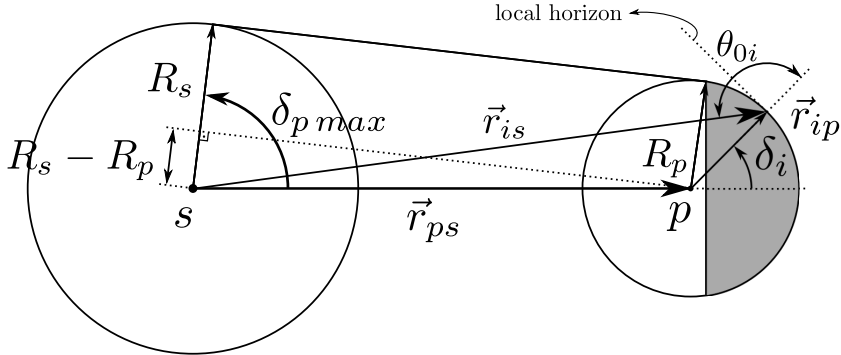


Figure 3.11: Geometry involved in the determination of the night side of the planetary disk. The night side on the lunar disk is determined in a parallel way. Pixels with $\delta_i < \delta_{p\ max}$ are considered to fall within the night area of the disk. The pixel-based δ_i angle is defined as the angle between the star–planet direction and \vec{r}_{is} , the position vector of pixel i with respect to the star. \vec{r}_{ps} stands for the position vector of the planet (radius R_p) with respect to the star (radius R_s). Distances between bodies and radii are not to scale in order to emphasize the geometry of the system.

The geometry description of the extrasolar system presented in this chapter allows us at compute the reflected starlight of the planet–moon system without taking into account the possible mutual events between bodies, i.e. partial or total shadowing and occulting of the planet and/or moon. Chapter 4 addresses the description and mathematical elaboration of all possible mutual events between bodies.

4

Mutual events

As stated in Chapter 1, transits' theory was thoroughly developed with the growing interest in exoplanets research. Recent studies include the presence of exomoons in transits simulation [see Kipping, 2011]. On the other hand, the detailed mathematical description on eclipse events on the Moon–Earth system was developed by Link [1969]. Based on his work, we develop a simplified numerical model for the computation of eclipses, and determine the pixels that stay hidden during transit events.

Unambiguous definition of the terms *transit* and *eclipse* are provided in Section 4.1, while a description of all possible mutual events is provided in Section 4.2. The assumptions underlying the presented transit and eclipse models are discussed in Section 4.3. Detailed information on the numerical background of computing eclipses and transits is provided in Sections 4.4 and 4.5. These models have been implemented and verified (see Appendix A).

4.1. Definition of mutual events

Considering the lunar orbital motion around the planet, as well as the planet–moon motion around the star, favourable orbital configurations may lead to sporadic time-dependent observed radiation variations due to a partial blocking of light. This phenomenon is at the heart of the transit photometry method [see e.g. Winn, 2010b], and is expected to provide a bonanza of information on direct imaging of exoplanets, not only via flux variations [see Cabrera and Schneider, 2007] but also via the state of polarization of the observed radiation.

Thus, we define mutual event as the particular relative positioning between the star, planet, moon, and observer (and, if applicable, other bodies) which causes a fluctuation on the observed radiation of any of the bodies or the system in general. Disregarding the possible existence of planetary rings and laying aside unnoticeable fortuitous events such as the flyby of a big comet, we find two major mutual events between the bodies of a planetary system: transits and eclipses.

Transit: interposition of a body between the observer and the illuminated and visible disk of a second body under observation, causing a partial or total blockage of the light (both emitted and reflected) in the observer's field of view (see Figure 4.1a).

Eclipse: interposition of a body between the star and a second body under observation, casting a partial shadow on (or completely darkening) its illuminated and visible disk, i.e. causing a partial or total blockage of the reflected stellar light emitted towards the body (see Figure 4.1c).

A more detailed description of all the expected mutual event cases for a planet–moon–star system is provided below in Section 4.2.

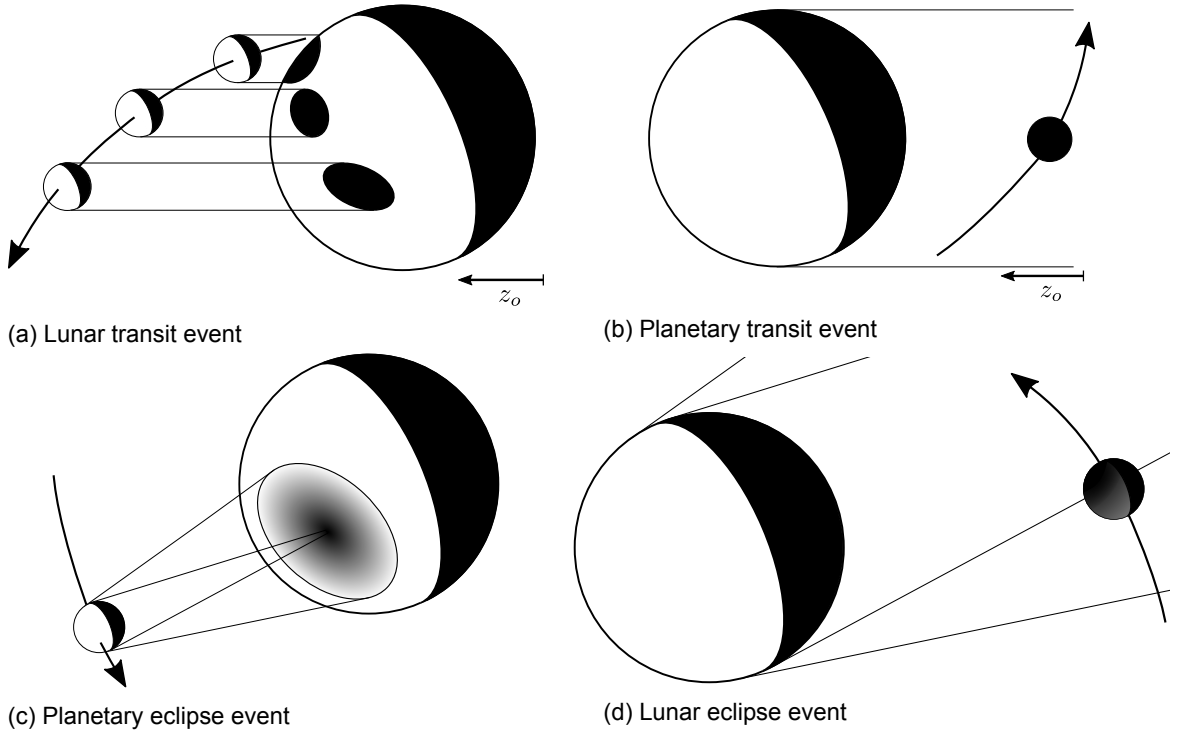


Figure 4.1: Sketch illustrating the modelled mutual events between bodies: a lunar transit (a), a planetary transit (b), a planetary eclipse (c), and a lunar eclipse (d). The observer is located towards the positive direction of the z_o -axis. White–black scale indicates full-null illumination of a body’s surface as viewed from the observer’s position. The orbital motion of the moon around the planet is indicated with an arrow. Distances between bodies are not to scale in order to emphasize the geometry of the system.

4.2. Mutual photometric phenomena

With the aim of clarifying the nomenclature employed for the different mutual events here modelled, we provide a breakdown of all possible mutual event instances that might occur within an isolated planet–moon–star system, as well as a short description of the phenomena. In total, we model four different possible scenarios:

1. Planetary eclipse:

The moon is in between the star and the planet, projecting a partial gradual shadow on the planetary surface which largely depends on the planet–star, moon–star distances, and the planetary and lunar radii.

2. Lunar eclipse:

The planet is in between the star and the moon, projecting a partial gradual shadow on the lunar surface. Depending on the lunar shadow cone and the trajectory of the moon, the moon might be totally or partial shadowed.

3. Planetary transit:

Planet transiting in front of the moon, i.e. in between the moon and the observer. Because the planet is larger than its companion, a total or partial occultation of the moon behind the star could occur depending on the planet–moon orbital plane inclination with respect to the observer line of sight.

4. Lunar transit:

Moon transiting in between the planet and the observer. As a result, a region of the planet is occulted, depending on the planet–moon radii ratio.

Besides these four cases, we identify four extra scenarios which complete the list of possible mutual photometric phenomena. These are out of the scope of this research and, thus, are not modelled in this study. However, our mutual events model could easily be adapted in order to carry out future studies based on the next scenarios:

5. Planetary–stellar transit:

Planet transiting in front of the star partially dimming the stellar light and causing a flux asymmetry that induces a change on the overall polarization state of the observed starlight.

6. Lunar–stellar transit:

Moon transiting in front of the star, partially blocking the stellar radiation in the observer's field of view. Measurement of lunar–stellar transits constitutes the basis for exomoon search through transit photometry (see Section 1.2).

7. Planetary occultation:

Planet occulted by the star, which interposes between the observer and the planet at phase angle $\alpha \approx 0^\circ$. In this case, the planet is not observed because it is behind the star.

8. Lunar occultation:

Similar to the planetary occultation, the moon is occulted by the star at phase angle $\alpha = 0^\circ$, yielding a decease of the planet–moon–star system measured flux.

The above presented list reflects individual mutual events. However, from a geometrical point of view, combinations of different scenarios are also possible for phase angles $\alpha \approx 0, 180^\circ$ in the case of the planet–moon–star system. More complex systems conformed by a higher number of planets and/or satellites may yield simultaneous combinations of transits and eclipses at $\alpha \neq 0, 180^\circ$. In the present work, the study of directly imaged planet–moon systems resolved from the parent star impedes observing the system at phase angles close to $\alpha = 0, 180^\circ$.

Our transits and eclipses computation model traces for mutual events in a systematic approach which assumes that simultaneous mutual events are possible, i.e. combinations of mutual events are always taken into account in our computations. In such a way, we can carry out mutual events characterization for an arbitrary number of bodies (planets and moons), leaving all paths opened towards the study of more complex planetary systems.

4.3. Mutual events model assumptions

As described by Link [1969], the illumination at a specific location (pixel i) on a shadowed body during an eclipse event depends on its distance to the star, the stellar radius, the flux distribution across the star (limb darkening across the disk), and on the transmission of stellar radiation through the atmosphere of the eclipsing body. Based on Link [1969], a simplified model for the computation of eclipses has been designed for this first implementation of the *ExoPy* tool, only considering the dimensions of the planet and moon bodies and their position with respect to the star.

Stellar light rays passing through the atmosphere of a body retain key information on its composition, as photons are absorbed, scattered and refracted by atmospheric gases and/or haze and cloud particles. This phenomenon allows to determine the Earth's transmission spectrum by observing the Moon during lunar eclipses [see Palle et al., 2009], as well as some atmospheric properties of exoplanets from transit spectroscopy observations [see Charbonneau et al., 2002]. For the sake of enhancing the comprehension of the numerous factors playing a role in the problem and therefore simplifying the model developed, the interaction of the stellar rays with an eclipsing body's atmosphere is not considered in our analysis¹. Moreover, the star is considered to emit a constant flux intensity along its disk, i.e. no limb darkening effect is considered. Likewise, the transits model implemented only takes into account the position and sizes of the two bodies involved in the event, excluding in first approximation the transmission of reflected light through the atmosphere of the transiting body.

For the modelling of transit events, we assume the observer to be infinitely distant, so that the shadow on the darkened body results from the geometrical intersection of a cylinder and a the body's

¹Other phenomena such as gravitational deflection of light are not considered.

sphere. Stellar transits are not modelled, as only reflected starlight on the planet and moon are considered in this study. In the case of the eclipses, we assume a conical stellar ray approach in which the umbra and penumbra shadows can be differentiated, contrary to the assumptions in the study carried out by Cabrera and Schneider [2007]. Furthermore, we grant total freedom to the lunar and planetary positions with respect to the star, considering all possible eclipse cases.

In the rest of this chapter, the mathematical elaboration of the models designed for the tracking and characterization of mutual events is presented. Section 4.4 describes the rationale and formulae behind the characterization of umbral, antumbral and penumbral eclipses.

4.4. Computing eclipses

An eclipse occurs when body A is positioned between the illuminating star S and body B such that the shadow of body A falls onto body B . Our aim is to model the (partial or total) darkening of body B due to the shadow through the pixel factor c_i ($i \in [0, 1]$, where $c_i = 0$ implies a totally eclipsed pixel and $c_i = 1$ applies for non-eclipsed pixels) in Equation 2.5 and, therefore, to assess the resulting change in the disk-integrated flux and polarization of body B .

The different types of eclipses modelled by *ExoPy* are described in Section 4.4.1, while the generic formulation for the computation of the magnitude of an eclipse is provided in Section 4.4.2. Then, we evaluate the condition required for the existence of an eclipse event in Section 4.4.3, and Sections 4.4.4, 4.4.5 and 4.4.6 describe the mathematical formulation for identifying and characterizing eclipsed pixels in the umbral, antumbral and penumbral regions, respectively. A summary of the steps carried out in the model are presented in Section 4.4.7, after we present the mathematical elaboration.

4.4.1. Types of eclipses

Simplified studies assessing the impact of planetary eclipses frequently assume starlight rays to be parallel at the shadowing body position. In such case, the eclipse is described by a cylinder with the radius of the body in which one finds no stellar radiation. Out of the cylinder region, a second body would be completely illuminated (see Figure 4.2).

The parallel stellar rays approach is valid for low orbit spacecraft, close-in objects eclipsed by a planetary body or planetary systems that are really far away from their parent star. In the case of the Earth-moon system, the shadow cast is far from resembling a cylinder. Hence, the model developed considers a three-dimensional star which, in the presence of an orbiting body, projects a non-uniform divergent conical shadow onto space, as observed in Figure 4.2. Depending on the position of the shadowed pixel i within the eclipse cone, three different types of eclipses can be found:

Umbral eclipse:

Also denominated total eclipse, the umbral eclipse is reached when pixel i falls within the umbra region of the shadow. In such case, seen from pixel i , the star is completely hidden by body A and the shadowed point is completely darkened.

Partial eclipse:

Pixels contained within the penumbra region of the shadow observe the star partially obscured by the eclipsing body.

Annular eclipse:

Lastly, points falling within the antumbra region experience an annular eclipse, i.e. the star is observed as a bright ring of light around the eclipsing body.

In the three cases, the eclipse intensity is proportional to the amount of radiation received from the visible region of the star in first approximation², as we detail in Section 4.4.2.

²Light transmission through the atmosphere of the eclipsing body ignored.

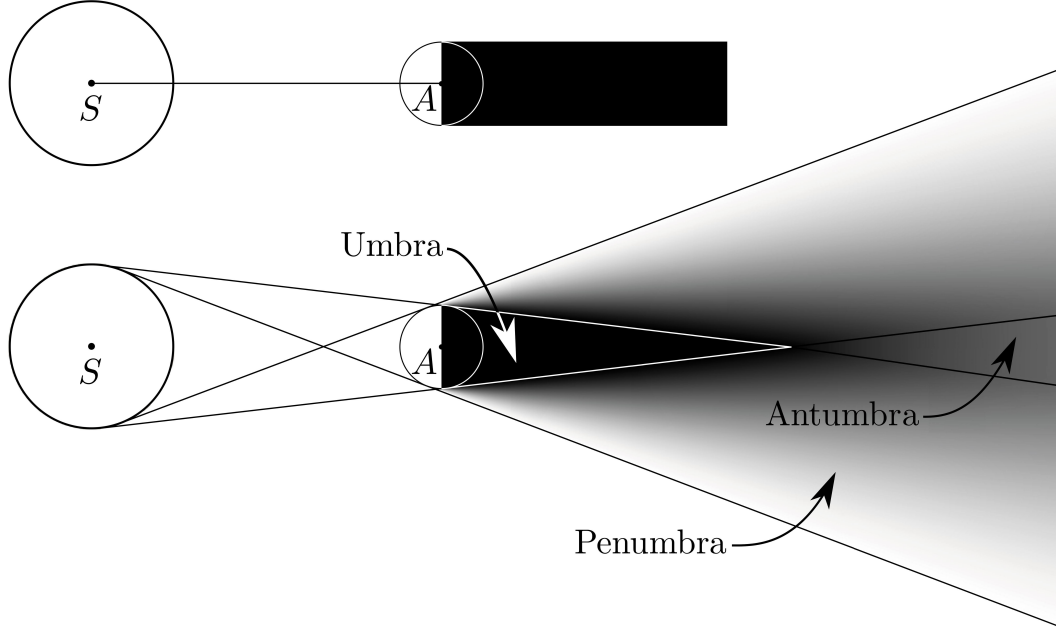


Figure 4.2: Graphical representation of a stellar eclipse caused by the interposition of body A between the shadowed body and the star S modelled using two different approaches. The drawing at the top stands for a parallel rays approach which results in a cylindrical shadow. The drawing at the bottom represents the more realistic conical approach in which the three-dimensional shape of the star is considered. In the latter case, three different regions are differentiated across the shadow cast by body A onto space: umbra, antumbra, penumbra. The white–black scale stands for illuminated–dark regions on space. Distances between bodies and radii are not to scale in order to emphasize the geometry of the system.

4.4.2. Computing the magnitude of an eclipse

The amount of flux arriving to a particular pixel i at a specific time epoch is determined by the apparent magnitude of the star as seen from the pixel position. In Equation 2.5, this is accounted by introducing the pixel factor c_i , ratio between the actual flux hitting pixel i , e_i , and the expected flux in the absence of eclipse, e'_i :

$$c_i = \frac{e_i}{e'_i}. \quad (4.1)$$

Computing the factor c_i for each pixel and time epoch requires modelling the dimming effect due to the partial stellar obscuration during an eclipse event. During the upcoming computations, we employ the following notations for a generic three-body system configuration (see Figure 4.4):

- A centre of eclipsing body (body A)
- B centre of shadowed body (body B)
- S centre of star
- R_S radius of the star
- R_A radius of eclipsing body A
- R_B radius of shadowed body B
- i centre of pixel i on the eclipsed body surface
- \vec{r}_{AS} vector position of the star S with respect to body A
- \vec{r}_{AB} vector position of body B with respect to body A
- \vec{r}_{Ai} vector position of pixel i from body A

As proposed by Link [1969], the illumination of location i can be computed by integration over the stellar disk as follows:

$$e_i = \int T(h_o) dq, \quad (4.2)$$

where $T(h_o)$ is the transmission of rays passing at a distance h_o from the center of eclipsing body A (grazing height), and dq is the differential of stellar flux coming from an elementary ring on the stellar disk circumscribed from the point E_1 at Figure 4.3 by the radius r , written down as:

$$dq = 2 \int_0^{r_o} b(R) r dr d\epsilon, \quad (4.3)$$

where $b(R)$ accounts for the brightness of the region on the solar disk at distance R from its center.

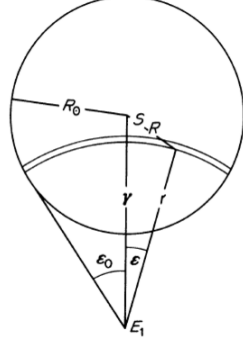


Figure 4.3: Illustration of a differential elementary ring for the integration of the total stellar flux hitting a specific pixel. In the figure, R_\odot stands for the stellar radius, S is the index for the star centre, and γ is the angular distance between the eclipsing body E_1 (body A using the notation for this report) and the star, as seen from a point on the shadowed body. R , r and ϵ describe the position of a point along the differential elementary ring with respect to the S and E_1 bodies. Figure retrieved from Link [1969].

As argued in Section 4.3, our model does not consider the stellar limb darkening. Thus, the star has constant brightness along the solar disk, i.e. $b(R) = b$. Moreover, the transmission of radiation through the eclipsing body atmosphere is neglected. As a result, in Equation 4.2, we simply assume:

$$T(h_o) = 0.0 \quad \text{if } h_o \leq R_A, \quad (4.4)$$

$$T(h_o) = 1.0 \quad \text{if } h_o > R_A. \quad (4.5)$$

Then, Equations 4.2 and 4.3 can be rewritten as:

$$e = 2 b \int \int r dr d\epsilon = b A_S, \quad (4.6)$$

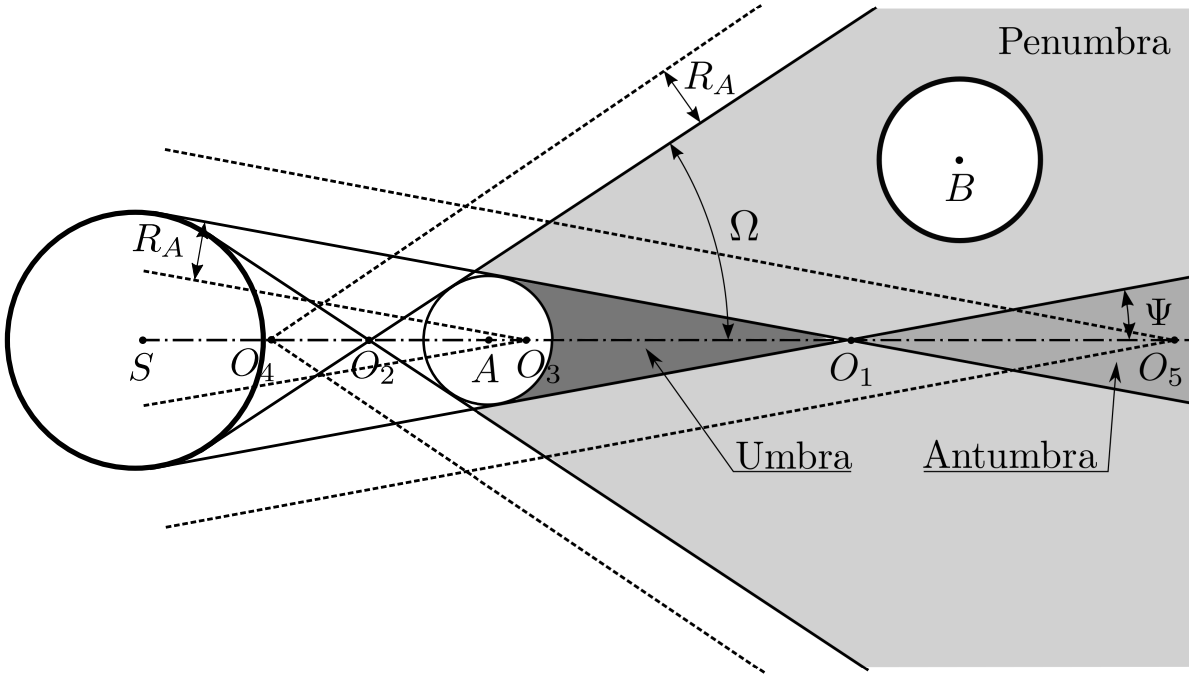
with A_S the total stellar disk area observed from a specific node.

Equation 4.6 yields a nodal illumination which is proportional to the visible stellar disk area or, alternatively, the total overlapped area A_o , i.e. the area of the eclipsing body which overlaps with the stellar disk. Consequently, the stellar flux arriving at pixel i is solely determined by the position and size of the bodies involved. The pixel factor c_i is then defined as the unity minus the eclipse obscuration, i.e. the fraction of star's surface area occulted by the eclipsing body:

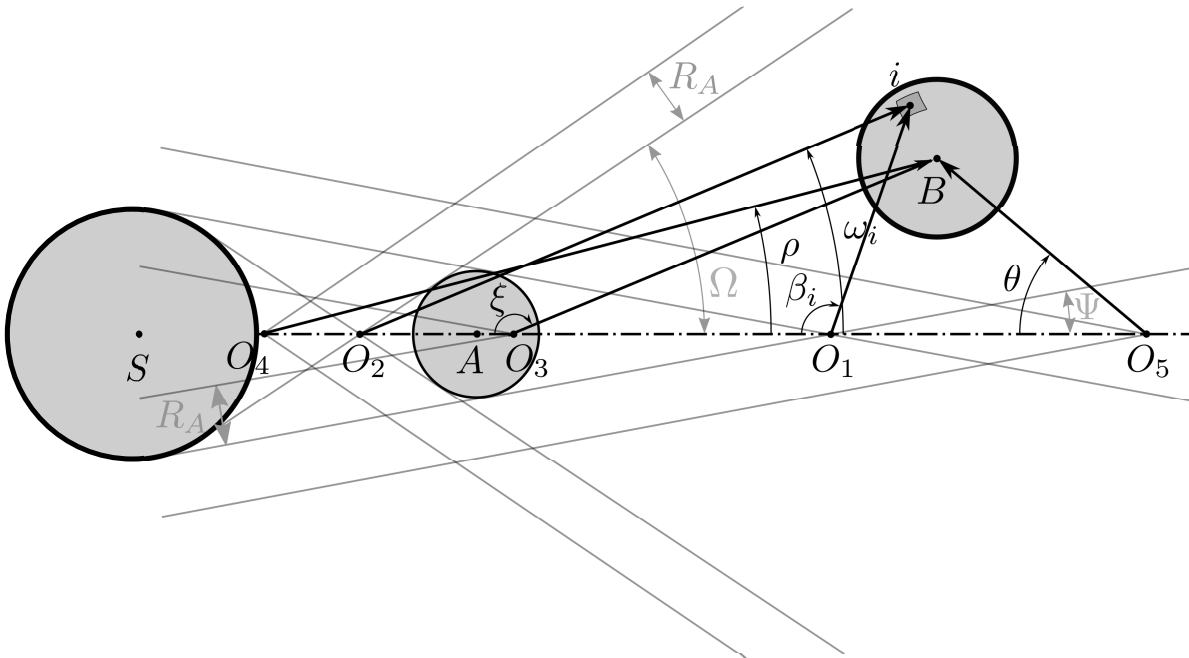
$$c_i = \frac{\text{Area observed stellar disk}}{\text{Area stellar disk}} = 1 - \frac{\text{Area overlapped}}{\text{Area stellar disk}}. \quad (4.7)$$

The basic eclipse geometry as provided in Figure 4.4 comprises the umbral and antumbral cones of apex O_1 and aperture 2Ψ and the penumbral cone of apex O_2 and aperture 2Ω . As follows from the tangency condition of the starlight rays delimiting these regions, the semi-aperture Ψ and Ω can be expressed as a function of the eclipsing body and star radii, and the distance among them as:

$$\sin \Psi = \frac{R_S - R_A}{\|\vec{r}_{AS}\|}, \quad (4.8)$$



(a) Geometrical definition of the umbral, antumbral and penumbral cones, as well as the auxiliary points O_1, O_2, O_3, O_4 and O_5 .



(b) Graphical definition of the angles ζ , ρ , ω_i , β_i and θ , involved in the calculation of the eclipse obscuration at an arbitrary pixel i on the surface of body B .

Figure 4.4: Geometrical description of a generic eclipse scenario in which the star \$S\$ is eclipsed by body \$A\$, casting a shadow on body \$B\$. The shadow projected by body \$A\$ onto space has rotational symmetry along the direction from the star to the body. The radii of the \$A\$ and \$B\$ bodies is denoted by \$R_A\$ and \$R_B\$, accordingly. The umbral and antumbral cones have apex \$O_1\$ and aperture \$2\Psi\$ and the penumbral cone has apex \$O_2\$ and aperture \$2\Omega\$. Angles are measured from the shadow cone axis, whilst \$\beta_i\$, \$\omega_i\$, \$\zeta\$, \$\rho\$, and \$\theta\$ are centred at \$O_1\$, \$O_2\$, \$O_3\$, \$O_4\$, and \$O_5\$, respectively. Distances between bodies and radii are not to scale in order to emphasize the geometry of the system.

$$\sin \Omega = \frac{R_S + R_A}{\|\vec{r}_{AS}\|}. \quad (4.9)$$

The mentioned cones share a common axis direction, defined by the unity vector \vec{u}_{AS} pointing from the eclipsing body towards the star:

$$\vec{u}_{AS} = \frac{\vec{r}_{AS}}{\|\vec{r}_{AS}\|}. \quad (4.10)$$

Eclipses are transient isolated events. The search for eclipsed pixels at every time epoch yields high computational times and computational effort with increasing values of N_{eq}^p and N_{eq}^m . As a solution, we assume as a starting point a non-eclipse scenario at all pixels and epochs, $c_i = 1.0$. Then, we identify the precise times at which body B is shadowed by body A as shown in Section 4.4.3.

4.4.3. Occurrence of eclipses

As a first step, eclipse epochs on body B are identified by checking the sphere centre position with respect to the penumbral cone, which defines the eclipsed region. For this purpose, the angle ρ is to be computed at each epoch (see Figure 4.4b), defined by:

$$\cos \rho_B = \frac{-\left(\vec{r}_{AB} - \overrightarrow{AO}_4\right) \cdot \vec{u}_{AS}}{\|\vec{r}_{AB} - \overrightarrow{AO}_4\|}, \quad (4.11)$$

where small values of ρ_B are expected (with $\rho_B \in [0, 90]^\circ$) and the vector \overrightarrow{AO}_4 is defined as a function of the shadowed and eclipsing bodies' radii and the sine of Ω :

$$\overrightarrow{AO}_4 = \frac{R_B + R_A}{\sin \Omega} \vec{u}_{AS}. \quad (4.12)$$

Hence, the time range to be evaluated can be shrunk into specific periods which satisfy the condition:

$$\sin \rho_B < \sin \Omega. \quad (4.13)$$

Eclipses are found at time epochs satisfying Equation 4.13. Due to pixel to pixel position variations, we can have different types of eclipses simultaneously, i.e. disk pixels at time epochs satisfying Equation 4.13 may fall within the umbra, antumbra, penumbra, or no-eclipse regions. Our eclipses model carries out a pixel-by-pixel sequential search. At every given time, pixel i is first checked for total eclipse (Section 4.4.4), followed by annular eclipse (Section 4.4.5) and partial eclipse (Section 4.4.6).

4.4.4. Umbra nodes

Pixels belonging to the umbral zone experience a total stellar eclipse scenario, characterized by an eclipse obscuration equal to 1.0, i.e. $c_i = 0.0$. For wide umbral cones and small enough shadowed bodies, as occurs in the lunar eclipse for our Earth-Moon-Sun system, the body B may fall entirely under the full shadow region. This situation can be checked through the condition:

$$\cos \xi_B > \cos \Psi, \quad (4.14)$$

where $\cos \Psi$ follows by making use of Equation 4.8 and the Pythagorean identity, and ξ_B is given by the equation below:

$$\cos \xi_B = \frac{\left(\vec{r}_{AB} - \overrightarrow{AO}_3\right) \cdot \vec{u}_{AS}}{\|\vec{r}_{AB} - \overrightarrow{AO}_3\|}, \quad (4.15)$$

where

$$\overrightarrow{AO}_3 = -\frac{R_A - R_B}{\sin \Psi} \vec{u}_{AS}. \quad (4.16)$$

Alternatively, the body B may partially fall within the umbral cone. As follows from Figure 4.4, this scenario occurs at time epochs satisfying the following two conditions:

$$\begin{cases} \cos \theta_B > \cos \Psi \\ \|\overrightarrow{O_5B}\| > \frac{R_B}{\tan \Psi} \text{ or } \|\overrightarrow{O_1B}\| < R_B \end{cases}, \quad (4.17)$$

with the $\cos \theta_B$, and the $\overrightarrow{O_5B}$ and $\overrightarrow{O_1B}$ vectors rewritten as:

$$\cos \theta_B = \frac{(\vec{r}_{AB} - \overrightarrow{AO}_5) \cdot \vec{u}_{AS}}{\|\vec{r}_{AB} - \overrightarrow{AO}_5\|}, \quad (4.18)$$

$$\overrightarrow{O_5B} = \vec{r}_{AB} - \overrightarrow{AO}_5, \quad (4.19)$$

and

$$\overrightarrow{O_1B} = \vec{r}_{AB} - \overrightarrow{AO}_1, \quad (4.20)$$

where

$$\overrightarrow{AO}_5 = -\frac{R_B + R_A}{\sin \Psi} \vec{u}_{AS}, \quad (4.21)$$

and

$$\overrightarrow{AO}_1 = -\frac{R_A}{\sin \Psi} \vec{u}_{AS}. \quad (4.22)$$

While full umbra epochs immediately imply the full darkness of all disk pixels, partial umbra epochs require to perform a pixel-by-pixel verification. As can be observed in Figure 4.4, nodes falling inside the umbral cone satisfy the condition $\beta_i < \Psi$, which can be reformulated as:

$$\sin \beta_i < \sin \Psi, \quad (4.23)$$

taking into consideration that only nodes on the bright hemisphere of the body are checked for eclipse existence. The β_i angle at each node is given by the expression:

$$\cos \beta_i = \frac{(\vec{r}_{Ai} - \overrightarrow{AO}_1) \cdot \vec{u}_{AS}}{\|\vec{r}_{Ai} - \overrightarrow{AO}_1\|}, \quad (4.24)$$

where \overrightarrow{AO}_1 follows from Equation 4.22.

Pixels meeting Equation 4.23 at a certain time are located within the umbra zone and are completely dark, so that $c_i = 0.0$. Where Equation 4.23 is not satisfied, we continue the quest for pixels at the antumbra zone, as detailed in Section 4.4.5.

4.4.5. Antumbra nodes

All time epochs for which body B does not cross the umbral cone are susceptible of experiencing an antumbral (annular) eclipse, in which the apparent eclipsing body size does not completely cover the stellar disk. Being excluded the possibility of encountering an umbral eclipse, time epochs at which annular eclipses are given by the condition here exposed, as follows from Figure 4.4b:

$$\cos \xi_B < -\cos \Psi, \quad (4.25)$$

where $\cos \xi_B$ and Ψ follow from Equations 4.15 and 4.8, accordingly.

Time epochs satisfying Equation 4.25 are then selected for a pixel-by-pixel verification, as already described in Section 4.4.4. In this case, $180^\circ - \beta_i < \Psi$ is required condition to determine eclipsed disk pixels, what is translated to:

$$\cos \beta_i < -\cos \Psi. \quad (4.26)$$

For each of the nodes within the antumbral cone, the total incoming flux is solely determined by the stellar and eclipsing body viewing angles, $2\alpha_S$ and $2\alpha_A$ accordingly (see Figure 4.4 and Figure 4.5), which are given by the expressions:

$$\alpha_S = \arcsin \frac{R_S}{\|\vec{r}_{Si}\|}, \quad (4.27)$$

$$\alpha_A = \arcsin \frac{R_A}{\|\vec{r}_{Si}\|}. \quad (4.28)$$

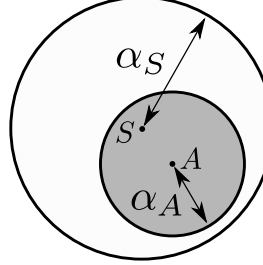


Figure 4.5: Stellar (S) and eclipsing body (A) disks as seen from a pixel on the shadowed body during an annular (or antumbral) eclipse. α_S and α_A stand for the angular radius of the bodies.

Therefore, the magnitude of eclipse at pixel i , given by the pixel factor c_i , is given by Equation 4.7 and can be written as:

$$c_i = \frac{\pi\alpha_S^2 - \pi\alpha_A^2}{\pi\alpha_S^2} = 1 - \left(\frac{\alpha_A}{\alpha_S}\right)^2. \quad (4.29)$$

4.4.6. Penumbra nodes

All remaining pixels satisfying Equation 4.13 are finally examined for penumbra. In this case, pixels satisfying $\omega_i < \Omega$ are contained within the penumbral cone limits, as observed in Figure 4.4b. This inequality can be rewritten in terms of the cosine function of the angles as:

$$\cos \omega_i > \cos \Psi, \quad (4.30)$$

where $\cos \Psi$ follows from Equation 4.8 and the cosine of the ω_i angle can be written as:

$$\cos \omega_i = \frac{-\left(\vec{r}_{Ai} - \overrightarrow{AO}_2\right) \cdot \vec{u}_{AS}}{\|\vec{r}_{Ai} - \overrightarrow{AO}_2\|}, \quad (4.31)$$

with

$$\overrightarrow{AO}_2 = \frac{R_A}{\sin \Omega} \vec{u}_{AS}. \quad (4.32)$$

Thus, according to Equation 4.7, the magnitude of eclipse at pixel i , c_i , can be calculated by means of the stellar and eclipsing body viewing angles, i.e. the angular diameter of the bodies, $2\alpha_S$ and $2\alpha_A$, and the eclipsing body-to-star angular distance as seen from the shadowed body, δ . Then, as follows from Figure 4.6, c_i can be expressed as:

$$c_i = \frac{\pi\alpha_S^2 - A_1 - A_2}{\pi\alpha_S^2} = 1 - \frac{A_1 + A_2}{\pi\alpha_S^2}, \quad (4.33)$$

with

$$A_1 = \begin{cases} \frac{\theta_A - \sin \theta_A}{2} \alpha_A^2 & \text{if } \delta \geq l_S \\ \pi - \frac{\theta_A - \sin \theta_A}{2} \alpha_A^2 & \text{if } \delta < l_S \end{cases}, \quad (4.34)$$

$$A_2 = \begin{cases} \frac{\theta_S - \sin \theta_S}{2} \alpha_S^2 & \text{if } \delta \geq l_A \\ \pi - \frac{\theta_S - \sin \theta_S}{2} \alpha_S^2 & \text{if } \delta < l_A \end{cases}, \quad (4.35)$$

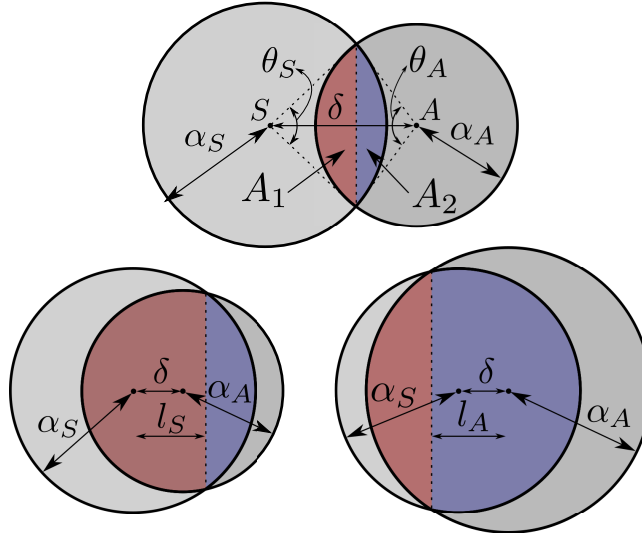


Figure 4.6: Stellar (S) and eclipsing body (A) disks as seen from a pixel on the shadowed body during a penumbral eclipse. The stellar shadowed area is decomposed in two components A_1 and A_2 . α_S and α_A stand for the angular radius of the bodies, and δ is the angular separation between the bodies' centre. θ_S and θ_A are the central angles of the circular segments defined by the common cord of the intersecting stellar and eclipsing body disks. The minimum distance from the star/eclipsing body centre to the common chord is defined as l_S/l_A .

where l_S and l_A are the distances from the stellar disk centre and the eclipsing body disk centre, respectively, to the chord resulting from the two intersection points of the stellar and eclipsing body circumferences. Moreover, the central angles θ_S and θ_A (see Figure 4.6) follow by making use of the Heron's formula:

$$\theta_A = 2 \arcsin \left(\frac{2}{\alpha_A \delta} \sqrt{S(S - \alpha_S)(S - \alpha_A)(S - \delta)} \right), \quad (4.36)$$

$$\theta_S = 2 \arcsin \left(\frac{2}{\alpha_S \delta} \sqrt{S(S - \alpha_S)(S - \alpha_A)(S - \delta)} \right), \quad (4.37)$$

with

$$S = \frac{1}{2} (\alpha_A + \alpha_S + \delta). \quad (4.38)$$

Pixels on body B which satisfy Equation 4.13 but do not meet the conditions established by Equations 4.14, 4.17, 4.26 and 4.30 fall out of the shadow projected by body A at a specific time epoch and, thus, maintain an eclipse factor $c_i = 1.0$.

In such way, we cover all possible eclipse conditions in a computationally efficient way. As a summary of the process described in Sections 4.4.4, 4.4.5 and 4.4.6, we provide a step-by-step overview of the computational logic of the model below.

4.4.7. Computational steps

With the aim of enhancing visualization of the successive computational steps carried out by the *ExoPy* eclipses module towards the computation of the factor c_i at every pixel and time epoch, we provide a clear breakdown of steps. For each pair of eclipsing body A and shadowed body B , result of the permutation of bodies present in the system (in this case the planet and the moon), we:

1. Initially assume all pixels at all epochs to be non-eclipsed, i.e. $c_i = 1.0$.
2. Identify eclipse epochs using Equation 4.13. At non-eclipse times, no further steps are carried out.
3. Look for fully darkened disk epochs satisfying Equation 4.14, for which all pixels are completely shadowed, i.e. $c_i = 0.0$.

4. Look for total eclipsed nodes through pixel-by-pixel characterization at eclipse times not meeting Equation 4.14. Pixels satisfying Equation 4.17 fall within the umbra region of the shadow and result fully darkened, being characterized by $c_i = 0.0$.
5. Identify annular eclipse times via Equation 4.15.
6. Look for pixels experiencing annular eclipses at annular eclipse times with Equation 4.26.
7. Compute the eclipse factor c_i of pixels within the antumbra region using Equation 4.29.
8. Look for pixels falling in the penumbra region. Pixels not satisfying the conditions for total or annular eclipses at eclipse time epochs are checked for partial eclipse with Equation 4.30.
9. Compute the eclipse factor c_i of pixels within the penumbra region using Equation 4.33.

The list presented above covers all possible phenomena at all time epochs for a specific selection of bodies A and B . It is emphasized that, in order to cover all possible eclipses between bodies, every specific planet or moon has to be checked for shadowing by the other bodies. Hence, the proposed algorithm needs to be executed $n!/(n - 2)!$ times, with n the total number of bodies orbiting the star. Because in our case, two bodies orbit the star, $n = 2$, and the algorithm needs to be executed 2 times. We have implemented a vectorized version of the algorithm here presented, which allows to check the different eclipse conditions and compute the eclipse magnitude of all pixels and all time epochs at the same time, drastically reducing the computational time at the cost of a higher use of memory.

Once described the mathematical model for the computation of mutual eclipses between bodies, we direct our attention to the modelling of transit events, blocking the reflected starlight by the planet and moon bodies.

4.5. Mathematical description of transit events calculation

We understand by transit the blockage of reflected light by the interposition of a second body in between the observer and the observed body (see Section 4.4.1). The procedure and formulae implemented for the computation of transit events is described below. The notation employed for a generic transiting body A and hidden body B configuration is as follows:

A	centre of transiting body (body A)
B	centre of shadowed body (body B)
R_A	radius of transiting body A
R_B	radius of shadowed body B
i	centre of pixel i on the eclipsed body surface
\vec{r}_{SA}	vector position of body A with respect to the star S
\vec{r}_{SB}	vector position of body B with respect to the star S
\vec{r}_{AB}	vector position of body B with respect to body A
\vec{r}_{Ai}	vector position of pixel i with respect to body A

In order to be consistent with Section 4.4, and in agreement with the assumptions presented in Section 4.3, it has been decided to not consider the transmission and refraction of light through the atmosphere of the transiting body, considerably reducing the complexity of the problem.

Since pixels blocked by a transiting body are not recorded by the observer, these may just be handled as dead pixels. The problem is then reduced to determine which pixels are hidden by a transiting body A passing in between the shadowed body B and the observer. As observed in Figure 4.7, we make use of the observer's coordinate system S_0 , which clearly describes the position of the bodies with respect to the observer position. In order to minimize the number of operations, the time epochs for which transit events occur are determined. Transit epochs satisfy:

$$\left\| \vec{d}_{AB}|^{S_0} \right\| < R_B + R_A \quad \text{and} \quad \vec{r}_{SA}|^{S_0} \cdot \begin{bmatrix} 0 \\ 0 \\ 1 \end{bmatrix}^T > \vec{r}_{SB}|^{S_0} \cdot \begin{bmatrix} 0 \\ 0 \\ 1 \end{bmatrix}^T, \quad (4.39)$$

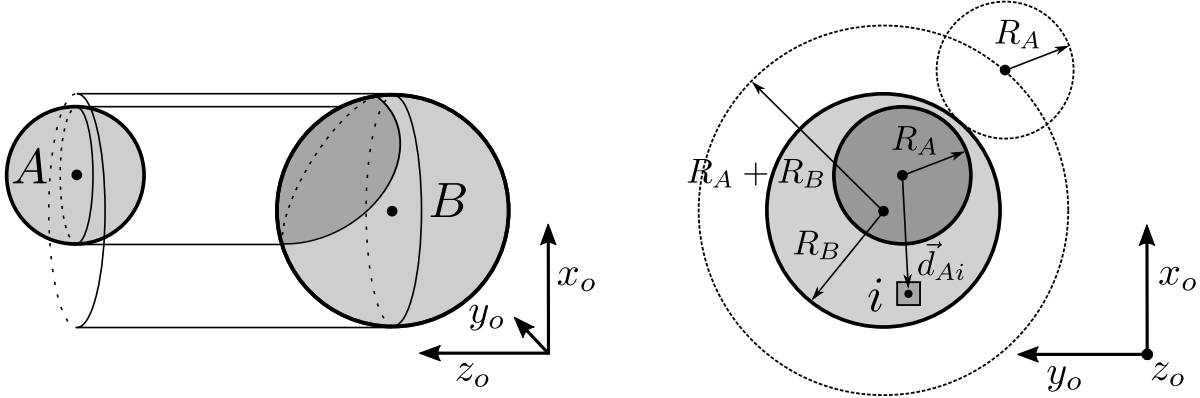


Figure 4.7: Geometrical description of a generic transit scenario in which a transiting body A passes in between the star and the shadowed body B . Left, a three-dimensional view of the event is shown; right, we show a sketch of the transit geometry as seen from the observer's position. R_A and R_B stand for the radii of bodies A and B . \vec{d}_{Ai} stand for the position vector of pixel i with respect to the transiting body A , projected onto the plane of sky x_0-y_0 . Transits are only possible if the distance between the bodies A and B projected onto the plane of sky is smaller than $R_A + R_B$.

where the second condition ensures that body A is closer to the observer than body B , and $|\vec{d}_{AB}|^{S_0}$ accounts for the projection of $|\vec{r}_{AB}|^{S_0}$ onto the x_0-y_0 plane.

For all time epochs satisfying Equation 4.40, a pixel-by-pixel verification is performed along the disk of body B . As also follows from Figure 4.7, the condition to be satisfied by a pixel i is:

$$\left\| \vec{d}_{Ai} |^{S_0} \right\| < R_A, \quad (4.40)$$

where \vec{d}_{Ai} is the projection of \vec{r}_{Ai} onto the x_0-y_0 plane.

All pixels satisfying Equation 4.40 are hidden from the view of the observer and, thus, do not contribute to Equation 2.5. This is accounted through the same factor as used for eclipsed nodes: hidden pixels are black, i.e. $b_i = 0.0$.

As done in the case of the eclipses module, a matrix-based algorithm has been implemented in *ExoPy*, based on the expressions here posed. In order to cover all possible transits between bodies in the planetary system, every body is to be checked for transits by the other bodies. The proposed algorithm needs to be executed $n!/(n-2)!$ times, with n the total number of bodies on the planetary system (including the star). In this study, the stellar flux contribution is not considered, and planetary-and lunar–stellar transits are not modelled reducing the number of executions from 6 to 4.

In this section, we have presented the mathematical description and the rationale behind our transits and eclipses models. Once described the time dependant position of the planet and moon bodies, the angular description of all pixels along the discretized disks, and determined the actual illumination of shadowed and hidden pixels due to mutual events, we present the total flux and state of polarization of starlight reflected by the unresolved Earth–Moon–like planetary system in Chapter 5.

5

Results: reflected starlight by edge-on unresolved Earth–Moon planetary system

As a first step towards the complete understanding of the influence of mutual events on the expected observed signal, this chapter analyses the flux and state of polarisation of an Earth–Moon–like unresolved system orbiting in a so-called edge–on configuration.

First, we describe the set-up for the simulations in Section 5.1. Then, the individual contributions of the planet and moon bodies are discussed in Section 5.2, laying the bases for the understanding of the signal of the unresolved bodies. We present the computed reflected starlight of the unresolved system in Section 5.3, analysing the influence of the lunar presence on the overall signal. Then, we characterize the various events found in the phase curves, both in terms of total flux and degree of polarization for all types of found mutual events, in Section 5.4. Finally, we study the possibility of indirect lunar detection through mutual events in Section 5.5.

5.1. Earth–Moon system set-up

In this section, we introduce the set-up configuration for the simulations. First, the orbital characteristics of the planet–moon–star system are itemized in Section 5.1.1. Then, we present the main parameters employed for modelling the reflection by the planetary and lunar bodies in Section 5.1.2.

5.1.1. Orbital geometry

Exoplanets observed in an edge–on perspective are targets for exoplanet search observatories such as PLATO and CHEOPS. Such configuration guarantees the encounter of mutual transit and eclipse events, as we show in Section 5.3. The edge–on alignment for the star, planet, and moon lays down a series of restraints when selecting the orbital motion parameters (see Section 3.2.2). Using the default observing direction ($\theta_{ob} = \varphi_{ob} = 0.0$), i.e. the observer’s coordinate system S_0 coincides with the orbital motion coordinate system S_1 , the observer’s line of sight is perpendicular to reference plane p_1 (see Figure 3.1). Thus, the inclination angle of the barycentre’s orbit around the star is 90° . Defined with respect to the barycentre’s orbital plane, the inclination of the lunar orbit around it is set to 0° .

In an attempt to carry out a progressive analysis of the results obtained for systems of increasing complexity, the selected baseline geometry consists of circular orbits (i.e. $e = 0$). The orbits’ radii have been selected to match those for the Earth–Moon system [David R. Williams, 2017]. In the case of the barycentre’s orbit around the star, we assume that the Earth–barycentre distance is negligible, so that $a_{bs} = 1$ AU. The Moon–barycentre semi-major axis, a_{mb} , is computed from the Moon–Earth semi-major axis, a_{mp} , making use of the definition of barycentre, as:

$$a_{mb} = a_{mp} \frac{m_p}{m_p + m_m} = 2.5696 \times 10^{-3} \text{ AU} \frac{5.97 \times 10^{24} \text{ kg}}{5.97 \times 10^{24} \text{ kg} + 7.3 \times 10^{22} \text{ kg}} \approx 2.539 \times 10^{-3} \text{ AU}, \quad (5.1)$$

where m_p and m_m are the masses of the planet and the moon, respectively.

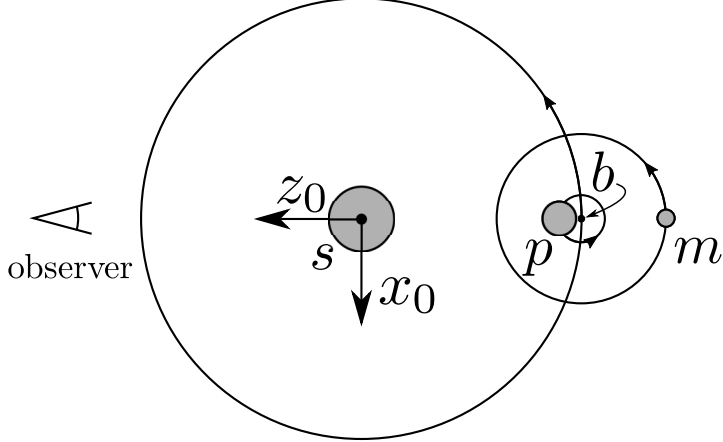


Figure 5.1: Sketch illustrating the orbital geometry of the edge-on planetary system at time $t = 0$ as seen from the positive y axis (left) and the positive z axis (right). The latter coincides with the observer's line of sight. The orbital motion of the planet, moon, and barycentre has been indicated with arrows along the orbits. Distances between bodies and radii are not to scale in order to emphasize the geometry of the system.

As discussed in Section 3.2.2, the barycentre's right ascension of the ascending node, Ω_b , can be set to zero as it merely supposes a rotation around the observer's line of sight¹. In the case of the lunar orbit, we find that the ascending node is undefined [Wertz and for Space Technology , U.S.] so that Ω_m does not alter the orbital geometry. Thus, it is given an arbitrary value of zero, which facilitates the visualization of the ap periastron and true anomaly angles. Theoretically, the perigee of a circular orbit is undefined and, by extension, the argument of periapsis ω [Wertz and for Space Technology , U.S.]. In our case, ω is perfectly defined from a numerical point of view and, together with the time of periapsis (t_0), serves to set the exact position of the bodies at time zero. The barycentre's argument of periapsis is chosen to place the body right behind the star at the initial time $t = t_0 = 0$, i.e. $\omega_b = 270^\circ$. Consequently, this position defines the periapsis of the orbit for values of $e \neq 0$. In the case of the moon, ω_m is set to zero, so that the line of apsides coincides with that of the barycentre at $t = 0$. The resulting orbital geometry is sketched in Figure 5.1. The orbital elements are given in Table 5.1.

Table 5.1: Planet-moon system barycentre ('barycentre') and moon's orbital elements for the edge-on extrasolar system. a is the orbital semi-major axis, e is the eccentricity, i is the inclination, ω is the argument of perihelion, Ω is the right ascension of the ascending node, and t_0 is the time of periapsis passage.

	a [AU]	e [-]	i [deg]	ω [deg]	Ω [deg]	t_0 [s]
Barycentre	1.0	0.0	90.0	270.0	0.0	0.0
Moon	0.00253	0.0	0.0	0.0	0.0	0.0

Given the symmetry of the geometry, the orbits of the bodies have only been calculated for $\nu_b \in [0, 180]$. Henceforth, the starlight reflection results correspond to a timespan of half the period of the barycentre's orbit.

5.1.2. Modelling the reflection properties of the bodies

As detailed in Section 2.4, the reflected starlight has been computed for a wavelength of 450 nm, corresponding to the Earth-characteristic blue color for a clear atmosphere. As for the atmospheric

¹Only applies for an observer located at 90 ° elevation angle in the extrasolar system reference frame.

and surface properties of the bodies, the reader is directed to Section 2.4. We analyse the impact of using cloudy and clear planetary atmosphere models in Appendix B.1. As a result of this analysis, we decided to employ a clear sky model for the Earth-like planet, which does not change significantly the shape of the phase curves obtained at wavelength 450 nm, as compared to those of a cloudy planet [Rossi and Stam, 2017, Stam, 2008], albeit a higher degree of polarization is reached. Furthermore, when including cloud aerosol particles in the atmospheric model, the required computational time per simulation shoots up to values which would severely limit the variety and number of case studies carried out for the present work.

As a trade-off between spatial resolution, radiometric and polarimetric accuracy, and computational time, we decided to employ $N_{eq}^p = 50$ and $N_{eq}^m = 14$ pixels along the equator of the planet and moon bodies (see Appendix B.2). This makes a total of 1956 and 156 pixels along the disks of the bodies. Moreover, 40 Gauss points ($n_{mug} = 40$) are employed to guarantee a correct modelling of the planetary atmosphere. In the case of the moon, the absence of gas layers over the surfaces allows us to drastically reduce the computational time for the planet–moon system.

The parameters employed for modelling the reflection by the planet and moon, as well as the required physical properties [David R. Williams, 2017], are provided in Table 5.2, which complements the information given in Table 2.1.

Table 5.2: Relation of parameters defining the planet and moon reflection properties. N_{eq} stands for the number of pixels along the disk equator, and n_{mug} is the number of Gauss points on the Fourier-series expansion of the first column of the reflection matrix, \mathbf{R}_1 . The physical properties of the bodies have been retrieved from NASA's planetary factsheets [David R. Williams, 2017].

	Planet	Moon
Atmospheric model	Clear atmosphere	No atmosphere
Surface model	Lambertian	Lambertian
N_{eq}	50	14
n_{mug}	40	-
Mass [10^{24}kg]	5.9723	0.07346
Radius [km]	6371	1737.4
Surface gravity [m/s^2]	9.81	-

5.2. Starlight reflected by the individual planet & moon bodies

In this section, we lay down the ground for the analysis of the unresolved planet–moon reflected signal by discussing the reflected starlight of each body disk. The here exposed and discussed results correspond to the planet and moon pixel Stokes vectors \mathbf{F}_i^p and \mathbf{F}_i^m before final integration at phase angle values $\alpha = 0^\circ$ and $\alpha = 50^\circ$, see Figure 5.2. A complete overview of the Stokes parameters and direction of polarization from $\alpha = 0^\circ$ to 180° is available via this link².

Phase angle $\alpha = 0^\circ$

At $\alpha = 0^\circ$, both planet and moon exhibit similar distributions of reflected light flux, characterized by a maximum flux value at the substellar point and darkening towards the limb. This yields spherically symmetric flux pixel distributions. Given the lack of atmosphere and the Lambertian reflectance of the moon, the reflected starlight is unpolarized. Henceforth, the direction of polarization is not defined across the lunar disk.

Rayleigh scattering in the planetary atmosphere leaves the reflected light polarized. As Figure 5.2a reveals, light is vertically (horizontally)³ polarized along the x (y) axis of the grid, while diagonal ($\pm 45^\circ$) linear polarization is found along the angle bisector. The spherical symmetry pattern shown by the

²Animation illustrating the evolution of Stokes parameters F , Q , U , and direction of polarization for the Earth-like planet and Moon-like moon accessible via <http://tinyurl.com/FQUP-gif>.

³The direction of polarization is described with respect to the horizontal and vertical axes in Figure 5.2.

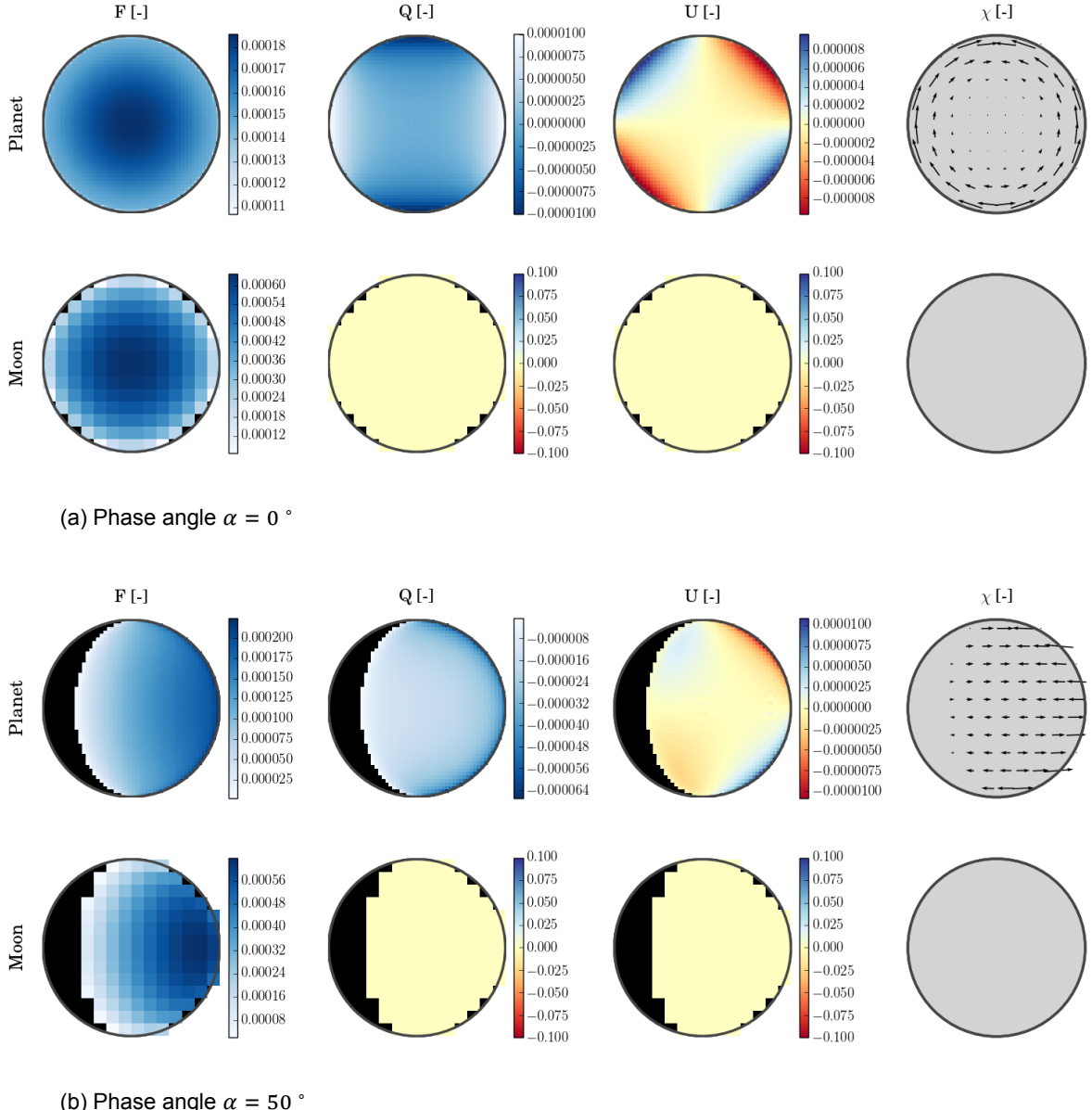


Figure 5.2: Pixel distribution of the three first Stokes parameters (F , Q , U) and the direction of polarization (χ) for the planet and moon (F^p and F^m) at phase angles $\alpha = 0^\circ$, 50° . The linearly polarized fluxes Q and U are zero at every pixel on the moon's disk. The fluxes shown are before integration, i.e. they account for the pixel flux contribution. Fluxes have been normalized so that the integrated flux at $\alpha = 0^\circ$ equals the geometric albedo of each body. Planetary and lunar pixel fluxes are not comparable as the number of pixels employed in each case is not equal. The number of pixels for the planetary and lunar disks are $N_p^{eq} = 50$ and $N_m^{eq} = 14$.

linearly polarized fluxes Q and U compensates pixels with positive and negative fluxes⁴ when all pixel contributions are integrated along the disk, yielding a null total polarization degree at $\alpha = 0^\circ$. This symmetry is broken for $\alpha > 0^\circ$, when part of the observed disk falls in the night side of the planet.

Phase angle $\alpha = 50^\circ$

Driven by the pure isotropic surface reflection of the moon and the absence of scattering, the reflected flux does not directly depend on the observer position for $\alpha > 0^\circ$, but only on the angle of incidence of the starlight. Thus, Figure 5.2b shows a peak on lunar reflected light flux at the substellar point and a

⁴Positive and negative linearly polarized fluxes Q and U determine the direction of polarization as defined in Section 2.1. Q and U contribute positively to the total reflected flux, regardless the sign.

decrease towards the terminator.

In the case of the planet, a different distribution is seen. On the one hand, solar-z zenith angles close to zero (substellar region) show similar pixel reflected light flux as seen for $\alpha = 0^\circ$. On the other hand, at higher solar zenith angles, light has a longer path through the atmosphere increasing the reflected flux through scattering. Contrary to the lunar case, the observed scattered flux strongly depends on the zenith-observer angle, as the peak flux values are found along the planetary limb, i.e. where the observer's line of sight path through the planetary atmosphere is maximum. Therefore, the atmospheric scattering breaks the concentric flux distribution pattern with respect to the substellar point.

As a result of the increasing night side, the horizontal symmetry of F , Q and U distributions is increasingly distorted with increasing α . Still, Figure 5.2b reveals relevant symmetry patterns. Q values are symmetrically distributed with respect to the scattering plane (vertical symmetry), while U shows a vertically antisymmetric pattern of values that results in a null disk integrated U contribution for any α . Moreover, 5.2b reveals negative Q values along the planetary disk which, together with U values one order of magnitude lower than Q , entail a distribution of horizontally polarized light (see Figure 2.1).

This characterization of the reflectance behaviour of the bodies will help us understand the results of the signals of the unresolved planet and moon presented hereunder.

5.3. Baseline reflected starlight by the planet–moon system

This section presents the results obtained for the unresolved planet–moon system, given by circular coplanar orbits of radii matching those for the Earth–Moon system, as specified in Section 5.2.

At this point, the implemented orbital and geometrical model, together with the mutual events model, allows us to search, and characterize lunar traces on unresolved signals. Figure 5.3 shows the starlight's total reflected flux (F), the linearly polarized fluxes (Q and U), and the degree of linear polarization (P) as a function of phase angle for a) the unresolved planet & moon system, b) the isolated planet and c) the isolated moon. In the latter two cases, no interaction between bodies has been simulated, what allows to compare the expected observed unresolved signals to those of the individual bodies. These first results allow us to search for lunar traces on the combined signal.

A glance at the reflected flux curves in Figure 5.3 is enough to observe that the unresolved planet–moon system's flux, from here on simply called 'flux', is lower than the algebraic summation of the isolated planet and moon's signal. Reason for that is that the difference in radii between the planet and moon bodies requires scaling the individual contributions (cf. Equation 2.5). The computed lunar geometric albedo is ~ 0.24 , matching the theoretical geometric albedo of a Lambertian reflecting body of surface albedo 0.36.⁵, while the planetary geometric albedo is 1.6 times its theoretical Lambertian one, as a result of scattering at the atmosphere. The difference in bodies' radii and distance to star requires to scale the lunar Stokes vector (see Equation 2.5) resulting in a final signal of equivalent geometric albedo⁶ of around 0.34 (solid line in Figure 5.3).

As expected, the flux curves reach their maximum value at $\alpha = 0^\circ$ and continuously decrease with increasing phase angle, reaching zero reflected flux at $\alpha \approx 180^\circ$ ⁷, i.e. when the bodies are in between the star and the observer and only the night side of the bodies are observed.

When focussing on the signal for the moon, Figure 5.3 shows a constant zero value of the linearly polarized fluxes Q and U which easily follows from the results provided in Section 5.2. Figure 5.3 also shows a constant zero value of the flux U for the planetary body. This can also be explained via the results shown in Figure 5.2. In essence, the assumed spherical symmetry of the planetary body yields an antisymmetric distribution of the pixel contribution to the linearly polarized U flux with respect to the scattering plane. This entails a null total integrated contribution of U at any time and position along the planetary orbit and, therefore, any phase angle.

Despite the non–polarizing behaviour of the moon, Figure 5.3 shows a variation of the unresolved planet–moon system degree of polarization, from here on simply referred to as 'degree of polarization',

⁵The theoretical geometric albedo of a Lambertian reflecting body is $\frac{2}{3}$ of its surface albedo.

⁶We understand under equivalent geometric albedo the ratio of the unresolved system (comprised by the planet and moon bodies) brightness as seen at phase angle zero to that of an idealized flat Lambertian disk with same cross-section as the planet.

⁷Theoretically, the light curve reaches its maximum and minimum values at $\alpha = 0^\circ$ and $\alpha = 180^\circ$. In practice, a body cannot be observed at $\alpha = 0^\circ$ as it lies behind its parent star. On top of that, phase angles close to $\alpha = 0^\circ$ and $\alpha = 180^\circ$ do not allow direct imaging of the planet–moon system, due to the higher amount of the stellar flux contribution and the presence of speckles on the observations.

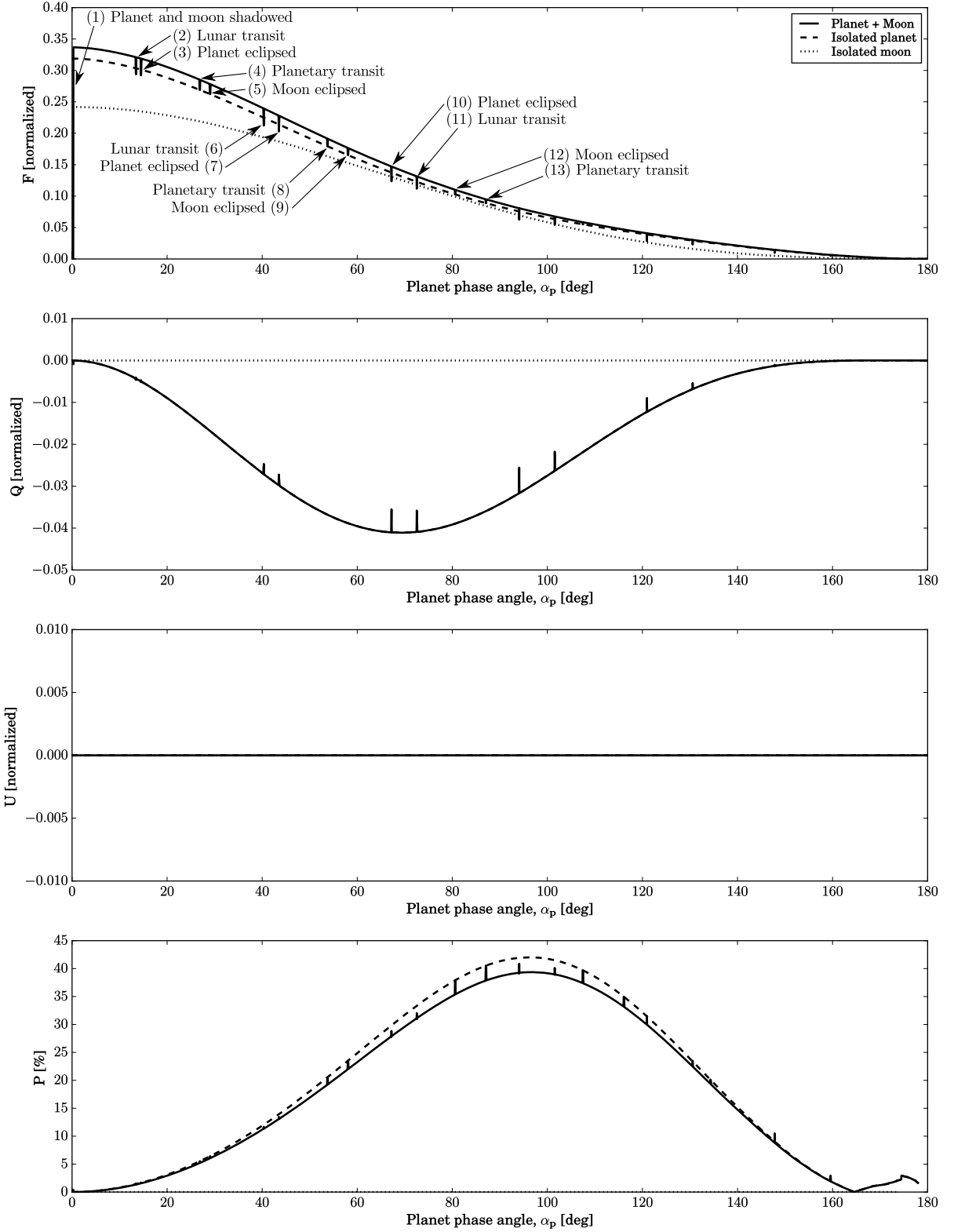


Figure 5.3: Total flux (F), linearly polarized fluxes (Q and U) and degree of linear polarization (P) results as a function of phase angle for an edge on system. The results are shown for an isolated planet (dashed line) and moon (dotted line) which do no interact between each other, and the unresolved planet–moon system (solid line). The results shown for the isolated bodies assume they have the same size, allowing to objectively weight their reflection properties. Fluxes have been normalized so that F at $\alpha = 0^\circ$ equals the geometric albedo of each body (geometric albedo of the planet–moon system in the case of the combined signal). We enumerate and label some of the mutual events experienced for a fraction of the phase curve. The next events follow the same succession as shown. The linearly polarized flux Q and degree of polarization P are zero for both the isolated moon, while the curves for the isolated planet and the combined planet–moon system overlap. The linearly polarized flux U is zero for all cases and phase angles. A jump in P is observed for $165^\circ < \alpha < 180^\circ$ as Q becomes positive ($Q \sim 10^{-5}$) and F approaches zero. The simulation settings are $N_p^{\text{eq}} = 60$, $N_m^{\text{eq}} = 16$, $\Delta t = 30\text{min}$, $t_f = \frac{T_{\text{bs}}}{2}$.

when compared to the degree of polarization of the isolated planet. Indeed, the presence of the moon increases the total reflected flux of the system, while it does not contribute to the polarized fluxes Q and U . As a result, the degree of polarization of the system suffers a slight oscillation due to the presence of an exomoon which stands as the cornerstone for the search of exomoon traces in polarization curves.

While the overall curve trend of the unresolved results shown in Figure 5.3 (solid line) are not a direct evidence of the presence of an orbiting moon, the orbital alignment drives to a situation in which the planet and moon transit and eclipse each other at every lunar period (see Figure 5.4), resulting in a series of peaks and shadows on the observed total flux and polarization degree which appear as spikes in Figure 5.3. Both the planet and the moon are initially ($\alpha = 0$) hidden behind the star (1), i.e. the planet is occulted by the star and the moon is occulted by both the star and the planet. Given the prograde rotation of the moon, this event is followed by a lunar transit (2) and a planetary solar eclipse (3). Once the first lunar period is completed, the moon is again shadowed by the planet in a so-called planetary transit (4), followed by a lunar solar eclipse (5). This sequence is repeated and continued along the barycentre's orbit at each lunar revolution.

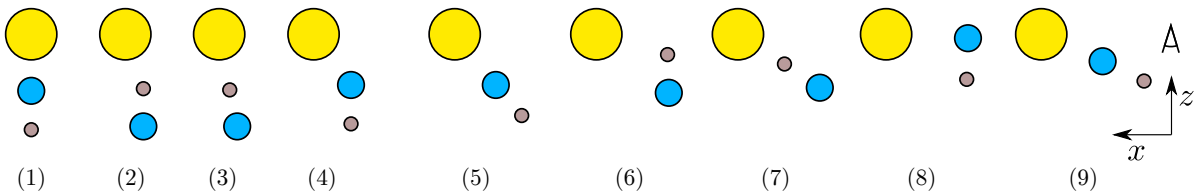


Figure 5.4: Sketch illustrating the sequence of planetary (1, 4, 8 ...) and lunar (2, 6 ...) transits, as well as planetary (3, 7 ...) and lunar (1, 5, 9 ...) eclipses for a fraction of the planet–moon system barycentre's orbit on an edge-on system. The observer is located along the positive z_0 -axis. Position 1 corresponds to phase angle and time zero in our simulation.

Therefore, we identify how the presence of an orbiting moon stands out on the baseline flux and polarization phase curves through the modelled mutual events. A closer look and an in-depth characterization of these events is provided in Section 5.4.

5.4. Characterization of planet–moon events

As illustrated by Figure 5.3, the observation and characterization of flux and polarization spikes resulting from planet–moon mutual events constitutes the basic elements for the detection and potential characterization of the bodies. In this section, we first describe the general characteristics of these planet–moon events as observed in Figure 5.3 (Section 5.4.1). Then, we study the shape of different transit and eclipse events in detail in Sections 5.4.2 and 5.4.3, respectively.

5.4.1. General characteristics

Figure 5.3 ranges from phase angle 0° to 180° , corresponding to half the orbit of the planet around the star, i.e. ~ 183 solar days. Far from being punctual signatures, the observed mutual event spikes take a fraction of a day, as we'll study in Sections 5.4.2 and 5.4.3. However, some conclusions can directly be raised from the plots presented in the previous section.

Flux valleys

It is highlighted that the mutual events between the planet and the moon are always translated into valleys in the observed total flux of the reflected light. Acting as reflecting bodies, the moon and planet contribute positively to the total observed flux, which decreases as the total illuminated area of the bodies is reduced. Both in the case of the transit and eclipse events, part of the light arriving or departing from the bodies is blocked, reducing the effective illumination of these. Consequently, mutual events always entail a decrease on the observed unresolved planet–moon system total flux.

Degree of polarization peaks

At first sight, the mutual events appear in Figure 5.3 as peaks on the combined degree of polarization curve, opposite to the behaviour shown by the flux phase curve. As further discussed in Sections 5.4.2 and 5.4.3, a zoomed-in study of the events allow to identify oscillations (with multiple peaks and drops) in the degree of polarization when any of the bodies is shadowed. These oscillations depend, at least,

on the shadowed disk region, its polarization properties, the planet–moon radii and orbital configuration. Indeed, when one of the bodies is darkened, the variation of degree of polarization is given by the rate of change of flux F compared to the variation of linearly polarized fluxes Q and U .

Variation of spikes' amplitude

If we put our attention on the amplitude of the spikes observed in Figure 5.3, we notice a variation of amplitude with phase angle. Valleys found in F present their maximum at $\alpha \approx 0^\circ$, when the observer's line of sight is parallel to the starlight incidence angle, as also follows from the simulations from Cabrera and Schneider [2007]. At this moment, the illumination of the bodies is maximum and in the case of mutual events, the eclipse shadowed area or the transited area partially or totally covers the substellar region of the shadowed body. Unfortunately, this would mean that the maximum variations in flux due to moon–planet interaction events cannot be observed, as $\alpha \approx 0^\circ$ falls out of the observable region.

In the case of the linearly polarized flux Q , the maximum amplitude is found at $\alpha \approx 70^\circ$, when the absolute value of the Q phase curve reaches its zenith. The lunar orbit being coplanar with the planetary orbit (see Section 5.1.1), the occurrence of mutual events does not break the symmetry of the U pixel distribution shown in Figure 5.2 and, therefore, we experience no contribution from the linearly polarized flux U . Consequently, the amplitude of the events found on the degree of polarization phase curve are driven by F and Q , resulting in a maximum peak amplitude at phase angles where $\alpha \approx 90^\circ$. This is particularly convenient for exomoon detection purposes with direct imaging techniques, as it implies that the lunar traces in polarization are more relevant at those phase angles at which the planet system is better resolved from its parent star.

In addition, we highlight the different impact of lunar darkening events (planetary transits and lunar eclipses) and planetary darkening events (lunar transits and planetary eclipses) on the amplitude of the observed spikes in both flux and polarization phase curves. On the one hand, the partial or total shadowing of the lunar disk results in a drop in F while not influencing the linearly polarized fluxes because the moon is unpolarized. Hence, Equation 2.2 yields a rise in P during planetary transits and lunar eclipses. In the case of shadowing the planetary disk, the decrease in $|Q|$ alleviates the variation of the degree of linear polarization. As a result, moon shadowing events stand out when looking at the degree of linear polarization while planet shadowing events excel in the total reflected flux.

Maximum amplitude of mutual events

The baseline results shown in Figure 5.3 are now compared to those obtained for a non-interacting planet–moon system. This scenario is named 'continuum' simulation, given the absence of the characteristic peak and valley features. Hence, we define ΔF and ΔP as the difference between a standard simulation and a continuum simulation, what puts the focus on the impact of mutual events between bodies, allowing a better characterization and analysis:

$$\Delta F(\alpha) = F(\alpha) - F_{\text{continuum}}(\alpha), \quad (5.2)$$

$$\Delta P(\alpha) = P(\alpha) - P_{\text{continuum}}(\alpha). \quad (5.3)$$

The percentage variation of flux can be described in two ways: a) related to the continuum simulation results, $\Delta F_{\text{continuum}}$, (see Equation 5.4) and b) related to the system's albedo, ΔF_{alb} , (see Equation 5.5).

$$\Delta F_{\text{continuum}}(\alpha) = \left| \frac{\Delta F(\alpha)}{F_{\text{continuum}}(\alpha)} \right|, \quad (5.4)$$

$$\Delta F_{\text{alb}}(\alpha) = \left| \frac{\Delta F(\alpha)}{F_{\text{alb}}} \right|, \quad (5.5)$$

with F_{alb} equal to $F_{\text{continuum}}(\alpha = 0)$, i.e. the ratio between the unresolved planet–moon reflected flux and the stellar incoming flux at zero phase angle.

The expressions in Equation 5.4 have been plotted in Figures 5.5 and 5.6 for the present baseline simulation. Figure 5.5 displays maximum reflected flux drops of 33% of the expected reflected light at large phase angles ($\alpha \approx 145^\circ$), and 8% of the total system's albedo at small phase angles ($\alpha \approx 10^\circ - 40^\circ$), corresponding in both cases to lunar transits or planetary eclipse events in which the planetary disks is temporarily darkened. Regarding the degree of linear polarization, a maximum jump of 2.66%

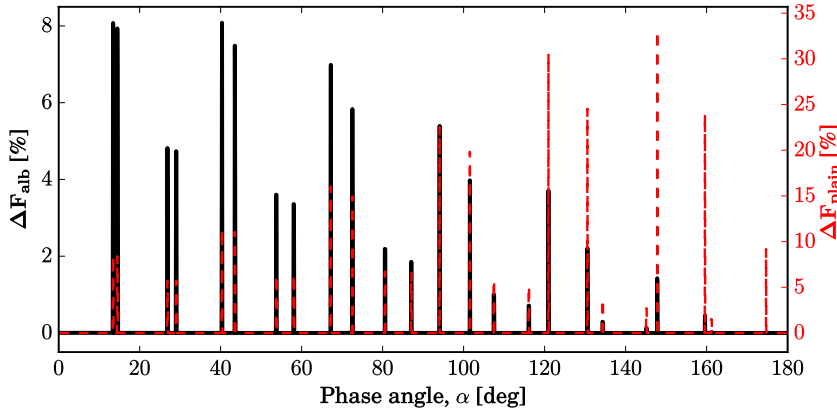


Figure 5.5: Flux relative difference between the baseline simulation results containing mutual events and the continuum expected signals in which bodies do not interact with each other with phase angle. Black curve stands for the percentage difference with respect to the total albedo of the planet–moon system, ΔF_{alb} , while red dashed line stands for the percentage difference relative to the continuum simulation results, ΔF_{plain} , at each phase angle. The results suggest maximum flux variations in the order of 8% of the system albedo and 33% of the continuum signal. The simulation settings are $N_p^{\text{eq}} = 60$, $N_m^{\text{eq}} = 16$, $\Delta t = 30\text{min}$, $t_f = \frac{T_{\text{bs}}}{2}$.

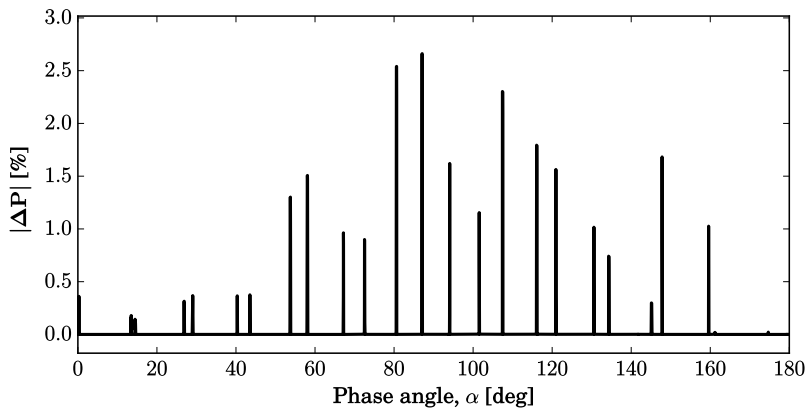


Figure 5.6: Absolute value of the degree of polarization difference, $|\Delta P|$, between the baseline simulation results containing mutual events and the continuum signal, in which bodies do not interact with each other, with phase angle. The results show a maximum $|\Delta P|$ peak of $\sim 2.7\%$ at $\alpha \approx 90^\circ$. The simulation settings are $N_p^{\text{eq}} = 60$, $N_m^{\text{eq}} = 16$, $\Delta t = 30\text{min}$, $t_f = \frac{T_{\text{bs}}}{2}$.

is experienced at middle phase angles where $\alpha \approx 90^\circ$, corresponding to planetary transit and moon eclipse events in which the lunar disk gets completely darkened.

Period of repetition of events

As observed in the flux and degree of polarization shown in Figures 5.3, 5.5 and 5.6, there exists a repetition pattern for the mutual events captured in the flux and polarization phase curves. A closer look at these figures reveals that there exists a de-synchronization between the encountered transit and eclipse events in phase angle, i.e. the gap between lunar transit and planetary eclipse (or planetary transit and lunar eclipse) increases with increasing phase angle. As the orbital speed of the bodies is constant, this also applies in time domain⁸. On the one hand, planetary and lunar transits have a characteristic period matching the orbital period of the moon (and planet) around the barycentre, T_{mb} ⁹. This is due to the fact that an observer-planet-moon alignment is achieved twice per lunar orbit (at $\nu_m = 0, 180$ deg as defined in Section 5.1.1). On the other hand, the timespan between two consecutive eclipses is observed to increase with phase angle as a result of the impact of the motion of the barycentre along its orbit. Such eclipse alignment is only possible if $\nu_D = \nu_m - 180$ deg, what is translated into time domain accounting for the barycentre and lunar orbits' semi-major axis and eccentricity.

⁸The motion of the planet around the barycentre implies a non linear relation between planetary phase angle and time that is not appreciated in the presented phase curves.

⁹Planetary and lunar transits intersperse every half lunar orbit, $\frac{T_{mb}}{2}$.

Therefore, a measurement of the time between consecutive transit events yields immediate information about the planet-moon system period (and thus semi-major axis¹⁰). Further details on the repetition pattern of events are provided in Section 5.5.3, where we study its importance on exomoon detection.

Consequently, leaving aside the required instrument performance and sensibility, we showed that the observation of a planet–moon system might contain detectable traces of exomoons which are only one order of magnitude lower than the expected signal for the edge–on Earth–Moon–like system employed here. Extracting meaningful information from astronomical data is a goal that requires, on the one hand, full knowledge of how the orbital and physical characteristics of both the planet and moon (if only one) influence the expected observed signal and, on the other hand, the sufficient technical development that would give us the opportunity to resolve the presented features.

As a next step, we present more detailed analysis of the characteristic shape and duration of the transit and eclipse events in the edge-on system described in Section 5.1. Given the different peculiarities found for the transits and eclipses, these are studied separately, starting with a characterization of the transit events in Section 5.4.2.

5.4.2. Analysis of transit events

In this section, the focus is on the in-depth characterization of the observed transit events, e.g. their shape, symmetry, periodicity, magnitude, duration, and their relation with the atmospheric and surface models of the Earth– and Moon–like bodies under study.

A closer look at Figure 5.3 allows us to get an overview of how the expected reflected starlight and degree of polarization vary with phase angle during transit events. The differences in flux and degree of polarization (see Equations 5.2 and 5.5) have been plotted for different phase angles in Figures 5.8, 5.10, 5.11, and 5.13. Because the lunar direction of periapsis is opposite to the observer position, lunar transits correspond to lunar true anomaly values close to $\nu_{mb} = 180^\circ$, while planetary transits are found around $\nu_{mb} = 0^\circ$ (360° in Figures 5.11 and 5.13).

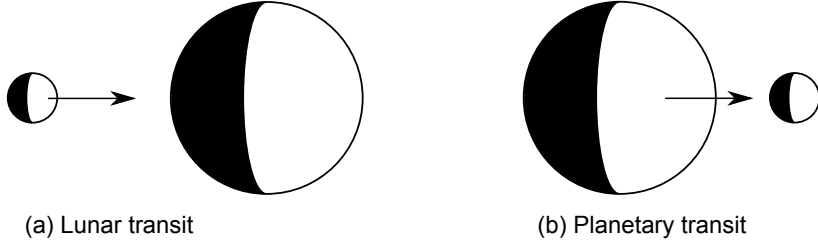


Figure 5.7: Sketch of the ingress direction of the moon during a lunar transit (a) and the planet during a planetary transit (b). The transiting body ingresses through the terminator and egresses through the bright limb of the darkened body. Black/white colors stand for the night/bright areas of the planet and moon disks.

With the aim of clarifying and enhancing the visualization of the results here shown, we remind the reader that the results cover the prograde orbital motion of the coplanar planet and moon bodies along half the orbit of the barycentre around the star. Bodies are initially aligned with the observer–star line, hidden by the stellar body, as sketched by position 1 in Figure 5.4. Therefore, transiting bodies approach the darkened body through the terminator and exit the bright limb for true anomaly values ranging from 0° to 180° , as observed in Figure 5.7.

Lunar transits

As follows from Figure 5.2a, the equatorial transit¹¹ of the moon in front of the planet disks at zero phase angle yields symmetric events on flux and polarization curves, given the symmetric and antisymmetric distribution of fluxes F , Q and U for both the planet and moon bodies (neglecting the small difference in phase angle originated during the transit event¹²).

¹⁰Specific energy of the orbit.

¹¹Here, we understand by equator the direction parallel to the x_0 -axis of the observers coordinate system passing through the centre of the observed body

¹²The symmetry might not exist for large lunar orbital periods, comparable to the lunar period of the barycentre around the star, i.e. planet–moon systems with $o(T_{mb}) = o(T_{bs})$.

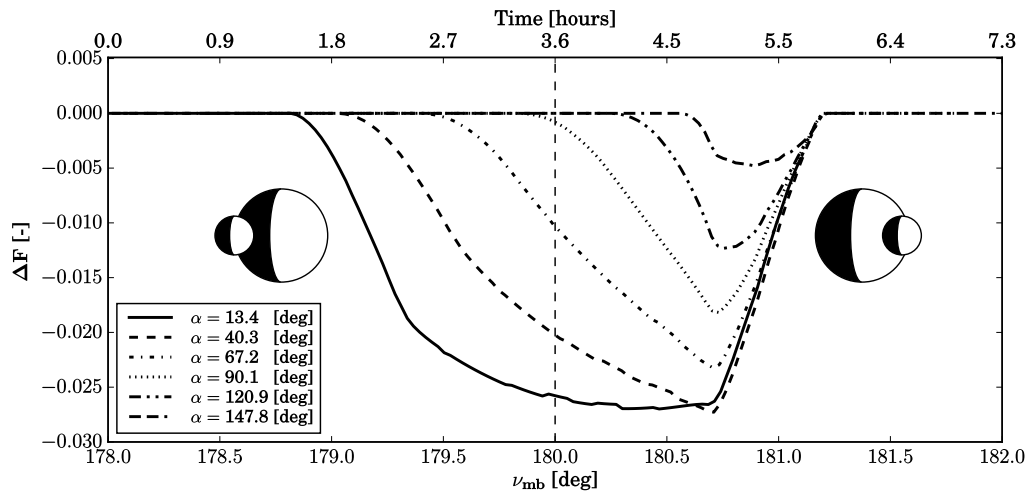


Figure 5.8: Difference between the planet–moon system reflected flux and the continuum background flux signal, ΔF , as a function of lunar true anomaly, ν_{mb} , and relative time during lunar transits at increasing phase angles. Fluxes have been normalized so that F at $\alpha = 0^\circ$ equals the geometric albedo of the planet–moon system. $\nu_{mb} = 180^\circ$ corresponds to the concentric alignment of the planet and moon bodies as seen from the observer. The simulation settings are $N_p^{\text{eq}} = 60$, $N_m^{\text{eq}} = 16$, $\Delta t = 3\text{min}$.

We first put our attention on the change of reflected flux during lunar transits (see Figure 5.8). As observed, the aforementioned symmetry is increasingly distorted with increasing phase angles. Increasing phase angle values involve a raise of the dark or night area of the observed planetary and lunar disks. As a result, the duration of the lunar transit event quickly falls with increasing phase angle as it follows from the sketch in Figure 5.9. Because egress takes place over the limb, all curves in Figure 5.8 merge together at the egress time. Together with the shortening of the total duration of the events, increasing phase angles bring a reduction on the flux peak magnitude during lunar transits. This is a result of the decreasing contribution of the equatorial region on the reflected flux with increasing phase angle.

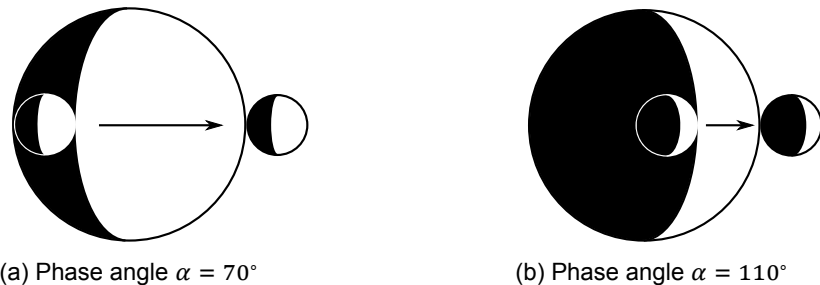


Figure 5.9: Sketch of the ingress and egress of the moon from the bright area of the planetary disk during a lunar transit for $\alpha = 70^\circ$ (a) and $\alpha = 110^\circ$ (b). The differences in ingress position with phase angle yield a variation in the total transit duration. Black/white colors stand for the night/bright areas of the planet and moon disks. The arrow indicates the direction of motion of the moon in front of the planet.

Figure 5.8 also shows a prominent change in slope at any phase angle. In fact, two different regions are identified on the flux curves during lunar transits. On the one hand, the planetary darkening towards the terminator (see Figure 5.2b) yields a smooth flux drop during the lunar ingress. On the other hand, the planetary reflected flux is maximum along the limb, what yields an abrupt increase of flux during the lunar egress. These two trends are distorted for large phase angles, in which the moon (being the lunar radius $R_m \approx 0.27R_p$) darkens the terminator and limb planetary regions at the same time along its transit.

Continuing with the analysis, Figure 5.10 shows the variation of degree of polarization of the unresolved planet–moon system during lunar transits at increasing phase angles. The curves shown for increasing phase angle do not only break the symmetry found at $\alpha \approx 0^\circ$ (also found in flux variations) but yield a strong variation in shape. As discussed in Section 5.4.1, the mutual events found on the

polarization phase curves in Figure 5.3 resemble mere spikes. The closer look provided in Figure 5.10 shows a different layout, which is explained by the physical properties of the planetary and lunar bodies as discussed below.

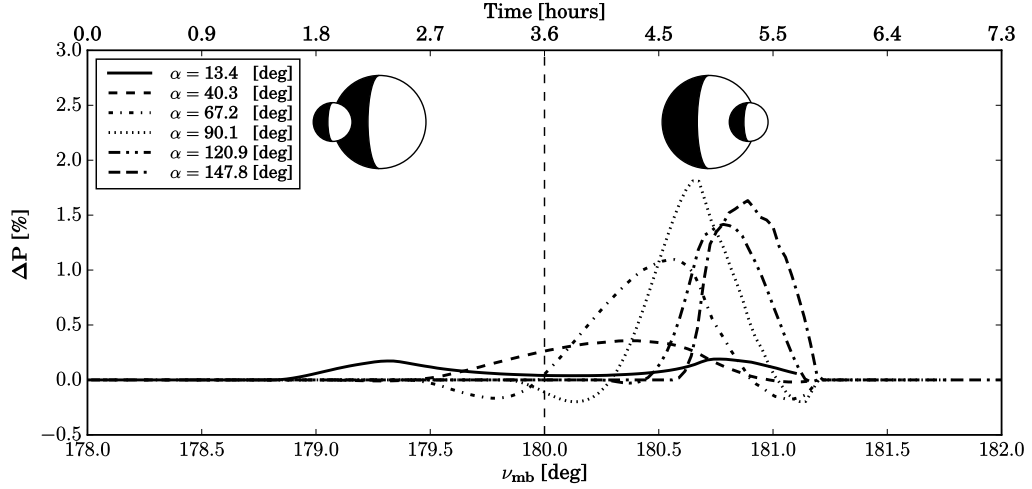


Figure 5.10: Difference between the planet–moon system degree of polarization and the continuum background signal, ΔP , as a function of lunar true anomaly, ν_{mb} , and relative time during lunar transits at increasing phase angles. $\nu_{mb} = 180^\circ$ corresponds to the concentric alignment of the planet and moon bodies as seen from the observer. The simulation settings are $N_p^{\text{eq}} = 60$, $N_m^{\text{eq}} = 16$, $\Delta t = 3\text{min}$.

As follows from Figure 5.2, the degree of polarization reached during the partial blockage of the planetary disk strongly depends on the linearly polarized pixel fluxes Q and U at the occulted region. In our case, the lunar transit occurs along the equator¹³ of the planet, where the vertical antisymmetry of the U pixel map yields a null net contribution during transit events. Therefore, the observed variation of the degree of polarization is explained by the variation in Q and the total flux F .

At zero phase angle, Q is maximum at the ingress and egress limb, while it reaches its minimum value along the equator at the centre of the body. Similarly, the total flux F is minimum at the ingress and egress and maximum at the centre of the body. This explains the peak on ΔP during the lunar ingress and egress for $\alpha = 13.4^\circ$, as well as the drop in polarization at $\nu_{mb} \approx 180^\circ$ in Figure 5.10. For $\alpha \neq 0$, the shape of the curves in Figure 5.10 strongly depends on the combination of pixel values for F and Q at each cases. Negative ΔP values, i.e. a reduction of the degree of polarization compared to the results obtained in the continuum simulation (without mutual events), are reached for phase angles $\alpha \approx 60^\circ - 120^\circ$ across the lunar ingress and egress on the bright side of the planet. At these phase angles, the ingress and egress planetary regions display a higher polarizing behaviour, i.e. higher ratio $\frac{Q}{F}$, which yields a drop in ΔP when such areas are darkened.

As a last remark, we observe that the maximum variation of degree polarization is reached at $\alpha \approx 90^\circ$. Furthermore, we highlight that Figure 5.10, shows similar ΔP amplitudes ranging from 1% – 1.8% at phase angles $\alpha \approx 70^\circ - 150^\circ$.

Planetary transits

Following the same reasoning as for the lunar transits, planetary transits yield symmetric events on flux and polarization curves at $\alpha = 0^\circ$, ignoring phase angle variations during mutual events. The planetary transit event corresponding to $\alpha = 0^\circ$ is not plotted in Figures 5.11 and 5.13, as both the moon and the planet are hidden behind the stellar disk (see Figure 5.4).

We first put our attention on the change of reflected flux during planetary transits presented in Figure 5.11. The obtained results strongly differ from those obtained for the lunar transit (see Figure 5.8). While lunar transits induce a prominently increasing asymmetry for increasing phase angles, planetary transits only introduce a slight variation of the ingress time. The smaller lunar disk dimension (being the lunar radius $R_m \approx 0.27R_p$) implies that the duration of the event is largely dominated by the planetary size as visualized in Figure 5.12. Thus, increasing phase angles induces a slight asymmetry

¹³See footnote 9.

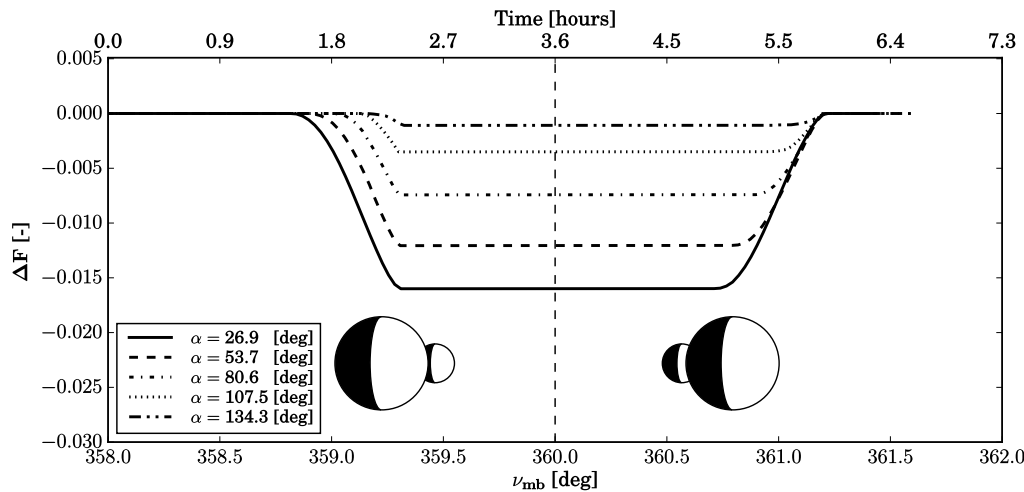


Figure 5.11: Difference between the planet–moon system reflected flux and the continuum background flux signal, ΔF , as a function of lunar true anomaly, ν_{mb} , and relative time during planetary transits at increasing phase angles. Fluxes have been normalized so that F at $\alpha = 0^\circ$ equals the geometric albedo of the planet–moon system. $\nu_{mb} = 360^\circ$ corresponds to the concentric alignment of the planet and moon bodies as seen from the observer. The simulation settings are $N_p^{\text{eq}} = 60$, $N_m^{\text{eq}} = 16$, $\Delta t = 3\text{min}$.

with respect to the moon–observer line (true anomaly $\nu_{mb} = 360^\circ$) while curves maintain a symmetric shape with respect to the middle point of the transit event.

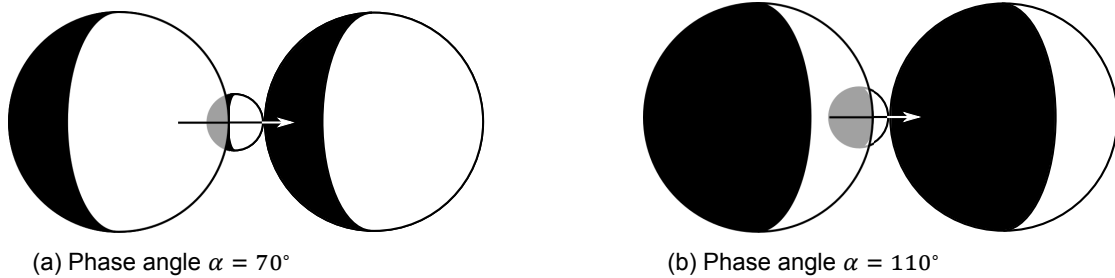


Figure 5.12: Sketch of the ingress and egress of the planet from the bright area of the lunar disk during a planetary transit for $\alpha = 70^\circ$ (a) and $\alpha = 110^\circ$ (b). The differences in ingress position with phase angle yield a variation in the total transit duration. Black/white colors stand for the night/bright areas of the planet and moon disks. The arrow indicates the direction of motion of the planet in front of the moon.

The asymmetry and the variation of planetary transit duration are still noticeable at a lower scale. The flux signatures induced by planetary transits are mostly dominated by the total time of lunar occultation behind the planet, apparent from the virtually constant shape of the transit flux. Moreover, increasing phase angles bring a reduction of the peak flux variation which is fully driven by the total integrated lunar reflected flux. The lunar illuminated side decreases with phase angle, reducing the flux drop during lunar occultation behind the planet.

Regarding the change in polarization during mutual events, Figure 5.13 shows the variation of degree of polarization of the unresolved planet–moon system during planetary transits at increasing phase angles. Figure 5.13 reveals the imprint of planetary transits on the polarization curve behaves similar to the flux curve discussed before. As follows from Figure 5.2 and already introduced in Section 5.4, the absence of atmosphere and the non-polarizing lunar surface yield a non-polarized lunar reflected flux. Therefore, the drop on total reflected flux due to the interposition of the planet between the moon and the observer yields a finite pulse jump of P preceded and superceded by monotonous transitions.

During planetary transits, a maximum variation of degree of polarization of $\Delta P \approx 2.5\%$ is observed at $\alpha \approx 80^\circ$. Contrary to what lunar transit curves show, the maximum variation of polarization curves during planetary transits quickly decreases for smaller and larger phase angles than 90° .

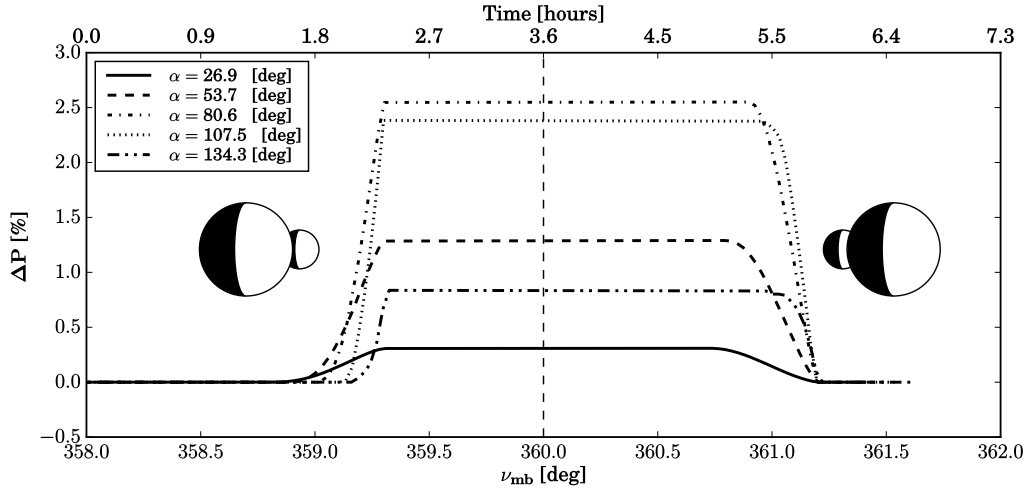


Figure 5.13: Difference between the planet–moon system degree of polarization and the continuum background signal, ΔP , as a function of lunar true anomaly, ν_{mb} , and relative time during planetary transits at increasing phase angles. $\nu_{mb} = 360^\circ$ corresponds to the concentric alignment of the planet and moon bodies as seen from the observer. The simulation settings are $N_p^{\text{eq}} = 60$, $N_m^{\text{eq}} = 16$, $\Delta t = 3\text{min}$.

5.4.3. Analysis of eclipse events

As a last step in the analysis of the flux and polarization signal of the edge–on Earth–Moon–like system, we present a characterization of the observed eclipse events. In particular, we focus on the main differences with respect to the transit events described in Section 5.4.2.

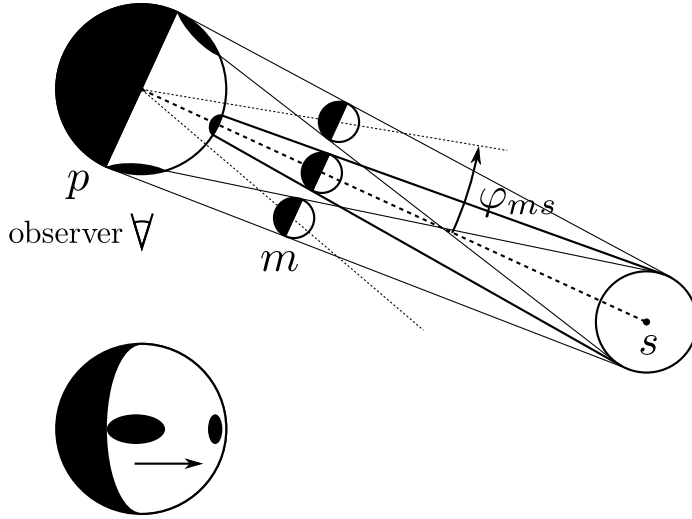


Figure 5.14: Top, geometrical definition of the φ_{ms} angle as the moon passes in between the planet and the star; bottom, evolution of the eclipse umbral shadow on the planet as seen from the observer. Indexes p , m , and s stand for the planet, moon and star position. The scale of the bodies' size has been altered in order to enhance the visualization of φ_{ms} . Distances between bodies and radii are not to scale in order to emphasize the geometry of the system.

The direction of motion of the eclipse shadow follows the same route as the transit discussed before. Because we only discuss half of the barycentre's orbit, the eclipse shadow enters the shadowed body through the terminator and leaves through the bright limb, as illustrated in Figures 5.9 and 5.14. The occurrence of eclipses is not immediately linked to the true anomaly of any of the bodies. Instead, the figures shown here use the angle φ_{ms} between the star and the moon measured from the planet position, and φ_{ps} , the angle between the star and the planet measured from the lunar centre position, both defined positive in the counter clockwise direction, as sketched in Figure 5.14. Angles φ_{ms} and φ_{ps} are used as relative measures of the succession of eclipse events, which are linearly related to time, given the circular orbital motion of the bodies.

Planetary eclipses

As described in the case of the transit events, eclipses take place along the planetary equator¹⁴. Thus, flux and polarization variations also produce symmetric curves at $\alpha = 0^\circ$. The flux and polarization curves obtained for some of the eclipse events enumerated in Section 5.3 (see Figures 5.3 and 5.4) are shown in Figures 5.15 and 5.16.

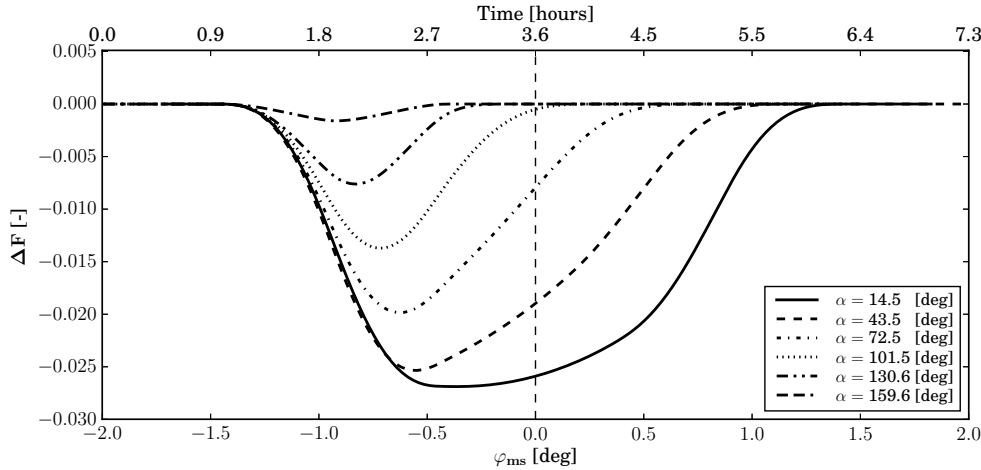


Figure 5.15: Difference between the planet–moon system reflected flux and the continuum background flux signal, ΔF , as a function of angle φ_{ms} and relative time during lunar eclipses at increasing phase angles. Fluxes have been normalized so that F at $\alpha = 0^\circ$ equals the geometric albedo of the planet–moon system. $\varphi_{ms} = 0^\circ$ corresponds to the concentric alignment of the planet and moon bodies as seen from the star. The simulation settings are $N_p^{eq} = 60$, $N_m^{eq} = 16$, $\Delta t = 3\text{min}$.

We first focus on the change of reflected flux during planetary eclipses (see Figure 5.15). The same argumentation provided in Section 5.4.2 with respect to the distortion of the symmetry of flux and polarization signatures applies in the case of the eclipses with one important difference. While the start time of transit events is increasingly delayed with increasing phase angles, successive eclipse features bring forward the end time of the event maintaining the same starting time. This fundamental difference between the transit and eclipse events lies in the fact that eclipses depend on the star position at every time, and not on the observer’s position. However, the observer’s position influences the fraction of eclipse that is recorded, as observed in Figure 5.14. While the eclipsing shadow for the edge-on planet–moon system sweeps the bright face of the shadowed body, only the first fraction of this event is observed from the ingress of the shadow at the body’s terminator. Thus, the increase of night region observed with increasing phase angle yields a progressive time reduction of the actual eclipse observed.

Besides, the planet travels through the penumbra region of the eclipse shadow before entering the umbral cone, resulting in a progressively shadowed planetary surface. Therefore, the flux variation yields smoother curves compared to those obtained for lunar transits (see Figure 5.8) in which not only the ingress but also the egress of the shadow are characterized by smooth curves.

The variation of degree of polarization of the unresolved system during planetary eclipses is shown in Figure 5.16. The same conclusions regarding the impact of the planetary atmosphere and surface as discussed in the case of the lunar transit events can be drawn in this case. It is also remarkable that a similar amplitude is observed in polarization during planetary eclipses at different phase angles. Furthermore, we highlight that Figure 5.16, shows similar ΔP amplitudes ranging from 0.9% – 1.2% at phase angles $\alpha \approx 70^\circ – 160^\circ$. The peak value remains pretty constant along the range provided, so that the maximum variation of degree polarization is reached at $\alpha \approx 101^\circ$ and $\alpha \approx 160^\circ$.

Lunar eclipses

The flux and polarization curves obtained during lunar eclipse events have been plotted in Figures 5.17 and 5.18. Similar to the planetary transits, during a lunar eclipse the moon is completely darkened by

¹⁴Here, we understand by equator the direction parallel to the x_0 -axis of the observers coordinate system passing through the centre of the observed body

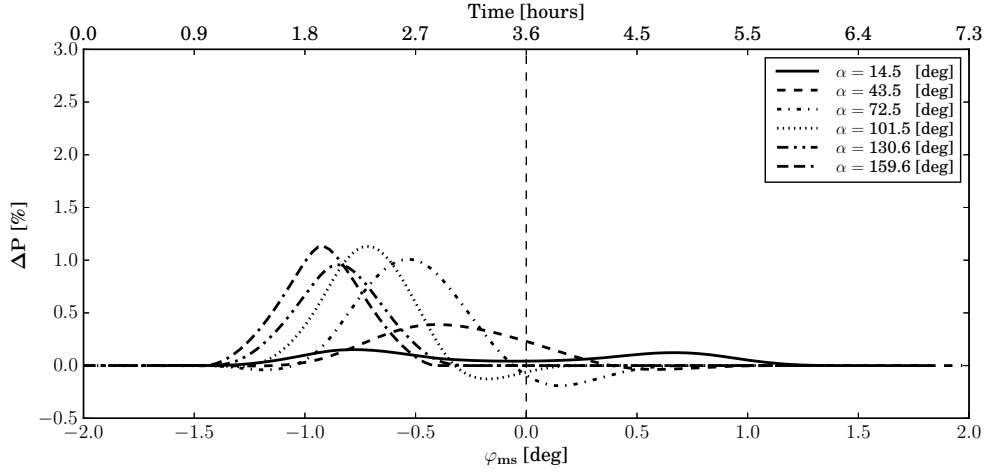


Figure 5.16: Difference between the planet–moon system degree of polarization and the continuum background signal, ΔP , as a function of angle φ_{ms} and relative time during planetary eclipses at increasing phase angles. $\varphi_{ms} = 0^\circ$ corresponds to the concentric alignment of the planet and moon bodies as seen from the observer. The simulation settings are $N_p^{eq} = 60$, $N_m^{eq} = 16$, $\Delta t = 3\text{min}$.

the shadow cast by the planet, as it is in the umbral region of the planetary shadow (see Figure 4.4a), resulting in a constant occultation region recorded both in the flux and the degree of polarization curves (see Figures 5.17 and 5.18). However, the difference between the transit and eclipse events yields a series of fundamental variations regarding the duration of the recorded events.

Tables 5.3 and 5.4 collect the ingress and egress times, defined as the time to the start and end of total lunar occultation, the occultation duration, as well as the total time of event for both planetary transits and lunar eclipses at different phase angles. The darkening produced by a transit results from the cylindrical projection of the transiting shape onto the darkened body. However, the realistic conical approach implemented for the mutual eclipses yields larger total duration and lower total occultation duration times in the case lunar eclipses compared to planetary transits at any phase angle.

In fact, the moon enters the divergent penumbra region of the eclipse shadow earlier than the cylindrical projection of a transit foresees, considerably increasing the total time of ingress and egress compared to the planetary transit (factor of 3–4 at high phase angles). The total lunar eclipse occultation

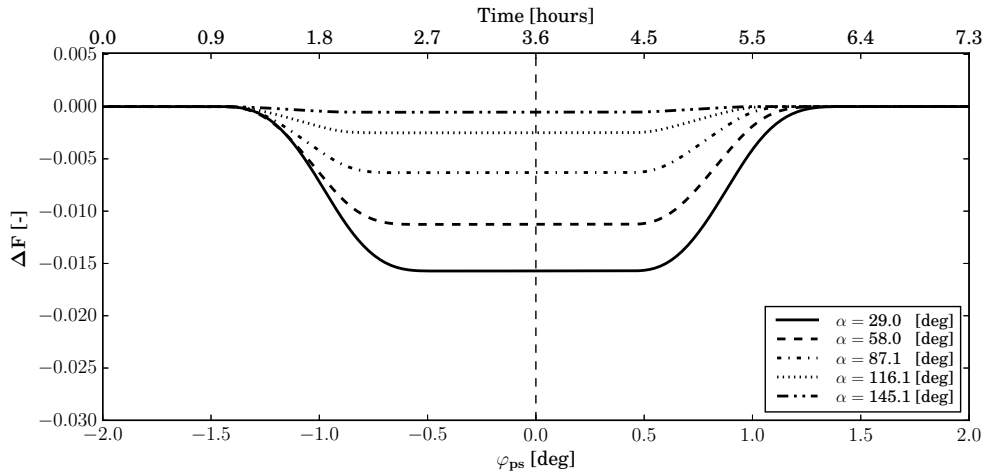


Figure 5.17: Difference between the planet–moon system reflected flux and the continuum background flux signal, ΔF , as a function of angle φ_{ps} and relative time during lunar eclipses at increasing phase angles. Fluxes have been normalized so that F at $\alpha = 0^\circ$ equals the geometric albedo of the planet–moon system. $\varphi_{ps} = 0^\circ$ corresponds to the concentric alignment of the planet and moon bodies as seen from the star. The simulation settings are $N_p^{eq} = 60$, $N_m^{eq} = 16$, $\Delta t = 3\text{min}$.

Table 5.3: Ingress time, egress time, duration of total occultation and total duration of planetary transit events for increasing phase angles. Time resolution is 0.05 hours. The effect of the course resolution can be observed in the ingress and egress times.

Phase angle, α [deg]	26.4	53.7	80.6	107.5	134.3
Ingress time [h]	0.90	0.75	0.50	0.40	0.30
Egress time [h]	0.90	0.80	0.60	0.50	0.40
Occultation duration [h]	2.55	2.65	2.80	2.85	2.90
Total duration [h]	4.35	4.20	3.90	3.75	3.60

Table 5.4: Ingress time, egress time, duration of total occultation and total duration of lunar eclipse events for increasing phase angles. Time resolution is 0.05 hours. The effect of the course resolution can be observed in the ingress and egress times.

Phase angle, α [deg]	29.0	58.0	87.1	116.1	145.1
Ingress time [h]	2.00	1.80	1.60	1.55	1.45
Egress time [h]	1.95	1.80	1.55	1.40	1.30
Occultation duration [h]	1.80	1.90	2.15	2.25	2.30
Total duration [h]	5.75	5.50	5.30	5.20	5.05

duration is smaller than the duration of the planetary transit, as the effective umbral darkening area is smaller than the transit blocking area, given the convergence of the umbral cone (see e.g. Figures 4.1 and 4.2). Occultation duration times in Tables 5.3 and 5.4 increase with phase angle as a result of the smaller lunar illuminated area, which yields total lunar reflected light blockage before the moon is completely occulted by the planet.

As for the variation of degree of polarization curves during lunar eclipse shown in Figure 5.18, the same conclusions as drawn for the variation of polarization during planetary transits apply, as, in both cases, the moon does not contribute to the observed reflected starlight. The maximum polarization peak ascends to $\Delta P \approx 2.7\%$ corresponding to a phase angle $\alpha \approx 90^\circ$.

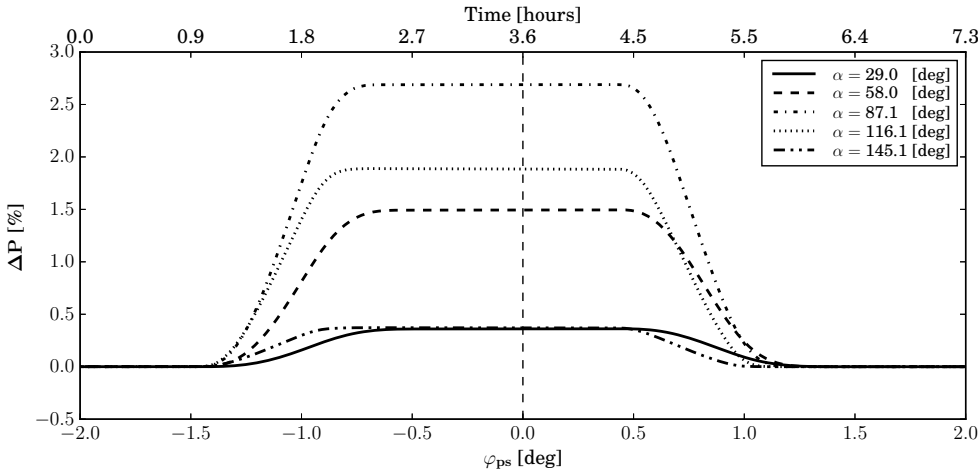


Figure 5.18: Difference between the planet–moon system degree of polarization and the continuum background signal, ΔP , as a function of angle φ_{ps} and relative time during lunar eclipses at increasing phase angles. $\varphi_{ps} = 0^\circ$ corresponds to the concentric alignment of the planet and moon bodies as seen from the observer. The simulation settings are $N_p^{eq} = 60$, $N_m^{eq} = 16$, $\Delta t = 3\text{min}$.

In this section, we have studied the characteristics of the mutual events features recorded on flux and polarization phase curves at different phase angles, for the simulated planet–moon system. These events occur in a periodic manner and are observed as drops in reflected flux and oscillations in the degree of polarization of the reflected starlight during planetary darkening events (i.e. lunar transits and planetary eclipses). Such oscillations strongly depend on the reflection properties across the planetary disk and the particular darkened region at every epoch. In the case of lunar darkening events (i.e. planetary transits and lunar eclipses) a constant drop in flux and increase in polarization are observed during total lunar occultation epochs.

The curves obtained for planetary eclipses and lunar transits show different slopes in the ingress and egress phases of the events, experiencing a steeper change in flux when the shadow travels through the planetary limb. Moreover, we notice that planetary eclipse events yield smoother curves as a result of the planet travelling through the penumbra region of the shadow.

We observed maximum flux decreases of 0.027 ($\sim 8\%$ of the total system albedo) at small phase angles $\alpha = 10\% - 40\%$ during planetary darkening events, while the maximum flux drop experienced during lunar darkening events (i.e. planetary transits and lunar eclipses) is reduced by a factor of 0.56. The flux drop magnitude decreases with increasing phase angle α , being this maximum at $\alpha = 0^\circ$. As for the polarization, a maximum degree of polarization variation of $\sim 2.66\%$ is experienced at $\alpha \approx 90^\circ$ during lunar darkening events. Moon and planet darkening signatures are not equally reproduced in flux and polarization: moon darkening events stand out when looking at the polarization curve features, $\Delta P \approx 1\% - 1.8\%$ for $67^\circ < \alpha < 121^\circ$ during lunar transits while $\Delta P \approx 1.25\% - 2.66\%$ for $54^\circ < \alpha < 108^\circ$ during planetary transits; planet darkening events excel in flux (as argued before). Furthermore, we notice that planetary eclipses yield lower ΔP values than lunar transits. Variations in F and P are dominated by the total darkening of the moon during planetary transits and lunar eclipses, thus obtaining similar variations in both cases.

The resulting duration of lunar darkening events is in the order of 4 hours (transits) and 5 hours (eclipses) at any phase angle. These values are in agreement with the results obtained by Cabrera and Schneider [2007]. Similar planetary darkening events duration are obtained for low phase angles, while this number quickly falls with increasing phase angle.

The results presented correspond to half of the planetary orbit around the star. Similar results are expected for the second part of the orbit, with one difference: transit and eclipses ingress take place through the limb of the darkened body, resulting in mirrored curves with respect to the central event time.

The magnitude, duration, and shape of the flux results obtained are in agreement with those simulated by Cabrera and Schneider [2007]. Moreover, both the flux and polarization curves resemble those modelled for exoplanet transits across the stellar disk [see Kostogryz et al., 2015]. For the latter, the variations in degree of polarization are much lower than we observe for the planet–moon system ($\sim 10^{-6}$) and always show a symmetric pattern (in the absence of starspots).

5.5. On the detection of mutual events

The improvement in polarimetry techniques allows monitoring the degree of linear polarization in the case of known exoplanets [see Bott et al., 2016]. Moreover, the measurement of the total emitted flux by exoplanet through direct imaging could hide information on the presence of a moon. However, as described in Section 5.4, lunar traces are typically short compared to the total duration of observations and suppose a relatively small variation¹⁵ with respect to the background signal, which could be hidden on instrument and/or stellar noise.

In Section 5.5.1, we analyse the geometrical probability of encountering a mutual event on edge-on exoplanet observations. In an attempt to extend our conclusions beyond edge-on systems, different viewing perspectives are assessed in Section 5.5.2. Finally, we study the possibility of carrying out indirect lunar detections by looking for periodic signals on phase curves in Section 5.5.3.

¹⁵Different lunar parameters than the ones used in this chapter lead to larger lunar impact on the unresolved planet–moon system as shown in Chapter 6.

5.5.1. Geometrical probability of mutual event direct observation in an edge-on Earth–Moon system

From Figure 5.3, we estimate the total time of mutual event occurrence at around 86.6 h, while the phase curve spans for half the orbital period of the barycentre around the star, i.e. around 182.8 days. Therefore, mutual events cover around the 2% of the total phase curve, for the particular modelled geometry (see Section 3.2.2).

However, the actual probability of observing lunar traces on exomoon signals directly depends, at least, on (1) the duration of the mutual events, (2) the lunar period, (3) the moon–planet orbital geometry, (4) the sampling time, (5) the observation time, (6) the instrument resolution, (7) the instrument accuracy, (8) the maximum and minimum phase angles for which the planet–moon system can be resolved from the parent star. In this section we estimate the geometrical probability of observing a mutual event. For this, we assume that the background noise of the signal is zero, and focus our results on an edge-on system.

Typical angular separations for exoplanets fall within the range 0–1 arcsec [Traub and Oppenheimer, 2010b, see], while the SPHERE planet finder instrument at the VLT provides imaging contrasts of one part in a million at angular separation of a few tenths of an arcsecond [Wagner et al., 2016b]. In our case, the extreme contrast of the Earth-like exoplanet ($\sim 10^{-10}$) makes such body impossible to be resolved with current technology. In order to have a representative initial study on the probability of observing a mutual event, we consider the planet–moon system to be resolvable during a fraction of the planet’s orbit. Given the lack of realistic instrument performance for our modelled scenario, we consider a phase angle observable range of $40^\circ \leq \alpha \leq 140^\circ$, which corresponds with maximum angular variations of 12 mas¹⁶ (minimum angular separation of 38 mas) at a reference star distance of 20 pc to the Earth.

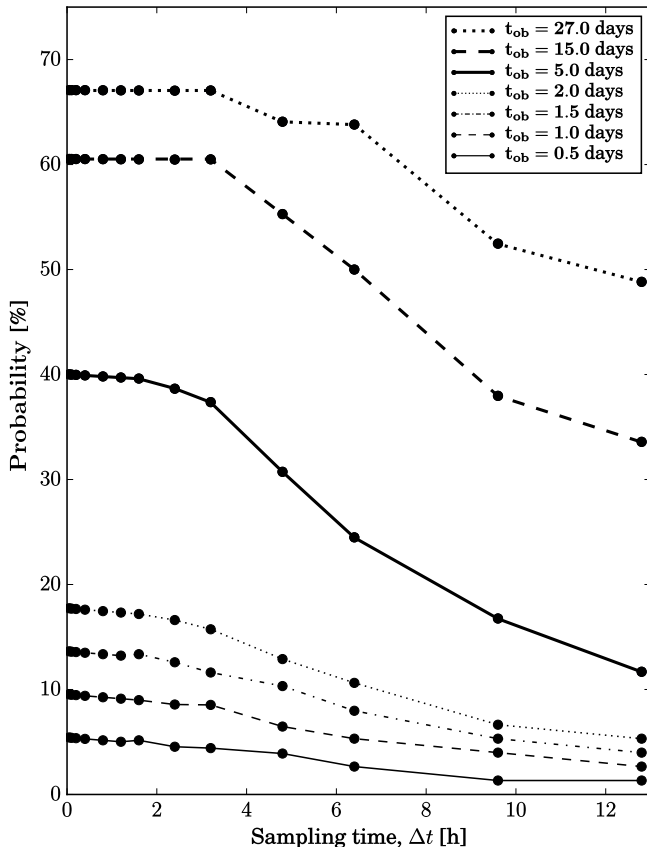


Figure 5.19: Discrete probability of mutual event observation as a function of sampling time, Δt , and total observation time t_{ob} . The results show an increasing probability for increasing sampling frequencies (decreasing sampling times) and increasing total observation time periods.

¹⁶Milliarcsecond (mas).

Then, we numerically compute an estimation of the geometrical discrete probability distribution, P , of performing observations during mutual event time intervals (assuming the moon–planet system is edge–on) as a function of the constant sampling time Δt and the total observation time t_{ob} . The results have been plotted in Figure 5.19 for observation times ranging from half a day to one lunar period (~ 27 days). These must be understood in the context of the discrete signal computed in the present work, so that the probability of observing a mutual event when Δt approaches t_{ob} is given by the discrete total number of points of the signal and the number of points at which we find mutual events, yielding:

$$\lim_{\Delta t \rightarrow t_{\text{ob}}} P \approx 1.33\%, \quad (5.6)$$

where the value obtained differs from the 2% of mutual events coverage along the phase curve due to the imposed limitation on observed phase angles. In any case, the 1.33% probability obtained differs from the 0% probability that a continuous probability distribution would yield for such a natural event.

While the maximum separation between mutual events is half the lunar orbital period $t_{mb}/2$ (see Figure 5.3), Figure 5.19 does not display the expected 100% probability for sampling times shorter than the minimum duration of a mutual event ($\Delta t \rightarrow 0$ h). This is due to the fact that our probability estimation takes into account the likely event of observing the system at phase angles $140^\circ < \alpha < 40^\circ$, from which no information can be retrieved. This possibility notably reduces the total probability of mutual events encounter.

Figure 5.19 shows, for every t_{ob} almost no variation in probability for sampling times up to ~ 4 hours, typical time of duration of the mutual events, followed by a continuous decrease of the probability with increasing Δt . It is worth highlighting that the probability of exomoon encounter in the simulated edge–on Earth–Moon–like system raises up to $\sim 10\%$ for relatively short 1 day long observations. This probability scales nearly linearly with the total time of observation for observation duration times lower than ~ 10 days, as Figure 5.20 shows.

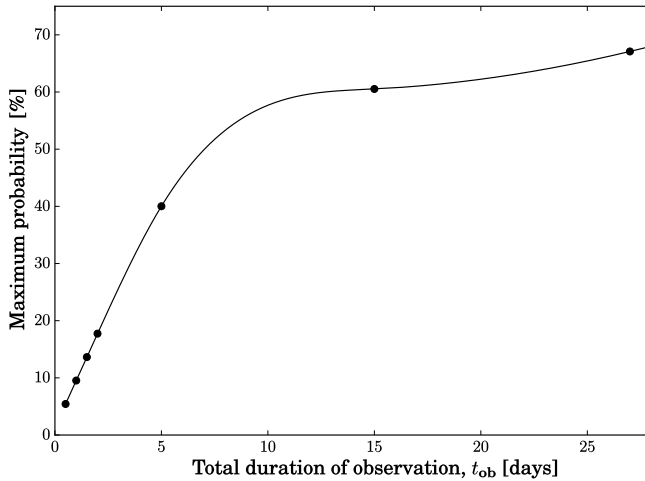


Figure 5.20: Maximum probability of mutual events observation as a function of the total duration of the observation t_{ob} . The resulting curves show linear behaviour for total duration of observation times in the order of days, while the increment of probability achieved by further increasing the observation time quickly falls.

It can be concluded that, in the event of observing an edge–on Earth–Moon–like exoplanetary system, relatively high probability of observing a mutual event exists, ranging 5% to 40% for observation times ranging from 0.5 to 5 solar days. Observation times in the order of the lunar period do not guarantee detection of the exomoon for edge–on systems.

5.5.2. Different observer position in coplanar Earth–Moon system

The results and conclusions presented so far make use of the particular coplanar planet–moon orbital geometry observed edge–on, which allow recording all transit and eclipse events on the resulting curves. However, the observation of such system from an edge–on perspective is a matter of fortune. In this section, we evaluate the influence of observing a coplanar Earth–Moon–like planetary system from a different viewing direction.

Transit events rely on the proper alignment between the transiting body, the darkened body, and the observer, as modelled in Section 5.4.2. Standing as one of the limitations of transit spectroscopy techniques, transits are only present in edge-on or near edge-on exoplanets. On the other hand, the occurrence of eclipses does not depend on the observer position but the local alignment of the bodies within the observed planetary system. Hence, we expect exomoons to be detectable through the observation of mutual eclipse beyond the edge-on system configurations.

Opposite to the edge-on system we find the face-on system (described in Section 3.2.2), in which both the planetary and lunar orbital plane coincides with the plane of the sky at the observer's position. In this situation, the bodies are observed at a constant phase angle $\alpha = 90^\circ$. Thus, as follows from Figures 5.10, 5.13, 5.16 and 5.18, the maximum variation in degree of polarization is expected to be

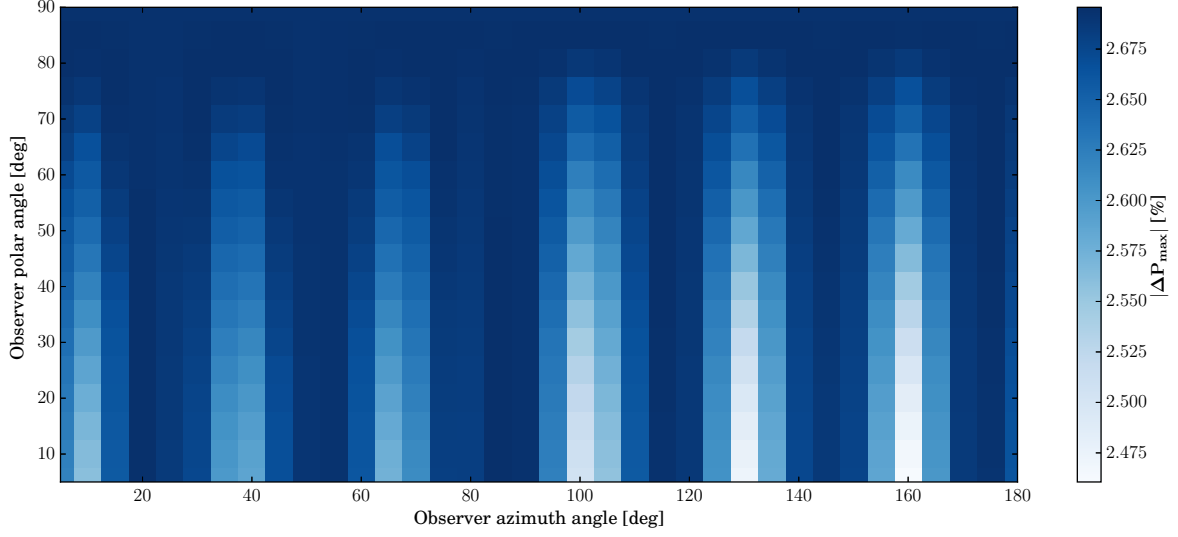
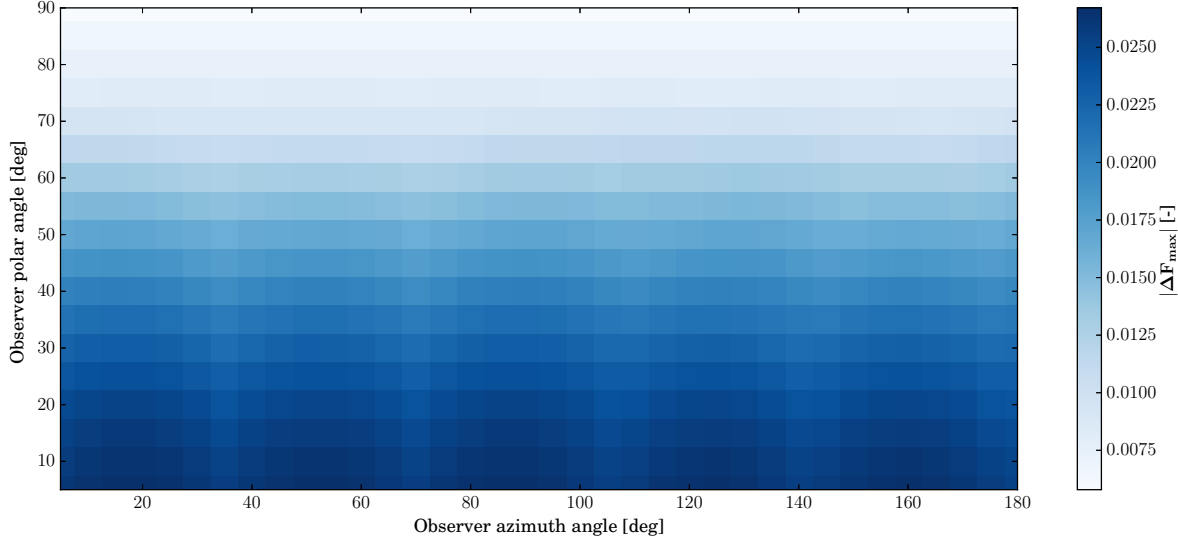
(a) $|\Delta P_{\max}|$ map(b) $|\Delta F_{\max}|$ map

Figure 5.21: Absolute value of the maximum difference between the planet–moon system degree of polarization and the continuum background signal along the phase curve $|\Delta P_{\max}|$ (a), and absolute value of the maximum difference between the unresolved reflected flux and the continuum background signal $|\Delta F_{\max}|$ (b), both as a function of observer azimuth angle φ_{ob} and observer polar angle, θ_{ob} . Fluxes have been normalized so that F at $\alpha = 0^\circ$ equals the geometric albedo of the planet–moon system. The simulation time resolution is $\Delta t = 90\text{min}$, while φ_{ob} and θ_{ob} angles have been evaluated every 5° .

recorded on face-on polarization curves. In between an edge-on and an face-on configuration, we find a whole range of observing perspectives which we have studied by varying the azimuthal, φ_{ob} , and polar angle, θ_{ob} , of the observer in coordinate system S_1 (see Section 3.3). Using an angular step of 5° , a total number of ~ 700 simulations have been conducted with a time resolution of 1.5 hours, identifying the largest ΔP value for every pair of φ_{ob} and θ_{ob} angles. The maximum ΔP and ΔF results obtained have been plotted in Figure 5.21, whilst the phase angle matching the maximum recorded ΔP and ΔF values have been mapped in Figure 5.22.

As immediately observed in Figure 5.21a, all viewing directions provide a maximum ΔP value ranging from 2.46% to 2.72% which, as follows from Figure 5.22a, correspond in all cases to phase angles close to 90° . Both figures show characteristic vertical patterns which respond to the variation of observed phase angle at which the eclipses take place with varying observer position, i.e. eclipses do

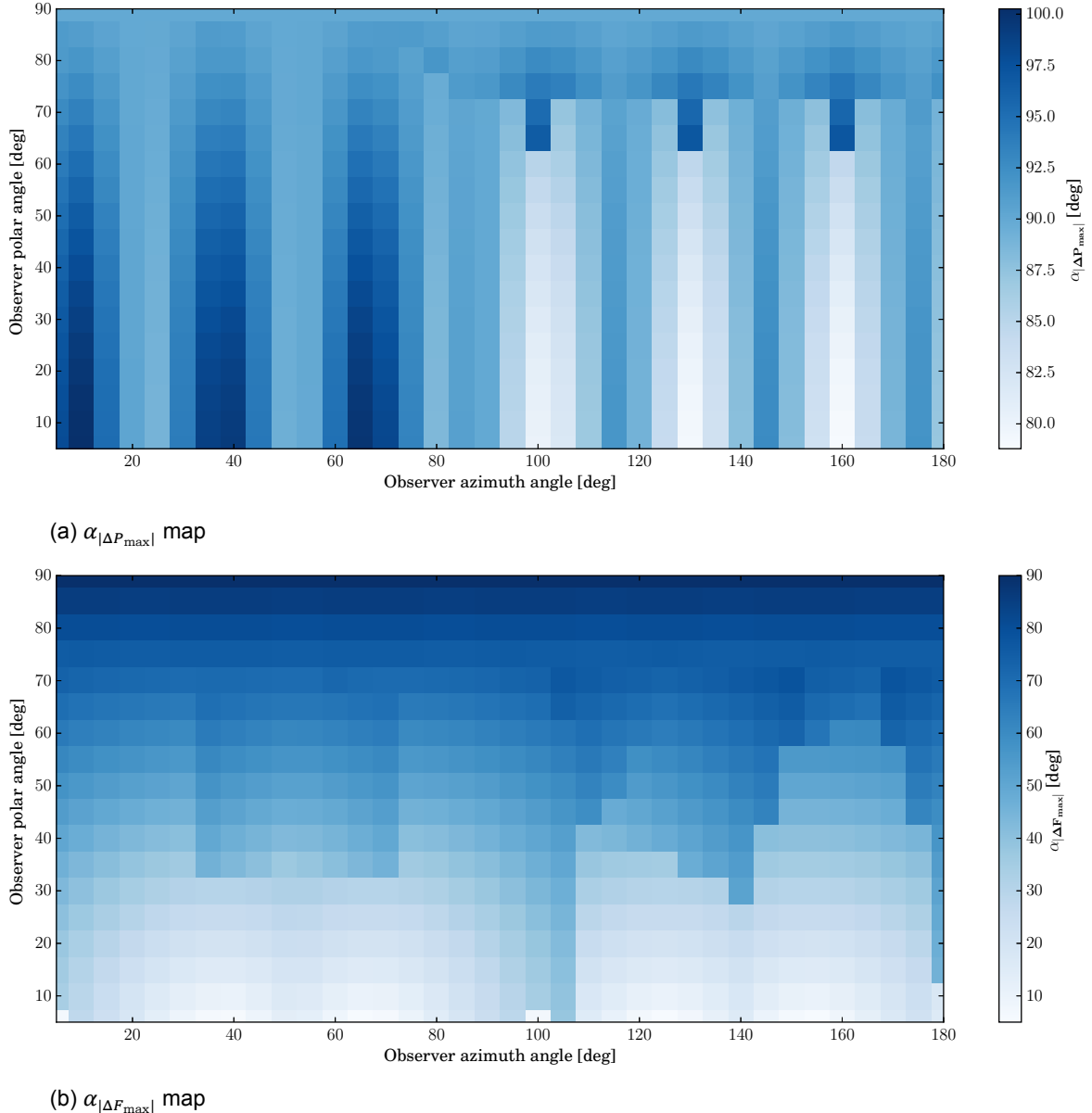


Figure 5.22: Phase angle for maximum difference between the planet–moon system degree of polarization and the continuum background signal along the phase curve $\alpha_{|\Delta P_{\max}|}$ (a), and phase angle for maximum difference between the unresolved reflected flux and the continuum background signal $\alpha_{|\Delta F_{\max}|}$ (b), both as a function of observer azimuth angle φ_{ob} and observer polar angle, θ_{ob} . The simulation time resolution is $\Delta t = 90\text{min}$, while φ_{ob} and θ_{ob} angles have been evaluated every 5° .

not always occur at $\alpha = 90^\circ$. For $\theta_{ob} = 90^\circ$ the system is observed face-on and a constant maximum ΔP value is obtained at a constant $\alpha = 90^\circ$ phase angle.

In the case of the reflected flux F , Figure 5.21b yields a monotonic decrease of ΔF_{\max} with θ_{ob} . The maximum flux drops are observed at $\alpha \approx 0^\circ$, as also follows from Figures 5.8, 5.11, 5.15 and 5.17. In fact, increasing the observer polar angle θ_{ob} progressively raises the minimum phase angle at which the planet–moon system is observed, as well as the phase angle of maximum ΔF , $\alpha|_{\Delta_{\max}}$ (see Figure 5.22b). The variation of observer azimuth angle φ_{ob} for a constant θ_{ob} implies observing a different fraction of the planet orbit at minimum phase angle. Consequently, $|\Delta F_{\max}|$ and $\alpha|_{\Delta_{\max}}$ display an oscillating behaviour with φ_{ob} .

As conclusion, we remark that the search of exomoons in polarization data is not limited to edge-on exoplanets, but can be extended to all configurations as far as the lunar companion’s orbit is (nearly) coplanar with the planetary orbit.

5.5.3. Study of the frequency of mutual events

Frequency analyses on Kepler’s photometry data [Borucki, 2016] are carried out by many researchers with different objectives ranging from the retrieval of the orbital period of transiting exoplanets to the detection of planetary climatic variations [see e.g. Cowan et al., 2017]. In this section, we study the impact of a lunar companion on periodograms extracted from long-term observations of the degree of polarization of the unresolved planet–moon system.

As previously discussed in Section 5.4, the modelled mutual events show themselves in a regular periodic manner in the observed light and polarization curves for circular planetary and lunar orbits (see Section 6.4 for an analysis on varying lunar eccentricity). The orbital period of the moon is defined as the sidereal lunar period, T_{mb} , i.e. the period with respect to distant stars. Assuming the orbits of the moon around the planet and the barycentre around the star to be circular, we find transits to occur every half lunar sidereal period, $\frac{T_{mb}}{2}$, or, alternatively, lunar and planetary transits occur every sidereal period with a time shift of half sidereal period (see Figure 5.23).

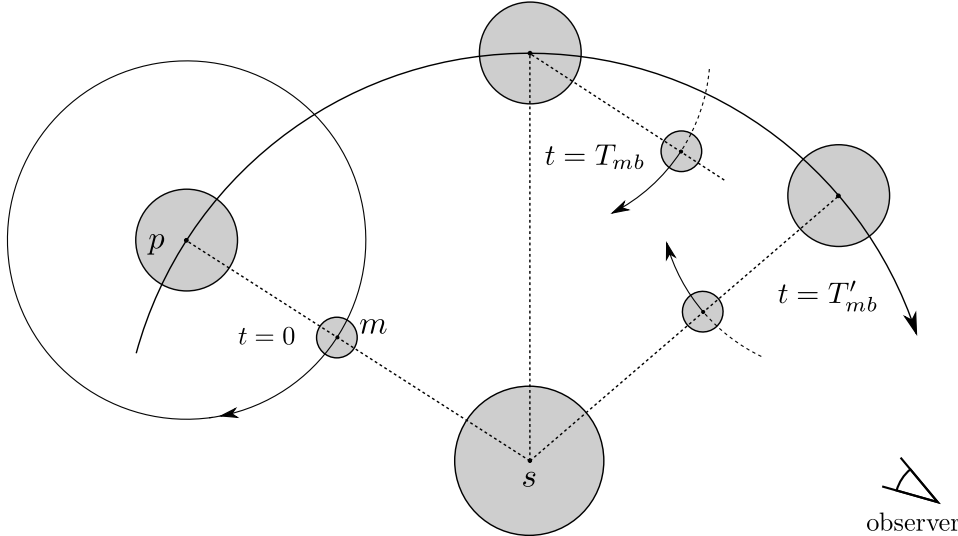


Figure 5.23: Graphical definition of the sidereal, T_{mb} , and lunar synodic periods, T'_{mb} . At time zero, the planet, moon and star are aligned as seen by the observer, constituting an unobservable lunar transit and planetary eclipse scenario. During its prograde motion around the planet, the moon transits in front of the planet again after one sidereal period, and posteriorly eclipses the star, after one stellar period from time zero. Distances between bodies and radii are not to scale in order to emphasize the geometry of the system.

Alternatively to the sidereal period, we introduce the lunar synodic period T'_{mb} , based on the assumption of coplanar circular lunar and planetary orbits. Under these assumptions, we define T'_{mb} as the time between lunar conjunctions (closest apparent approaches) with the star, i.e. the time between consecutive planetary eclipses¹⁷. Subsequently, we find a constant period of repetition of eclipses

¹⁷The use of eccentric orbits yields to different time intervals between successive eclipses. This difference is directly proportional to the eccentricity of the orbit.

which, in the case of prograde moons, is shorter than the sidereal period and related to it through the number of lunar period repetition after one revolution of the barycentre around the star as (see Figure 5.23):

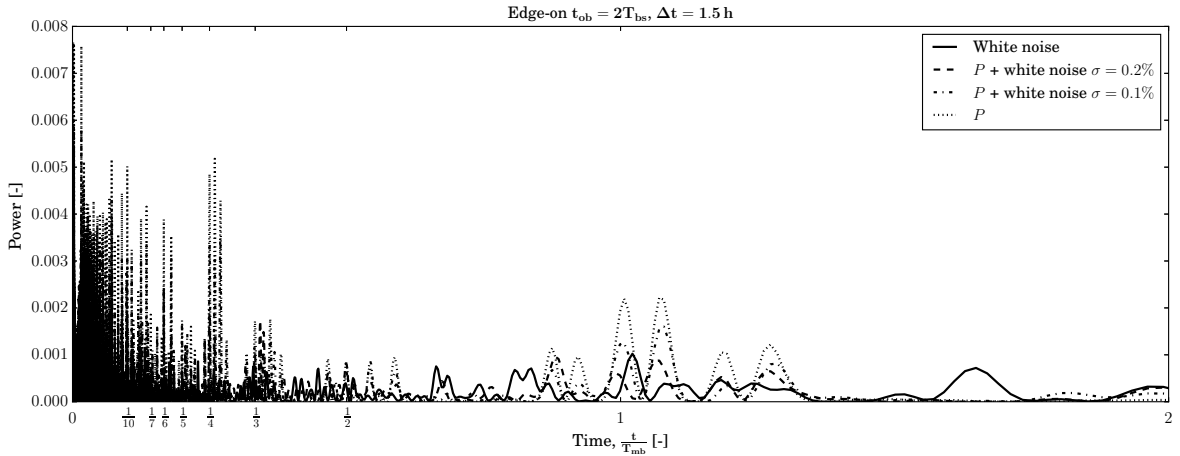
$$\text{number of sidereal periods per barycentre revolution} =$$

$$1 + \text{number of synodic periods per barycentre revolution}, \quad (5.7)$$

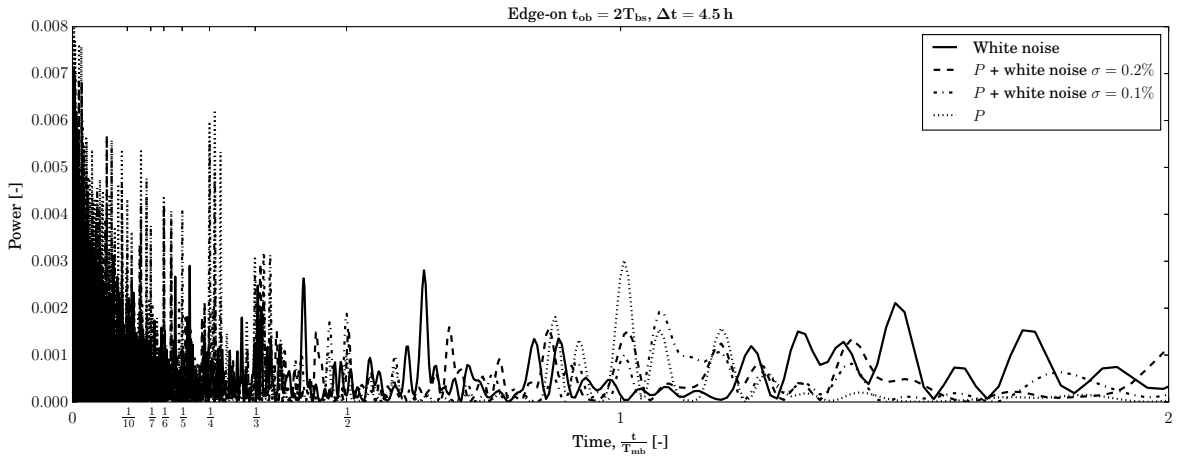
what, assuming $T_{ps} \approx T_{bs}$, can be rewritten as:

$$T'_{mb} = \frac{T_{mb}}{1 - \frac{T_{mb}}{T_{ps}}}. \quad (5.8)$$

Equation 5.8 yields a lunar synodic period $T'_{mb} \approx 29.5$ days for a sidereal lunar period $T_{mb} \approx 27.29$ days. Therefore, conversion of polarization phase curves into frequency domain is expected to yield power peaks at frequencies matching T_{mb} and T'_{mb} . In order to verify such hypothesis with



(a) Sampling time $\Delta t = 1.5$ h



(b) Sampling time $\Delta t = 4.5$ h

Figure 5.24: Power Spectral Density (PSD) of the unresolved planet–moon system polarization signal for an edge-on system without added noise (dotted line), and with added Gaussian white noise of $\sigma = 0.1\%$ (dash-dotted line) and $\sigma = 0.2\%$ (dashed line), as a function of time periodicity (inverse of frequency). The PSD of a randomly generated Gaussian white noise signal is also shown (solid line). The curves are plotted for a sampling time of 1.5 hours (a) and 4.5 hours (b). The total simulated observation time is $t_{ob} = 2T_{bs}$. Time is nondimensionalized with respect to the lunar sidereal period T_{mb} .

the results obtained with our model, we simulate reflected starlight curves for both edge-on and face-on planet–moon configurations, with total observation times $t_{\text{ob}} = 2T_{\text{bs}}, 3T_{\text{bs}}, 5T_{\text{bs}}$, and an integration times $\Delta t = 1.5\text{h}, 4.5\text{h}, 10.5\text{h}$, and Gaussian noise standard deviations $\sigma = 0.1\% - 1\%$. As argued in Section 5.5.1, we assume that the planet–moon system can only be observed at phase angles $140^\circ < \alpha < 40^\circ$. For each scenario we compute the Lomb–Scargle periodogram [Lomb, 1976; Scargle, 1982], which allows to detect periodic signals in unevenly–spaced observations, and compare it to the background noise level. The Power Spectral Density (PSD) results are shown in Figure 5.24 and 5.25 for the cases of higher relevance, and discussed below.

In the case of edge–on systems, we find that the obtained degree of polarization signal is strongly driven by a frequency of $T_{\text{bs}}/2$, as the continuum polarization curve repeats after half a planetary orbit around the star. A estimation of the background continuum polarization signal by averaging (and interpolation when needed) yields the absolute change in polarization ΔP at the cost of an increased background noise. This, together with the highly variable ΔP magnitudes found along the phase curve makes the distinction between the mutual events signal and random Gaussian noise extremely challenging. In fact, this is only possible for very long observation times (in the order of T_{bs}), reduced background noise levels (in the order of $\sigma \approx 0.001$) and short data acquisition intervals. As an example, Figure 5.24a presents the histogram obtained after two planet orbital revolutions and a integration

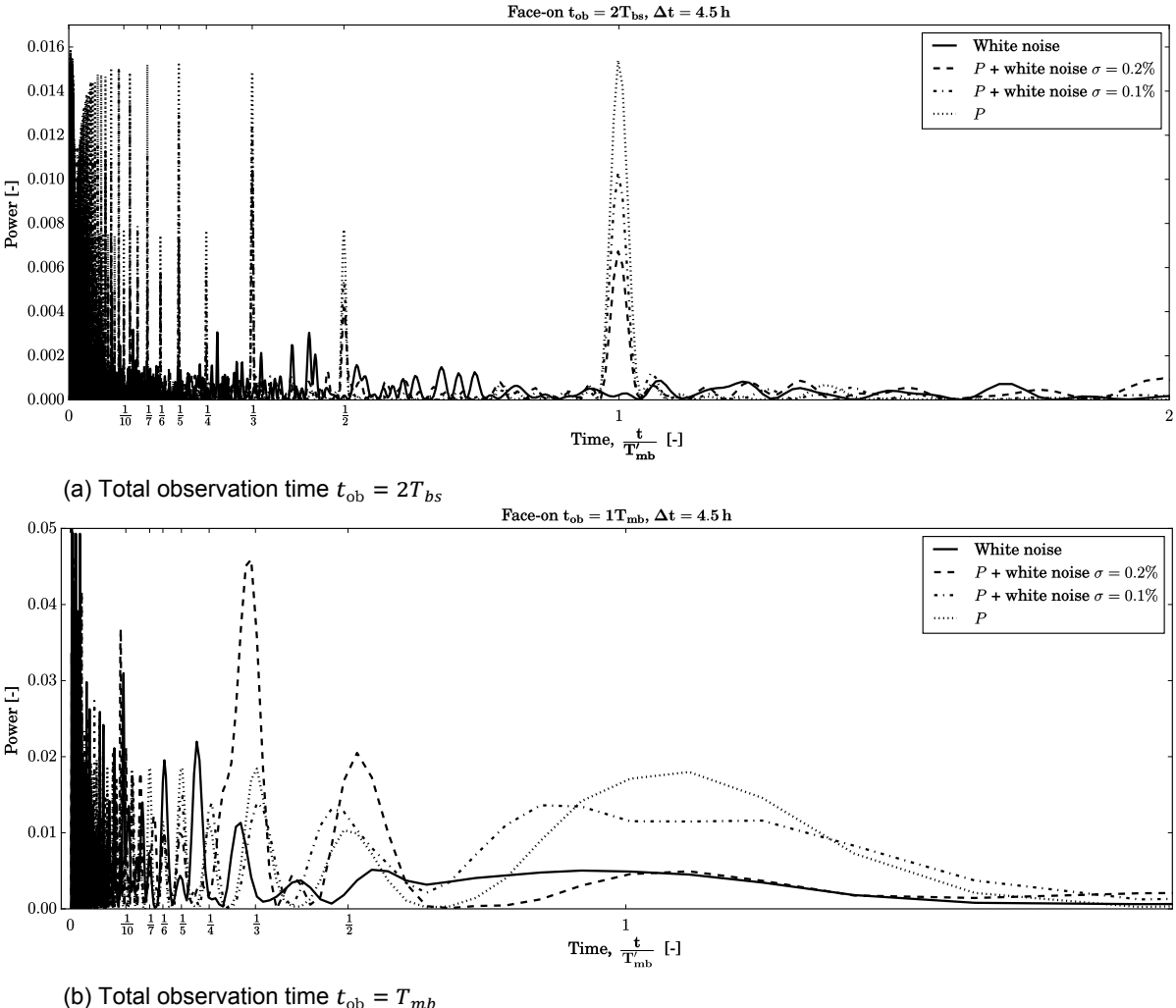


Figure 5.25: Power Spectral Density (PSD) of the unresolved planet–moon system polarization signal for a face–on system without added noise (dotted line), and with added Gaussian white noise of $\sigma = 0.1\%$ (dash–dotted line) and $\sigma = 0.2\%$ (dashed line), as a function of time periodicity (inverse of frequency). The PSD of a randomly generated Gaussian white noise signal is also shown (solid line). The curves are plotted for a total simulated observation of $2T_{\text{bs}}$ (a) and $1T_{\text{mb}}$ (b). The sampling time is $\Delta t = 4.5\text{h}$. Time is nondimensionalized with respect to the lunar stellar period T'_{mb} .

time $\Delta t = 1.5\text{h}$. The non-sinusoidal nature of the features observed yields to the appearance of peaks for the different harmonics of periods T_{mb} and T'_{mb} . Moreover, we observe the presence of spurious frequencies which only fade away for extremely large observation times and/or reduced integration times and noise levels. As illustrated in Figure 5.24b for a integration time of 4.5 hours, the short duration of the mutual events registered yields to a loss of meaningful data that works against the reduction of background noise as the integration time increases. Consequently, we do not observe an improvement of the results by increasing Δt .

While the edge-on configuration represents an extremely challenging scenario for lunar detection via frequency analyses, the periodograms obtained for face-on systems are more encouraging. In this case, a observation period of $t_{\text{ob}} = 2T_{\text{bs}}$ and a integration time $\Delta t = 4.5\text{h}$ yields neat peaks and low magnitude sidelobes at all harmonics of the frequency matching the eclipse periodicity, for noise values $\sigma = 0.1\%$, 0.2% . This occurs due to the fact that face-on planet–moon system polarization values do not vary with the position of the planet along its orbit, as it is always observed at $\alpha = 90^\circ$). In contrast, P shows a smooth low amplitude sinusoidal variation as a result of lunar reflected light variations along its orbit around the planet, as the distance between the star and the moon varies with lunar true anomaly v_{mb} . The low magnitude of such oscillation is strengthen by the regular (both in time and amplitude) eclipse events found along the lunar orbit, matching the peaks of maximum and minimum reflected flux (minimum and maximum polarization peaks). Figure 5.25b shows that observation times as short as one lunar orbit could reveal the presence of a lunar companion with limited accuracy, as the computed PSD curves are easily differentiated from that of Gaussian noise.

Therefore, we conclude from our results that the presence of an exomoon could be detected on long polarization observation series, being such an achievement easier to accomplish when looking at face-on exoplanets. However, the analysis carried must be complemented with future studies considering more realistic noise values, as well as the consideration of alternative features that could introduce additional characteristic frequencies (e.g. the presence of a higher number of exomoons or the slow rotation of non-spherically symmetric exoplanets).

In this section we have concluded that, assuming the existence of a lunar companion in edge-on configuration and given the physical and reflection properties of the modelled bodies, the probability of observing a mutual event raises up to 5% – 40% for observation period of 0.5 – 5 days and sampling times $\Delta t < 4$ hours, scaling linearly with observation time. Larger observation periods yield smaller increments of probability, i.e. 40% for 5 days and 67% for 27 days of observation.

Moreover, we show that moons orbiting along the ecliptic plane might be detected from any observer's perspective, not limited to edge-on configurations, as eclipses are expected to occur regardless the observer's position. As an extreme case, moons observed in face-on configuration ($\alpha = 90^\circ = \text{cte}$) yield the maximum possible variation in degree of polarization at every lunar eclipse. This scenario is ideal for direct imaging observations, as the planet–moon system is constantly observed at their maximum distance to the star.

Finally, we show that exomoons might be indirectly detected on long polarization data series through frequency analysis. Our simulation results show that this technique is particularly promising for the detection of face-on systems. In such scenario observation periods of one lunar orbit and integration times ~ 4.5 hours are expected to unveil the presence of a periodic signal matching the lunar synodic period, considering a maximum background noise of $\sigma = 0.2\%$.

Hereafter, we continue our study by generalizing the results and conclusions shown in this chapter. For this we analyse the sensitivity of mutual events recorded in flux and polarization with varying lunar parameters in Chapter 6.

6

Results: variation of reflected signal with lunar parameters

Previous sections presented and analysed the lunar traces found for a particular planet–moon configuration. In this chapter, we study the dependence of reflected light flux and degree of polarisation on five lunar model parameters. In Section 6.1 we analyse the signal variation with lunar period (or semi-major axis). Then, we investigate the impact of varying lunar albedo in Section 6.2, followed by an analysis on lunar radius in 6.3. Section 6.4 assesses the impact of increasing moon orbit eccentricity, and we finalize the study by determining the impact of moon orbit inclination in Section 6.5. The chapter concludes with a summary of the most relevant results from the conducted studies in Section 6.6.

6.1. Variation with lunar period, T_{mb}

We start our analysis on lunar parameters by briefly discussing the impact of varying lunar orbital period on the results shown in Chapter 5. As shown in Figure 5.3, mutual events are periodically repeated for circular edge-on orbits (see Section 6.4 for a discussion on eccentric lunar orbits). Their period of repetition is proportional (equal in the case of transits) to the lunar orbital period. Hence, increasing lunar periods, i.e. increasing lunar semi-major axes a_{mb} , yield a higher time gap between events. Furthermore, close-in moons rotate faster around the parent planet. Therefore, the duration of mutual events is expected to increase with increasing orbital period, being directly proportional to the square root of the orbital radius¹. Doubling the lunar–planet distance yields a duration increment of 41%.

Besides that, a variation in lunar period does not alter the magnitude of flux and degree of polarization variations during lunar and planetary transits, as well as lunar eclipses. On the contrary, we observe variations both in flux and polarization during any planetary eclipse with varying lunar semi-major axis. These correspond to the alteration of the shadow cast by the moon at the planetary position with increasing a_{mb} , i.e. close-in moons project a larger umbra spot on the planet's surface while total eclipses give rise to annular eclipses on the planet with increasing lunar orbit radius. We provide the maximum flux drop, $|\Delta F_{\max}|$, and change in degree of polarization, ΔP_{\max} , with increasing a_{mb} for three different lunar radii in an Earth–Moon–like system in Figures 6.1 and 6.2 respectively. The employed a_{mb} values fall in between the Roche radius, i.e. the minimum orbital radius necessary for dust or particles to form a moon with $R_{\text{Roche}} \approx 18400$ km ($R_{\text{Roche}} \approx 0.05a_m$), and the Earth's Hill sphere radius, i.e. the region in which the Earth dominates the attraction of satellites with $R_{\text{Hill}} \approx 1496000$ km ($R_{\text{Hill}} \approx 3.89a_m$).

We first focus on the maximum change in flux. Figure 6.1 shows a monotonically decreasing relationship between $|\Delta F_{\max}|$ and a_{mb} , which is moderately strengthened with increasing lunar radius obtaining 2.1%, 2.6% and 3.1% maximum flux drop variations along the considered a_{mb} values for

¹The velocity of a body describing a circular orbit is given by $v = \sqrt{\frac{\mu}{r}}$, with μ the standard gravitational parameter of the body and r the radius of the orbit.

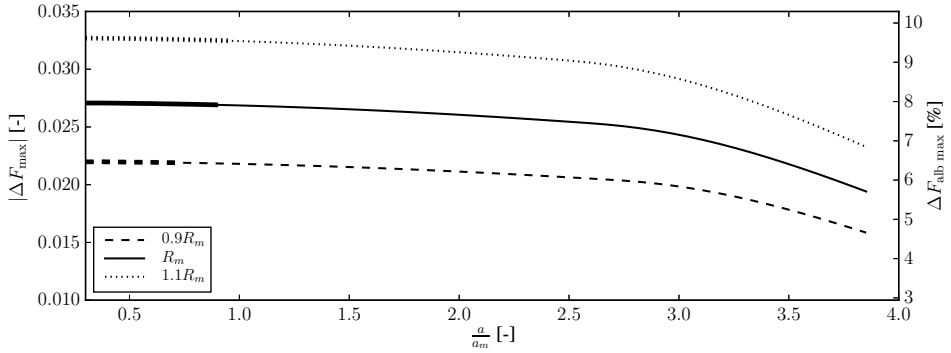


Figure 6.1: Absolute value of the maximum difference between the planet–moon system reflected flux and the continuum background flux signal, $|\Delta F_{\text{max}}|$, as a function of lunar semi–major axis, a , for varying lunar radii: $0.9R_m$ (dashed line), R_m (solid line), and $1.1R_m$ (dotted line), with R_m the size of our Moon. The right vertical scale shows the corresponding relative flux difference with respect to the planet–moon system albedo, $\Delta F_{\text{alb max}}$. The lunar semi–major axis has been nondimensionalized with the semi–major axis of the Moon orbit around the planet Earth, a_m . Thickness is increased for semi–major axis values yielding umbral eclipses and diminished for antumbral eclipses. Fluxes have been normalized so that F at $\alpha = 0^\circ$ equals the geometric albedo of the planet–moon system.

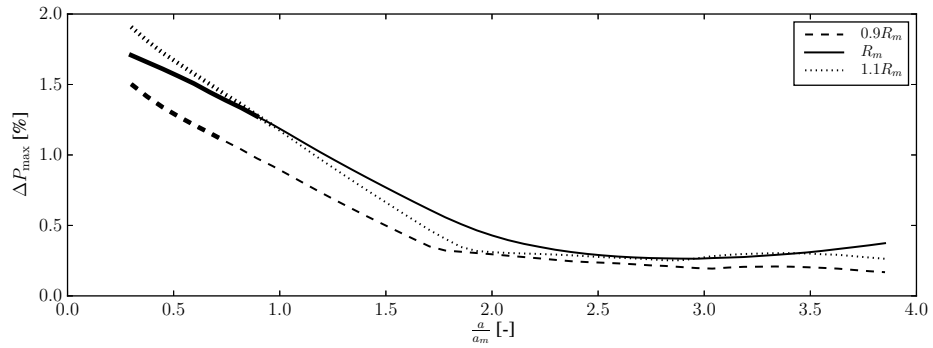


Figure 6.2: Maximum difference between the planet–moon system degree of polarization and the continuum background signal, ΔP_{max} , as a function of lunar semi–major axis, a , for varying lunar radii: $0.9R_m$ (dashed line), R_m (solid line), and $1.1R_m$ (dotted line), with R_m the size of our Moon. The lunar semi–major axis has been nondimensionalized with the semi–major axis of the Moon orbit around the planet Earth, a_m . Thickness is increased for semi–major axis values yielding umbral eclipses and diminished for antumbral eclipses.

radii $0.9R_m$, R_m and $1.1R_m$, respectively. Moreover, we observe a steeper curve slope for high a_{mb} values (where the differences between lunar radii are minimized), as the stellar disk surface hidden by the moon as observed from the planet rapidly diminishes for very distant exomoons (the projected lunar radius on the stellar disk falls linearly with increasing distance to the planet, while the shadowed area is proportional to the projected lunar radius square, yielding hidden stellar disk $\propto a_{mb}^2$).

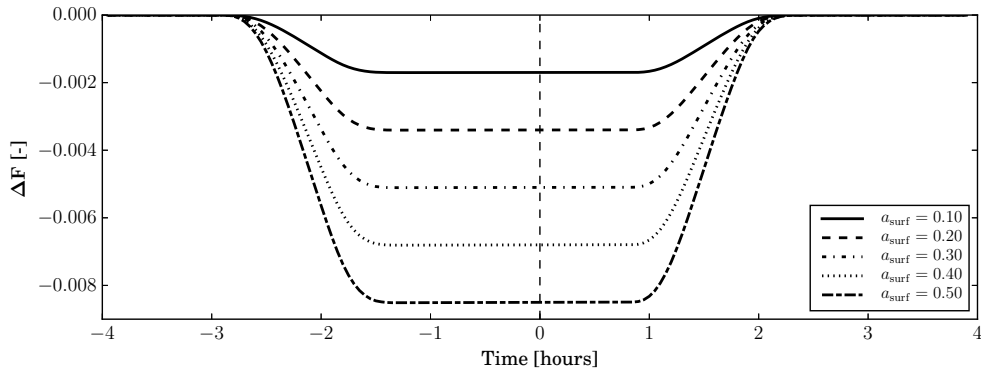
We now concentrate on the maximum change of polarization. Figure 6.2 yields a steep decrease of ΔP_{max} with small increasing a_{mb} , a result of the increasingly larger penumbral shadow cast on the planetary surface. This, as seen in Figure 6.1, keeps an nearly constant total flux drop for $0.3a_m < a_{mb} < 2.0a_m$, while the linearly polarized flux Q (concentrated along the planetary limb) drops rapidly, yielding a drop in polarization. When annular eclipses seen at the planet get sufficiently mild ($a_{mb} > 2a_m$), the homogeneity of the spread shadow yields almost no variation in ΔP_{max} . Moreover, we highlight that, contrary to what we observe in flux, the variation of polarization with a_{mb} does not depend linearly on the lunar radius. In essence, larger exomoons do not entail a larger maximum variation of degree of polarization at any a_{mb} . This conclusion is in-line with the results on lunar radius R_m obtained in Section 6.3.

The effect of varying lunar period is, thus, not limited to a variation of mutual events duration and periodicity, but also impacts the reflectance behaviour of the planet during planetary eclipses in a scale that should be taking into account when driving conclusions on the planetary surface and atmospheric properties from flux and polarization curves.

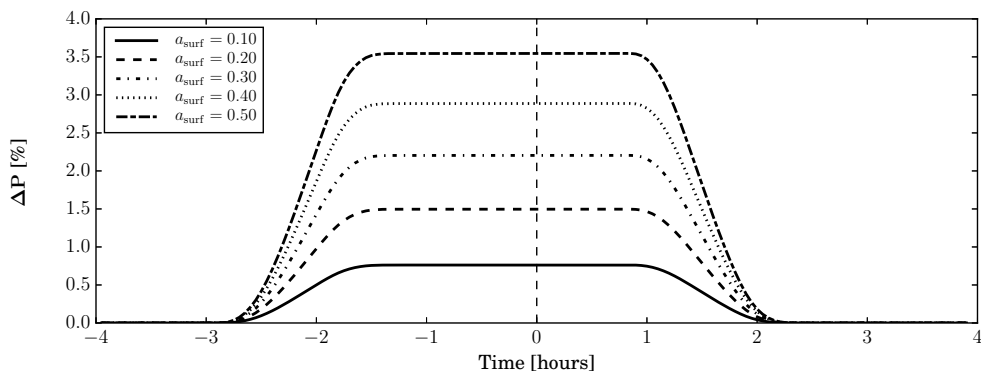
6.2. Variation with lunar albedo, a_{surf}

In this section, we evaluate the impact of lunar albedo on the unresolved planet–moon system reflected flux and degree of polarization. The results that we presented so far in this study made use of a Lambertian moon model of surface albedo $a_{\text{surf}} = 0.36$, i.e. brighter than our Moon. The impact of varying lunar albedo is here presented for the lunar eclipse and planetary eclipse events at $\alpha = 87.1^\circ, 72.5^\circ$ respectively. As complementary material, we show complete continuum phase curves, as well as the refined flux and polarization curves for mutual events at varying phase angle (both in absolute relative magnitude) in Figures C.3 – C.8 in Appendix C.

An increasingly brighter non–polarizing lunar companion yields an enhanced reflected flux by the unresolved planet–moon system (apparent unresolved system’s geometric albedo equals 0.324, 0.329, 0.334, 0.339, and 0.344 for lunar surface albedos 0.10, 0.20, 0.30, 0.40 and 0.50 respectively) which brings a decrease in polarization with $P_{\max} = 40.9\%, 40.2\%, 39.5\%, 38.8\%, 38.1\%$ for lunar surface albedos 0.10, 0.20, 0.30, 0.40, and 0.50 (see Figure C.3). Consequently, a progressively higher impact of lunar occultation events on flux and polarization is expected. The results in Figure 6.3 for a lunar eclipse (see Appendix C for results on planetary transits) endorse this affirmation. The observed drops of F and rises of P (solely driven by the drop of F) during lunar eclipses and planetary transits scale linearly with lunar albedo, reaching a 3.5% polarization rise for the lunar eclipse at $\alpha = 87.1^\circ$ in the case of a moon with albedo 0.50. In such same scenario, the drop in flux ascends to ~ 0.0083 ($\sim 2.4\%$ of system’s albedo), while this figure increases for lower phase angles, e.g. ~ 0.0225 ($\sim 6.5\%$ of system’s albedo) for the planetary transit at $\alpha = 26.9^\circ$.



(a) Flux curves during lunar eclipse, $\alpha = 87.1^\circ$

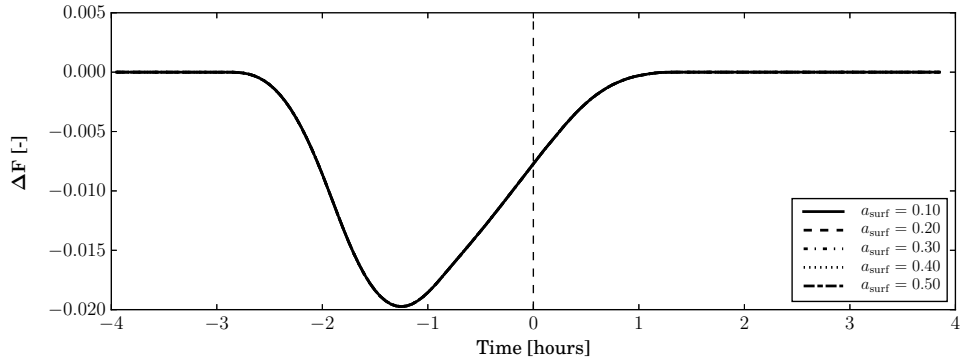


(b) Degree of polarization curves during lunar eclipse, $\alpha = 87.1^\circ$

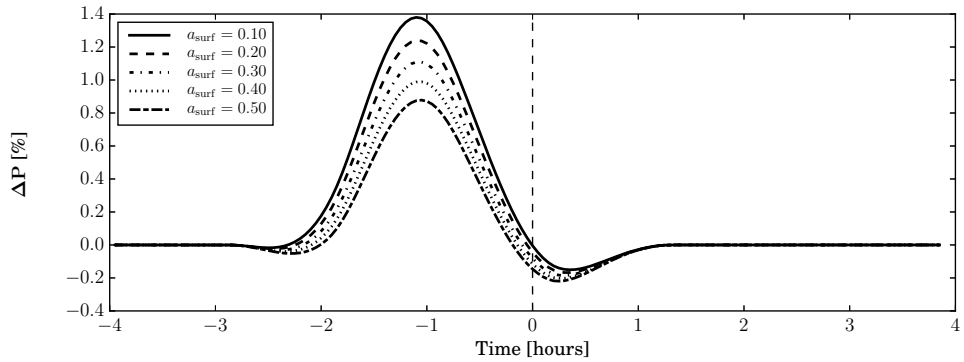
Figure 6.3: Difference between the planet–moon system reflected flux and the continuum flux signal, ΔF (a), and difference between the degree of polarization of the unresolved system and the continuum signal, ΔP (b), as a function of relative time for varying lunar surface albedo values during a lunar eclipse at phase angle $\alpha = 87.1^\circ$. Time equal to zero corresponds to the concentric alignment of the planet and moon bodies as seen from the star. Flux has been normalized so that F at $\alpha = 0^\circ$ equals the geometric albedo of the planet–moon system. The simulation time resolution is $\Delta t = 3\text{min}$.

During planetary darkening events, i.e. lunar transits and planetary eclipses, the reflected flux drop does not depend on the lunar albedo (see Figure 6.4a). However, we observe a general decline of ΔP with lunar a_{surf} (see Figure 6.4b). In fact, while the blocked polarized fluxes on the planet's surface remain equal, the total flux of the system increases with increasing lunar albedo, yielding a lower change in polarization during planetary darkening events. This behaviour is opposite to the one found in ΔP for lunar occultation events.

Therefore, Moon-like Lambertian exomoons with $a_{\text{surf}} \approx 0.10$ leave a greater trace during lunar transits and planetary eclipses, while brighter exomoons yield increasingly higher variations of ΔP (3.5% for lunar albedo 0.5) during lunar eclipses and planetary transits.



(a) Flux curves during planetary eclipse, $\alpha = 72.5^\circ$



(b) Degree of polarization curves during planetary eclipse, $\alpha = 72.5^\circ$

Figure 6.4: Difference between the planet–moon system reflected flux and the continuum flux signal, ΔF (a), and difference between the degree of polarization of the unresolved system and the continuum signal, ΔP (b), as a function of relative time for varying lunar surface albedo values during a planetary eclipse at phase angle $\alpha = 72.5^\circ$. Time equal to zero corresponds to the concentric alignment of the planet and moon bodies as seen from the star. Flux has been normalized so that F at $\alpha = 0^\circ$ equals the geometric albedo of the planet–moon system. The simulation time resolution is $\Delta t = 3\text{min}$.

6.3. Variation with lunar radius, R_m

In this section, we analyse the impact of larger exomoons in edge-on configuration on the unresolved planet–moon system reflected signal. The flux and degree of polarization phase curves obtained have been plotted in Figure 6.5 for varying values of the lunar-to-planetary radius ratio $r = R_m/R_p$, with R_m and R_p the lunar and planetary radii.

As observed in Figure 6.5a, and as follows from Equation 2.5, an increase of lunar radius yields a larger bright lunar area and, thus, a higher total reflected flux. The flux increment is maximum for small phase angles. As a consequence of the increase of lunar reflected unpolarized light, the continuum total degree of polarization is decreased with a maximum P drop at phase angle 90° – 100° , as Figure 6.5b shows. A closer look at Figure 6.5 unveils varying flux and degree of polarization amplitude peaks during mutual events at any phase angle.

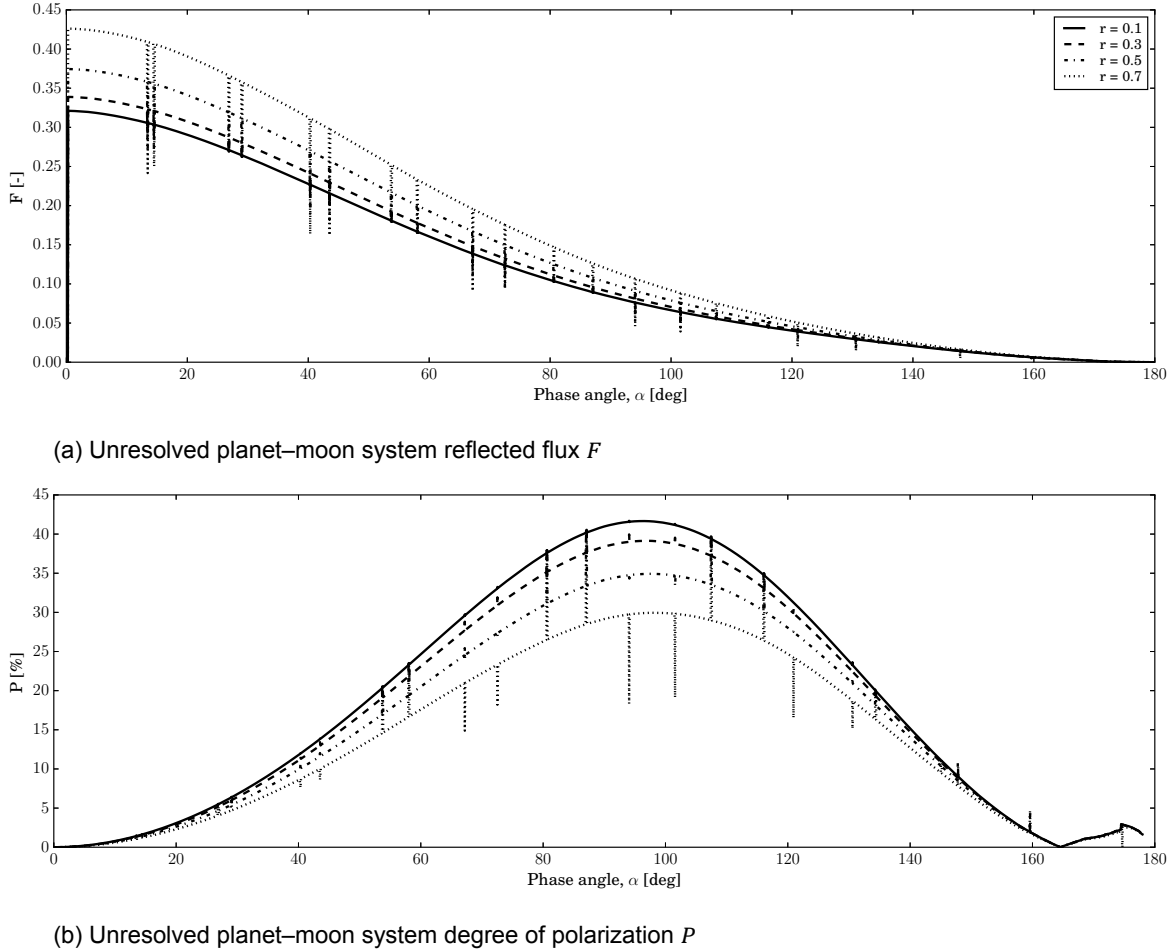


Figure 6.5: Unresolved planet–moon system reflected flux F and degree of polarization P as a function of phase angle α for varying moon-to-planet radius ratio $r = \frac{R_m}{R_p}$. Flux has been normalized so that F at $\alpha = 0^\circ$ equals the geometric albedo of the planet–moon system. The simulation time resolution is $\Delta t = 1\text{h}$.

We present below a zoom at mutual events found between phase angles 65° and 90° . A more extensive exposition of flux and degree of polarization curves and variations of flux and degree of polarization, ΔF and ΔP , during mutual events is provided in Figures C.10–C.14 in Appendix C. Firstly, we analyse the impact of varying lunar radius during planetary darkening events, i.e. lunar transits and planetary eclipses (see Figure 6.6) and then put our attention on the lunar darkening events, i.e. planetary transits and lunar eclipses (see Figure 6.10).

Planetary darkening: lunar transits and planetary eclipses

During lunar transit events, the shadow cast on the planet is proportional to the square of the lunar radius, R_m^2 . In the case of a planetary eclipse, the total shadow is wider than the transit region and progressively darkens towards the umbral cone axis. Figures 6.6a and 6.6c show increasing peak absolute magnitudes of the reflected flux F during lunar transit and planetary eclipse events (see Figures C.13 and C.14 for results on ΔF) with increasing lunar radius. For each lunar radius, the maximum flux drop strongly depends on the phase angle. In Figure 6.7 we plot the absolute value of the maximum flux variation $|\Delta F_{\max}|$ as well as the maximum relative flux variation with respect to the unresolved system's albedo, $\Delta F_{\text{alb max}}$ (see Equation 5.5).

The results displayed in Figure 6.7 show that the maximum normalized flux drop during planetary darkening events is directly proportional to the lunar area only at small lunar-to-planetary radius ratios and/or low phase angles, $|F_{\max}| \propto R_m^2$, if $r \ll 1$, $\alpha \approx 0^\circ$. Larger moons and larger phase angles display lower maximum ΔF peaks than the square law foresees. In fact, these are proportional to

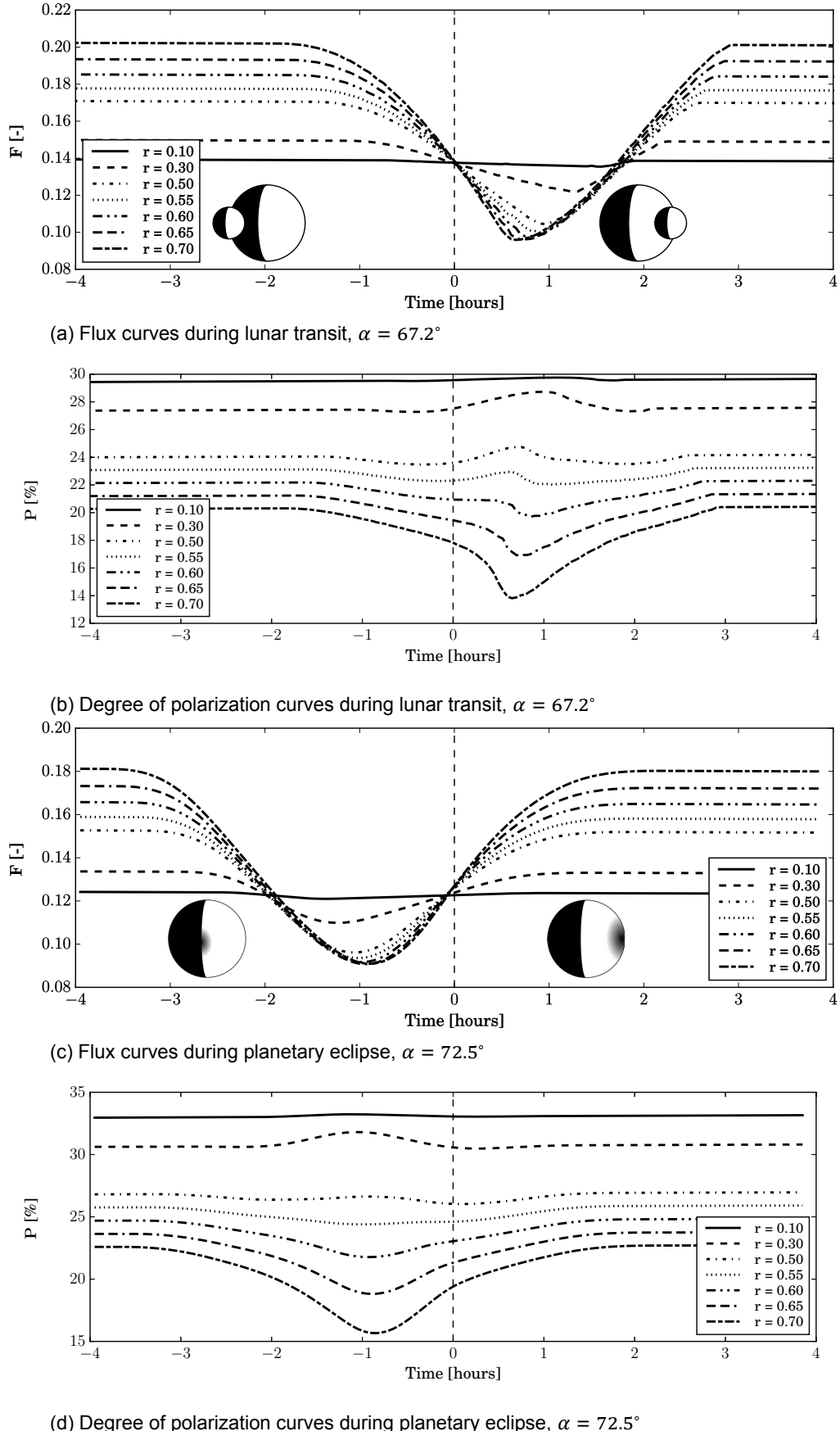


Figure 6.6: Flux and degree of polarization curves during planetary darkening events for varying lunar-to-planetary radius ratio $r = \frac{R_m}{R_p}$. The unresolved planet–moon system reflected flux, F , and degree of polarization, P , are shown for a lunar transit at $\alpha = 67.2^\circ$ (a) and (b), and a planetary eclipse at $\alpha = 72.5^\circ$ (c) and (d). Fluxes have been normalized so that F at $\alpha = 0^\circ$ equals the geometric albedo of the planet–moon system. Time equal to zero corresponds to the concentric alignment of the planet and moon bodies as seen from the star/observer in the case of eclipse/transit. The simulation time resolution is $\Delta t = 3\text{min}$.

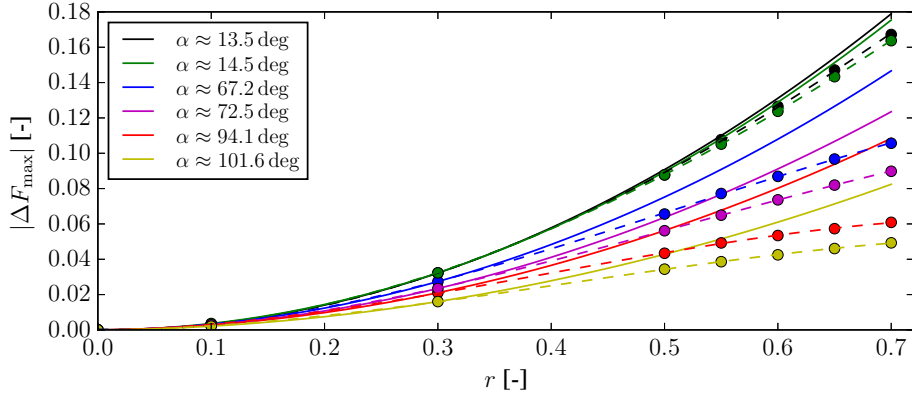


Figure 6.7: Absolute value of the maximum difference between the planet–moon system reflected flux and the continuum background flux signal, $|\Delta F_{\max}|$, as a function of moon–to–planet radius ratio $r = \frac{R_m}{R_p}$ during planetary darkening events (i.e. lunar transits and planetary eclipses) occurring at different phase angles α (circular dots). Solid lines stand for a quadratic fitting curve, while dashed lines correspond to a cubic fit through the computed data points.

the negative value of the lunar radius cubed $F_{\max} \propto (-R)^3$, if $r \gg 0$ $\alpha > 0^\circ$, as a result of the non-symmetric reflecting properties across the planetary disk. Small exomoons with $r = 0.1$ yield maximum flux variations between 0.002 – 0.0036, 0.6% – 1.1% of the system’s geometric albedo (see Figure C.9a). For a lunar size ratio similar to the Earth–Moon system, $r \approx 0.3$, the computed maximum flux drops vary between 0.016 – 0.032, 4.5% – 9.5% of the system’s geometric albedo (see Figure C.9a), for $13.5^\circ \leq \alpha \leq 101.6^\circ$. Very large moons, or binary systems, with $r \geq 0.5$ show maximum flux variations larger than 10% of the system’s albedo for $\alpha \leq 101.6^\circ$, reaching 38.3% for $r = 0.7$ and $\alpha = 13.5^\circ$. Larger r makes a higher impact on the maximum flux drop for small phase angles, while the curves in Figure 6.7 show a decreasing slope with increasing α .

Regarding the degree of polarization, Figures 6.6b and 6.6d show increasing polarization peaks for increasing r with $r \leq 0.3$ at $\alpha = 67.2^\circ$ and 72.5° , respectively. Larger moons yield a dampening of the peak in P , changing the sign of ΔP . In such case, a drop in polarization is observed for large exomoons at $\alpha = 67.2^\circ, 72.5^\circ$. In this process, the absolute value of polarization variation decreases for $0.3 < r < 0.6$, increasing again for $r \leq 0.6$. This behaviour is highly dependent on phase angle, as seen in the extra figures in Appendix C.

Figure 6.8 shows the absolute value of the maximum polarization variation $|\Delta P_{\max}|$ for a phase angle interval $13.5^\circ \leq \alpha \leq 101.6^\circ$. The $|\Delta P_{\max}|$ values obtained at small phase angles $\alpha = 13.5^\circ, 14.5^\circ$ fall

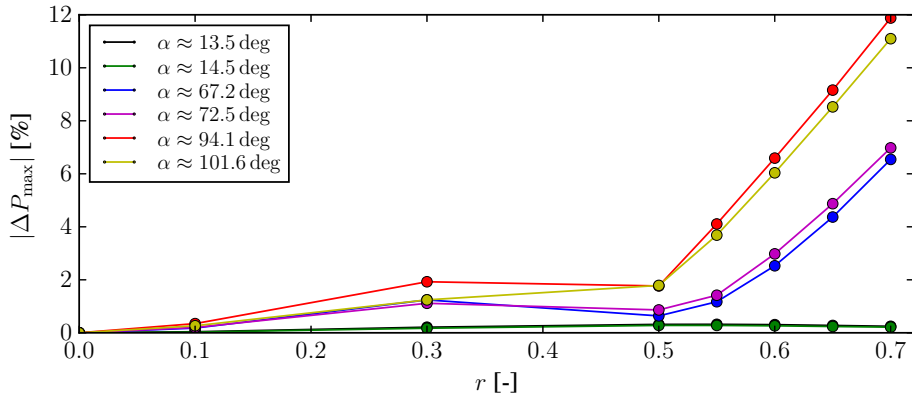


Figure 6.8: Absolute value of the maximum difference between the planet–moon system degree of polarization and the continuum background signal, $|\Delta P_{\max}|$, as a function of moon–to–planet radius ratio $r = \frac{R_m}{R_p}$ during planetary darkening events (i.e. lunar transits and planetary eclipses) occurring at different phase angles α (solid line and circular dots).

below 0.5% for any computed lunar radius. The planetary darkening events found for $\alpha \geq 67.2^\circ$ yield, in all computed cases, a non-linear dependence of $|\Delta P_{\max}|$ on r . From our results in Figure 6.8 we find that exomoons with $r = 0.3, 0.5$ yield a similar maximum variation of polarization of 1.7%-1.9% found at $\alpha = 94.1^\circ$. Larger exomoons, $0.5 < r \leq 0.7$, yield larger $|\Delta P_{\max}|$ values up to 12% for $r = 0.7$ observed at phase angle $\alpha = 94.1^\circ$). Consequently, our simulations show that larger moon companions do not directly entail a larger change in polarization during planetary darkening events, as this strongly depends on the polarization and reflection properties of the planet.

As a last remark related to the analysis of Figure 6.6, we highlight the fact that varying lunar sizes alter the starting and ending time of the computed mutual events. In fact, the ingress time during a planetary darkening event by an exomoon in edge-on configuration is increasingly delayed with decreasing lunar radius, while the opposite behaviour applies for the egress time. This yields an overall decrease of the mutual events duration with decreasing lunar radius.

Lunar darkening: planetary transits and lunar eclipses

The flux and degree of polarization curves during planetary transits and lunar eclipse events are shown in Figure 6.10 for increasing lunar radius. In the event of lunar shadowing, in contrast to planetary shadowing events, the moon gets completely occulted². The unresolved planet-moon system's reflected flux shown in Figures 6.10a and 6.10b, for planetary transits and lunar eclipses respectively, shows an increasing background flux with increasing lunar radius and a constant reflected flux for all r during full lunar darkening epochs. As already discussed in Section 5.4, flux variations during eclipses display smoother curves than transits. With the aim to analyse the maximum obtained flux variations, we plot $|\Delta F_{\max}|$ as a function of lunar radius for varying phase angles ($13.5^\circ \leq \alpha \leq 101.6^\circ$ matching the planetary transits and lunar eclipses experienced along the phase curve) in Figure 6.9.

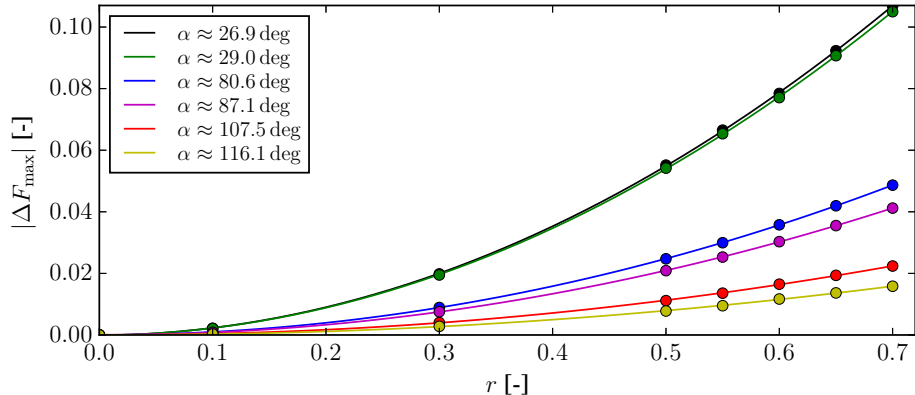


Figure 6.9: Absolute value of the maximum difference between the planet-moon system reflected flux and the continuum background flux signal, $|\Delta F_{\max}|$, as a function of moon-to-planet radius ratio $r = \frac{R_m}{R_p}$ during lunar darkening events (i.e. planetary transits and lunar eclipses) occurring at different phase angles α (circular dots). Solid lines stand for linear fitting curves through the computed data points.

The results in Figure 6.9 show that the maximum normalized flux drop during lunar occultation events is directly proportional to the radius of the moon squared, $|\Delta F_{\max}| \propto R_m^2$, with slope directly proportional to minus the phase angle, $|\Delta F_{\max}| \propto (-\alpha)$. The maximum flux figures obtained for all r values are smaller than the ones for planetary darkening events, e.g. an occulted moon of radius $r = 0.7$ yields the same maximum drop in flux ($\sim 20\%$ of system's albedo) as a moon of radius $r = 0.5$ during planetary darkening events.

As already argued in Section 5.4, the change in polarization induced during lunar darkening events is solely determined by the drop in lunar reflected flux. Therefore, the shape of the polarization results in Figures 6.10b and 6.10d for planetary transits and lunar eclipse events respectively resemble those obtained for the flux variations. In this case, increasing lunar size yields a smaller background polarization, while the complete occultation of the moon brings back the degree of polarization of the isolated

²This holds true for an edge-on lunar configuration (see Section 3.2.2)

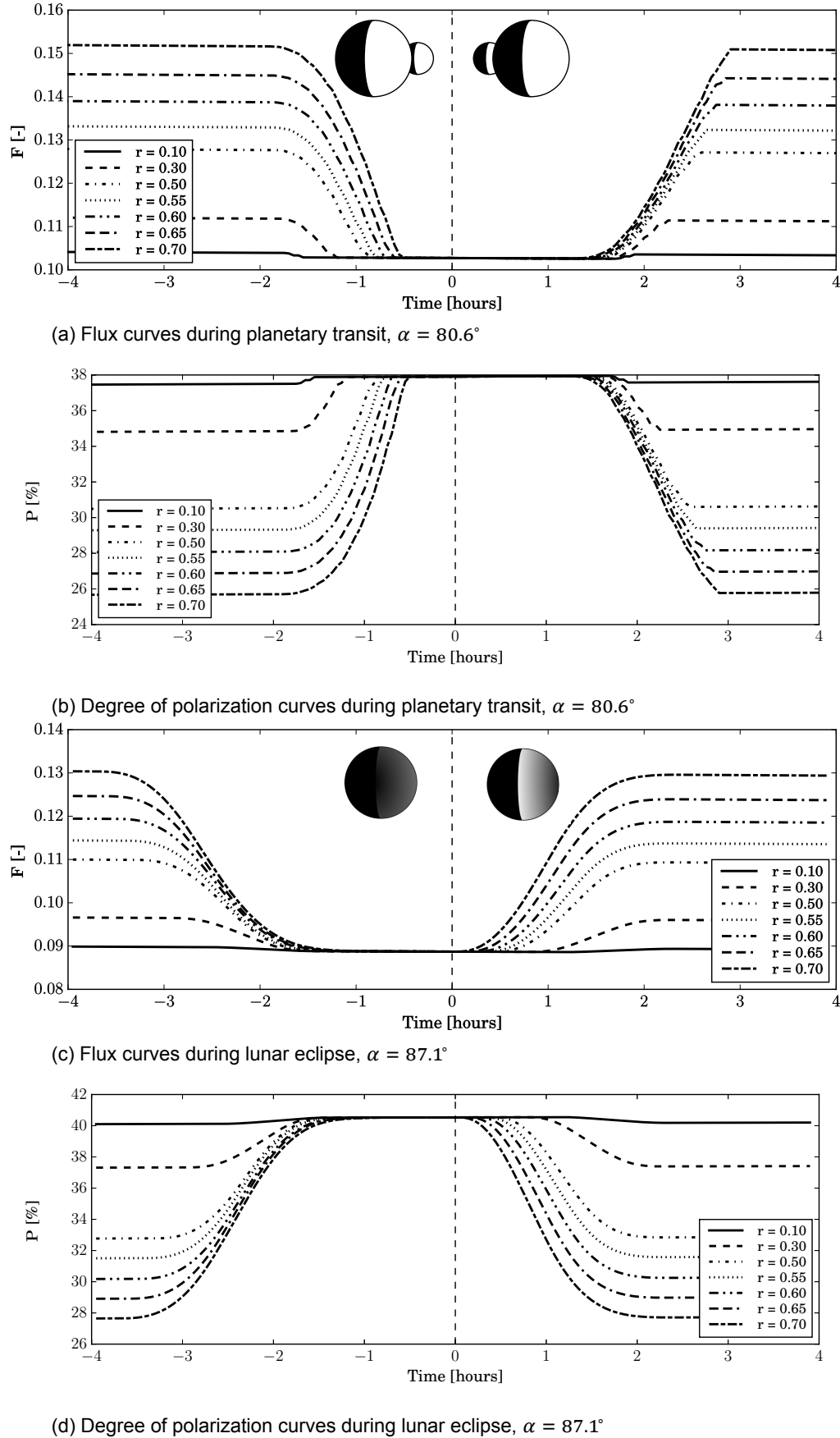


Figure 6.10: Flux and degree of polarization curves during lunar darkening events for varying lunar-to-planetary radius ratio $r = \frac{R_m}{R_p}$. The unresolved planet-moon system reflected flux, F , and degree of polarization, P , are shown for a planetary transit at $\alpha = 80.6^\circ$ (a) and (b), and a lunar eclipse at $\alpha = 87.1^\circ$ (c) and (d). Fluxes have been normalized so that F at $\alpha = 0^\circ$ equals the geometric albedo of the planet-moon system. Time equal to zero corresponds to the concentric alignment of the planet and moon bodies as seen from the star/observer in the case of eclipse/transit. The simulation time resolution is $\Delta t = 3\text{min}$.

planet. Hence, larger exomoons entail a larger increase in polarization during lunar darkening events. We show in Figure 6.11 the absolute value of the maximum polarization variation $|\Delta P_{\max}|$ for a phase angle interval $13.5^\circ \leq \alpha \leq 101.6^\circ$.

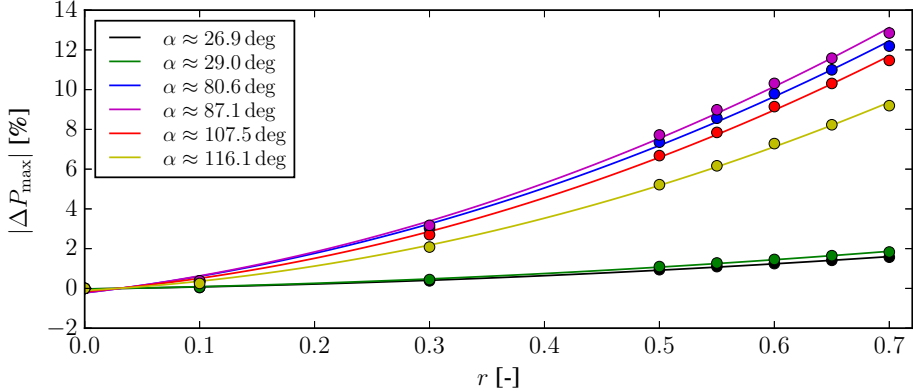


Figure 6.11: Absolute value of the maximum difference between the planet–moon system degree of polarization and the continuum background signal, $|\Delta P_{\max}|$, as a function of moon-to-planet radius ratio $r = \frac{R_m}{R_p}$ during lunar darkening events (i.e. planetary transits and lunar eclipses) occurring at different phase angles α (circular dots). Solid lines stand for linear fitting curves through the computed data points.

The results obtained in Figure 6.11 completely differ from those in Figure 6.8 for planetary darkening events. In this case, the maximum variation of degree of polarization during moon occultation events are linearly proportional to the lunar radius squared, $|\Delta P_{\max}| \propto R_m^2$. For any given r , $|\Delta P_{\max}|$ is maximum at phase angle $\alpha = 87.1^\circ$. Moreover, we find that the maximum $|\Delta P_{\max}|$ is always larger during lunar darkening events than during planetary darkening events for any r , but of the same order of magnitude (from 0% to 13% for $0.1 \leq r \leq 0.7$).

As in the case of lunar transits and planetary eclipses, the total duration of lunar darkening events slightly shrinks with decreasing lunar radius, with a total difference in the order of 1 hour between the results for $r = 0.1$ and $r = 0.7$. Moreover, the curves in Figure 6.10 show increasing ingress/egress times and decreasing total lunar occultation times for increasingly larger exomoons.

6.4. Variation with lunar eccentricity, e_m

A non-circular lunar orbit grants the moon with varying speed along its trajectory, being this maximum at the periapsis and minimum at the apoapsis. In such case, variations in the mutual events registered in reflected flux and polarization would be expected. For the simulations in this section, we employ the reference edge-on orbital geometry described in Section 3.2.2, the line of periapsis being aligned with the observer's position, and vary the value of lunar eccentricity e_m from 0 to 0.5. The results shown below correspond to the lunar transit event at phase angles $\alpha \approx 67.2^\circ, 80.6^\circ$, which are employed for illustrating the impact of e_m on flux F and degree of polarization P during mutual events. More extensive results for varying phase angle along the phase curve are provided in Figures C.15, C.16, C.17 and C.18 in Appendix C. Two major effects of e_m are discussed below: the change in periodicity of transit and eclipse events, and the timing variations during mutual events.

Change in periodicity of events

The results shown in Chapter 5 assume a perfectly circular lunar orbit and, consequently, the transits and eclipses are regularly repeated with a constant periodicity. In general, the periodicity of transit and eclipse events strongly depend on first instance on the lunar eccentricity and, in second instance, on the orientation of the apse line with respect to the observer's line of sight. Figures 6.12a and 6.12b show two consecutive mutual events (lunar transit at $\alpha \approx 67.2^\circ$ and posterior planetary eclipse, and planetary transit at $\alpha \approx 80.6^\circ$ and posterior lunar eclipse, respectively) for varying lunar eccentricity. We first fix our attention on the time span between events.

We observe in Figure 6.12a that the time between lunar transit and planetary eclipse increases with

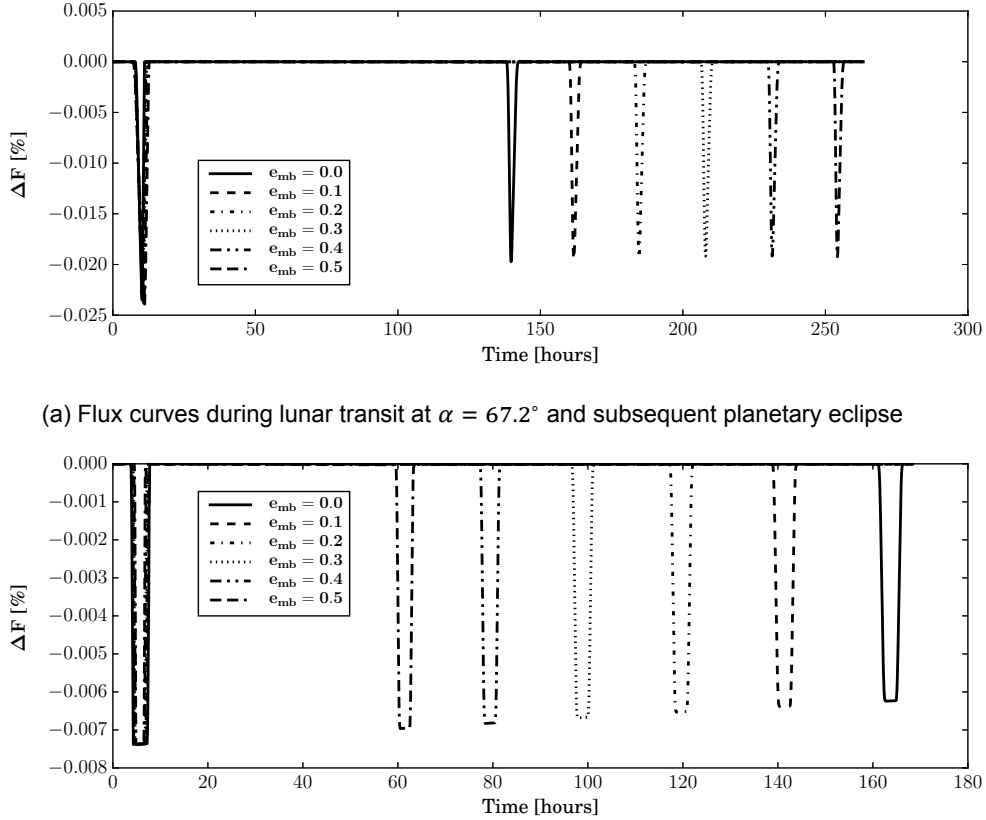
(a) Flux curves during lunar transit at $\alpha = 67.2^\circ$ and subsequent planetary eclipse(b) Flux curves during planetary transit $\alpha = 80.6^\circ$ and subsequent lunar eclipse

Figure 6.12: Difference between the planet–moon system reflected flux and the continuum background flux signal, ΔF , during the lunar transit at $\alpha = 67.2^\circ$ and subsequent planetary eclipse (a) and the planetary transit at $\alpha = 80.6^\circ$ and subsequent lunar eclipse(b) as a function of relative time for increasing lunar eccentricity. Fluxes have been normalized so that F at $\alpha = 0^\circ$ equals the geometric albedo of the planet–moon system. The simulation time resolution is $\Delta t = 3\text{min}$.

increasing lunar orbit eccentricity (doubling its value from $e_m = 0.0$ to $e_m = 0.5$), while Figure 6.12b shows decreasing time spans between planetary transits and lunar eclipses with increasing lunar orbit eccentricity (reducing its value to one third from $e_m = 0$ to $e_m = 0.5$). This only holds true for the selected orbital configuration as lunar transits occur at the apoapsis of the lunar orbit, where the orbital speed is minimum (and decreases with e_m), and the moon needs a longer time to move forward on its orbit until reaching the star–moon–planet alignment required for a planetary eclipse. Alongside this, planetary transits occur at the periapsis, where the moon has maximum orbital speed (increasing with e_m) and need less time to reach the lunar eclipse star–planet–moon alignment for higher eccentricity values. If the lunar line of apsides were rotated 180° on the lunar plane, the observed effect would have been the opposite.

A more generic scenario is sketched in Figure 6.13 where the lunar apse line is assumed to be randomly oriented with respect to the observer. In such case, the resulting time gap between successive mutual events strongly depends on the relative angles between the directions towards the observer, the star, and the apse line³. Also, the periodicity between successive transit events is partially broken for $e_m \neq 0$. As Figure 6.13a shows, the observer's line of sight splits the lunar orbit into two differentiated regions of different area (white and grey) which, according to the second law of Kepler, are swept in a different period of time. Again, this depends on both e_m and the orientation of the apse line. In such case, the independent lunar and planetary transit events would still occur every lunar period, while it is the time gap between these two events which would be altered. In the case of the eclipses, the same argumentation applies, with the added factor of a varying planet–star vector direction with respect to the lunar apse line as the moon orbits the planet. This issue eradicates any type of periodicity between

³Assuming edge-on lunar orbit.

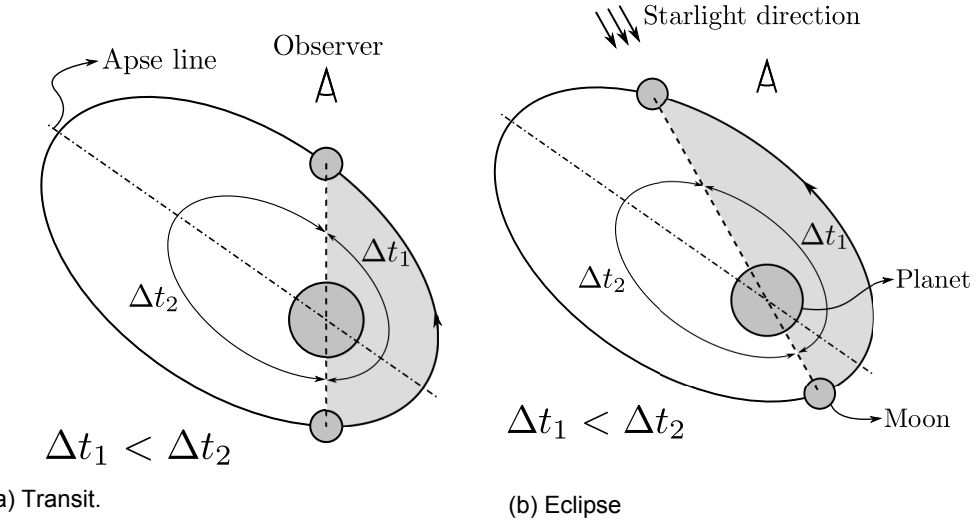


Figure 6.13: Generic edge-on eccentric lunar orbit configuration around the planet. The figures show mutual event snapshots for both a transit (a) and eclipse (b) scenarios. In both cases, the time between successive mutual events varies as both the direction towards the observer and the incident starlight rays split the orbit in two asymmetric parts which are swept in different periods of time.

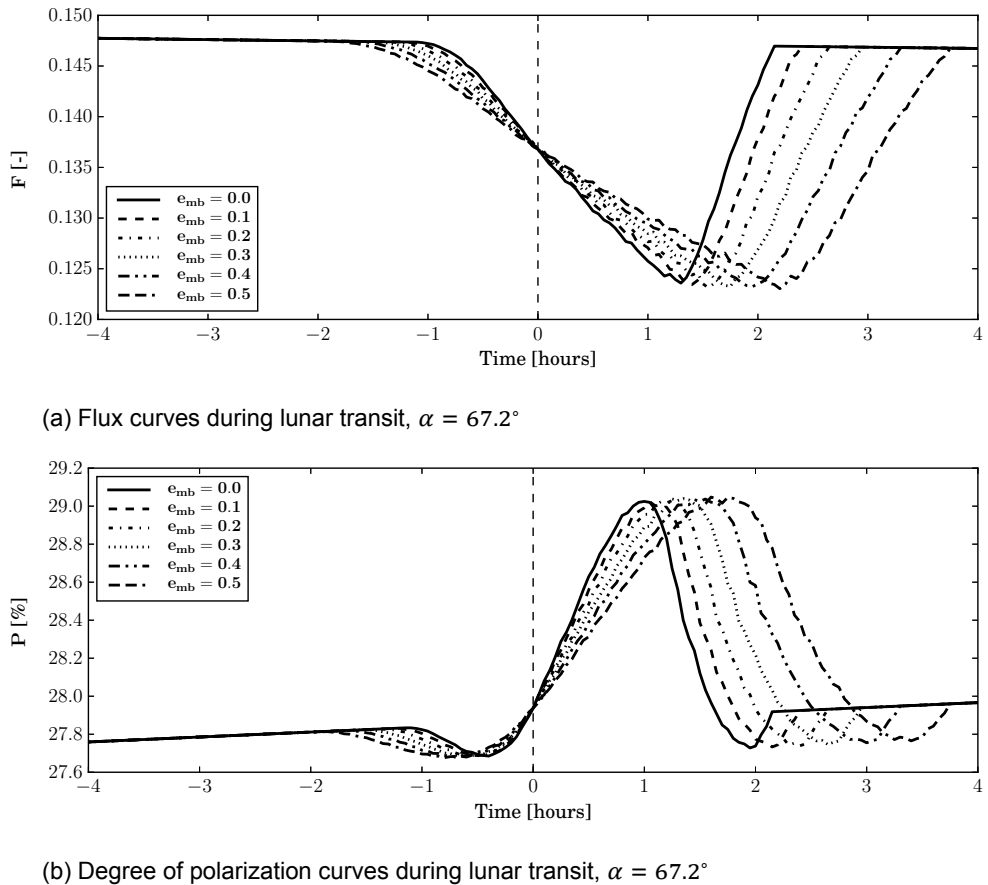


Figure 6.14: Unresolved planet–moon system reflected flux, F , (a) and degree of polarization curves, P , (b) during lunar transit at $\alpha = 67.2^\circ$ for varying lunar eccentricity e_{mb} . Fluxes have been normalized so that F at $\alpha = 0^\circ$ equals the geometric albedo of the planet–moon system. Time equal to zero corresponds to the concentric alignment of the planet and moon bodies as seen from the observer. The simulation time resolution is $\Delta t = 3\text{min}$.

eclipse events for eccentricity values $e_m \neq 0$. As a consequence of the loss of periodicity with lunar eccentricity, non-circular orbiting moons are expected to be harder to detect via frequency analyses (see Section 5.5.3), even though a more detailed investigation is required to be carried out in this direction.

Mutual events duration variations

As a result of the varying lunar orbital speed with time, the registered mutual events may speed up or down compared to the results obtained for circular orbits, depending on the lunar position along its orbit. While lunar and planetary transits span the same time in circular orbits, this does not hold true for eccentric orbits as shown in Figure 6.14. In our simulation, the duration of lunar transits (apoapsis) increase with e_m , while the duration of planetary transits (periapses) is reduced, with maximum time oscillations in the order of 2–2.5 hours for $e_m = 0.5$ compared to the results for $e_m = 0$. Again, we point out that this phenomenon is driven by the actual lunar orbital speed during the mutual event, so that accurate measurement of timing variations between events could yield a good estimation of the apse line orientation and lunar orbital eccentricity.

6.5. Variation with lunar inclination, i_m

As defined in Section 3.2.2, lunar companions orbiting in edge-on configuration are characterized by an orbital inclination of 0° ⁴. Due to the large distance between the planet and the moon, even small inclination angles may break the alignment required for transits and eclipses to happen. In the worst case (see Figure 6.15), neglecting the eccentricity of the lunar orbit and assuming a parent planet at 90° inclination angle, the maximum inclination allowed for lunar and planetary transits to exist follows from:

$$a_m \sin i_m < R_p + R_m, \quad (6.1)$$

where a_m is the lunar semi-major axis and R_p is the planetary radius.

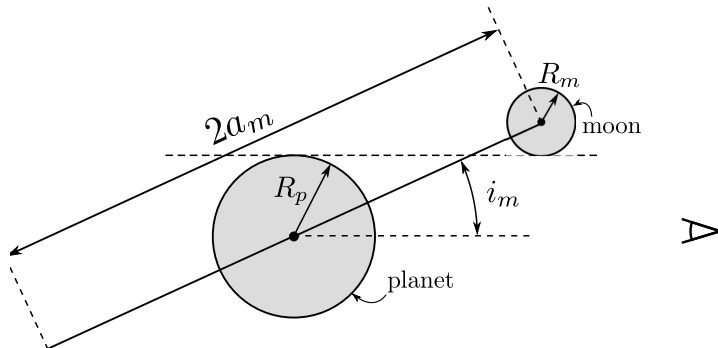


Figure 6.15: Sketch of the maximum lunar inclination for transits occurrence, assuming an edge-on planet and circular lunar orbit. Parameters are a_m for the lunar orbital radius, i_m for the lunar inclination, R_m for the lunar radius, and R_p for the planetary radius.

As seen above, the existence of transit events is subjected to the inclination of the planetary orbit. In contrast, this is not the case of eclipses, which only depend on the lunar orbit inclination. Again, neglecting the lunar orbit eccentricity, an approximated maximum value for the lunar inclination for lunar eclipses to occur follows from:

$$a_m \sin i_m < d \sin \Omega, \quad (6.2)$$

with Ω the semiaperture of the umbral cone and d , see Figure 6.16, equal to:

$$d = \sqrt{a_m^2 + \left(\frac{R_p}{R_s + R_p}\right)^2 a_p^2 + 2a_m a_p \left(\frac{R_p}{R_s + R_p}\right) \cos i}. \quad (6.3)$$

⁴Lunar orbit inclination is defined with respect to the planet orbital plane (see Section 3.2.2).

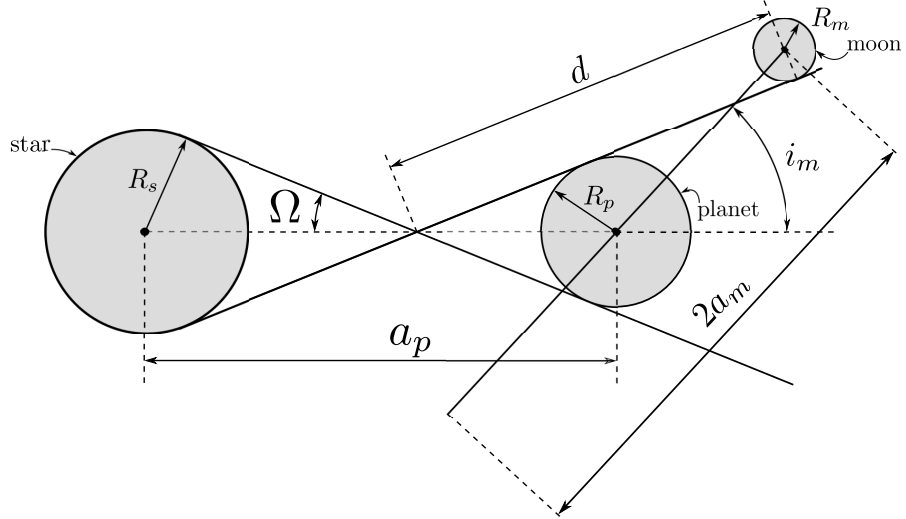


Figure 6.16: Sketch of the maximum lunar inclination for lunar eclipses occurrence, assuming an edge-on planet and circular lunar orbit. Parameters are a_m for the lunar orbital radius, a_p for the planetary semi-major axis, i_m for the lunar inclination, R_m for the lunar radius, R_p for the planetary radius, R_s for the stellar radius, and Ω for the semi-aperture of the penumbral cone.

After some mathematical elaboration, the lunar orbital inclination angle is bounded by Ω , the planetary and stellar radii, R_p and R_s , and the semi-major axis of the lunar and planetary orbits, a_m and a_p as:

$$\cos i_m > \sin^2 \Omega \left(\sqrt{\hat{r}^2 + \frac{1}{\sin^4 \Omega}} - \frac{(1 + \hat{r}^2)}{\sin^2 \Omega} - \hat{r} \right), \quad (6.4)$$

where \hat{r} is defined as:

$$\hat{r} = \frac{R_p + R_m}{R_p + R_s} \frac{a_p}{a_m}. \quad (6.5)$$

In the Earth–Moon like system employed here, Equations 6.1 and 6.4 yield a maximum inclination angle of around 1.21° and 1.48° for the existence of transits (assuming a edge-on parent exoplanet) and eclipses, respectively. The effect of orbital inclination on transits is widely known for exoplanet stellar transit photometry, which makes use of the transit impact parameter b . The impact parameter measures the actual latitude of the transiting trajectory as observed in Figure 6.17a and is here defined as:

$$b = \frac{a_{mp} \sin i_m}{R_p + R_m}, \quad (6.6)$$

where it is assumed a lunar circular orbit. The size of the moon is taken into account in Equation 6.6.

Thus, as follows from Equations 6.6 and 6.1, transits are only possible for b values ranging from 0 to 1. Figure 6.18 shows the reflected flux and degree of polarization curves during lunar transits with varying impact parameter. When looking at the flux curves obtained at zero phase angle (see Figure 6.18a), the results resemble those obtained for stellar transits. In fact, the planet reflected flux at phase angle zero is similarly distributed as the emitted flux distribution on a star, taking into account the limb darkening effect along the disk. Consequently, the plotted curves show a reduction of maximum darkening peak and duration of the event with increasing impact parameter. We should also highlight the change in slope present in curves with $b < 0.7$, which stand for the moment of full lunar ingress on the planetary disk. For the results shown with $b \leq 0.7$ the moon does not completely penetrates into the planetary disk. Besides the flux, Figure 6.18b shows null degree of polarization at zero phase angle. Again, one observes differences in the ingress and egress times of the moon on the planetary disk reflected on a different total duration of the event. The symmetry conditions of fluxes F , Q and

U yield a null change in degree of polarization at the middle of the event for $b = 0$, when the moon is right at the centre of the planetary disk. As b increases, the moon transits further away from the planetary centre, increasing the asymmetry at such middle point of the event. It is highlighted that even for moons transiting far away from the planetary equator, the peak variation in degree of polarization does not drop until impact parameters larger than $b = 0.7$.

However, this conclusions only hold for zero phase angles, which are only interesting from a theoretical point of view, but are not expected to be observed by astronomers. A more realistic scenario is brought by Figures 6.18c and 6.18d, which present the flux and degree of polarization curves during a lunar transit at phase angle $\alpha \approx 90^\circ$, when only half the planetary disk is illuminated. The conclusions on these figures follow logically from the conclusions drawn for zero phase angle. Basically, Figure 6.18c shows a reduction of flux peak with increasing impact parameter. The planetary reflected flux peak is concentrated along the substellar point (along the planetary equator) and the planetary limb. Consequently, the flux drop peak is delayed in time with decreasing impact parameters, as the moon takes longer times to reach the planetary egress point. Moreover, the highest flux drop is reached for $b = 0$, as the moon blocks the higher flux reflectance regions along the planetary disk. Regarding the degree of polarization of the reflected light at phase angle $\alpha \approx 90^\circ$, the curve for $b = 0$ matches the results obtained in Section 5.4. Increasing impact parameters yield two opposed effects. On the one hand, as follows from Figure 5.2b, a blockage of the planetary disk at a certain distance from the equator given by b yields a debalance of the linearly polarized flux U along the disk that yields an increased U planetary integrated flux in absolute value. On the other hand, given the distribution of linearly polarized flux Q along the planetary disk (parallel to the planetary limb), such blockage entails

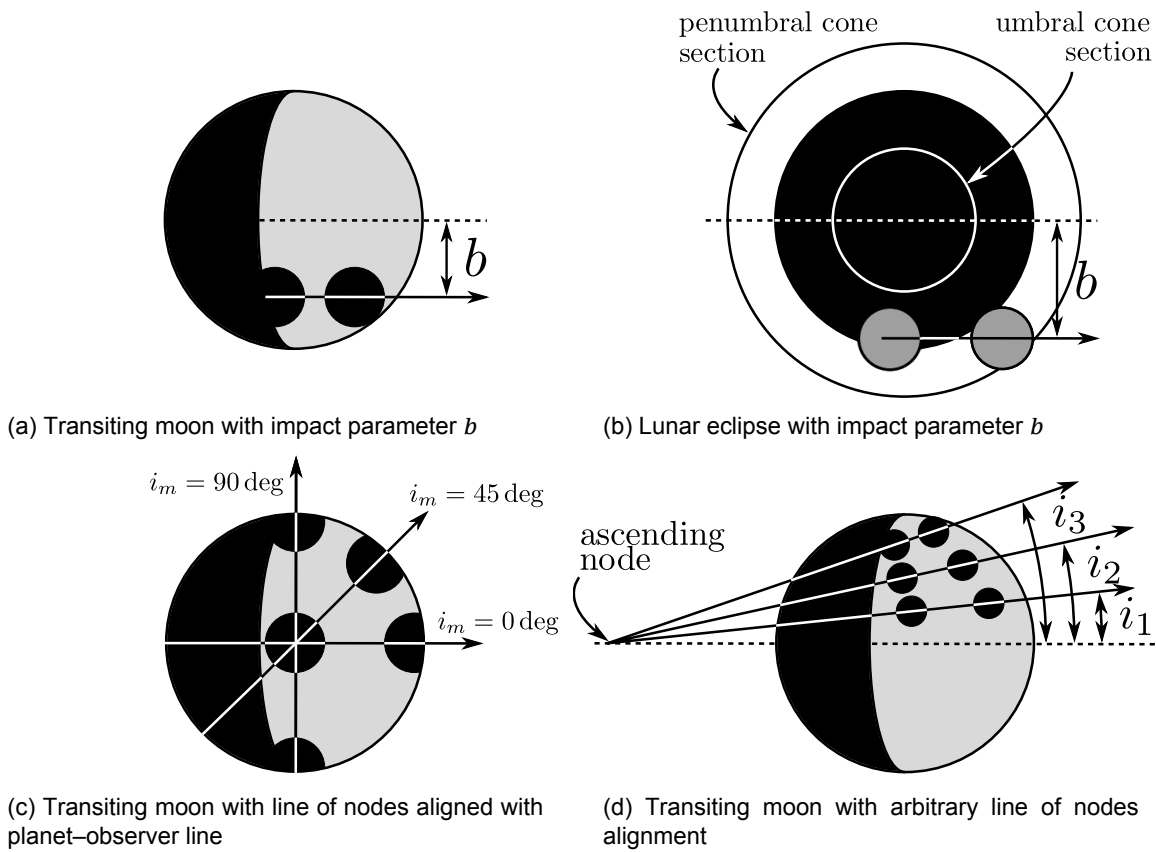


Figure 6.17: Sketch of various transit and eclipse scenarios with varying lunar impact parameter, inclination, and line of nodes orientation: (a) blockage of planetary reflected light by transiting moon at impact parameter b , (b) moon travelling through the eclipse shadow cone cast by the planet at impact parameter b (penumbral and umbral cone sections are shown at the lunar distance), (c) transiting moon at varying orbital inclinations with line of nodes aligned with planet–observer line, and (d) transiting moon at varying orbital inclinations with an arbitrary line of nodes alignment. Figures (a), (b) and (c) correspond to the planetary disk as seen by the observer. Figure (b) corresponds to a snapshot taken from the eclipse shadow cone axis. The lunar motion in front of the planet is indicated with an arrow.

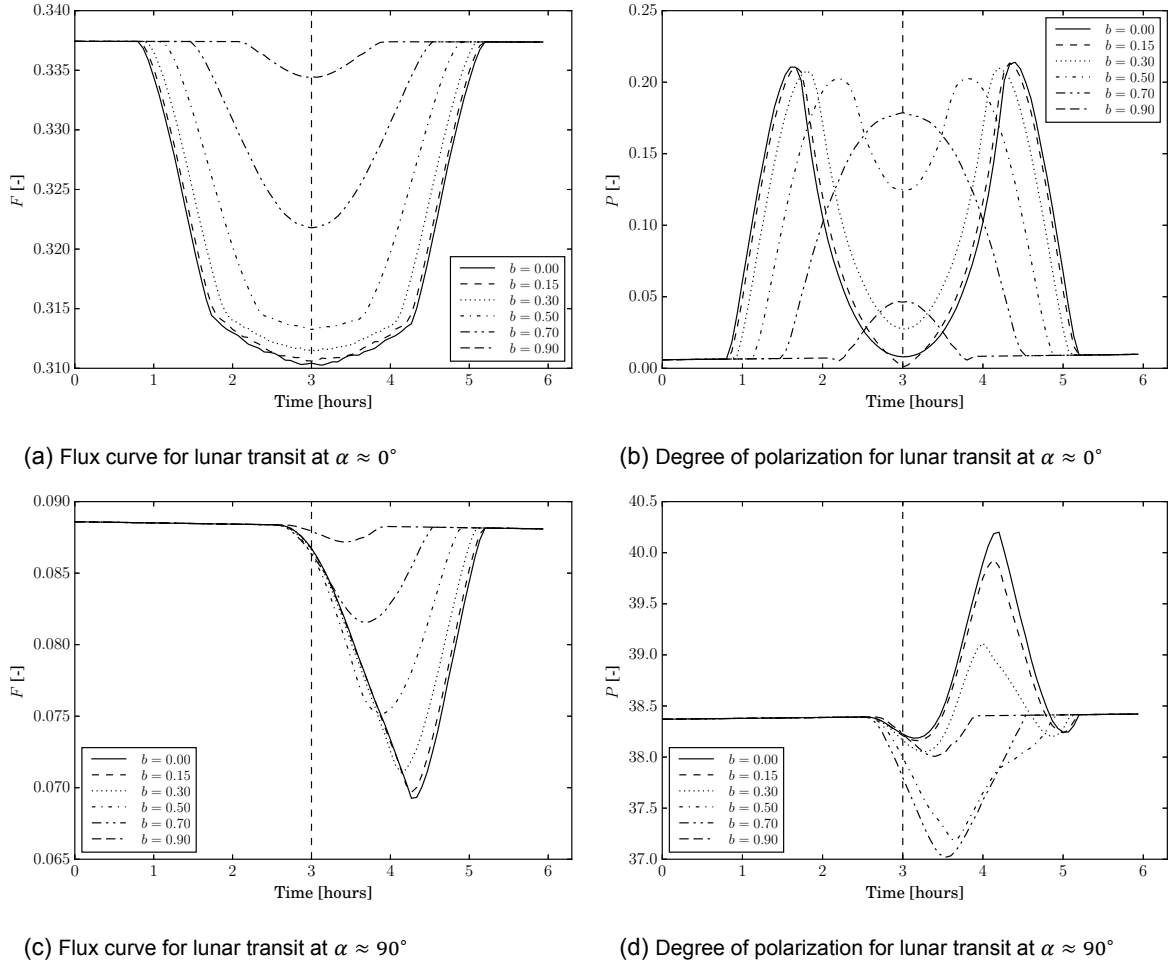


Figure 6.18: Unresolved planet–moon system reflected flux, F , and degree of polarization curves, P , during lunar transit at $\alpha = 0^\circ$ (a) (b), and lunar transit at $\alpha = 90^\circ$ (c) (d), as a function of relative time for varying lunar impact parameter b . Fluxes have been normalized so that F at $\alpha = 0^\circ$ equals the geometric albedo of the planet–moon system. Time equals 3 hours corresponds to the concentric alignment of the planet and moon bodies as seen from the observer. The simulation time resolution is $\Delta t = 3\text{min}$.

a fast decrease of the integrated absolute value of Q that overcomes the variation of U . As a consequence of these factors and the particular distribution of total flux F along the planetary disk (parallel to the terminator), the degree of polarization drops with increasing impact parameters, gradually going from taking positive ΔP values towards only taking negative ones. From the results provided in Figure 6.18d it can be concluded that a higher variation in degree of polarization imply a lunar transit closer to the planet equator ($\Delta P \approx 1.85\%$ for $b = 0$ and $\Delta P \approx -1.4\%$ for $b = 0.9$), while the amplitude of ΔP is not proportional with b ($|\Delta P| \approx 1.85\%$ for $b = 0.0$, $|\Delta P| \approx 1\%$ for $b = 0.3$, and $|\Delta P| \approx 1.1\%$ for $b = 0.7$).

As exemplified by Figures 6.15 and 6.16 and quantified by Equations 6.1 and 6.2, eclipses may occur at impact parameter values larger than 1. As observed in Figure 6.17b, depending on the impact parameter and the eclipse cones sections at the lunar distance, a moon eclipsed by its planet could travel through the umbra or penumbra region of the shadow. Parallel to the results shown for lunar transits, Figure 6.19 presents the results obtained for lunar eclipses with increasing impact parameter. The system's reflected flux variation at phase angles $\alpha \approx 0^\circ$ and $\alpha \approx 90^\circ$ shown in Figures 6.19a and 6.19c display similar behaviours. Curves with $b < 0.7$ display a flat region standing for the time the moon transits through the umbra shadow region. During these time epochs the moon is completely darkened and the observed flux comprises solely of the contribution from the planet. Curves with $b \geq 0.7$ correspond to moons passing further away from the star–planet axis for increasing impact parameter. The eclipse intensity drops as the moon goes through outer layers of the penumbral cone, so that the drop in reflected flux vanishes for increasing b values.

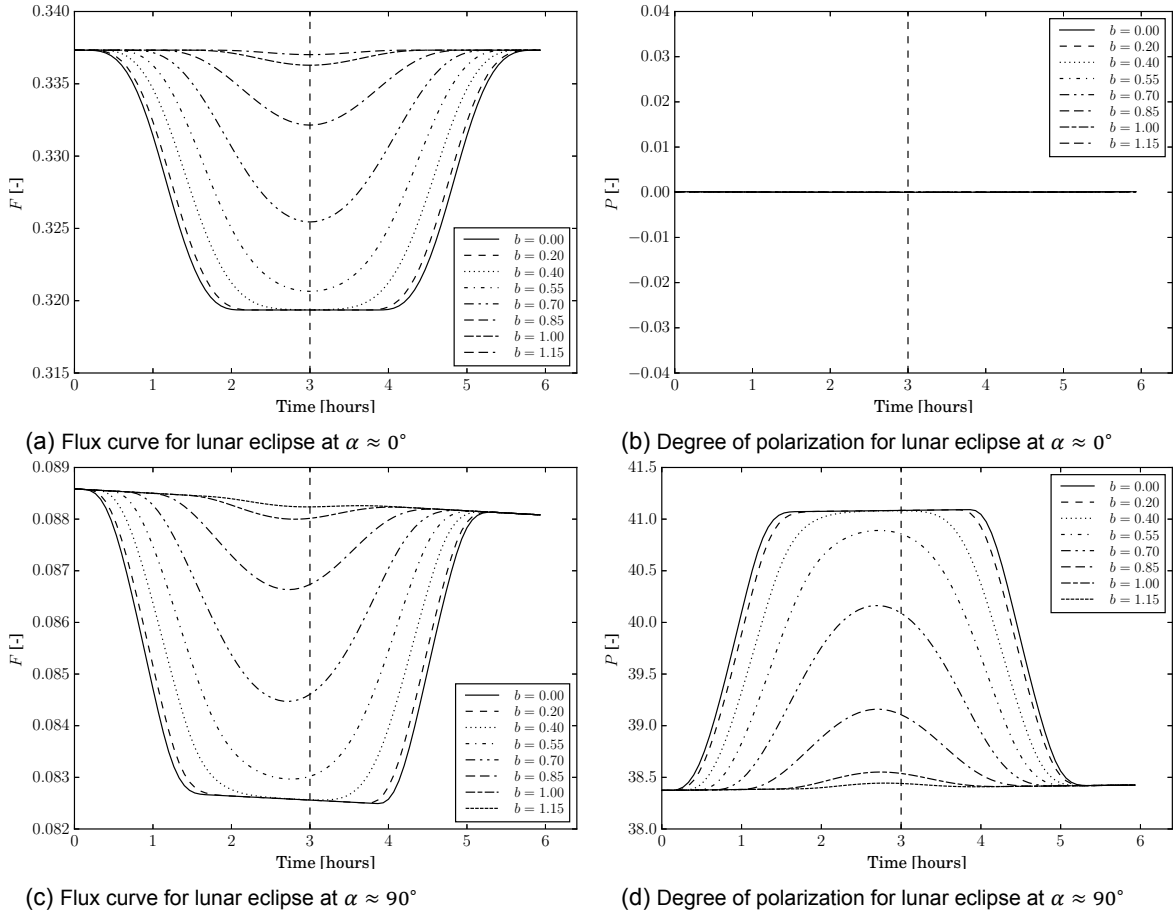


Figure 6.19: Unresolved planet–moon system reflected flux, F , and degree of polarization curves, P , during lunar eclipse at $\alpha = 0^\circ$ (a) (b), and lunar eclipse at $\alpha = 90^\circ$ (c) (d), as a function of relative time for varying lunar impact parameter b . Fluxes have been normalized so that F at $\alpha = 0^\circ$ equals the geometric albedo of the planet–moon system. Time equals 3 hours corresponds to the concentric alignment of the planet and moon bodies as seen from the star. The simulation time resolution is $\Delta t = 3\text{min}$.

Only two fundamental differences are observed between Figures 6.19a and 6.19c. Firstly, the baseline flux at $\alpha \approx 90^\circ$ has a more negative slope, which follows from the steeper variation of reflected flux with phase angle around $\alpha \approx 90^\circ$ compared to $\alpha \approx 0^\circ$. Moreover, Figure 6.19c shows a slight asymmetry and a misalignment with respect to the expected centre of the event (dashed line), due to the phase angle at which the moon is observed. In this case, an increasing observed lunar night area yields a hasten of the conclusion time of the observed eclipse (starting time at the opposite side of the lunar orbit).

If we put our attention on the results obtained for the degree of polarization, we observe that Figure 6.19b shows null degree of polarization for all impact parameter values at zero phase angle, as the net linearly polarized fluxes Q and U reflected by the planet and moon are null (see Figure 5.4). This is not the case at $\alpha \approx 90^\circ$ (see Figure 6.19d). In fact, the increase on degree of polarization at $\alpha \approx 90^\circ$ follows the same rationale as exposed in Section 5.4, this being solely determined by the drop in lunar reflected flux. The same conclusions as for Figure 6.19c apply.

The results shown so far in this section assumed a worst case scenario in which the lunar line of nodes is observed perpendicular to the observer line of sight. In practice, this is a too strict constraint on the existence of mutual events, as the impact of inclination is strongly dependent on the position of the lunar line of nodes. For instance, if we were observing through the line of nodes of the moon (as in our Earth–Moon model), transits would be recorded for any orbital inclination. This scenario is sketched in Figure 6.17c for inclination angles 0° , 45° and 90° . The simulation results for these scenarios are shown in Figure 6.20, which presents the flux and degree of polarization curves for mutual events at phase angles $\alpha = 67.2^\circ$, 80.6° . The results obtained at different phase angles have been plotted in

Figure C.19 in Appendix C.

Figures 6.20a and 6.20b show the variation in flux and degree of polarization during lunar transits at phase angle $\alpha \approx 67.2^\circ$. Given the spherically symmetric surface and atmospheric structures granted to the planet and moon bodies, both display horizontally symmetric pixel distributions of linearly polarized fluxes Q and U , as well as total flux F (see Figure 5.2). Thus, a moon orbiting at 90° inclination, $i_m = 90^\circ$, yields a symmetric variation of flux and degree of polarization during mutual events. This symmetry is broken for decreasing inclination angles, while the results for $i_m = 0.0^\circ$ match those shown in Section 5.4.2. As also observed in Figure C.19, different inclination angles imply a different shape for the variation in degree of polarization. In fact, as observed in the case of varying the lunar radius, different lunar trajectories darken different pixels along the planet. As polarized light is mainly originated along the planetary limb, a moon transiting with $i_m = 90^\circ$ will immediately block part of such polarized flux, yielding a decrease in degree of polarization, instead of the peak found for $i = 0^\circ$. For $i_m = 45^\circ$ the curves show an intermediate behaviour. In the case of lunar transits, the light blocking effect of small moons orbiting at $i_m = 90^\circ$ vanishes for phase angles larger than 90° , as the moon will transit the night region of the planet (see Figure C.19).

During planetary transits, the impact of lunar inclination is not as noticeable, especially for low phase angles. Variations in flux and degree of polarization during planetary transits have been plotted in Figures 6.20c and 6.20d. As the reader may observe, at high phase angles we appreciate an asymmetric behaviour of ΔF and ΔP for decreasing inclination angle values.

As a last remark on Figure 6.20, we point out that the curves shown for inclination values of 0° , 45° and 90° coincide at the central point where, in all cases, the bodies are perfectly aligned (the moon

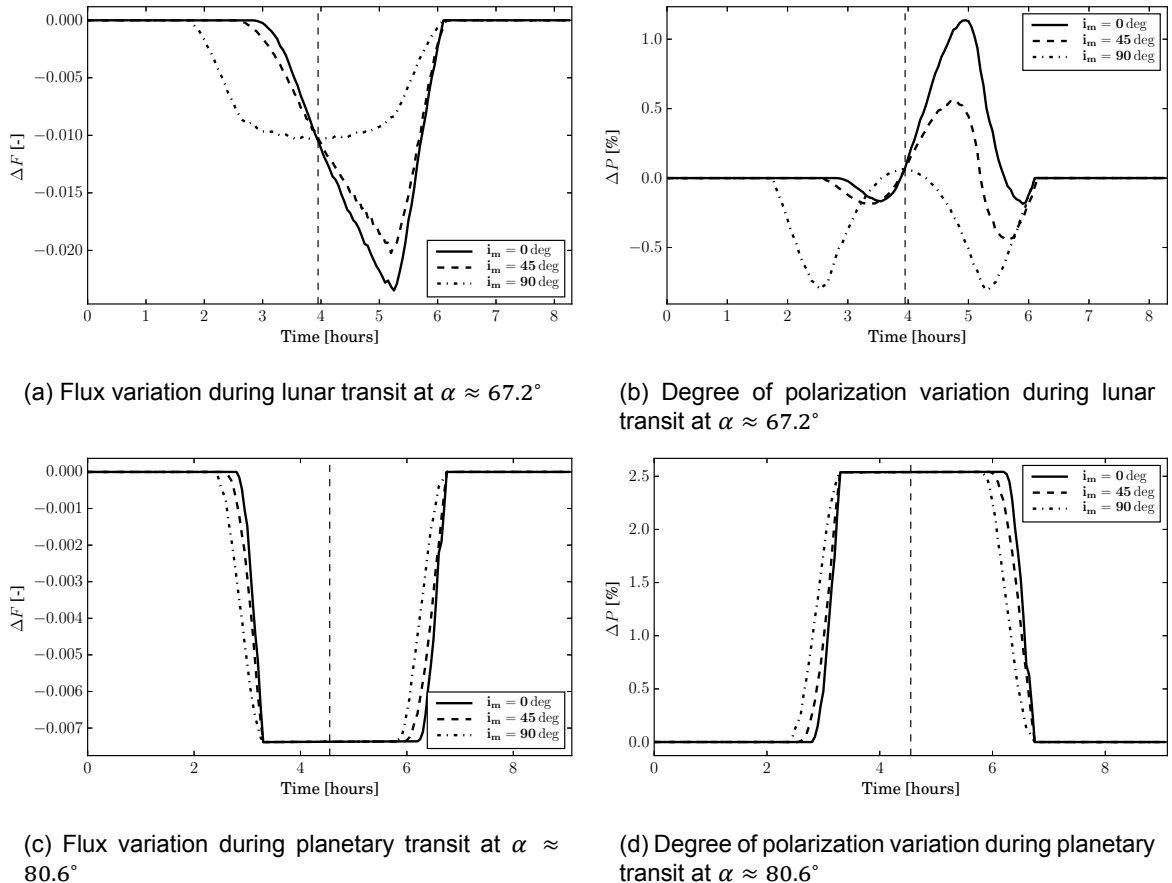


Figure 6.20: Difference between the planet–moon system reflected flux and the continuum background flux signal, ΔF , and difference between the unresolved degree of polarization and the background signal, ΔP , as a function of relative time during a lunar transit at phase angle $\alpha = 67.2^\circ$ and a planetary transit at phase angle $\alpha = 80.6^\circ$, for varying lunar orbital inclination. For this simulation, the lunar line of nodes is set to match the planet–observer direction. Fluxes have been normalized so that F at $\alpha = 0^\circ$ equals the geometric albedo of the planet–moon system. The simulation time resolution is $\Delta t = 3\text{min}$.

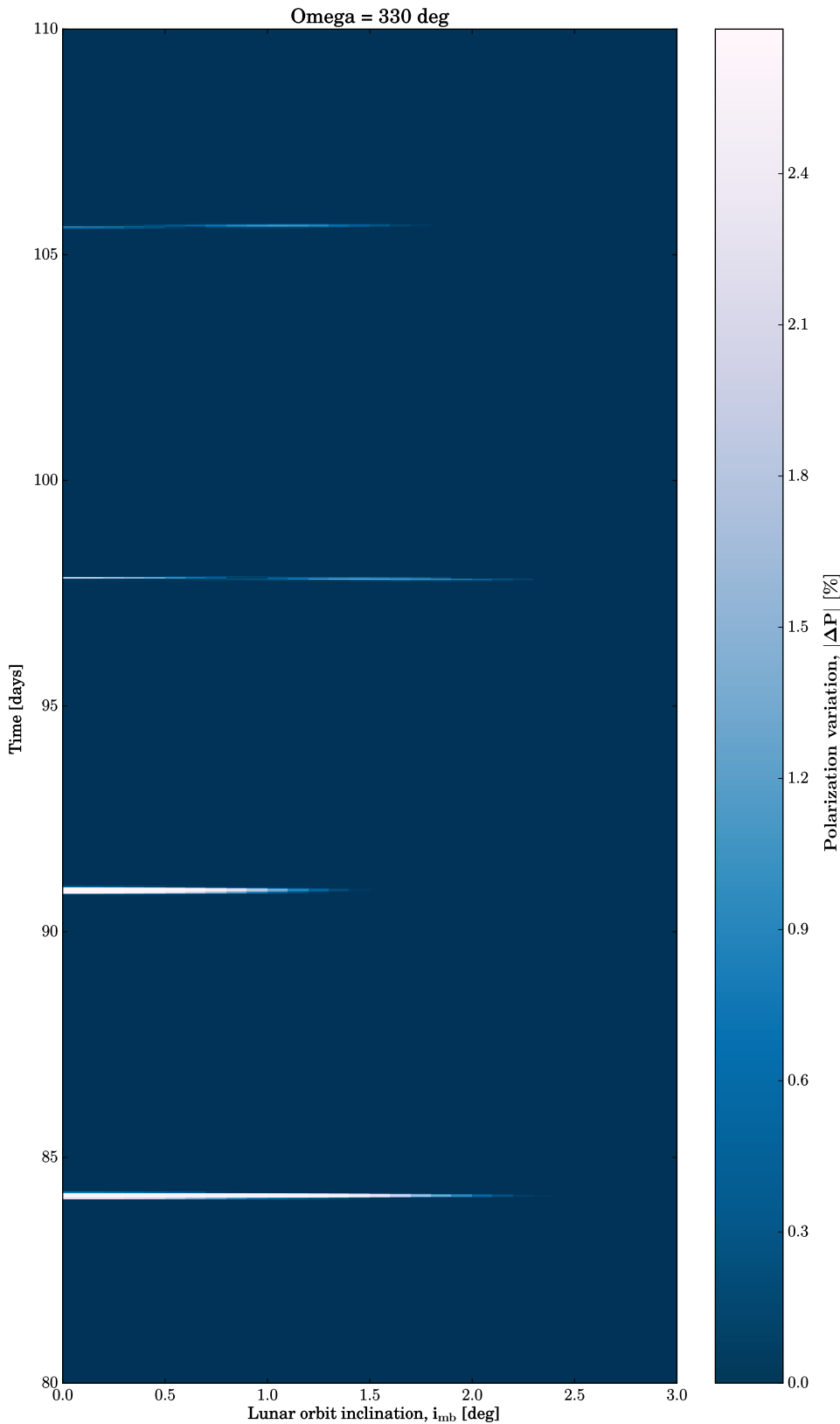


Figure 6.21: Absolute value of the difference between the unresolved planet–moon system degree of polarization and the continuum background signal, $|\Delta P|$, as a function of time and lunar orbit inclination, i_{mb} . For this simulation, the lunar right ascension of the ascending node orbital elements is set to $\Omega_{mb} = 330^\circ$. The resolution is $\Delta t = 40\text{min}$ in time domain and $\Delta i_{mb} = 0.1^\circ$ in angular domain.

is at the centre of the planet during lunar transit and the planet is at the centre of the moon for planetary transits).

Arbitrary planet–moon systems with slightly inclined lunar orbits may fall in between the two extreme cases presented so far. In essence, the line of nodes will be randomly oriented, yielding transits and eclipses at certain impact parameter values and trajectories which could be non-parallel with respect to the planetary equator. As an example, Figure 6.21 shows the results obtained for a more realistic scenario in which the right ascension of the ascending node of the lunar orbit is set to an arbitrary value of 330° , as a function of lunar orbit inclination. In essence, we plot the absolute value of the change in variation of the degree of polarization ΔP with time and lunar orbit inclination. The results show how mutual events (white spikes) vanish with increasing lunar inclination, progressively diminishing the duration of signatures recorded and maximum change in polarization. For the Earth–Moon like system employed we find mutual events to occur at higher inclinations than the ones foreseen by Equations 6.1 and 6.2, as follows from the relaxation of the lunar right ascension of the ascending node parameter.

6.6. Summary of results

In this chapter we have studied the dependence of flux, F , and polarization, P , signatures during mutual events on the following lunar parameters: period, surface albedo, radius, orbit eccentricity and inclination. For this, we considered the edge-on Earth–Moon–like planet–moon system described in Sections 2.4 and 3.2.2 as a starting point. The conclusions are here summarized for each of the analyses:

Lunar period

Wider lunar orbits around the planet (larger lunar orbital periods) yield an increase of mutual events duration, which scales with \sqrt{r} ⁵, and an increase in the time gap between mutual events. The observed mutual event features in F and P phase curves do not depend on the lunar period, except for lunar eclipses. In this case, decreasing ΔF and ΔP values are recorded as the moon travels through a more distant, and thus brighter, region of the eclipse shadow cone. This descend is steeper in polarization ($\Delta P_{\max} = 1.5\%, 0.25\%$ for $a_{mb} = 0.5, 3a_m$) than flux ($|\Delta F_{\max}| = 0.027, 0.024$ for $a_{mb} = 0.5a_m, 3a_m$)⁶.

Lunar surface albedo

With regard to the lunar albedo, we found that the drop in flux and the increase in polarization scale linearly with increasing albedo when the moon gets completely darkened by the planet, e.g. reaching a maximum increase in polarization of $\Delta P = 5\%$ for albedo of 0.5. In the case of planetary darkening events, we show that, as expected, the total flux drop does not depend on the lunar albedo. However, the observed variations in degree of polarization decrease with increasing surface albedo. Consequently, a Moon-like satellite with albedo $a_{surf} \approx 0.1$ stands out in polarization during planetary darkening events, while brighter moons are more easily detected during lunar darkening events.

Lunar radius

We have found the the maximum F and P variations are proportional to R_m^2 during total lunar occultation in planetary transits and lunar eclipses. In the case of planetary darkening events, the maximum flux variations are more accurately approximated by a cubic function of R_m ($\Delta F_{\max} \propto (-R_m)^3$). However, the polarization variations are not proportional to the lunar radius (i.e. larger exomoons do not always imply a larger ΔP), except for very large companions ($R_m > 0.5R_p$). Small satellites of radius $R_m = 0.1R_p$ are barely distinguishable in flux ($|\Delta F_{\text{alb max}}| < 1.1\%$ from Figure C.9a) and polarization curves ($|\Delta P_{\max}| < 0.4\%$). Large moons of radius $R_m = 0.3R_p$ yield large flux drops up to 9.5% of the system albedo (for planetary shadowing events at $\alpha \approx 27^\circ - 29^\circ$) and maximum changes in polarization up to 3.2% (for lunar shadowing events at $\alpha \approx 87^\circ - 108^\circ$). Large Lambertian companions conforming binary systems might be relatively easier to detect. For instance, a moon of radius $R_m = 0.7R_p$ results in maximum flux drops of $\sim 38\%$ of the system's albedo during planetary darkening events at small α and maximum polarization variations of $\sim 13\%$ during lunar darkening events at $\alpha \approx 90^\circ$.

Lunar orbit eccentricity

While transits still occur every lunar period, we have found that the time gap between consecutive lunar and planetary transit events is increasingly biased with increasing lunar eccentricity. In the case

⁵Parameter r stands for the moon orbit radius.

⁶Parameter a_m stands for the Moon orbit semi-major axis around the Earth.

of eclipse events, their periodicity is lost for $e_{mb} \neq 0$, turning the detection of exomoons via frequency analyses more challenging in the case of non-circular orbits. These effects strongly depend on the lunar orbit orientation with respect to the star and observer. Moreover, we observe variation in mutual events durations in our simulations, with a maximum variation of 2–2.5 hours for $e_{mb} = 0.5$ compared to a circular orbit.

Lunar orbit inclination

The modelled transits require the planet–moon system to be observed in edge-on configuration and the eclipses are only recorded in the presence of a moon orbiting along the ecliptic plane. We estimated that transits and eclipses always occur for maximum moon orbit inclination values 1.21° and 1.48° , respectively. Our results on flux and polarization curves for varying impact parameter b show that ΔF and ΔP are proportional to b except for the degree of polarization during planetary darkening events. In such case, our simulations yield non-linear $|\Delta P|$ values with b , e.g. $|\Delta P| = 1.4\%$ for both $b = 0.7$ and $b = 0.15$.

We concluded that mutual events can be observed at higher inclinations values, depending on the lunar right ascension of the ascending node, Ω_{mb} . For instance, if the line of nodes is aligned with the observer's viewing direction, transits are observed at all possible inclination angles, yielding symmetric flux and polarization curves for $i_{mb} = 90^\circ$ (as the moon transits perpendicular to the planetary equator). For an arbitrary value of $\Omega_{mb} = 330^\circ$, our simulations foresee mutual events to occur for $i_{mb} < \sim 2.5^\circ$, while increasing moon orbit inclination reduces the events' duration and maximum flux and polarization variations.

Therefore, we have proven that dependencies between the recorded F and P features and the physical and orbital lunar characteristics can be established. This leaves the door opened for the retrieval of extensive information on the planet and moon bodies through measurement of their unresolved reflected starlight, if the required technology would be available.

Conclusions and recommendations

In this study, we successfully developed a validated tool for the computation of reflected starlight by an unresolved extrasolar planet–moon system. The tool encompasses (1) numerical models for the simulation of the dynamical evolution of the system, (2) the simulation of the transits and eclipses, (3) the integration of reflected light (in Stokes vector formulation) from the planetary and lunar disks, and (4) the combination of the lunar and planetary reflection.

As a test case, we simulated a Moon-size Lambertian (depolarizing) lunar companion orbiting around an Earth-like exoplanet in edge-on configuration. Our results showed that the lunar presence can be detected and potentially characterized by measuring the total flux, F , and degree of polarization, P , of the reflected starlight by the unresolved planet–moon system at wavelength 450nm. The magnitude, shape and duration of the obtained flux signatures are in accordance with the results by Cabrera and Schneider [2007]. Moreover, the shape of the computed polarization curves resemble those modelled for stellar transits [Kostogryz et al., 2015] and lunar transits on self-luminous exoplanets [Sengupta and Marley, 2016]. We observed periodic drops in F and variations in P as the bodies shadow each other (eclipses) and interpose in between a second body and the observer (transits) along their orbit around the star.

The planetary darkening events simulated, i.e. planetary transits and lunar eclipses, showed flux drop curves which unveil the reflecting properties of the planet along its observed equator. The shape of P during planetary darkening events strongly depends on the proportion of polarized-to-total reflected flux distribution along the disk and the actual shadowed area. For the planet–moon system employed, we observe increases of P with negative lobes of low amplitude at egress for $\alpha = 67^\circ - 121^\circ$, resulting from the highly polarized flux accumulated along the planetary limb.

In the case of lunar darkening events, i.e. lunar transits and planetary eclipses, the moon gets completely occulted by the planet. The non-polarizing behaviour of the moon yields a steady drop of F and increase of P during mutual events. These are preceded and superceded by monotonous transitions at the planet ingress and egress on the lunar disk. The events' duration is fundamentally driven by the size of the planet, while increasing phase angles reduce the duration up to $\sim 1\text{h}$.

The magnitudes of the mutual event signatures vary with phase angle, such that an increase in α results in a net decrease of the illuminated area of the bodies, and the disk distribution of reflected linearly polarized fluxes Q and U becomes asymmetric. A maximum flux drop of $\sim 8\%$ of the system's geometric albedo (i.e. the nondimensionalized total reflected flux at $\alpha = 0^\circ$) was observed for phase angles $\alpha \approx 10^\circ - 40^\circ$ during planetary darkening events. Maximum P variations of $\sim 2.66\%$ were observed at $\alpha \approx 90^\circ$ during lunar darkening events. This implies that lunar traces in polarization are more relevant at those phase angles at which the planet system is better resolved from its parent star. Moon and planet darkening features are not equally reproduced in flux and polarization: moon darkening events stand out when looking at the polarization curves $\Delta P \approx 1\% - 1.8\%$ for $67^\circ < \alpha < 121^\circ$ during lunar transits while $\Delta P \approx 1.25\% - 2.66\%$ for $54^\circ < \alpha < 108^\circ$ during planetary transits; planet darkening events excel in flux. The typical duration of the simulated transits events is $\sim 4\text{h}$, in agreement with the results by Cabrera and Schneider [2007] while, in the case of eclipses, the divergent shadow cone increases their duration up to 6h.

Based on the simulated phase curves, we estimated the probability of direct observation of a mutual event on an edge-on planet–moon system to be $\sim 5\% – 40\%$ for observation periods of $0.5 – 5$ days respectively, and sampling times $\Delta t < 4$ hours, scaling linearly with observation time. Further increasing the observation time yield smaller increments of probability, i.e. 40% for 5 days and 67% for 27 days of observation. However, the observation of exomoons is not limited to edge-on configurations. Our simulations showed that, in the presence of a lunar companion orbiting on the ecliptic plane, F and P phase curves contain traces of mutual events regardless the angle of observation of the system. Alternatively to the direct observation of mutual events, we proposed to indirectly detect the exomoon presence on long polarization data series via frequency analysis. Our computed Lomb–Scargle periodograms showed that observation period of one lunar orbit and integration times of ~ 4.5 h might be sufficient to unveil the presence of an exomoon in face-on configuration, assuming a background noise of $\sigma = 0.2\%$.

In order to analyse the dependence of F and P on lunar physical properties and orbit geometry, we carried out a sensitivity study on lunar period, surface albedo, radius, and orbit eccentricity and inclination. In a nutshell, we concluded that:

- Larger lunar orbital periods (i.e. larger orbital radii) yield an increased duration of the events and increased time between them. During lunar eclipses, the moon travels through more distant regions of the shadow cone with increasing lunar radius, entailing decreasing ΔF and ΔP values ($\Delta P_{\max} = 1.5\%, 0.25\%$ for $a_{mb} = 0.5, 3a_m$).
- Increasingly brighter satellites are more likely to be observed during lunar occultation events, as ΔF and ΔP are linearly proportional to the lunar albedo. However, the opposite effect is observed in polarization during planetary darkening events. Thus, a Moon-like satellite with albedo ~ 0.1 stands out in polarization curves during planetary darkening events, experiencing a maximum change in polarization of $\sim 0.82\%$.
- ΔF and ΔP scale quadratically with the lunar radius during lunar occultation events. During planetary darkening events, the registered flux variations are smaller than the foreseen by the quadratic relation with radius, specially for large moons and large α . Small satellites of radius $R_m = 0.1R_p$ display $|\Delta P_{\max}| < 0.4\%$, while very large Lambertian companion in binary systems ($R_m = 0.7R_p$) yield $|\Delta P_{\max}| \approx 13\%$.
- Eccentric lunar orbits disrupt the periodicity of the registered events according to the orientation of the lunar orbit with respect to the star and observer. Moreover, we observed variations in the duration of mutual events of maximum $2 – 2.5$ h for eccentricity 0.5.
- Our results showed ΔF and ΔP values proportional to the impact parameter, except for the degree of polarization during planetary darkening events. Furthermore, we showed that a Moon-like satellite with orbital inclination lower than $1.21^\circ/1.48^\circ$ always experience transits/eclipses.

In conclusion, we found that lunar traces are not only distinguishable in flux phase curves, but also stamp their fingerprint on polarization. Moreover, the sensitivity analysis carried out showed direct relations between lunar parameters and the mutual events registered. This paves the way to lunar and planetary orbit and atmosphere characterization by measuring the flux and polarization signals.

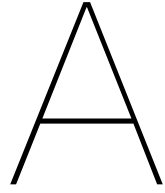
This work constituted a first step towards the discovery of exomoons via polarization. However, there is much that has to be done for the accomplishment of such a milestone. Hereafter, we provide a series of recommendations for future work:

1. Analyse the impact of stellar limb darkening on mutual event curves.
2. Analyse the potential use of polarimetry in current imaged exoplanets.
3. Study the instrument performance required for detecting an exomoon orbiting exoplanets distant from the star, which can be identified by radial velocity measurements.
4. Compare the results obtained in this study with experimental data, e.g. from eclipses in the Jovian system or polarization measurements on the Moon during solar eclipses.
5. Characterize the expected stellar polarization variations introducing noise in the polarization data.

-
6. Estimate the probability of mutual events observation for varying lunar radii and moon orbit parameters.
 7. Analyse the impact of orbital perturbations, e.g. lunar orbital precession, on the periodicity of mutual event signatures on a planet–moon system.
 8. Develop a parameter–estimation algorithm (e.g. Bayesian analysis) for retrieving planet/moon characteristics from flux and polarization data.

Finally, the flexibility and modularity of the developed *Exopy* tool allow for undertaking new research activities beyond the analyses here conducted by simply adding complementary modules. Among others, we highlight the possibility of carrying out studies on:

- Flux and degree of polarization of light emitted by hot exoplanets in the presence of an orbiting moon.
- Variations in planetary photometric wobble induced by a lunar companion.
- Impact of exorings and/or multiple exomoons on reflected starlight by exoplanets.
- Stellar polarization changes during exoplanet and exomoon transits.



Models verification

In this appendix, we present the verification of the transits model code in Section A.2, as well as the validation and verification of the eclipses model code in Section A.3. The implementation of both models is confirmed to be free of bugs and ready for carrying out simulations.

A.1. Radiance disk integration

The implementation of the radiative transfer model is here verified using a Lambertian sphere. The reflected flux by a Lambertian reflecting sphere is fully analytic [see e.g. Chandrasekhar, 1950, Russell, 1916, Van de Hulst, 1980] and is given by:

$$F_{\text{Lam}}(\alpha) = \frac{2}{3\pi} (\sin \alpha + (\pi - \alpha) \cos \alpha) . \quad (\text{A.1})$$

Equation A.1 holds true for an albedo equals 1.0 (geometric albedo equals 2/3). The analytic curve is compared to the numerical results obtained for a Moon-type of body of albedo 1.0 (see Section 2.4) and used to test the accuracy of the numerical integration across the disk and, thus, verify the implemented code. Figure A.1 shows the relative error ΔF_{alb} , referred to the geometric albedo (see Equation 5.5), and the absolute error $\Delta F(\alpha)$, defined as the difference between the reference and the

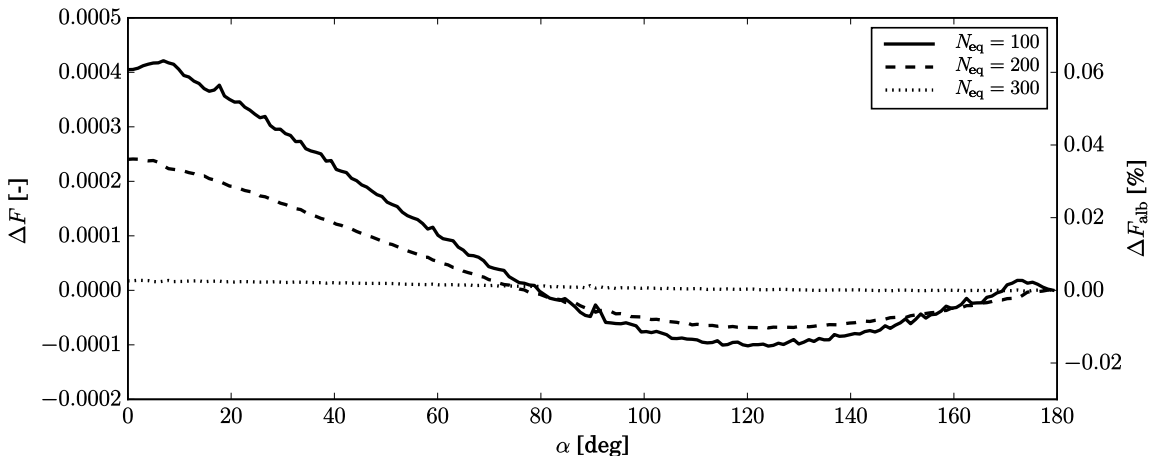


Figure A.1: Absolute error ΔF in the disk integrated flux F of a Lambertian reflecting body, for number of pixels along the disk equator N_{eq} equals 100 (solid line), 200 (dashed line), or 300 (dotted line). The errors are calculated as the numerically calculated values minus the analytically calculated values. Fluxes have been normalized so that F at $\alpha = 0^\circ$ equals the geometric albedo of the planet–moon system.

calculated reflected flux $\Delta F(\alpha) = F_{\text{Lam}}(\alpha) - F(\alpha)$, for different number of pixels along the disk equator N^{eq} . Errors for $N^{\text{eq}} = 400, 700, 1000$ have been calculated but are not shown in Figure A.1.

For $N^{\text{eq}} = 300$, the absolute value of the error ΔF is smaller than 2×10^{-5} ($\Delta F_{\text{alb}} < 0.0028\%$) across the whole phase angle range, with the peak error found for $\alpha \approx 0^\circ$. For increasing number of pixels the error quickly falls for all phase angles, while the order of magnitude of the error is one order of magnitude higher for small phase angles $\alpha < 90^\circ$ than for large phase angles $\alpha > 150^\circ$. We find increasing error for decreasing N^{eq} with a maximum value of the error ΔF smaller than 4.2×10^{-4} ($\Delta F_{\text{alb}} < 0.063\%$) for $N^{\text{eq}} = 100$. For $N^{\text{eq}} = 100, 200$ the flux is slightly underestimated ($\Delta F < 4.2 \times 10^{-4}$) for phase angles $0^\circ \leq \alpha < \sim 80^\circ$, while the flux is slightly overestimated ($\Delta F > -4.2 \times 10^{-4}$) for phase angles $0^\circ \leq \alpha < \sim 80^\circ$.

The results obtained show the convergence of the numerical integration with number of pixels and suggest high accuracy even for small N^{eq} (see Appendix B.2 for a trade-off analysis on N^{eq}). The integration of the linearly polarized fluxes Q and U , and consequently the degree of polarization, is performed alongside with the integration of F . Then, there is no numerical reason why the integration of U and V would lead to different errors than the ones we show here. However, we have indirectly compared our polarization results with Lambertian, and pure gas atmospheric models (with and without aerosols), verifying the accuracy of the integration results obtained. Therefore, we verify that our numerical integration algorithm is free of implementation errors.

A.2. Transits model

As detailed in Section 4.5, a transiting object blocks a circular region on the darkened body of radius equal to the radius of the transiting body. In order to verify the implementation of the transits model, we compare the size of the darkening area obtained during a lunar transit to the analytical projection of the moon sphere onto the planetary surface. The orbital geometry employed for the series of simulations carried out coincides with that in Table 5.1.

Then, for different lunar diameters and positions along the lunar transit path, we measure the discretized size of the planetary darkened region during lunar transit. We use a fine planetary pixel grid with spatial resolution of 10 km. As shown in Figure A.2¹, we count the number of black pixels falling out of the transit area, $N_{\text{points out}}$, and the total number of black pixels along the equator. The latter is then converted to distance units and presented, together with $N_{\text{points out}}$, in Table A.1.

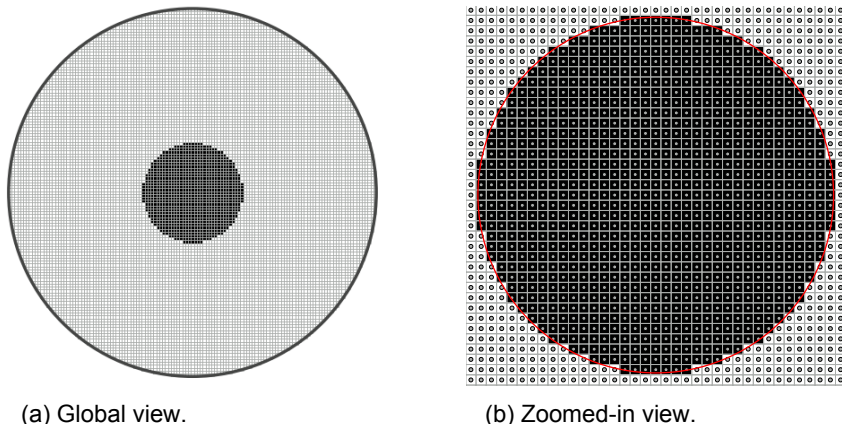


Figure A.2: Blocked reflected light on the planetary disk during lunar transit for phase angle $\alpha = 0^\circ$ and lunar true anomaly $v_{mb} = 0^\circ$ shown in a global (a) and zoomed-in view (b). The number of pixels along the equator is $N_p^{\text{eq}} = 127$ (total number of pixels is 12645), with a spatial resolution of 100 km. White–black color scale indicates full–null illumination. The central position of each pixel in (b) has been marked with a grey dot. The expected analytical darkened area has been indicated with a red circle.

¹Figure A.2 gives the reader an idea of the verification procedure followed for a case of lower spatial resolution (100 km). A snapshot could not be taken for 10 km spatial resolution as plotting the high amount of points involved was not feasible from a computational effort point of view.

Table A.1: Results of the transits model verification. The table shows the numerically computed diameter of a lunar transit blocked area on the planetary disk for varying lunar diameter and true anomaly, i.e. different positions along the lunar orbit. We also count the number of darkened pixels that fall out of the analytic dark area, $N_{\text{points out}}$ for each scenario. Lunar diameter is given as a fraction of the Moon diameter, D_m . The spatial resolution along the planetary grid is 10 km.

		Lunar true anomaly, ν_{mb}				
		179.3°	179.6°	179.9°	180.2°	180.5°
$3D_m/2 = 5212.2$	D [km]	-	5220 ± 10	5210 ± 10	5210 ± 10	5220 ± 10
	$N_{\text{points out}}$ [-]	0	0	0	0	0
$D_m = 3474.8$	D [km]	3470 ± 10	3470 ± 10	3480 ± 10	3480 ± 10	3480 ± 10
	$N_{\text{points out}}$ [-]	0	0	0	0	0
$D_m/2 = 1737.4$	D [km]	1740 ± 10	1740 ± 10	1740 ± 10	1740 ± 10	1740 ± 10
	$N_{\text{points out}}$ [-]	0	0	0	0	0
$D_m/3 = 1158.27$	D [km]	1160 ± 10	1160 ± 10	1160 ± 10	1160 ± 10	1160 ± 10
	$N_{\text{points out}}$ [-]	0	0	0	0	0
$D_m/4 = 868.7$	D [km]	870 ± 10	870 ± 10	870 ± 10	860 ± 10	870 ± 10
	$N_{\text{points out}}$ [-]	0	0	0	0	0

As the results in Table A.1 show, the computed transit regions reproduce (within the discretization resolution error margin) the transiting bodies' diameter and accurately take into account all pixels which centre falls within the expected transit area. Therefore, we verify that the transit model implementation is free of errors.

A.3. Eclipses model

The aim of the eclipses model introduced in Section 4.4 is to generate representative shadows during eclipses. In this section, we validate and verify our geometrical model by comparing the size and duration of the eclipses generated for an Earth–Moon system to those predicted for real solar and lunar eclipses on Earth. For this, we consider three solar eclipses corresponding to dates 8 April 2005, 9 March 2016 and 21 August 2017 (see Figure A.3). From the eclipse path², we make a rough estimate of the eclipse totality path width and eclipse penumbra shadow width at the Greatest Eclipse (GE) time³. We list the reference eclipse path width values in Table A.3.

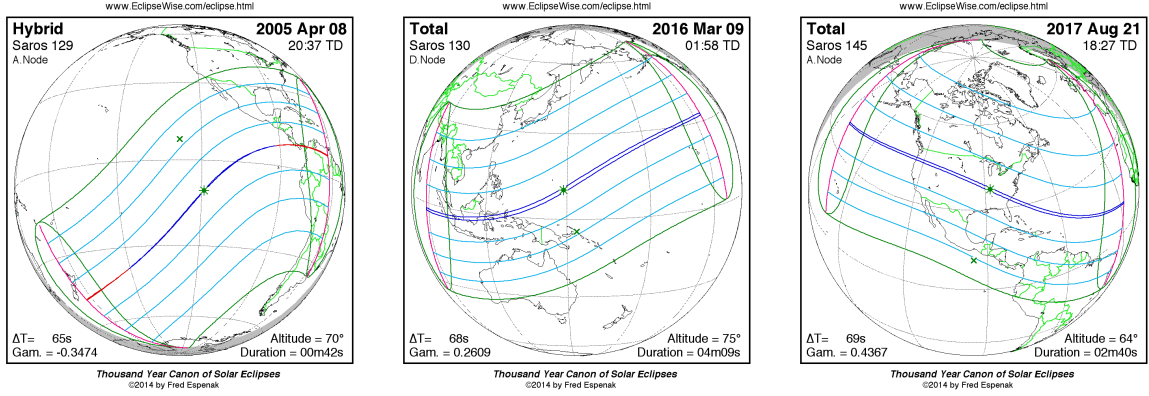
We now consider a simplified planetary eclipse scenario observed at phase angle $\alpha = 0$, both for a circular and eccentric lunar orbit, denominated 'moon circular' and 'moon eccentric', respectively. The orbital geometry configuration follows the orbital elements in Table 5.1 with modified lunar argument of periastron and lunar eccentricity values, as listed in Table A.2. For both lunar scenarios the eclipse model presented in Section 4.4 yields an umbral cone intersection with the Earth of ~ 11 km and ~ 164 km for a circular and eccentric orbit, as well as a penumbral cone intersection of ~ 7858 km and ~ 7635 km, respectively. These results correspond to observed eclipses at altitude 90° (seen from the shadowed body surface), while the chosen reference solar eclipses (see Figure A.3) yield an observed Sun at lower altitudes (64° – 75°).

Table A.2: Modified lunar orbital elements for the lunar orbit configurations ('moon circular' and 'moon perigee') employed during the verification of the eclipses model. ω_{mb} stand for the argument of periastron and e_{mb} stands for the eccentricity of the lunar orbit around the barycentre.

	ω_{mb} [deg]	e_{mb} [-]
Moon circular	180	0
Moon eccentric	180	0.0549

²Eclipse visibility maps available at eclipse.gsfc.nasa.gov.

³For solar eclipses, Greatest Eclipse (GE) stands for the instant when the axis of the Moon's umbral shadow cone passes closest to the Earth's center. More details are available at <https://eclipse.gsfc.nasa.gov/SEhelp/SEGlossary.html>.



(a) Hybrid solar eclipse 8 April 2005. (b) Total solar eclipse 9 Mars 2016. (c) Total solar eclipse 21 August 2017.

Figure A.3: Predicted eclipse path for three different solar eclipses at Earth. Dark blue lines account for the path of totality, i.e. the intersection of the umbral cone with the Earth. Eclipse on 8 April 2005 is hybrid, shifting between a total and annular eclipse. Red lines in Figure A.3a represent the path of annular eclipse. Dark green lines delineate the penumbra region, and light blue lines are lines of constant eclipse magnitude. Eclipse figures courtesy of Fred Espenak, NASA/Goddard Space Flight Center, from eclipsewise.com.

The values foreseen by our mathematical model described in Section 5.4.3, modelled (moon circular) and modelled (moon eccentric) in Table A.3, are consistent with the umbral and penumbral width values found for typical solar eclipses, validating the extension of eclipses considered in our study. Still, these values are to be checked for consistency with the numerically computed eclipse shadow on the discrete planetary disk. The small dimensions of the umbra shadow on Earth requires to employ a fine planetary grid. Due to computational effort constraints, we employ a spatial resolution of 5 km (2549 points along the equator, 5103125 total number of points). The discrete computed shadows yield an umbral shadow on Earth of 15 ± 5 km and 165 ± 5 km for a circular and eccentric orbit, as well as a penumbral cone intersection of 7855 ± 5 km and 7635 ± 5 km, respectively (see Table A.3 below).

Table A.3: Results of the eclipses model verification. We list the predicted umbral and penumbral shadow width on Earth for solar eclipses on 8 April 2005, 9 Mars 2016, and 21 August 2017. The umbral and penumbral shadow widths foreseen by our eclipse model are shown for both the 'circular' and 'perigee' planetary eclipse configurations, together with the computed numerical results. The spatial resolution along the planetary disk is 5 km. Eclipse data courtesy of Fred Espenak, NASA/Goddard Space Flight Center, from eclipse.gsfc.nasa.gov.

	Umbra width at GE [km]	Penumbra width at GE [km]
8 April 2005	~ 27	~ 8278
9 Mars 2016	~ 155	~ 7645
21 August 2017	~ 115	~ 9550
Modelled (moon circular)	~ 11	~ 7858
Computed (moon circular)	15 ± 5	7855 ± 5
Modelled (moon eccentric)	~ 164	~ 7638
Computed (moon eccentric)	165 ± 5	7635 ± 5

The computed discrete results match the values foreseen by the model, verifying that the implementation of the model is free of errors. The code is accepted to be reliable and ready to be employed in the computation of reflected starlight curves during eclipses events.

B

Trade-off analyses

B.1. Cloudy–clear sky models trade-off

Section 2.4 introduces two alternative planetary atmospheric models, one assuming a clear sky composed by an Earth-like gas mixture (clear sky model) and a second one assuming an homogeneous cloud coverage (cloudy model). In this appendix, we compare the flux and degree of polarization of reflected starlight by a body with a clear sky and cloudy atmospheric model. Moreover, we determine the atmospheric model to be employed for the results in this study, based on the advantages and disadvantages that each model offers.

We show in Figure B.1 the reflected flux for a clear sky atmosphere (solid line) and a cloudy atmosphere of increasing cloud particles effective radius r_{eff} (see Section 2.4 for further details). The clear simulation yields a smoothly decreasing flux with increasing phase angle α , with a geometric albedo $p \approx 0.33$. Adding a cloud coverage yields a 20–45% increment of reflected flux for all α , result of the increased back-scattered radiation. Regardless the value of r_{eff} , the geometric albedo for a cloudy scene increases to $p \approx 0.47$. Increasing cloud particle size yields the emergence of two scattering peaks at $\alpha \approx 0^\circ$ and $\alpha \approx 40^\circ$ (rainbow effect on water droplets).

Alongside with the reflected flux, we show the degree of polarization for the clear (solid line) and cloudy models in Figure B.2. The degree of polarization of the reflected light by a clear atmosphere planet yields a maximum polarization peak of $P \approx 41\%$ at phase angle $\alpha \approx 95^\circ$. The presence of a cloud coverage of effective size $r_{eff} = 4 \mu\text{m}$ yields a drop of the peak polarization value ($P \approx 25\%$ at $\alpha \approx 90^\circ$) as well as the emergence of two polarization peaks at $\alpha \approx 0^\circ$ and $\alpha \approx 40^\circ$ similar to the ones

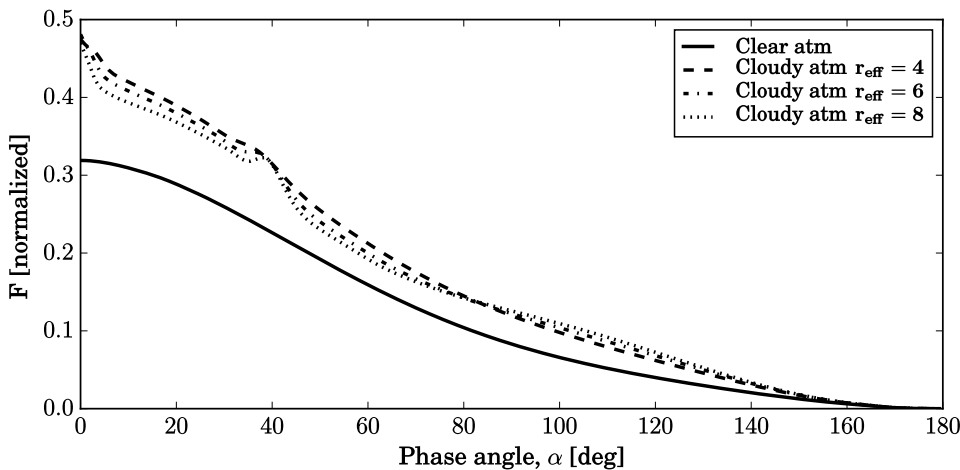


Figure B.1: Planetary reflected flux, F , as a function of phase angle, α , for a clear atmosphere (solid line), and varying cloud particle size $r_{eff} = 4, 6, 8 \mu\text{m}$ (dashed, dash-dotted and dotted lines). Fluxes have been normalized so that F at $\alpha = 0^\circ$ equals the geometric albedo of the planet.

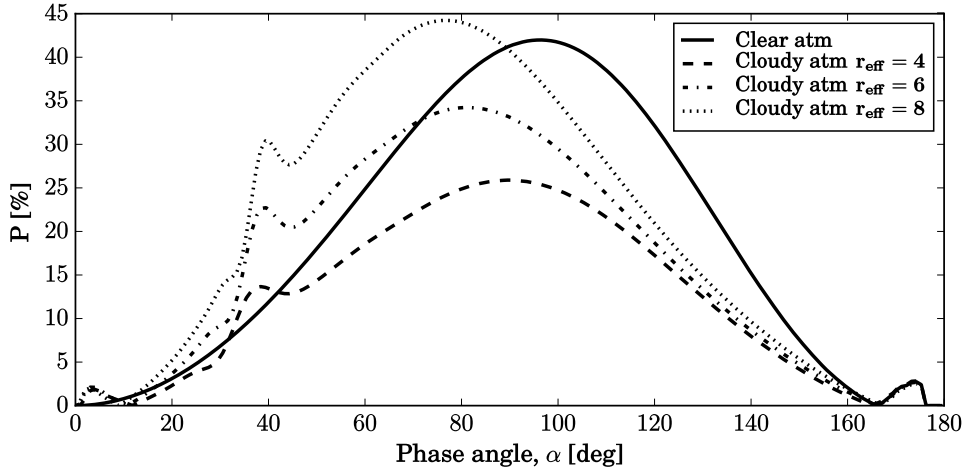


Figure B.2: Degree of polarization of the planetary reflected starlight, P , as a function of phase angle, α , for a clear atmosphere (solid line), and varying cloud particle size $r_{eff} = 4, 6, 8 \mu\text{m}$ (dashed, dash-dotted and dotted lines).

seen in flux (see Figure B.1). The peak degree of polarization increases with increasing cloud particle size, reaching $P \approx 45^\circ$ for $r_{eff} = 8 \mu\text{m}$. Moreover, increasing particle size yields a smaller phase angle of maximum polarization ($\alpha_{P_{max}} \approx 80^\circ$ for $r_{eff} = 4 \mu\text{m}$).

Beyond the emergence of the polarization peaks, the addition of a cloud coverage entails a mere slight shift of the peak polarization phase angle. The higher reflectance of the cloudy atmospheric model yield a higher flux drop during planetary shadowing mutual events. However, the magnitude of the variations on degree of polarization during planetary shadowing events remains the same. During lunar darkening or occultation events, smaller variations on degree of polarization are expected, as the lunar contribution to the total reflected flux of the unresolved planet–moon system is smaller. Thus, the employment of the cloudy model does not provide a significant advantage for the type of events and results pursued in this study.

As a last argument, we provide the computation time for each of the models in Table B.1, using the following simulation parameters: 50 pixels along the disk equator (see Appendix B.2), time step of 24 hours, total integration time of 183 Earth days. As observed, the computation time using the cloudy atmosphere model is around 50 times larger than the computation time for a clear atmosphere simulation.

Table B.1: Computation time for simulating the phase curve of a planet using the clear and cloudy atmosphere models with different cloud particle sizes. The simulation settings are $N_{eq} = 50$, $\Delta t = 24\text{h}$, $t_f = 183$ days. The relative computation time difference with respect to the clear atmosphere simulation is indicated in brackets.

	Computation time [min] (relative to clear [%])
Clear atmosphere	2.2 (-)
Cloudy atmosphere, $r_{eff} = 4$	59.4 (+2700%)
Cloudy atmosphere, $r_{eff} = 6$	77.1 (+3505%)
Cloudy atmosphere, $r_{eff} = 8$	108.6 (+4936%)

Being one of the goals of the research the characterization and analysis of the mutual events features introduced by the presence of an exomoon, a large amount of simulations at fine temporal grids are to be carried out. Hence, computation times in the order of 1 hours (for a coarse time step much larger than the expected duration of the modelled mutual events) are a no-go for the required generation of results, given the time availability. In conclusion, we use the clear scenario for our simulations, which is representative for the Earth atmosphere, does not strongly differ from the cloudy scene here calculated, and allow to perform fast simulations.

B.2. Number of pixels along the equator N_{eq} trade-off

The number of pixels along the equator of the planet, N_{eq}^p , and moon, N_{eq}^m , determine the spatial resolution of the locally reflected Stokes vector computed before integration and influences the final numerical integration error. These values are related through the planet–moon radii ratio as follows from Equation 2.7. In this section, we determine N_{eq}^p and N_{eq}^m as a result of a trade-off between reflected radiance accuracy and computational time, using time steps of 24 hours and a total number of Gauss points for the planet of 40 (see Appendix B.3). The trade-off analysis results are shown in Figure B.3 for a series of planetary pixels across the equator $N_{\text{eq}}^p = 10, 20, 30, 40, 50, 60, 70$ and the corresponding lunar number of pixels $N_{\text{eq}}^p = 3, 5, 8, 11, 14, 16, 19$. The employment of a larger number of pixels is discarded from the beginning of the analysis due to restrictions on the total computation time of the algorithm.

We compute the flux (Equation B.1) and degree of polarization (Equation B.2) relative errors between consecutive N_{eq} values as a function of α as given by Equations B.1 and B.2 for the planet and the moon. Then we plot the maximum (solid line) and mean (dashed line) errors across the phase angle interval of the planet and the moon in Figure B.3 together with the average disk integration time and the total phase curve computation time.

$$|\Delta F_n^{\text{rel}}(\alpha)| = \frac{|F_n(\alpha) - F_{n-1}(\alpha)|}{F_{n-1}(\alpha = 0^\circ)}, \quad (\text{B.1})$$

$$|\Delta P_n(\alpha)| = |P_n(\alpha) - P_{n-1}(\alpha)|, \quad (\text{B.2})$$

where $n - 1$ and n stand for two consecutive N_{eq} values.

Figures B.3a and B.3b show that the difference in flux between successive values of N_{eq} irregularly decreases with increasing number of pixels. For $N_{\text{eq}}^p < 40$, the maximum planetary reflected flux error between simulations is larger than 0.4%, and the average flux error is larger than 0.2%. In the case of the Moon, the smaller number of pixels yields larger errors, i.e. the maximum and average flux errors are larger than 2% for all $N_{\text{eq}}^m < 8$. The variation of planetary degree of polarization yields larger errors than the flux with maximum errors between 1% and 3% for $N_{\text{eq}}^p < 30$ and an almost constant maximum error of ~ 0.5 for $N_{\text{eq}}^p > 30$. The non-polarizing surface of the moon yields null degree of polarization for any N_{eq}^m as shown in Figure B.3d. In general, the results show that the flux and polarization curves have not completely converged for the range of N_{eq} values considered. However, increasing the number of pixels dangerously pushes up the integration time across the planetary disk, as Figure B.3e show.

Therefore, we choose a total of 50 points across the planetary disk equator, $N_{\text{eq}}^p = 50$, an a total of 14 points across the lunar disk equator, $N_{\text{eq}}^m = 14$, which guarantees a reasonable average integration time of ~ 8 seconds (overall phase curve computation time of ~ 2.4 minutes for a temporal resolution of 24 hours). The selected number of pixels have been proved to accurately and smoothly reproduce the dynamic transits and eclipses darkening events for fine temporal resolutions of up to 1 minute.

B.3. Number of Gauss points trade-off

As described in Section 2.2, the locally reflected starlight makes use of the first column of the reflection matrix, \mathbf{R}_1 , particularized according to the local observer–zenith angle, θ , local star–zenith angle, θ_0 , and local azimuthal difference angle, $\phi - \phi_0$, of a particular pixel at a given time. \mathbf{R}_1 is computed as a Fourier–series expansion for a particular atmospheric and surface model. The Fourier coefficients are computed for $\cos \theta_0$ and $\cos \theta$ values which follow a Gaussian distribution of total number of points n_{mug} ¹. Then, the accuracy on the radiance numerical integration across the disk depends on the number of Gauss points n_{mug} considered for a scattering atmospheric model.

Figures B.4 and B.5 present a trade-off analysis on n_{mug} based on the numerical accuracy and the computational time required to perform the numerical disk integration for a clear sky Earth-like model (see Section 2.4 for details on the Earth model and Appendix B.1 for a justification of the selection of the clear sky model for the current analysis). The computations here presented were carried out with 50 pixels across the equator of the disk ($N_{\text{eq}} = 50$), as argued in Appendix B.2. We have computed the complete flux and polarization phase curves ($0^\circ \leq \alpha \leq 180^\circ$) for a number of Gauss points

¹Additionally, Fourier coefficients are calculated at $\cos \theta_0 = 1$ ($\theta_0 = 0^\circ$) and $\cos \theta = 1$ ($\theta = 0^\circ$).

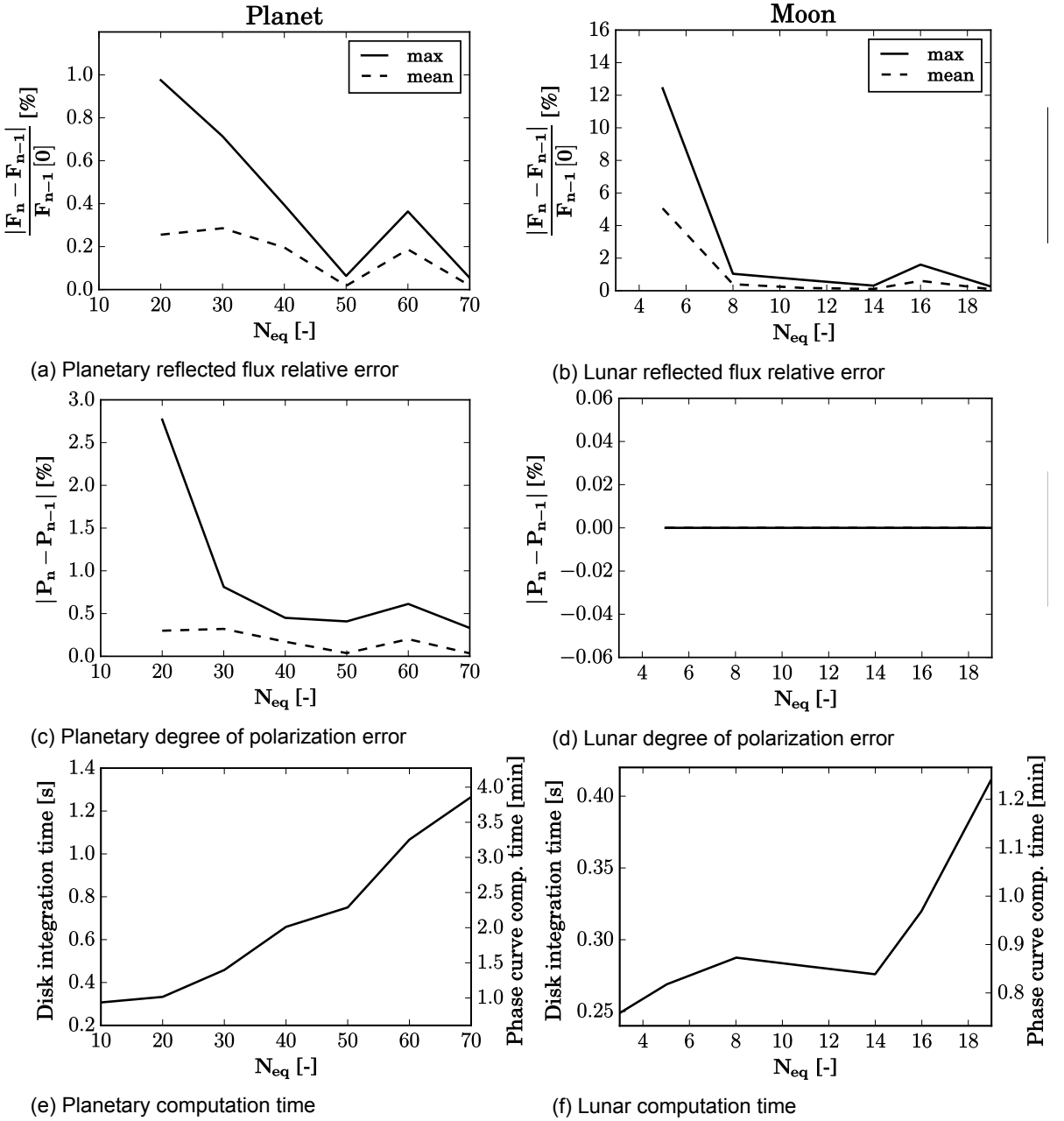


Figure B.3: Trade-off analysis on number of pixels along the equator N_{eq} . We show the maximum (solid line) and mean (dashed line) flux relative error between consecutive N_{eq} values, $|\Delta F_n^{rel}(\alpha)|$ for the planet and moon cases (a) (b), as well as the degree of polarization relative error $|\Delta P_n(\alpha)|$ (c) (d). Subplots (e) and (f) show the total phase curve computation time and average disk integration time for the planet and moon simulations, as a function of number of pixels.

$n_{mug} = 10, 15, 20, 25, 30, 35, 40, 45, 50$, and plotted in Figure B.4 the absolute errors in flux ΔF_n and polarization ΔP_n between consecutive values of n_{mug} as given by Equations B.3 and B.4. Figure B.4 shows the results obtained for $n_{mug} = 10, 15, 20, 25$.

$$\Delta F_n = F_n(\alpha) - F_{n-1}(\alpha), \quad (B.3)$$

$$\Delta P_n = P_n(\alpha) - P_{n-1}(\alpha), \quad (B.4)$$

where $n - 1$ and n stand for two consecutive n_{mug} values.

For $n_{mug} \geq 15$, the absolute value of the error ΔF_n is smaller than 1×10^{-4} for phase angles $10^\circ <$

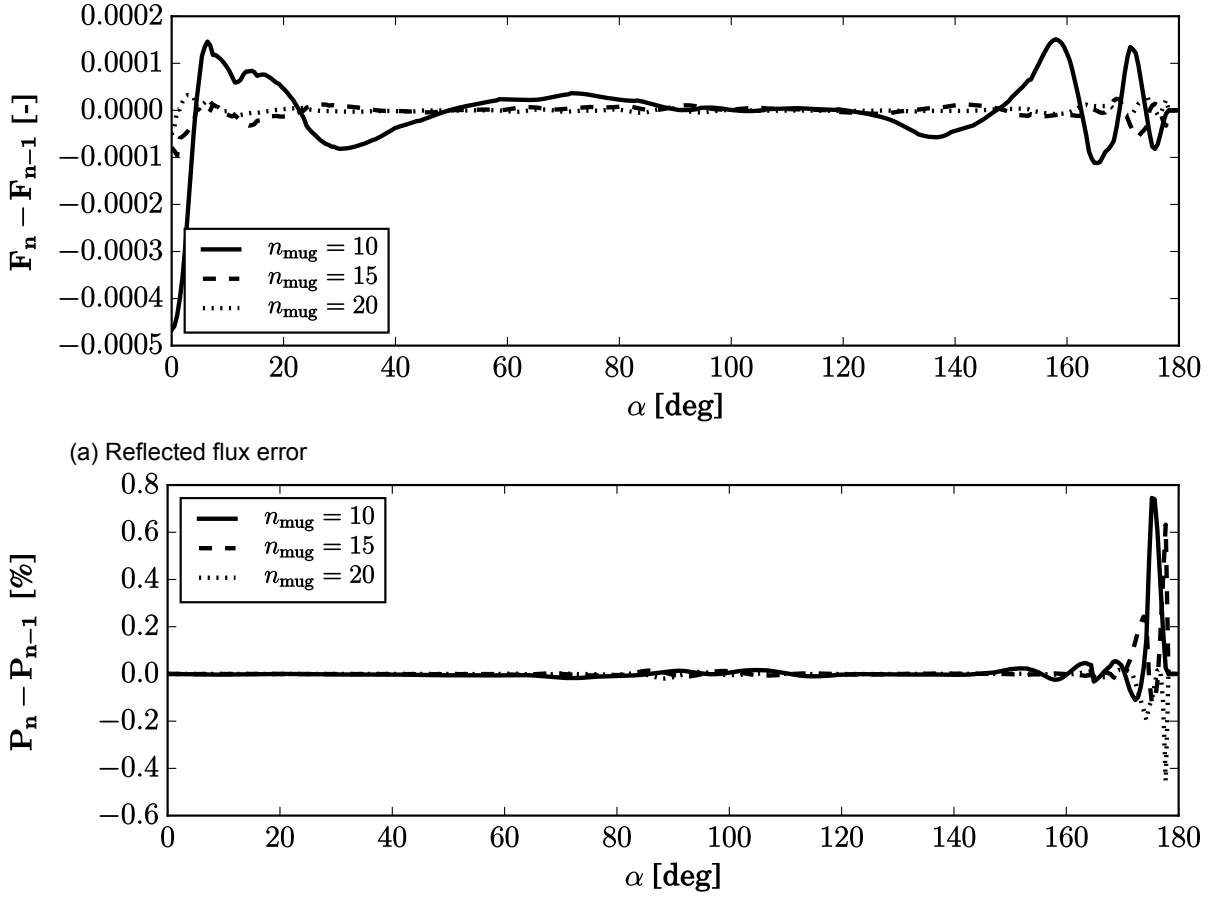


Figure B.4: Absolute reflected flux error ΔF_n (a) and absolute degree of polarization error ΔP_n (b) between consecutive values of number of Gauss points n_{mug} as a function of phase angle, for varying n_{mug} . Fluxes have been normalized so that F at $\alpha = 0^\circ$ equals the geometric albedo of the planet.

$\alpha < 155^\circ$. For smaller and larger α the absolute error increases up to 4.7×10^{-4} . The results in polarization for $n_{\text{mug}} \geq 15$ show bigger absolute error $\Delta P_n < 0.02\%$ for $\alpha < 150^\circ$, while the absolute error reaches $\sim 0.8\%$ for $\alpha > 150^\circ$. Figure B.4 shows a rapidly decreasing error with n_{mug} . In order to take a decision on the number of Gauss points to employ on our simulations, we calculate the flux (Equation B.5) and degree of polarization relative errors (Equation B.6) between consecutive n_{mug} values as a function of α , and we plot the maximum (solid line) and mean (dashed line) errors across the phase angle interval in Figure B.5 both in logarithmic and linear scales, together with the total numerical integration time.

$$|\Delta F_n^{\text{rel}}(\alpha)| = \frac{|F_n(\alpha) - F_{n-1}(\alpha)|}{F_{n-1}(\alpha = 0^\circ)}, \quad (\text{B.5})$$

$$|\Delta P_n(\alpha)| = |P_n(\alpha) - P_{n-1}(\alpha)|, \quad (\text{B.6})$$

where $n - 1$ and n stand for two consecutive n_{mug} values.

On the one hand, the computational time increases quadratically from 0.3 min to 4.5 min with increasing n_{mug} for the range of Gauss points considered. On the other hand, both $|\Delta F_n^{\text{rel}}|$ and $|\Delta P_n|$ show a decreasing logarithmic trend with increasing n_{mug} values. The maximum error in flux F is 0.15% for $n_{\text{mug}} = 15$, while the error in polarization increases to $\sim 0.75\%$, at phase angles $\alpha \approx 0^\circ$ and $\alpha \approx 180^\circ$ respectively, as seen in Figure B.4. In both flux and polarization, the mean error is one order of magnitude smaller than the maximum error at any phase angle. We use the maximum error as trade-off parameter for the selection of a suitable n_{mug} value.

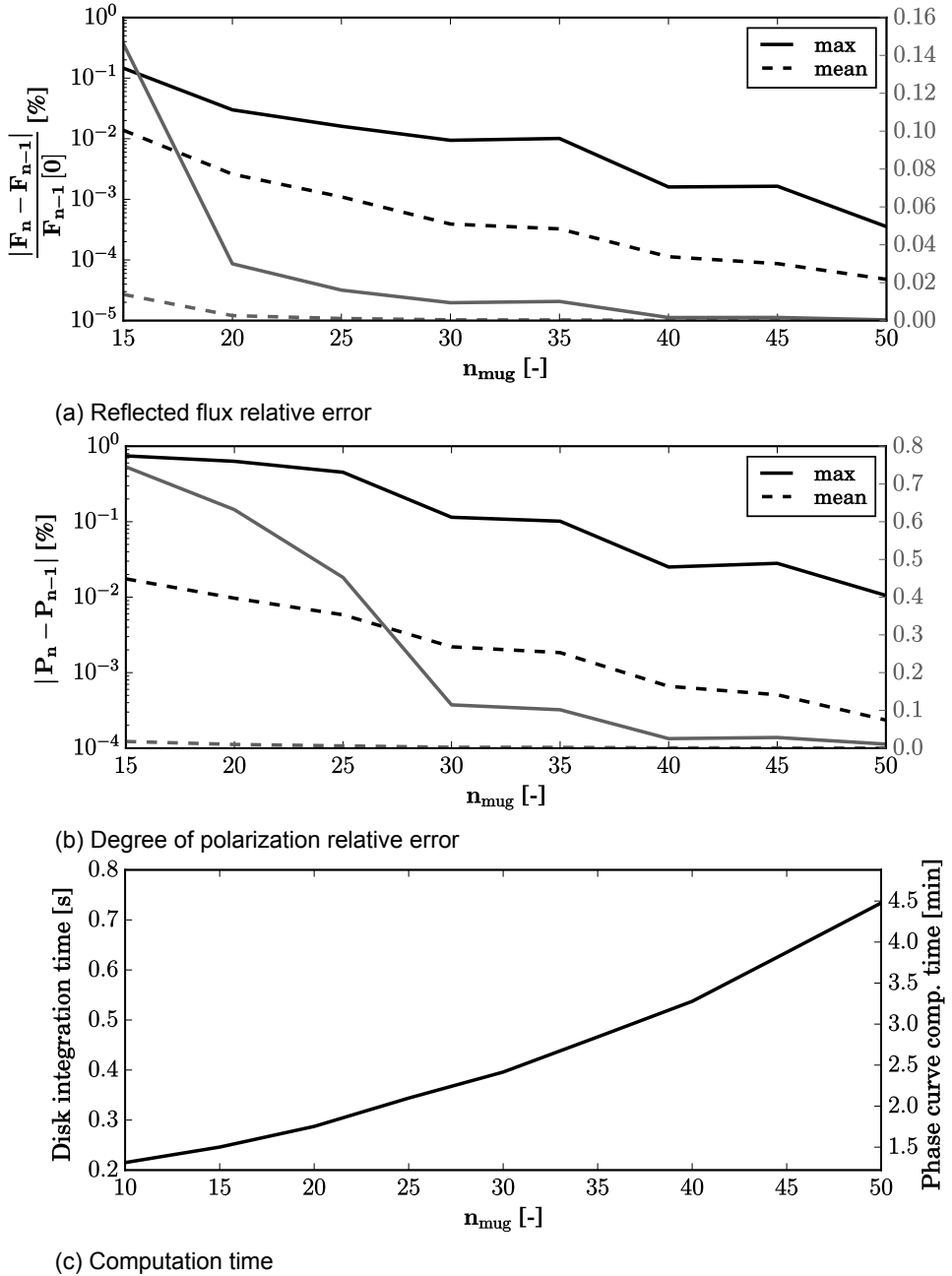
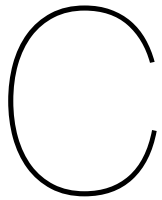


Figure B.5: Trade-off analysis on number Gauss points n_{mug} . We show the maximum (solid lines) and mean (dashed lines) flux relative error between consecutive n_{mug} values $|\Delta F_n^{\text{rel}}(\alpha)|$ (a), as well as the degree of polarization relative error $|\Delta P_n(\alpha)|$ (b). Left (right) vertical axes show results in logarithmic (linear) scale. Subplot (c) shows the total phase curve computation time and average disk integration time, as a function of n_{mug} .

We chose a value of $n_{\text{mug}} = 40$ for our planetary reflection computations as it guarantees small maximum relative errors in flux and polarization (with respect to a value $n_{\text{mug}} = 45$) $|\Delta F_n| < 0.0016\%$ and $|\Delta P_n| < 0.025\%$ across the whole phase angle range. Larger n_{mug} values imply a slight increase in accuracy at the cost of considerably larger integration times. Using 40 Gauss points also ensures a reasonable average computation time of ~ 0.54 seconds per disk integration and a overall phase curve computation time of ~ 3.3 minutes for a planetary disk with $N_{\text{eq}} = 50$ and a temporal resolution of 12 hours.



Extra figures

In this appendix we present an elaboration on the results shown in previous sections, accounting for additional mutual events and/or different representations of the flux and degree of polarization curves, among others. We refer to these figures during the presentation and discussion of the results, enhancing comprehension of the moon's impact on the unresolved planet–moon system.

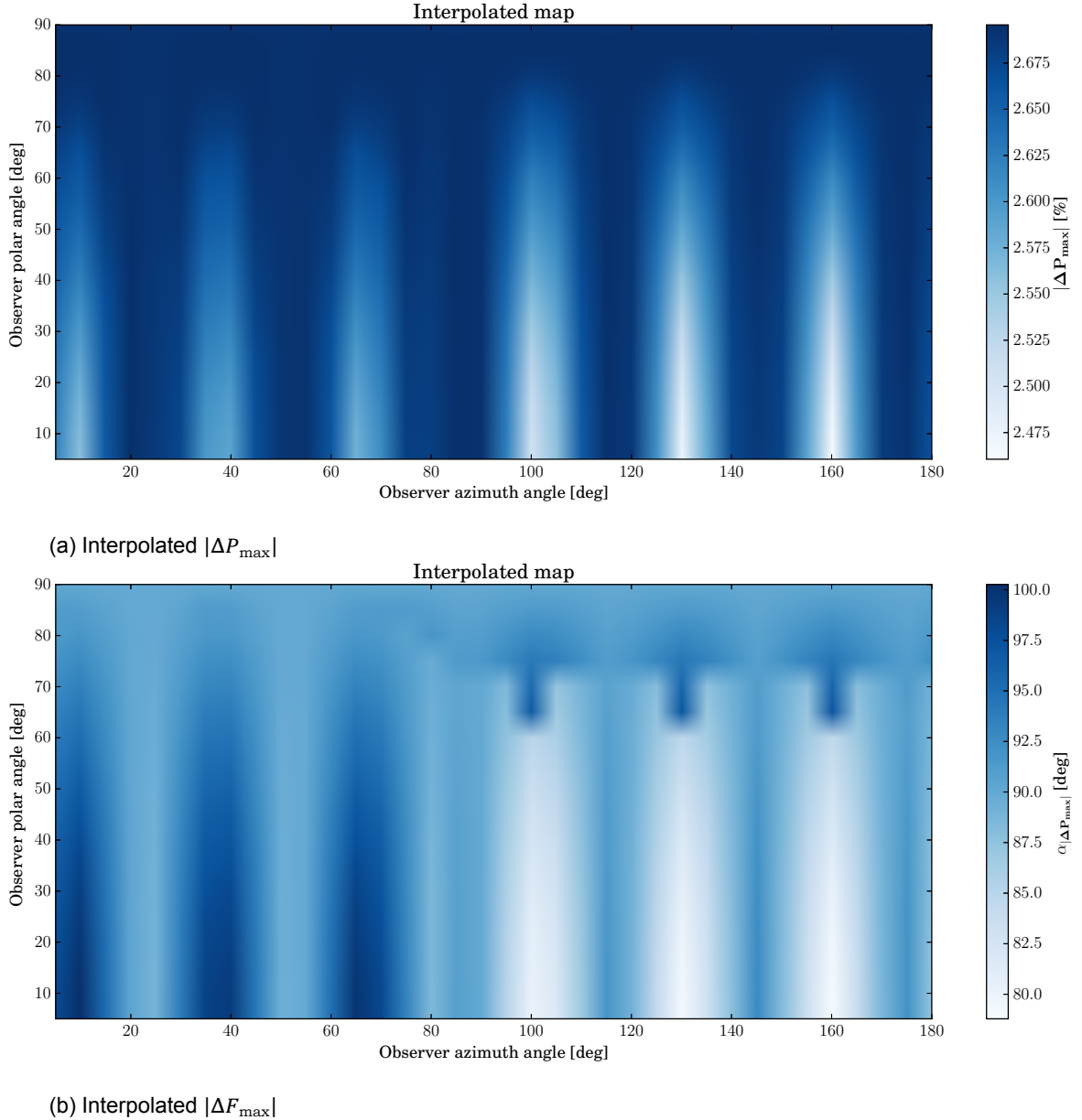


Figure C.1: Interpolated map of the absolute value of the maximum difference between the planet–moon system degree of polarization and the continuum background signal along the phase curve $|\Delta P_{\max}|$ (a), and interpolated map of the absolute value of the maximum difference between the unresolved reflected flux and the continuum background signal $|\Delta F_{\max}|$ (b), both as a function of observer azimuth angle φ_{ob} and observer polar angle, θ_{ob} . Fluxes have been normalized so that F at $\alpha = 0^\circ$ equals the geometric albedo of the planet–moon system. The simulation time resolution is $\Delta t = 90\text{min}$, while φ_{ob} and θ_{ob} angles have been evaluated every 5° and linearly interpolated at intermediate values.

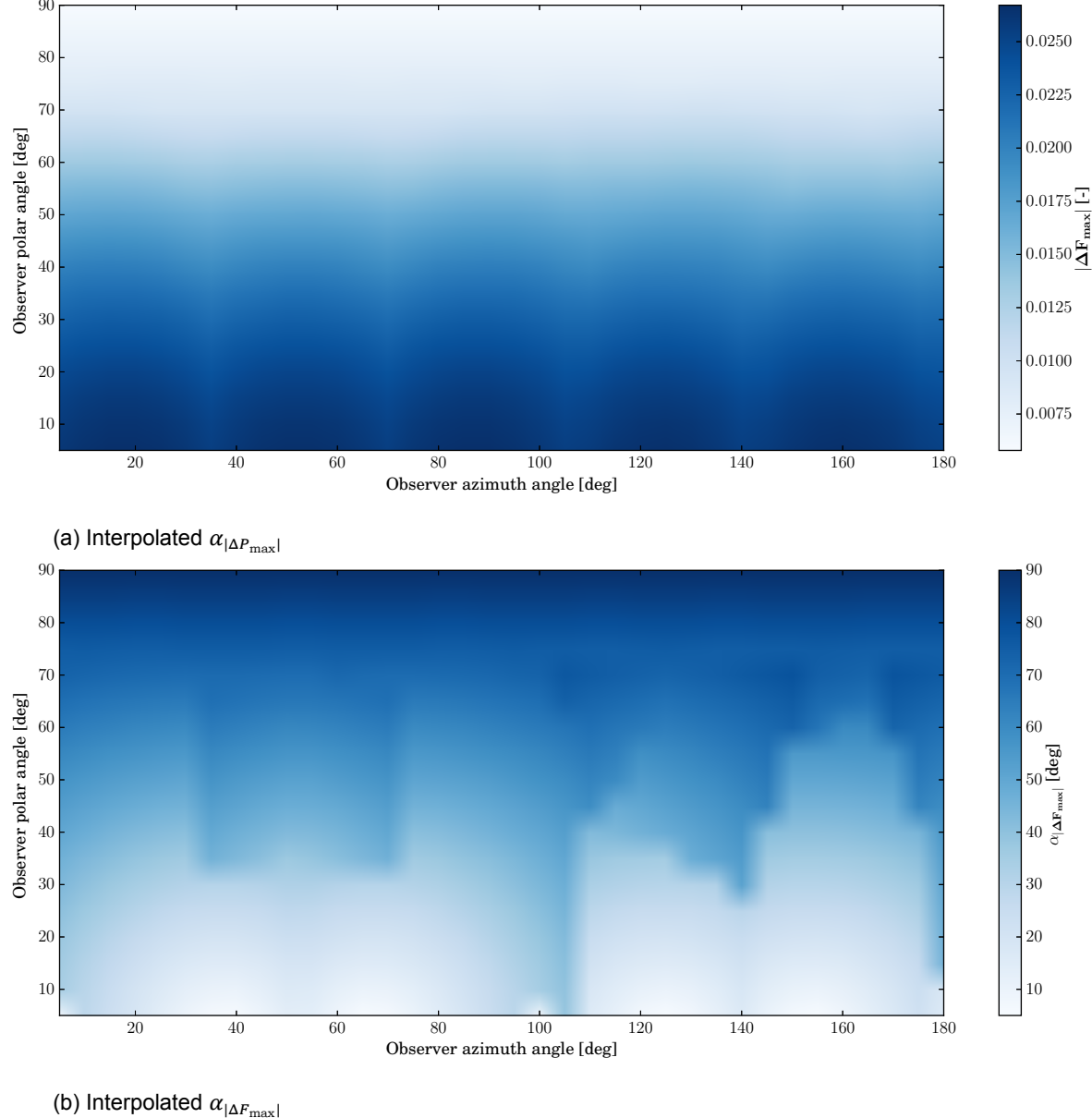


Figure C.2: Interpolated phase angle for maximum difference between the planet–moon system degree of polarization and the continuum background signal along the phase curve $\alpha_{|\Delta P_{\max}|}$ (a), and interpolated phase angle for maximum difference between the unresolved reflected flux and the continuum background signal $\alpha_{|\Delta F_{\max}|}$ (b), both as a function of observer azimuth angle φ_{ob} and observer polar angle, θ_{ob} . The simulation time resolution is $\Delta t = 90\text{min}$, while φ_{ob} and θ_{ob} angles have been evaluated every 5° and linearly interpolated at intermediate values.

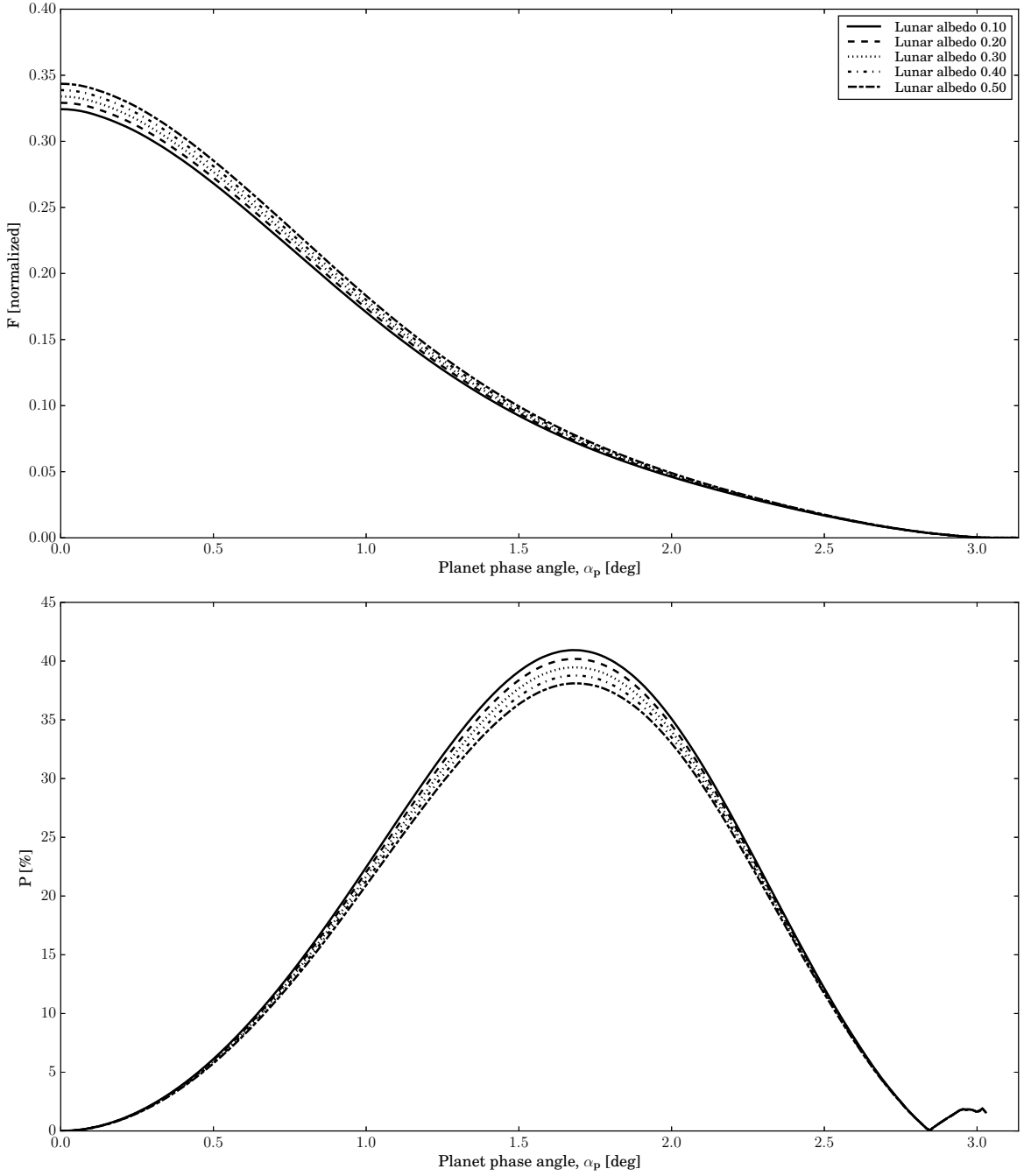


Figure C.3: Continuum unresolved planet–moon system reflected flux F and degree of polarization P as a function of phase angle α for varying lunar albedo. Mutual events are not simulated. Flux has been normalized so that F at $\alpha = 0^\circ$ equals the geometric albedo of the planet–moon system. The simulation time resolution is $\Delta t = 4\text{h}$.

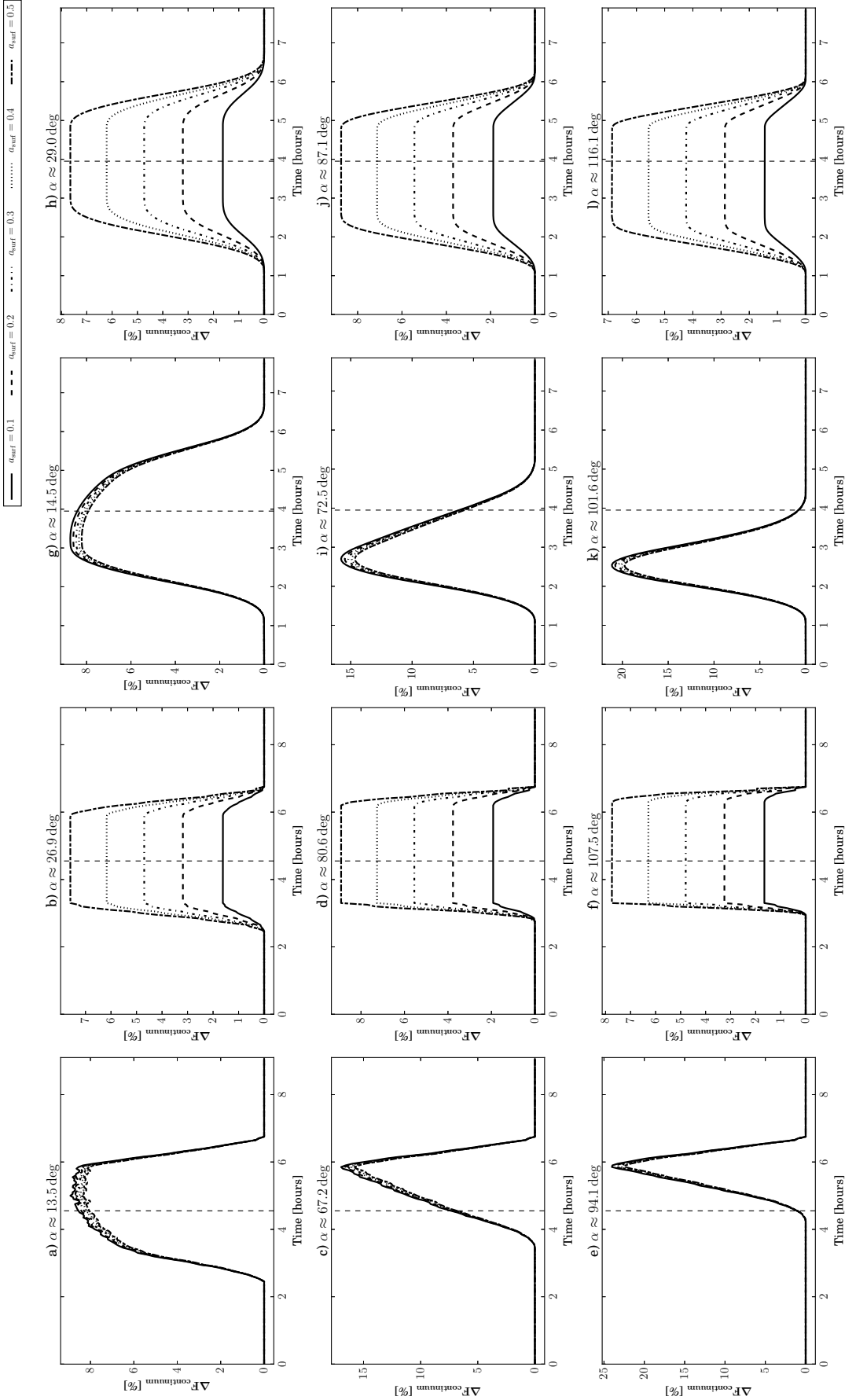


Figure C.4: Unresolved planet–moon system relative reflected flux with respect to the continuum background signal without mutual events, $\Delta F_{\text{continuum}}$, as a function of relative time, for increasing lunar surface albedo a_{surf} . Results are shown for various lunar transits (a) (c) (e), planetary transits (b) (d) (f), planetary eclipses (g) (i) (k), and lunar eclipses (h) (j) (l), at increasing phase angle α . The vertical dashed line corresponds to the time of concentric alignment of the planet and moon bodies as seen from the star/observer in the case of eclipse/transit. The simulation time resolution is $\Delta t = 3 \text{ min}$.

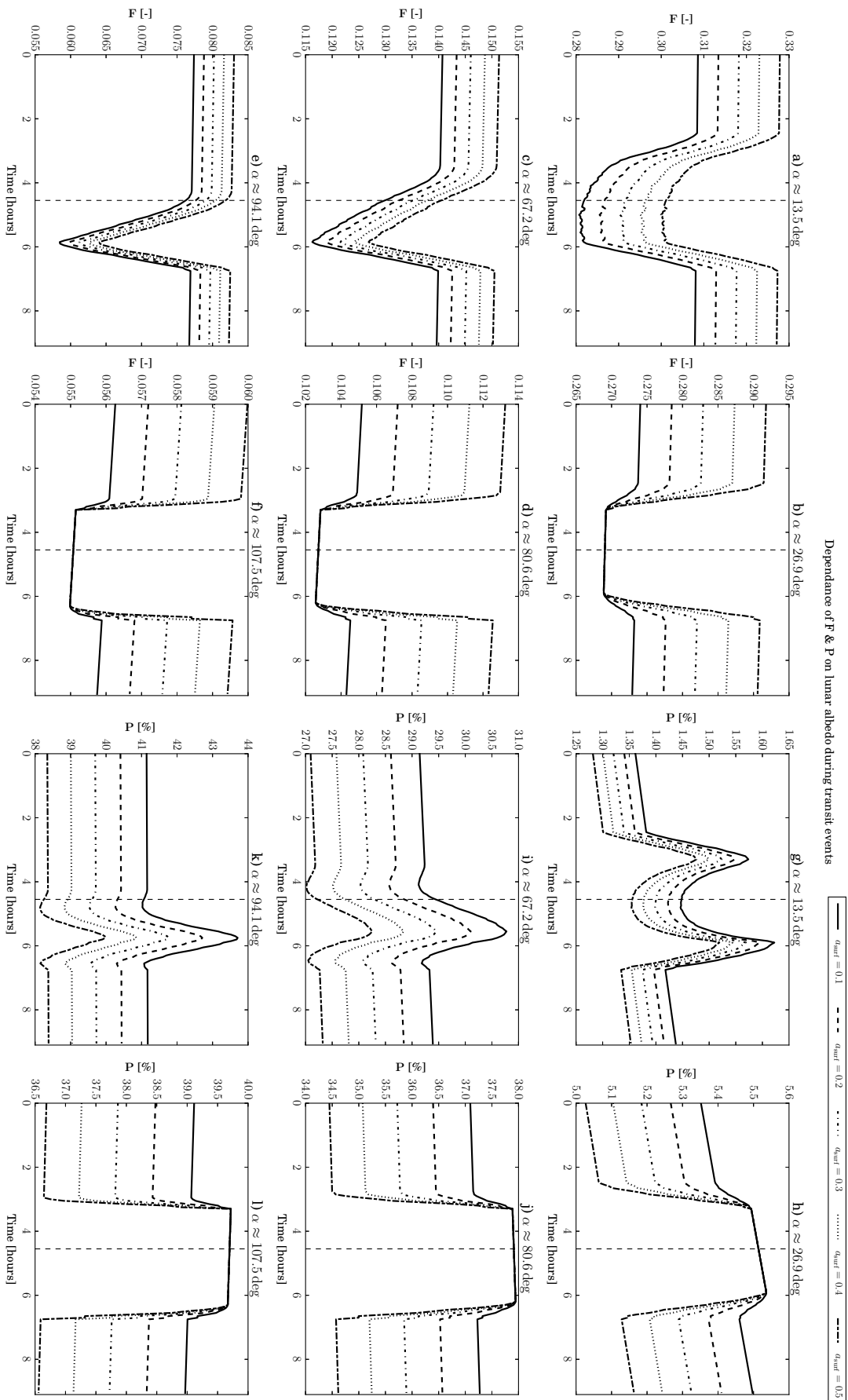


Figure C.5: Unresolved planet-moon system reflected flux, F , (a) (b) (c) (d) (e) (f), and degree of polarization, P , (g) (h) (i) (j) (k) (l) as a function of relative time, for increasing lunar surface albedo a_{lunar} . Results are shown for various lunar transits (a) (c) (e) (g) (i) (k), and planetary transits (b) (d) (f) (h) (j) (l) at increasing phase angles α . The vertical dashed line corresponds to the time of concentric alignment of the planet and moon bodies as seen from the observer. Fluxes have been normalized so that F at $\alpha = 0^\circ$ equals the geometric albedo of the planet-moon system. The simulation time resolution is $\Delta t = 3 \text{ min}$.

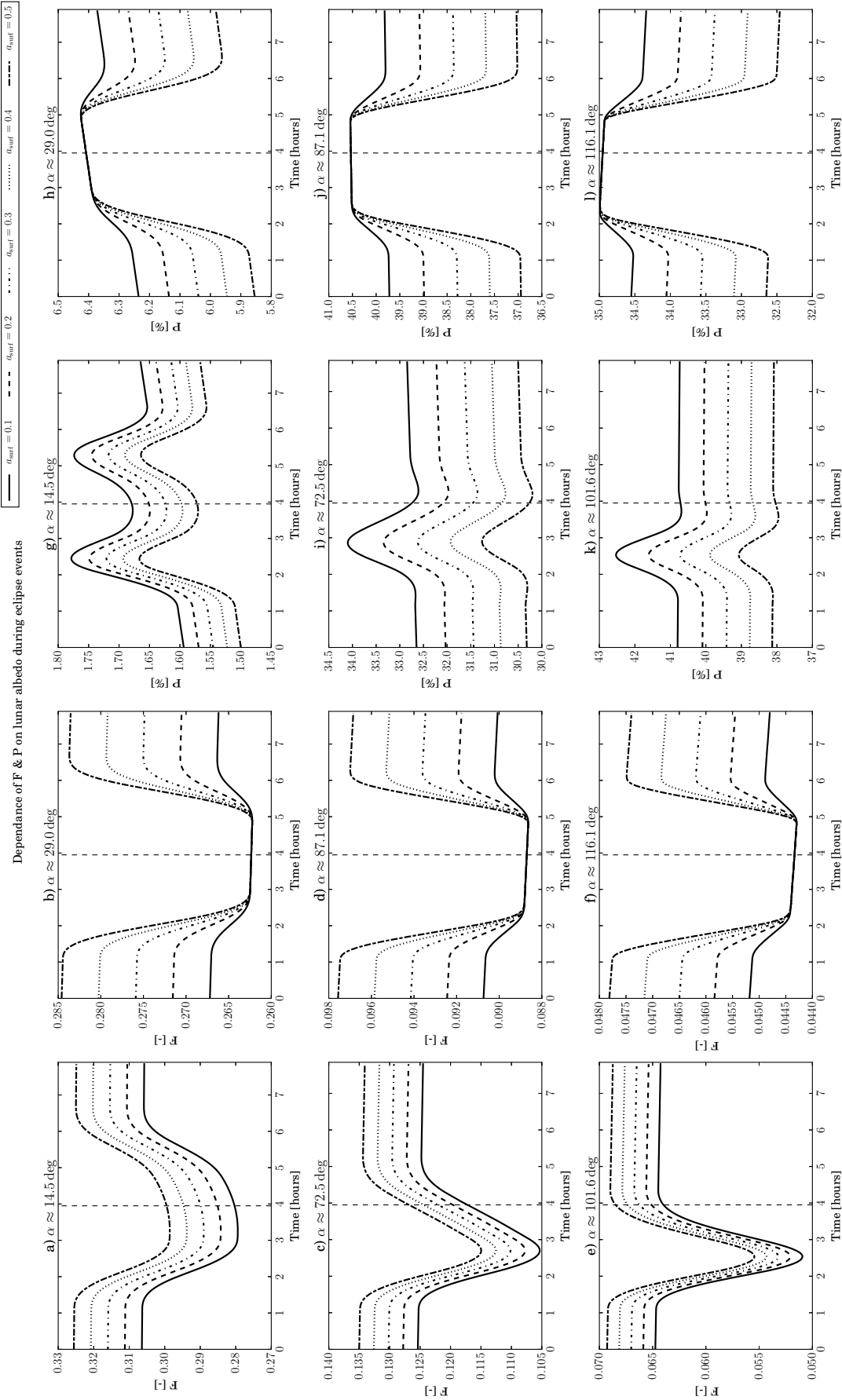


Figure C.6: Unresolved planet–moon system reflected flux, F , (a) (b) (c) (d) (e) (f), and degree of polarization, P , (g) (h) (i) (j) (k) as a function of relative time, for increasing lunar surface albedo a_{surf} . Results are shown for various planetary eclipses (a) (c) (e) (g) (i) (k), and lunar eclipses (b) (d) (f) (h) (j) (l) at increasing phase angles α . The vertical dashed line corresponds to the time of concentric alignment of the planet and moon bodies as seen from the observer. Fluxes have been normalized so that F at $\alpha = 0^\circ$ equals the geometric albedo of the planet–moon system. The simulation time resolution is $\Delta t = 3\text{ min}$.

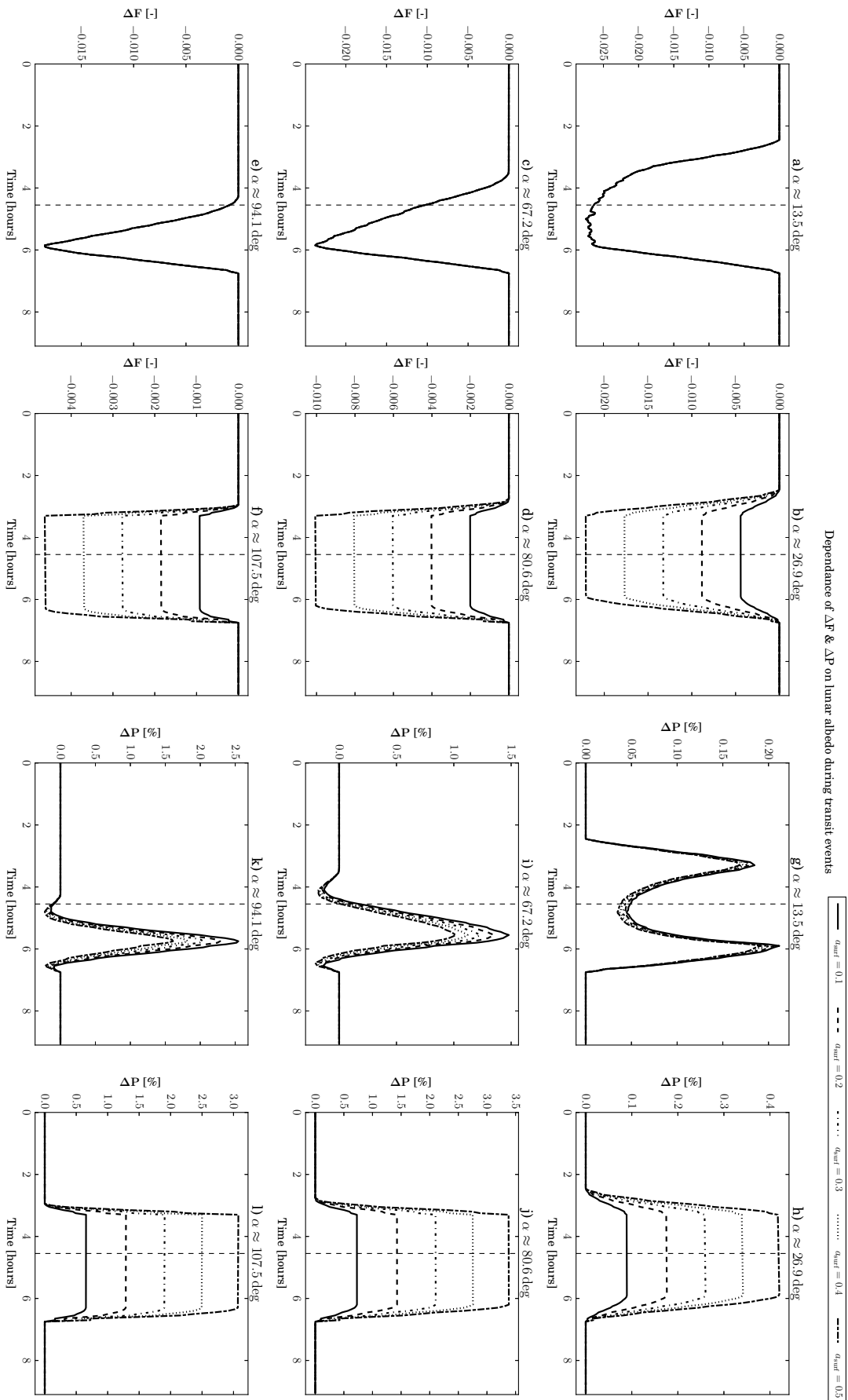


Figure C.7: Difference between the planet-moon system reflected flux and the continuum background flux signal, ΔF , (a) (b) (c) (d) (e) (f), and difference between the unresolved degree of polarization and the background signal, ΔP , (g) (h) (i) (j) (k) (l), as a function of relative time, for increasing lunar surface albedo a_{surf} . Results are shown for various lunar transits (a) (c) (e) (g) (i) (k), and planetary transits (b) (d) (f) (h) (j) (l) at increasing phase angles α . The vertical dashed line corresponds to the time of concentric alignment of the planet and moon bodies as seen from the observer. Fluxes have been normalized so that F at $\alpha = 0$ equals the geometric albedo of the planet-moon system. The simulation time resolution is $\Delta t = 3$ min.

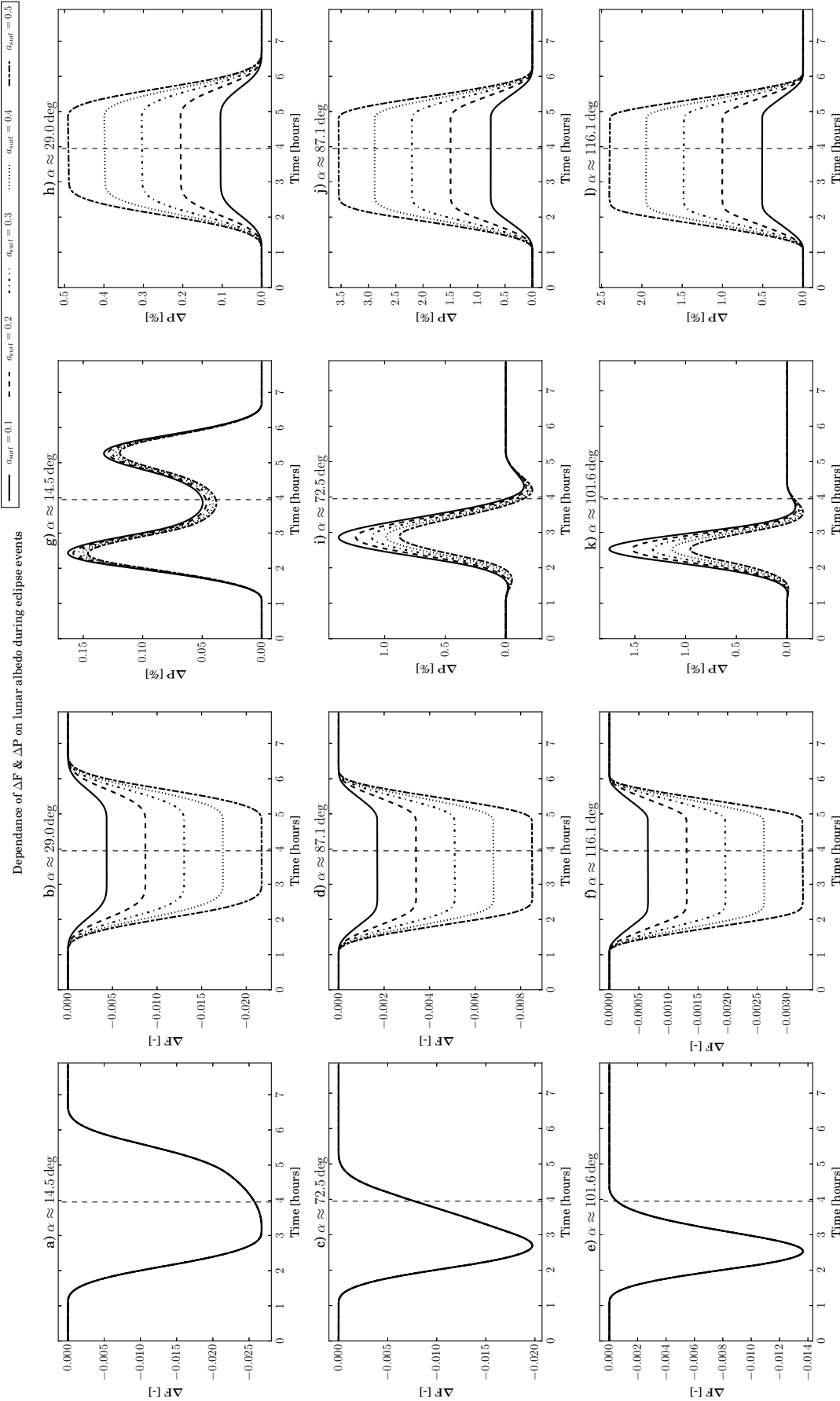


Figure C.8: Difference between the planet–moon system reflected flux and the continuum background flux signal, ΔF , (a) (b) (c) (d) (e) (f), and difference between the unresolved degree of polarization and the background signal, ΔP , (g) (h) (i) (j) (k) (l), as a function of relative time, for increasing lunar surface albedo a_{surf} . Results are shown for various planetary eclipses (a) (c) (e) (g) (i) (k), and lunar eclipses (b) (d) (f) (h) (j) (l) at increasing phase angles α . The vertical dashed line corresponds to the time of concentric alignment of the planet and moon bodies as seen from the observer. Fluxes have been normalized so that F at $\alpha = 0^\circ$ equals the geometric albedo of the planet–moon system. The simulation time resolution is $\Delta t = 3$ min.

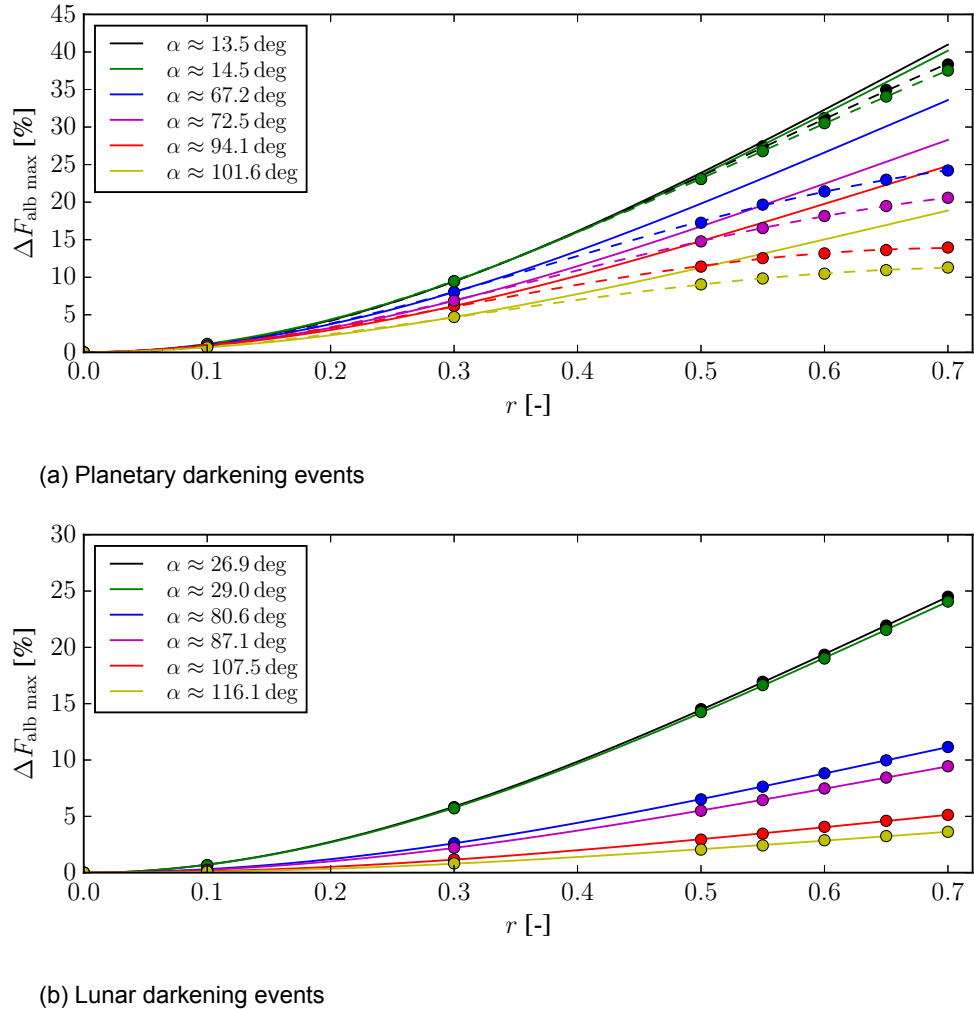


Figure C.9: Maximum difference between the planet–moon system reflected flux and the continuum background flux signal relative to the system's albedo, $\Delta F_{\text{alb max}}$, as a function of moon-to-planet radius ratio $r = \frac{R_m}{R_p}$ during (a) planetary darkening events (i.e. lunar transits and planetary eclipses) and (b) lunar darkening events (i.e. planetary transits and lunar eclipses) occurring at different phase angles α (circular dots). Solid lines stand for a quadratic fitting curve.

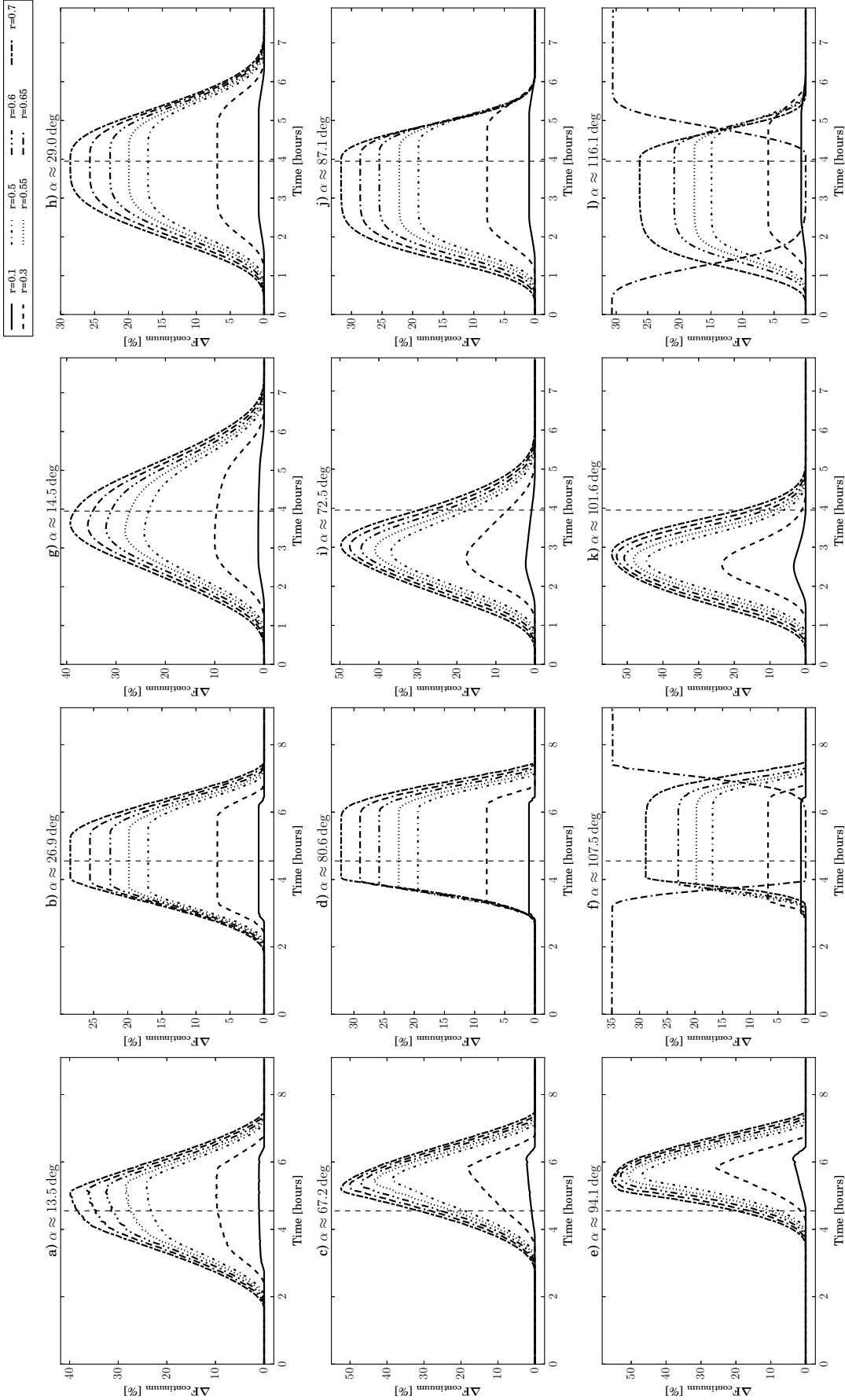


Figure C.10: Unresolved planet–moon system relative reflected flux with respect to the continuum background signal without mutual events, $\Delta F_{\text{continuum}}$, as a function of relative time, for increasing lunar-to-planetary radius ratio r . Results are shown for various lunar transits (a) (c) (e), planetary transits (b) (d) (f), planetary eclipses (g) (i) (k), and lunar eclipses (h) (j) (l), at increasing phase angle α . The vertical dashed line corresponds to the time of concentric alignment of the planet and moon bodies as seen from the star/observer in the case of eclipse/transit. The simulation time resolution is $\Delta t = 3 \text{ min}$.

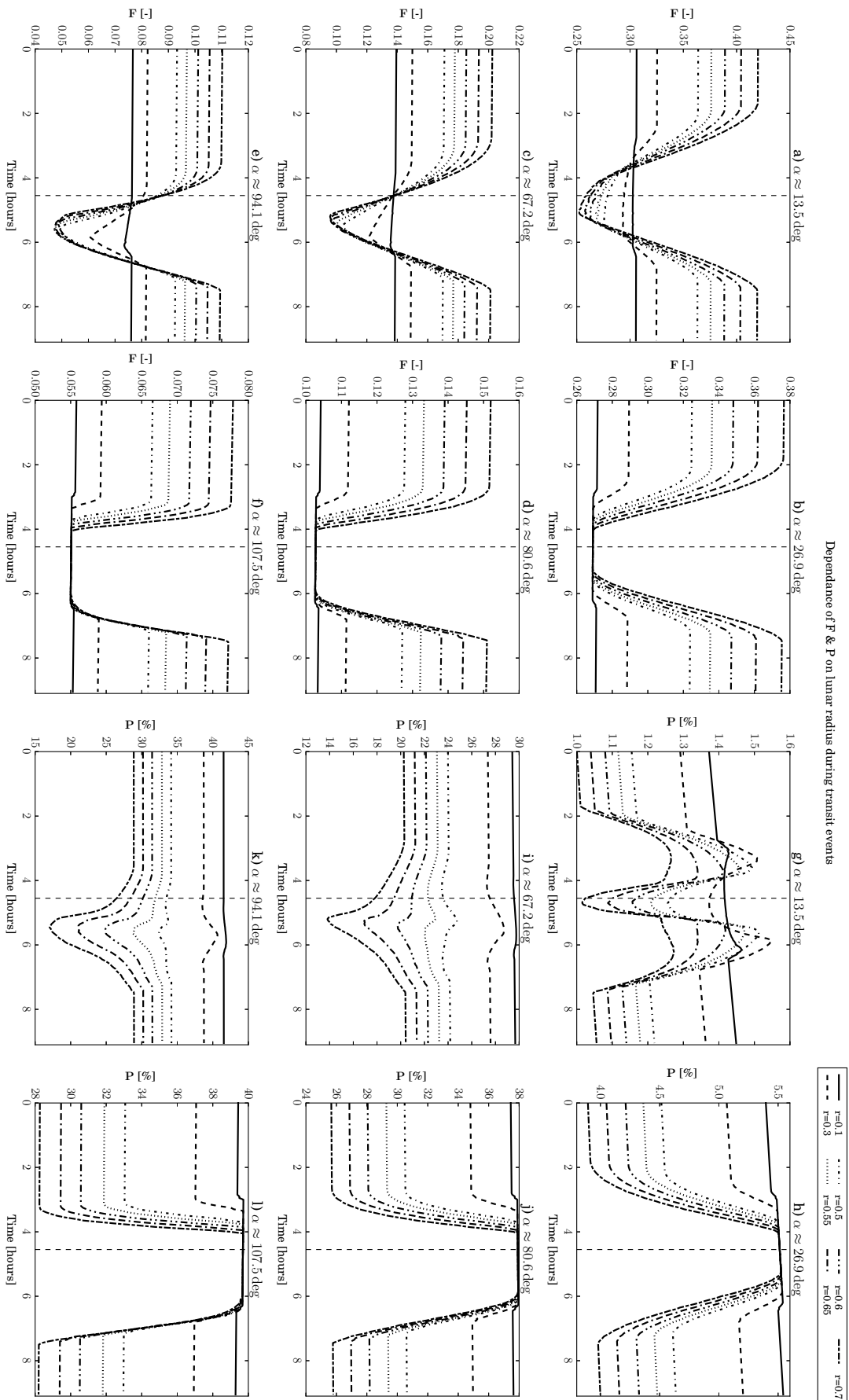


Figure C.11: Unresolved planet-moon system reflected flux, F , (a) (b) (c) (d) (e) (f), and degree of polarization, P , (g) (h) (i) (j) (k) (l) as a function of relative time, for increasing lunar-to-planetary radius ratio r . Results are shown for various lunar transits (a) (c) (e) (g) (i) (k), and planetary transits (b) (d) (f) (h) (j) (l) at increasing phase angles α . The vertical dashed line corresponds to the time of concentric alignment of the planet and moon bodies as seen from the observer. Fluxes have been normalized so that F at $\alpha = 0^\circ$ equals the geometric albedo of the planet-moon system. The simulation time resolution is $\Delta t = 3 \text{ min}$.

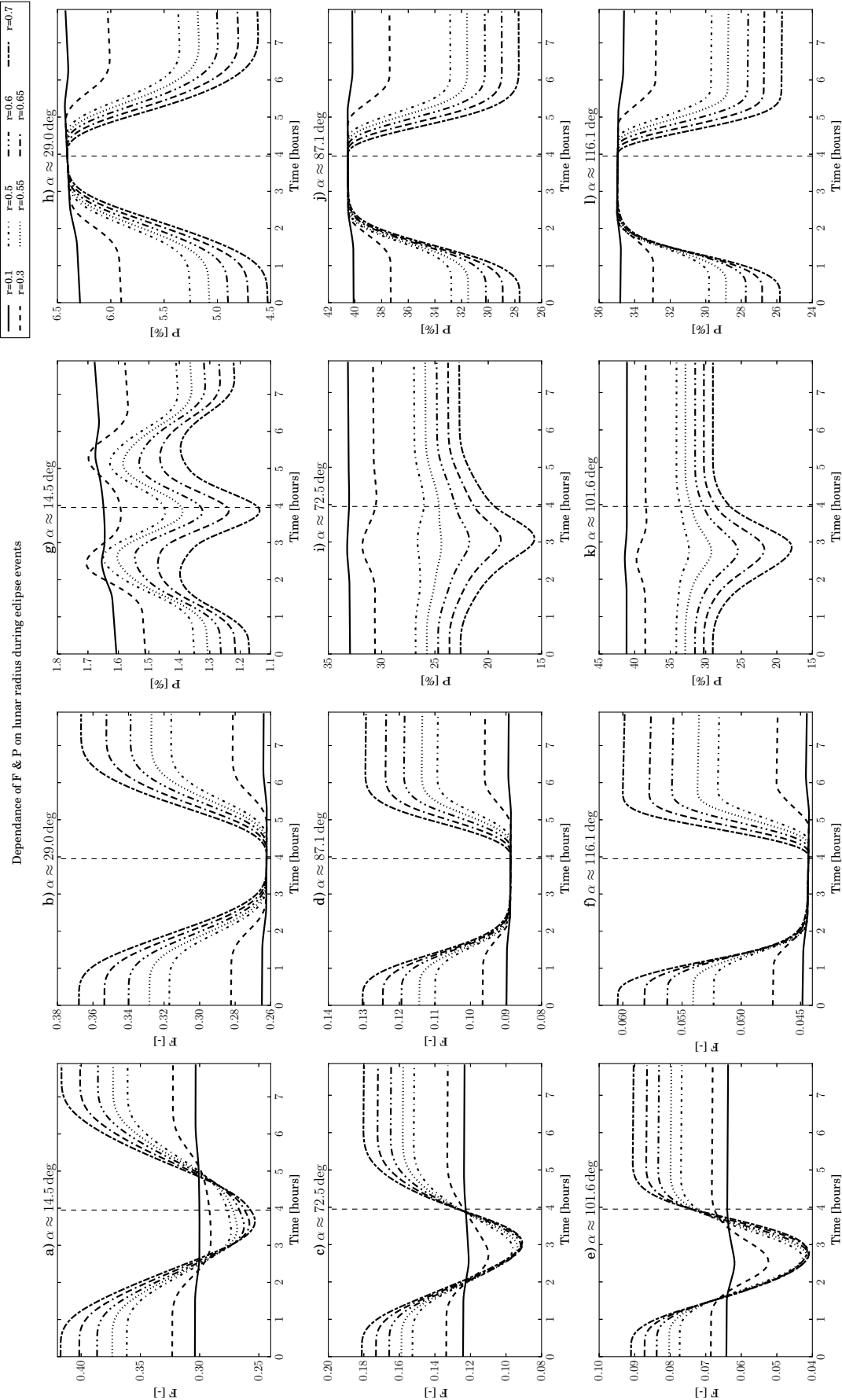


Figure C.12: Unresolved planet–moon system reflected flux, F , (a) (b) (c) (d) (e) (f), and degree of polarization, P , (g) (h) (i) (j) (k) (l) as a function of relative time, for increasing lunar-to-planetary radius ratio r . Results are shown for various planetary eclipses (a) (c) (e) (g) (i) (k), and lunar eclipses (b) (d) (f) (h) (j) (l) at increasing phase angles α . The vertical dashed line corresponds to the time of concentric alignment of the planet and moon bodies as seen from the observer. Fluxes have been normalized so that F at $\alpha = 0^\circ$ equals the geometric albedo of the planet–moon system. The simulation time resolution is $\Delta t = 3 \text{ min}$.

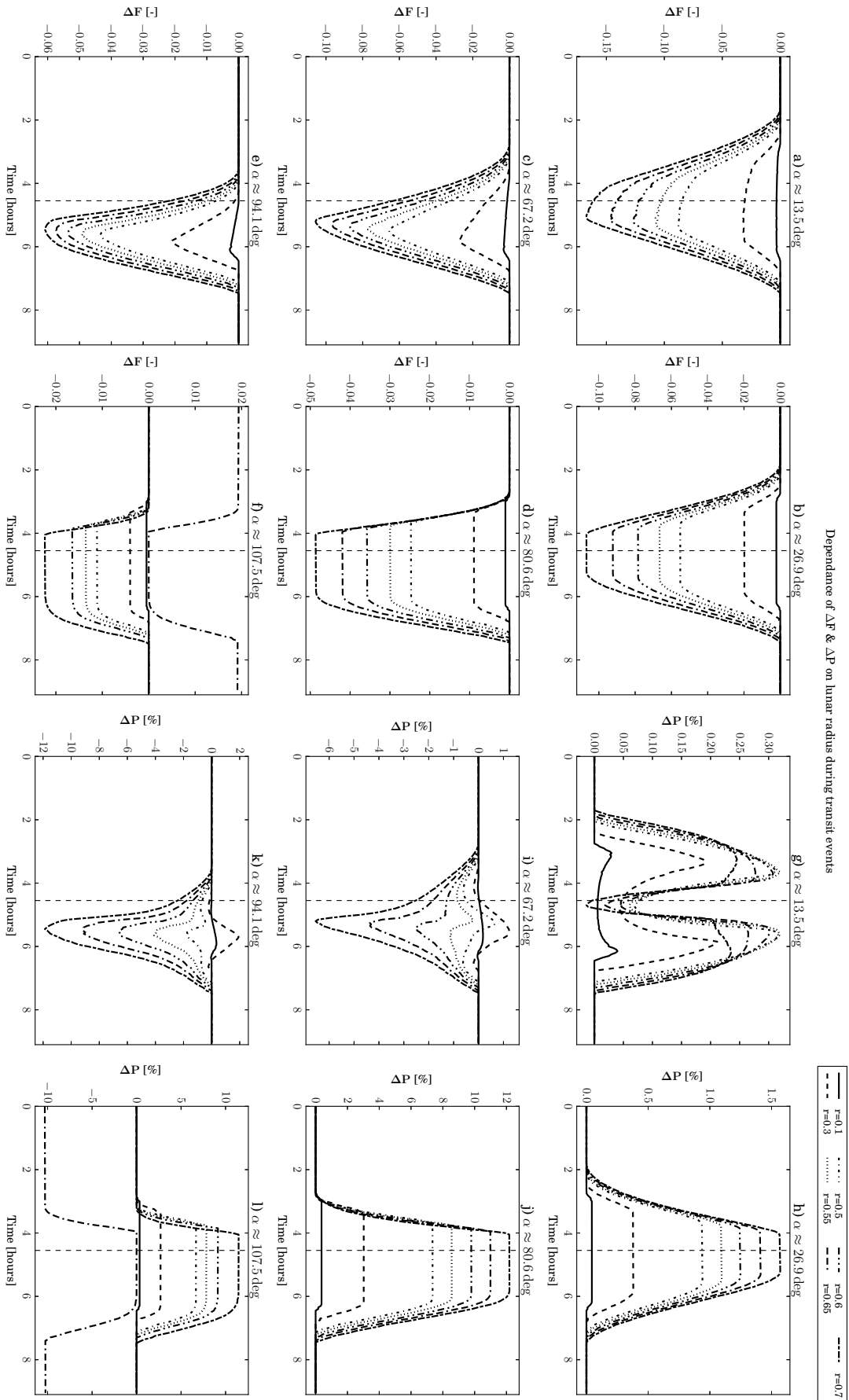


Figure C.13: Difference between the planet-moon system reflected flux and the continuum background flux signal, ΔF , (a) (b) (c) (d) (e) (f), and difference between the unresolved degree of polarization and the background signal, ΔP , (g) (h) (i) (j) (k) (l), as a function of relative time, for increasing lunar-to-planetary radius ratio r . Results are shown for various lunar transits (a) (c) (e) (g) (i) (k), and planetary transits (b) (d) (f) (h) (j) (l) at increasing phase angles α . The vertical dashed line corresponds to the time of concentric alignment of the planet and moon bodies as seen from the observer. Fluxes have been normalized so that F at $\alpha = 0^\circ$ equals the geometric albedo of the planet-moon system. The simulation time resolution is $\Delta t = 3 \text{ min}$.

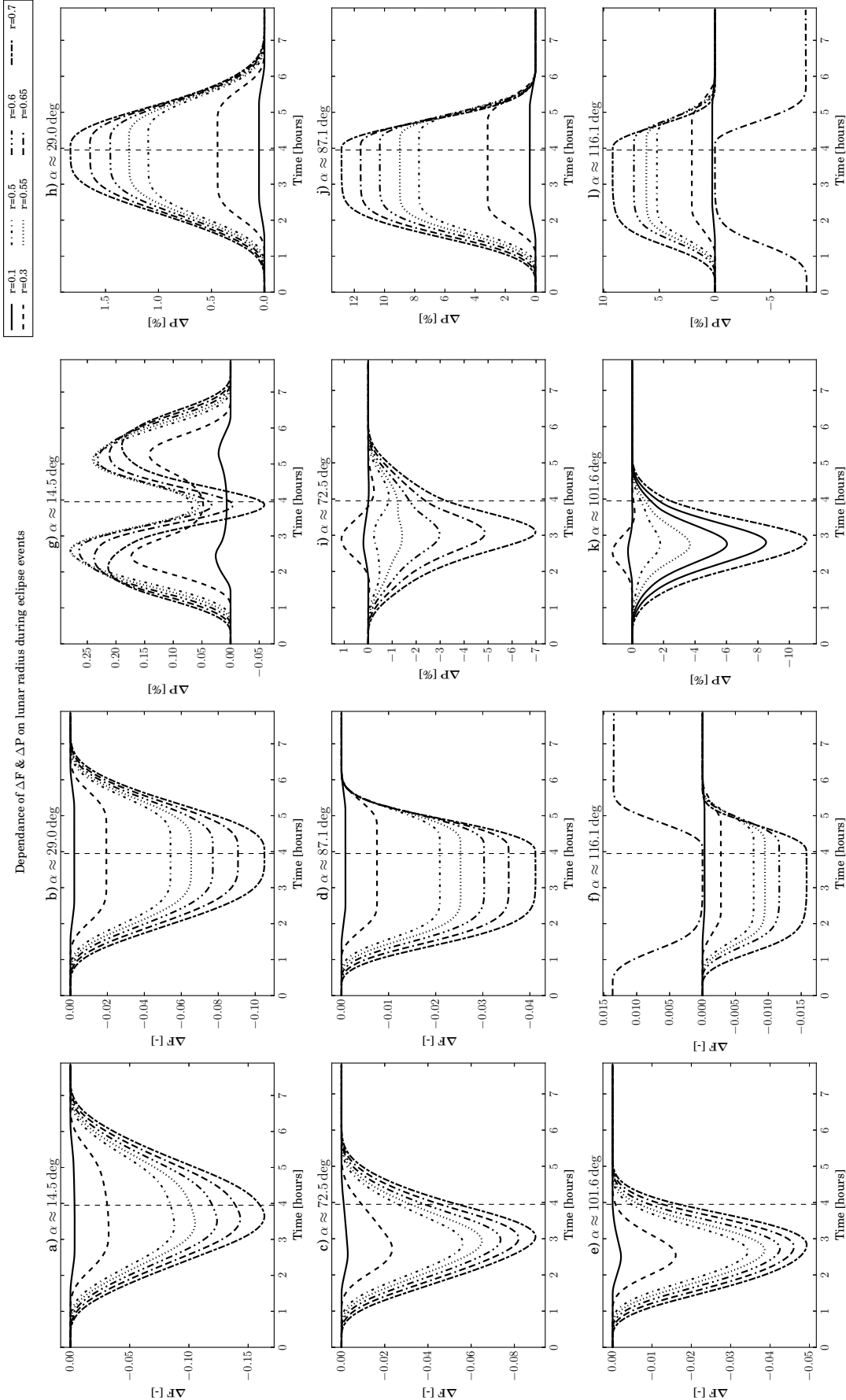


Figure C.14: Difference between the planet-moon system reflected flux and the continuum background flux signal, ΔF , (a) (b) (c) (d) (e) (f), and difference between the unresolved degree of polarization and the background signal, ΔP , (g) (h) (i) (k) (l), as a function of relative time, for increasing lunar-to-planetary radius ratio r . Results are shown for various planetary eclipses (a) (c) (e) (g) (i) (k), and lunar eclipses (b) (d) (f) (h) (j) (l) at increasing phase angles α . The vertical dashed line corresponds to the time of concentric alignment of the planet and moon bodies as seen from the observer. Fluxes have been normalized so that F at $\alpha = 0^\circ$ equals the geometric albedo of the planet-moon system. The simulation time resolution is $\Delta t = 3$ min.

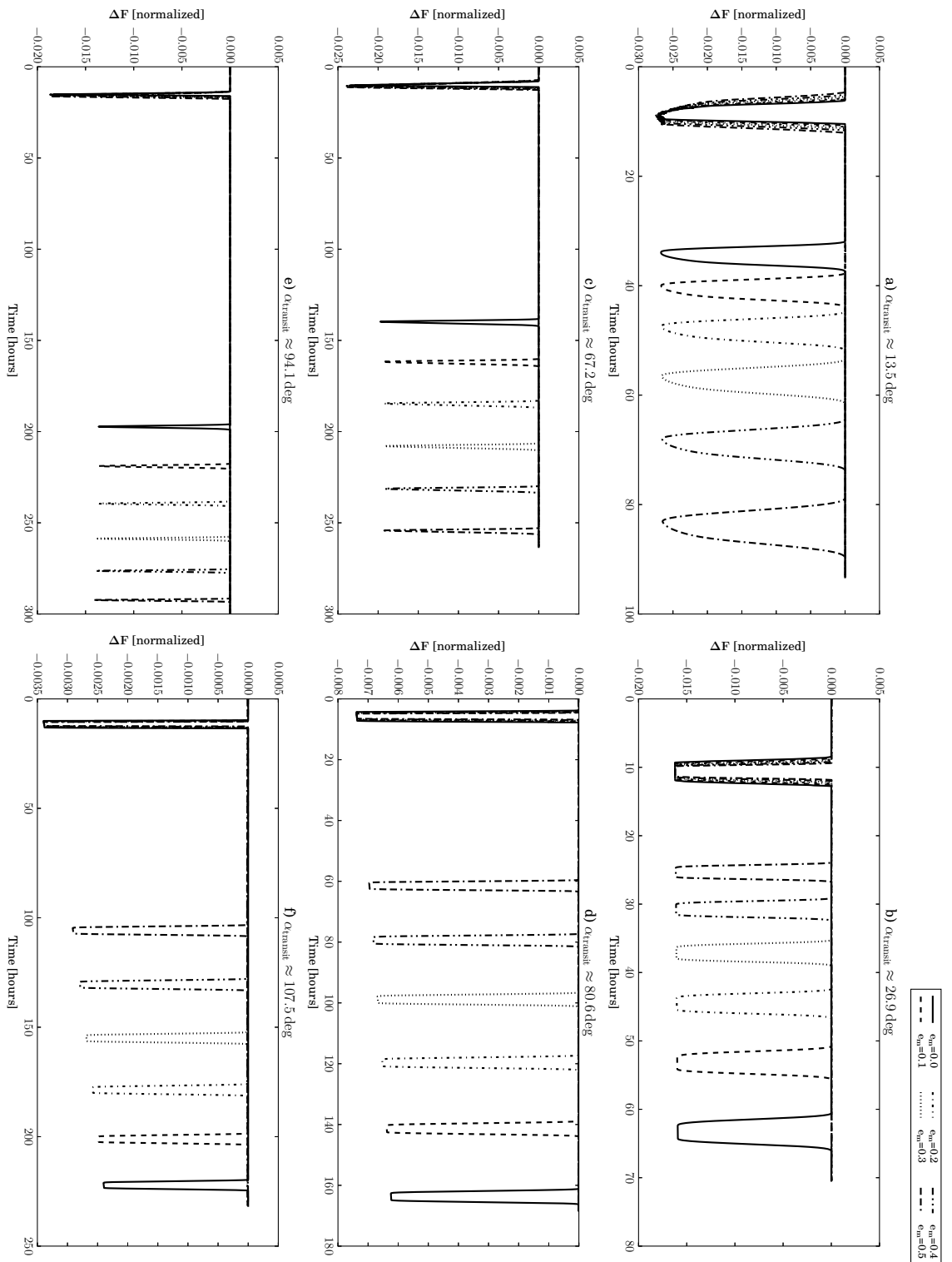


Figure C.15: Difference between the planet–moon system reflected flux and the continuum background flux signal, ΔF , during a series of lunar transits and subsequent planetary eclipses (a)–(e) and planetary transits and subsequent lunar eclipses (b)–(f) as a function of relative time for increasing lunar eccentricity. Fluxes have been normalized so that F at $\alpha = 0^\circ$ equals the geometric albedo of the planet–moon system. The simulation time resolution is $\Delta t = 3\text{min}$.

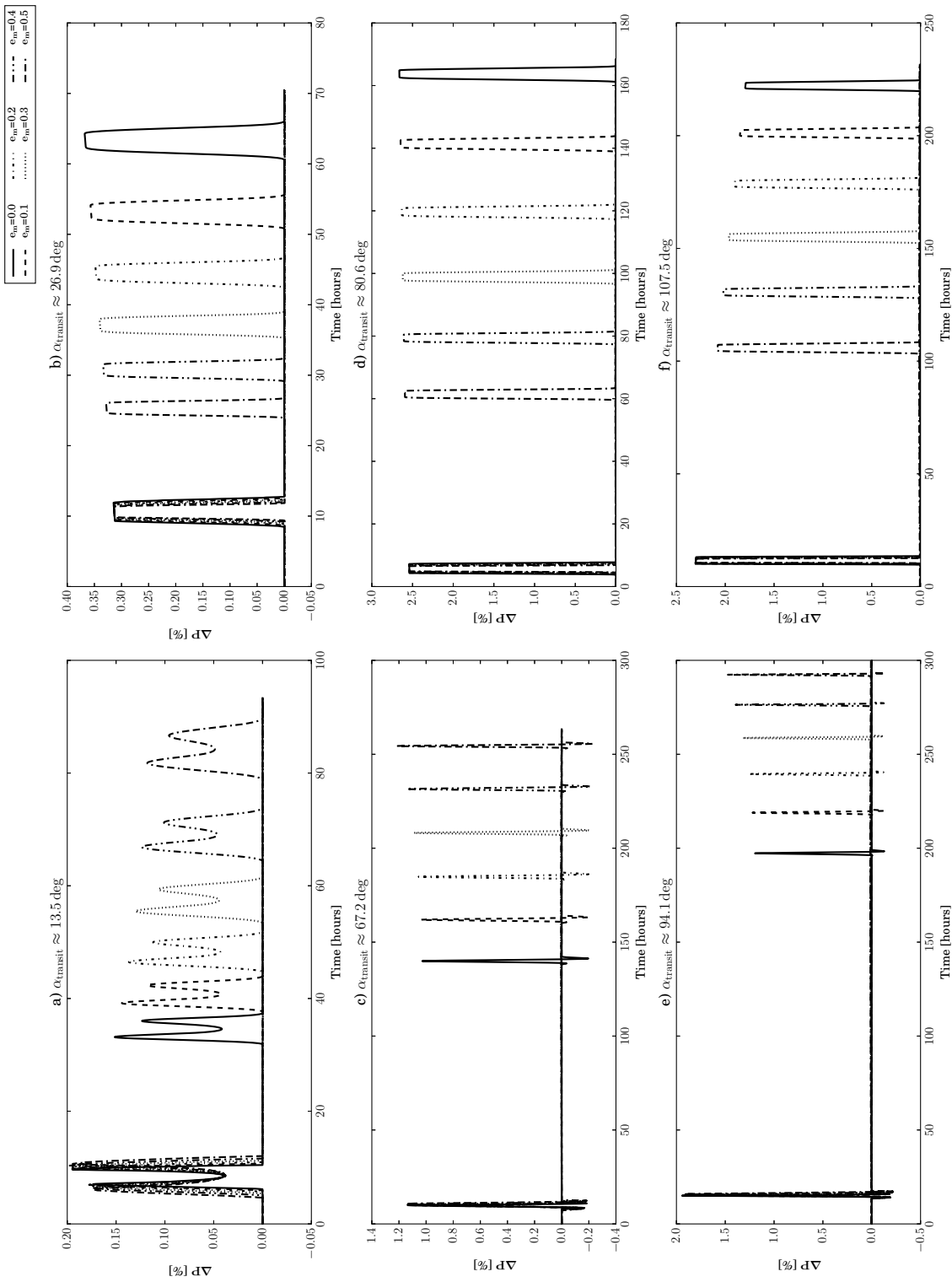


Figure C.16: Difference between the planet–moon system degree of polarization and the continuum background signal, ΔP , during a series of lunar eclipses (a) (c) (e) and planetary transits and subsequent planetary eclipses (b) (d) (f) as a function of relative time for increasing lunar eccentricity. The simulation time resolution is $\Delta t = 3 \text{ min}$.

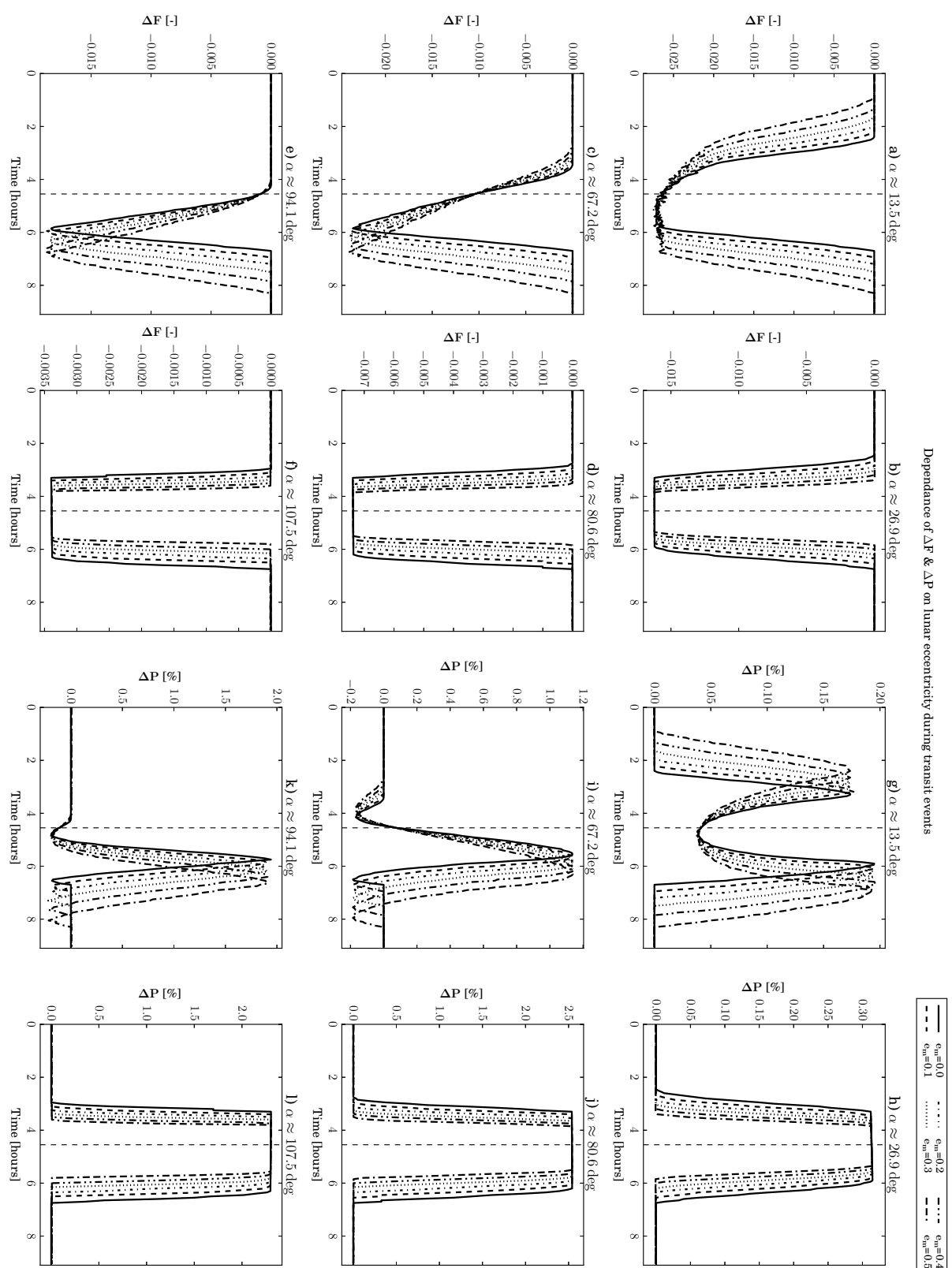


Figure C.17: Difference between the planet-moon system reflected flux and the continuum background flux signal, ΔF , (a) (b) (c) (d) (e) (f), and difference between the unresolved degree of polarization and the background signal, ΔP , (g) (h) (i) (j) (k) (l), as a function of relative time, for increasing moon orbit eccentricity e_{mb} . Results are shown for various lunar transits (a) (c) (e) (g) (i) (k), and planetary transits (b) (d) (f) (h) (j) (l) at increasing phase angles α . The vertical dashed line corresponds to the time of concentric alignment of the planet and moon bodies as seen from the observer. Fluxes have been normalized so that F at $\alpha = 0^\circ$ equals the geometric albedo of the planet-moon system. The simulation time resolution is $\Delta t = 3$ min.

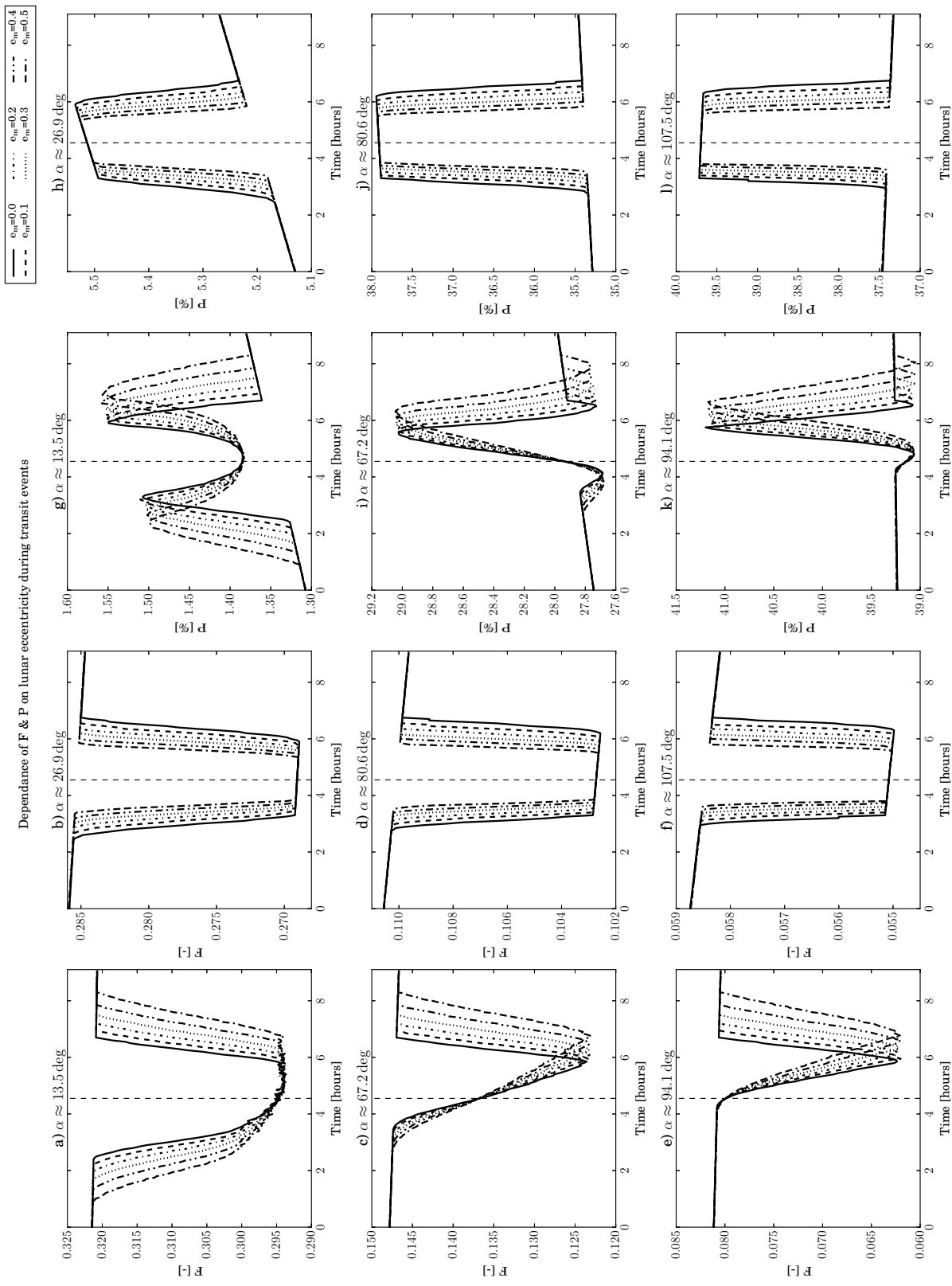


Figure C.18: Unresolved planet-moon system reflected flux, F , (a) (b) (c) (d) (e) (f), and degree of polarization, P , (g) (h) (i) (k) (l) as a function of relative time, for increasing moon orbit eccentricity e_{mb} . Results are shown for various lunar transits (a) (c) (e) (g) (i) (k), and planetary transits (b) (d) (f) (h) (j) (l) at increasing phase angles α . The vertical dashed line corresponds to the time of concentric alignment of the planet and moon bodies as seen from the observer. Fluxes have been normalized so that F at $\alpha = 0^\circ$ equals the geometric albedo of the planet-moon system. The simulation time resolution is $\Delta t = 3 \text{ min}$.

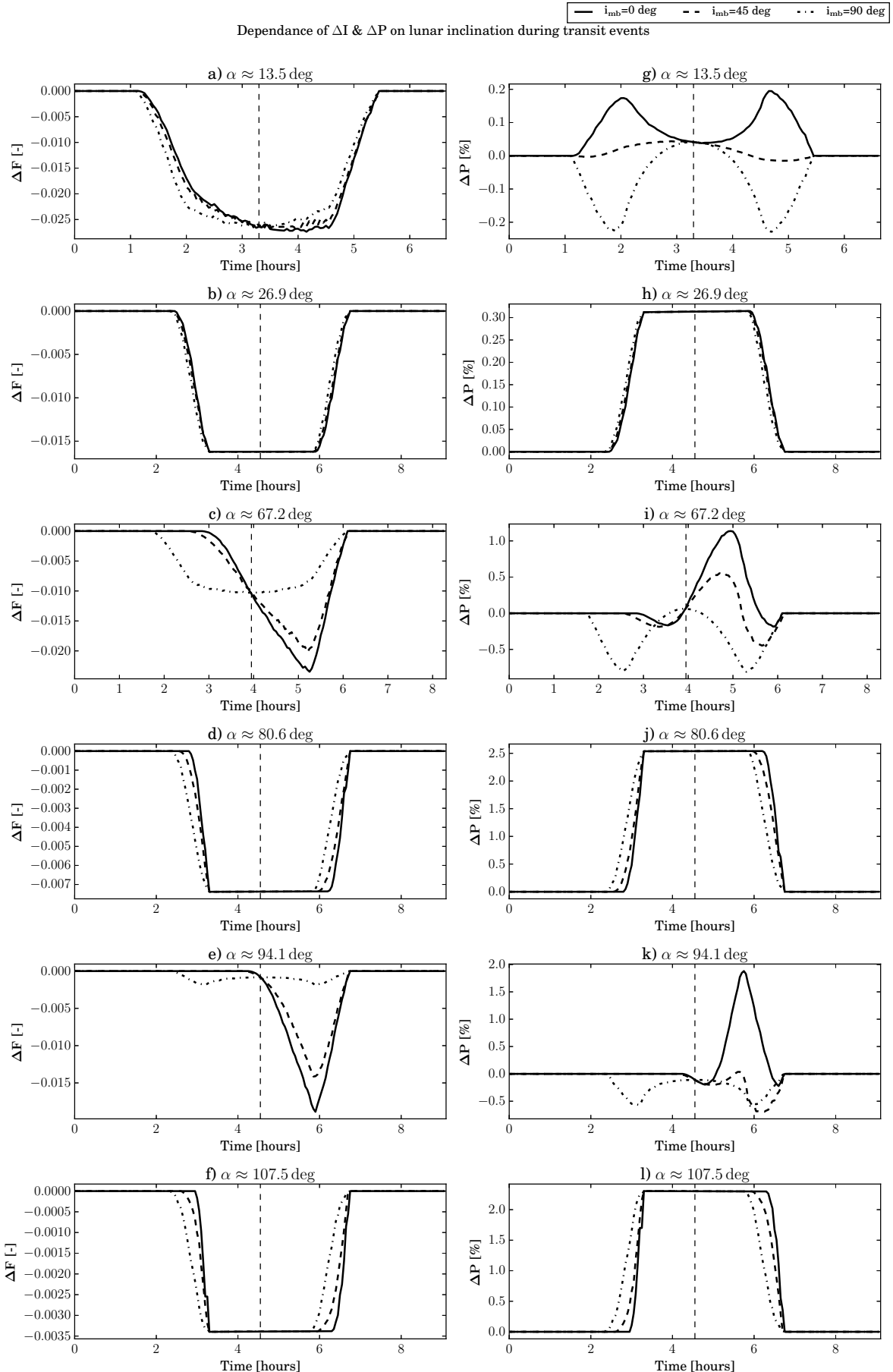


Figure C.19: Difference between the planet–moon system reflected flux and the continuum background flux signal, ΔF , (a) (b) (c) (d) (e) (f), and difference between the unresolved degree of polarization and the background signal, ΔP , (g) (h) (i) (j) (k) (l), as a function of relative time, for increasing moon orbit inclination i_{mb} . Results are shown for various lunar transits (a) (c) (e) (g) (i) (k), and planetary transits (b) (d) (f) (h) (j) (l) at increasing phase angles α . For this simulation, the lunar line of nodes is set to match the planet–observer direction. The vertical dashed line corresponds to the time of concentric alignment of the planet and moon bodies as seen from the observer. Fluxes have been normalized so that F at $\alpha = 0^\circ$ equals the geometric albedo of the planet–moon system. The simulation time resolution is $\Delta t = 3 \text{ min}$.

D

ExoPy introduction manual

In this appendix we attach a draft introductory manual for the *ExoPy* tool.

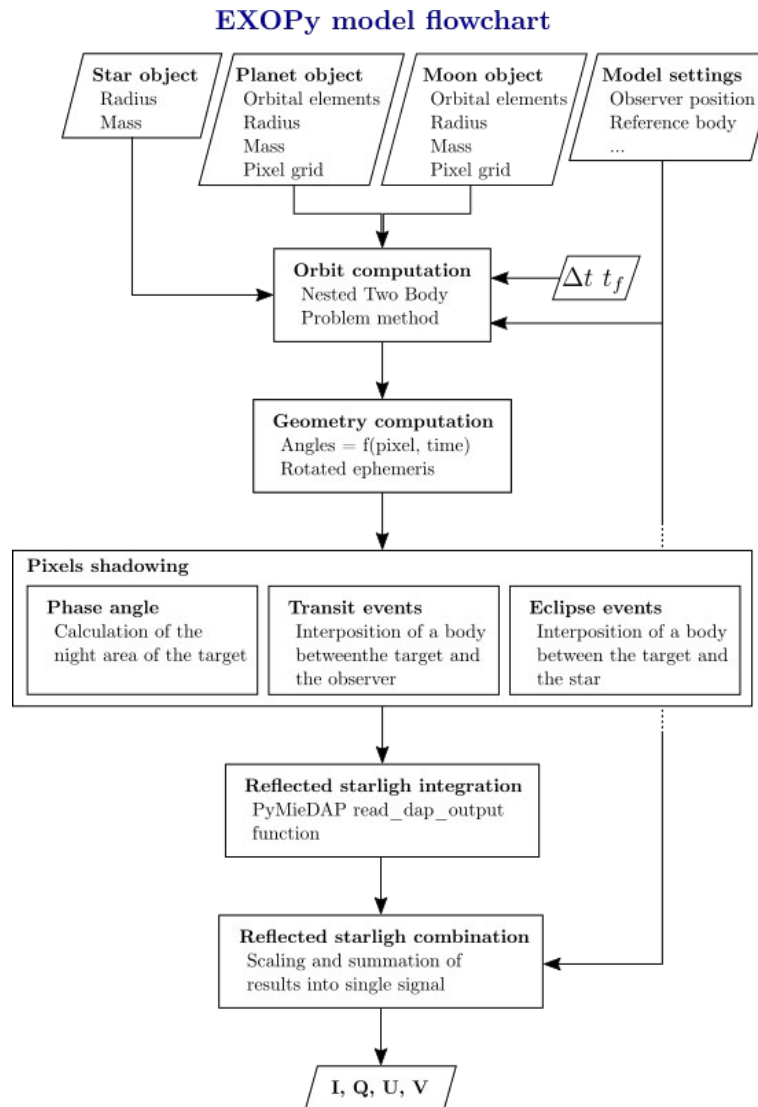
Introduction to EXOPy

Installation

The latest version of EXOPy is incorporated within the PyMieDAP program. Detailed instructions on how to install PyMieDAP are available through its [documentation file](#).

Overview of the model

A simplified flow diagram sketching the various components of EXOPy and their order of use, the overall inputs/outputs, as well as the interaction with the PyMieDAP tool, is found below.



All computations carried out by the EXOPy tool make use of what we call the 'body' type of python objects. These serve as container for all input parameters and output values, and as interface with the EXOPy functions, for each body involved in the planetary system.

Besides the user needs to specify a set of basic model settings such as which is the observer position with respect to the planetary system reference frame or which is the reference body used for combining the reflected starlight. More details on this operations are given afterwards in this tutorial.

Once defined and specified the inputs for each body object, the computation of the orbits can be conducted, as well as the determination of the geometric values which are required for further steps. Afterwards, the pixel shadowing of each body due to phase angle, transit and/or eclipse events are computed as follows from the flowchart.

Finally, the flux and polarization status of the reflected starlight by each body is computed by using some of the modules at PyMieDAP and the various results can be merged in a single planetary system signal.

```
In [1]: %matplotlib inline
import numpy as np
import matplotlib.pyplot as plt
```

Getting started

The EXOPy model is contained in the PyMieDAP model folder. To import it, the user can type:

```
In [2]: import pymiedap.exopy as exopy
```

being exopy the acronym employed for the model.

The functions contained in the exopy tool are:

- **exopy.new_body**: Function generating 'body objects'.
- **exopy.new_system**: Function loading a pre-defined system of 'body' objects.
- **exopy.cfg**: Configuration parameters of the EXOPy model.
- **exopy.compute**: EXOPy object containing all functions required to perform the simulation.
- **exopy.plot**: EXOPy object containing shorcut functions for visualization of results.
- **exopy.run_simulation**: Pre-defined script containing basic instructions for running an EXOPy simulation.

The first step towards carrying out the required simulations is the definition of the bodies involved. In this particular case, we're trying to model the Earth-Moon-Sun system, so:

```
In [3]: Earth = exopy.new_body('Earth', 'planet')
Moon = exopy.new_body('Moon', 'moon')
Sun = exopy.new_body('Sun', 'star')

✓ New planet Earth created!
✓ New moon Moon created!
✓ New star Sun created!
```

Basic properties of these bodies which need to be provided to EXOPy are found under the *properties* category, i.e. radius and mass (R, m).

```
In [4]: Earth.properties.R = 6370E3 # [m]
```

```
In [5]: Earth.properties.m = 6E24 # [kg]
```

This input values, together with the orbital elements of the bodies, can be stored at the `exopy.py` script and therefore retrieved through the `exopy.new_system` functions as:

```
In [6]: [Moon, Earth, Sun] = exopy.new_system('s_system')

! The object has been overwritten in the body list...
✓ New planet Earth created!
! The object has been overwritten in the body list...
✓ New moon Moon created!
! The object has been overwritten in the body list...
✓ New star Sun created!
```

where 'edge-on' is the string associated to the solar system predefined edge-on scenario (Earth-Moon-Sun system).

The orbital elements of the bodies can be modified as follows:

```
In [7]: Moon.orbital_elements.omega = 180
Earth.orbital_elements.omega_b = 300
```

Before continuing, the user needs to set up a couple of model configuration parameters:

- **Observer's location**: characterized by the spherical coordinates given by an azimuth and elevation angle in degrees.

```
In [8]: exopy.cfg.az = 0 # [deg]
exopy.cfg.el = 0 # [deg]
```

- **Reference elements:** reference line and reference body for the computation of reflected starlight.

```
In [9]: exopy.cfg.ref_body = 'Earth'
exopy.cfg.ref_line = 'Earth'
```

Documentation

All functions, methods and objects in EXOPy are accompanied with a brief documentation providing information regarding the purpose, usage and/or parameters stored in each case, as well as units and format information.

The user can access this documentation by typing '?', e.g.:

```
In [10]: exopy?
```

```
In [11]: exopy.new_system?
```

```
In [12]: Earth?
```

```
In [13]: Earth.grid?
```

Moreover, methods and objects can be mentioned and/or called for getting generic information regarding the parameters and variables involved or specific values at a particular time (pixel) index, e.g.:

```
In [14]: Earth.properties
```

```
Out[14]:
Relation of body properties:
```

```
Mass: m = 5.972e+24 kg
Radius: R = 6371008.0 m
```

Being the orbital elements already pre-defined, the user can print an overview of them as:

```
In [15]: Earth.orbital_elements
```

```
Out[15]:
Relation of orbital elements:
```

```
Bar. semi-major axis (a_b): 1.5e+11 m
Bar. eccentricity (e_b): 0.0167[-]
Bar. inclination (i_b): 90.0 deg
Bar. argument of periapsis (omega_b): 300 deg
Bar. right ascension of the ascending node (Omega_b): 0.0 deg
Bar. time from periapsis passage (t0_b): 0.0 s
Bar. eccentric anomaly (E_bs) = () array
Bar. mean anomaly (M_bs) = () array
Bar. true anomaly (nu_bs) = () array
```

```
In [16]: Moon.orbital_elements
```

```
Out[16]:
Relation of orbital elements:
```

```
Semi-major axis (a): 379750640.981 m
Eccentricity (e): 0.0549[-]
Inclination (i): 5.145 deg
Argument of periapsis (omega): 180 deg
Right ascension of the ascending node (Omega): 0.0 deg
Time from periapsis passage (t0): 0.0 s
Eccentric anomaly (E_mb) = () rad
Mean anomaly (M_mb) = () rad
True anomaly (nu_mb) = () rad
```

These values can be modified at any moment. For this, it is required to understand the conventions established, explained below.

Defining and computing the orbit position

The orbital motion of the moon and planet around the star is computed under the assumption of a Nested Two Body Problem, i.e. it is assumed that the star does not alter the movement of the moon around the planet-moon system barycentre, while the barycentre of the system describes a Kepler orbit around the star.

The input orbital elements required for carrying out the orbits computation is different for planet and moon type of bodies, while the star does not play any role. By convention, for a planet type of object we store the information of the planet-moon system barycentre:

- **a_b**: semi-major axis of the planet-moon system barycentre's orbit around the star [m] (float)
- **e_b**: eccentricity of the planet-moon system barycentre's orbit around the star [-] (float)
- **i_b**: inclination of the planet-moon system barycentre's orbit around the star [deg] (float)
- **Omega_b**: Right Ascension of the Ascending Node of the planet-moon system barycentre's orbit around the star [deg] (float)
- **omega_b**: Argument of periapsis of the planet-moon system barycentre's orbit around the star [deg] (float)
- **t0_b**: time since last periapsis passage of the planet-moon system barycentre's orbit around the star [s] (float)

In the case of the moon, the information of the moon's orbit around the planet-moon system barycentre is stored as:

- **a**: semi-major axis of the moon's orbit around the planet-moon system barycentre [m] (float)
- **e**: eccentricity of the moon's orbit around the planet-moon system barycentre [-] (float)
- **i**: inclination of the moon's orbit around the planet-moon system barycentre [deg] (float)
- **Omega**: Right Ascension of the Ascending Node of the moon's orbit around the planet-moon system barycentre [deg] (float)
- **omega**: Argument of periapsis of the moon's orbit around the planet-moon system barycentre [deg] (float)
- **t0**: time since last periapsis passage of the moon's orbit around the planet-moon system barycentre [s] (float)

Specified these values, the user can easily compute the position of the bodies via the `compute.orbit` exopy function:

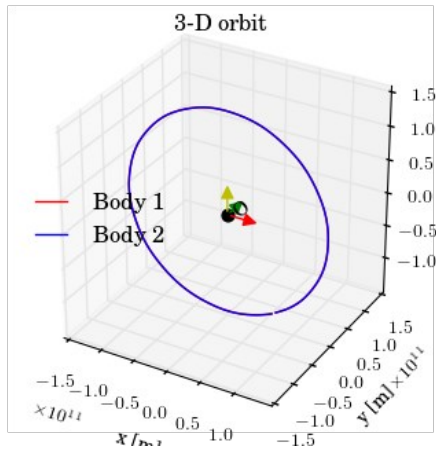
```
In [17]: [Moon, Planet, Star] = exopy.compute.orbit(Moon, Earth, Sun, delta_t = 60*60*24, final_t = 365*60*60*24)
```

✓ The trajectories of Moon, Earth, and Sun have been calculated.

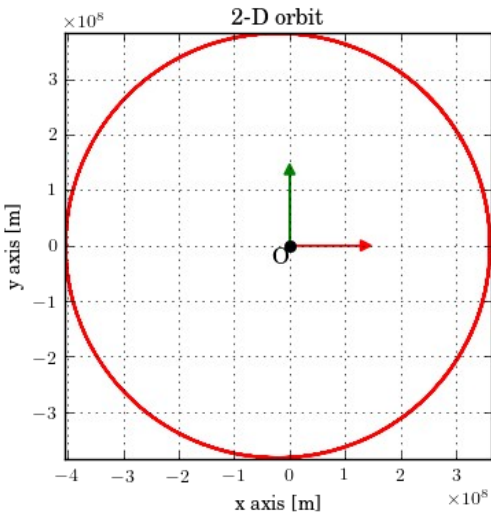
where the last two input parameters are the time step and final time of computation in seconds.

Use can be made of the `exopy.plot` functions to get an overview of the computed orbits.

```
In [18]: exopy.plot.XYZorbit(Earth.ephemeris.position3D_s, Moon.ephemeris.position3D_s)
```



```
In [19]: exopy.plot.xyorbit(Moon.ephemeris.position2D_mp)
```



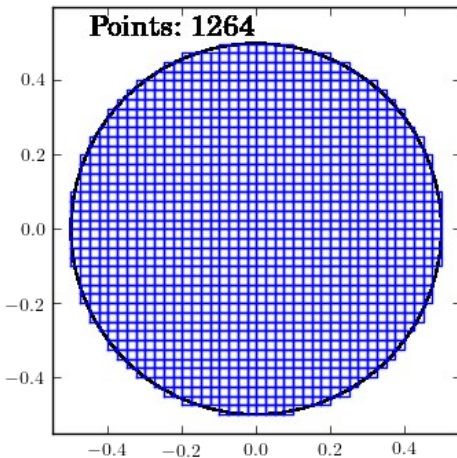
The employed `compute.orbit` exopy function computes the 3D and 2D position of each body with time and stores it inside the `ephemeris` category. However, it does not compute the angles of interest. For this, use is made of the `exopy.compute.geometry` function.

```
In [20]: # from pymiedap.exopy_functions import display_animation
In [21]: # animation = display_animation(exopy.plot.anim_orbit(Moon.ephemeris.time, Moon.ephemeris.position3D_s));
In [22]: # animation
```

Defining and computing the geometry of the problem

As a first step towards the computation of the full geometry of the problem (pixel and time dependent) is the definition of the grids to be used for the planet and moon bodies through the function `set_grid`. In this case, a regular squared pixels grid of 40 elements along the equator is set for the planet.

```
In [23]: Earth.grid.set_grid(grid_type = 'square', Nsq = 40)
Square grid created!
In [24]: Earth.grid.show_grid()
```

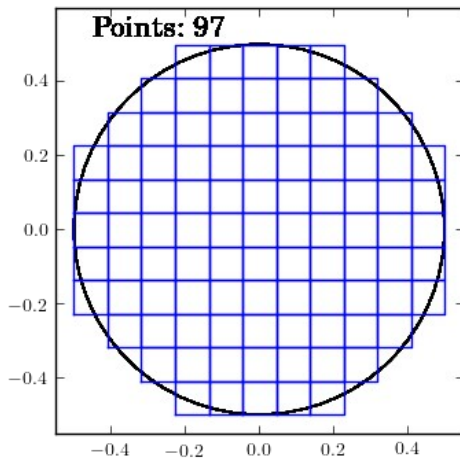


For the moon, the closest integer number of pixels along the equator that matches the ratio of radii between the planet and moon is selected:

```
In [25]: Moon.grid.set_grid(grid_type = 'square', Nsq = int(np.round(Earth.grid.Nsq*Moon.properties.R/Earth.properties.R)))
```

Square grid created!

In [26]: `Moon.grid.show_grid()`



The function `exopy.compute.geometry` is then used for computing the three-dimensional geometry of the planet-moon system:

In [27]: `Earth, Moon, Sun= exopy.compute.geometry([Earth, Moon, Sun])`

... geometry of planet Earth

... geometry of moon Moon

... geometry of star Sun

The new information generated is stored under the category `geometry` of each body. For instance, at time index 100 we have for planet Earth:

In [28]: `Earth.geometry(100, unit = 'deg')`

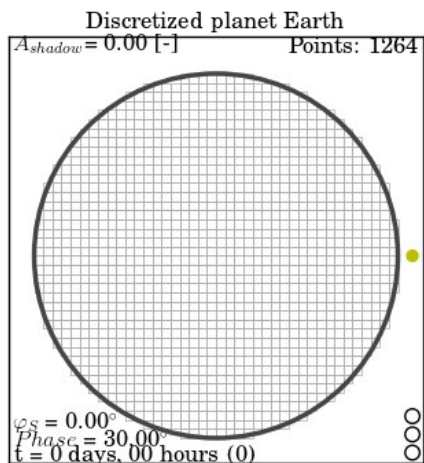
Relation of body geometry variables at time index 100:

```
phase_angle      = 130.066789049 deg
ref_line_angle   = 0.000173827770457 deg
ref_plane_angle  = 0.000173827770457 deg
ref_plane_to_ref_line_angle = 0.0 deg
solar_azimuth_angle = 0.0 deg
alpha = 49.9332109513 deg
```

At this point, the planet and moon bodies are considered to be fully illuminated as seen from the observer's position, as the plot below shows:

In [30]: `exopy.plot.shadow_d(Earth, t=0)`

```
⇒ Plotting shadow of planet Earth at t =0.0 seconds
... Caution: discrete phase data not available for planet Earth!
... Caution: discrete transit data not available for planet Earth!
... Caution: discrete eclipse data not available for planet Earth!
```



In order to compute the pixel darkening due to shadowing effects the user can employ the phase, transits and eclipses functions.

Computing the pixel darkening

ExoPy allows to compute the pixel darkening due to three different sources:

- **Phase angle:** Along the orbit, just part of the body will be visible from the observer's position. The function `exopy.compute.phases` takes care of this factor:

```
In [31]: Earth, Moon = exopy.compute.phases([Earth, Moon], Sun)
```

... phase of planet Earth

... phase of moon Moon

- **Transit events:** The interposition of one body between the targeted body and the observer results in a partial (or total) blockage of the reflected light:

```
In [32]: Moon, Earth, Sun = exopy.compute.transits([Moon, Earth, Sun])
```

... transits between moon Moon and planet Earth

... transits between moon Moon and star Sun

... transits between planet Earth and star Sun

- **Eclipse events:** The interposition of one body between the targeted body and the star results in a gradual blockage of the reflected light:

```
In [38]: Moon, Earth = exopy.compute.eclipses([Moon, Earth], Sun)
```

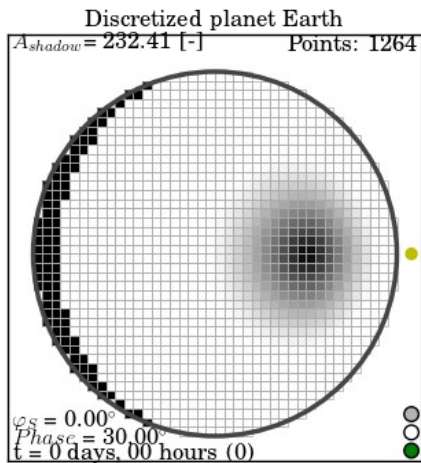
... eclipses between moon Moon and planet Earth

... eclipses between planet Earth and moon Moon

In our example, we can observe the moon eclipsing the Earth at time index equal 0:

```
In [39]: exopy.plot.shadow_d(Earth, t = 0)
```

⇒ Plotting shadow of planet Earth at t = 0.0 seconds



At this point, we can compute the reflected starlight.

Setting the atmosphere and surface properties

Computing the reflected starlight of each body requires to specify which are the surface and atmosphere properties as well as at which wavelength are we working on. For this, use is made of the PyMieDAP *atmosphere* class which can be configured according to the advice given in [here](#).

Alternatively, the user can employ one of the pre-defined atmospheric models and tune it through any of the available input values using the exopy module called *atm_model*.

In this case, the Earth has been granted with a cloudy model in the blue, while a lambertian surface model of albedo 0.1 has been employed for the Moon surface:

```
In [41]: Earth.atmosphere = exopy.atm_models.Earth()[0]
Moon.atmosphere = exopy.atm_models.Moon(alb = 0.1)[0]
```

Computing reflected starlight

As a last step, the reflected starlight at each pixel is integrated along the entire disk for computing the polarized reflected signal of each body independently. This is done through the function *exopy.compute.int_radiance* as:

! Mind that this process can take a long time depending on the Fourier files to be read, the number of pixels, and the time vector to be covered.

```
In [42]: [Earth, Moon] = exopy.compute.int_radiance([Earth, Moon])
... integrating radiance on planet Earth disk
```

```
1 out of 365
Beginning of Mie program
Wavelength 00.400
End of Mie program
Aerosols mixed!
Beginning of Mie program
Wavelength 00.400
End of Mie program
Aerosols mixed!
Beginning of Mie program
Wavelength 00.400
End of Mie program
Aerosols mixed!
Beginning of DAP program
Wavelength 00.400
C.sc.00.400
C.sc.00.400
C.sc.00.400
fou_0.400.dat
End of DAP program
2 out of 365
3 out of 365
4 out of 365
```

```

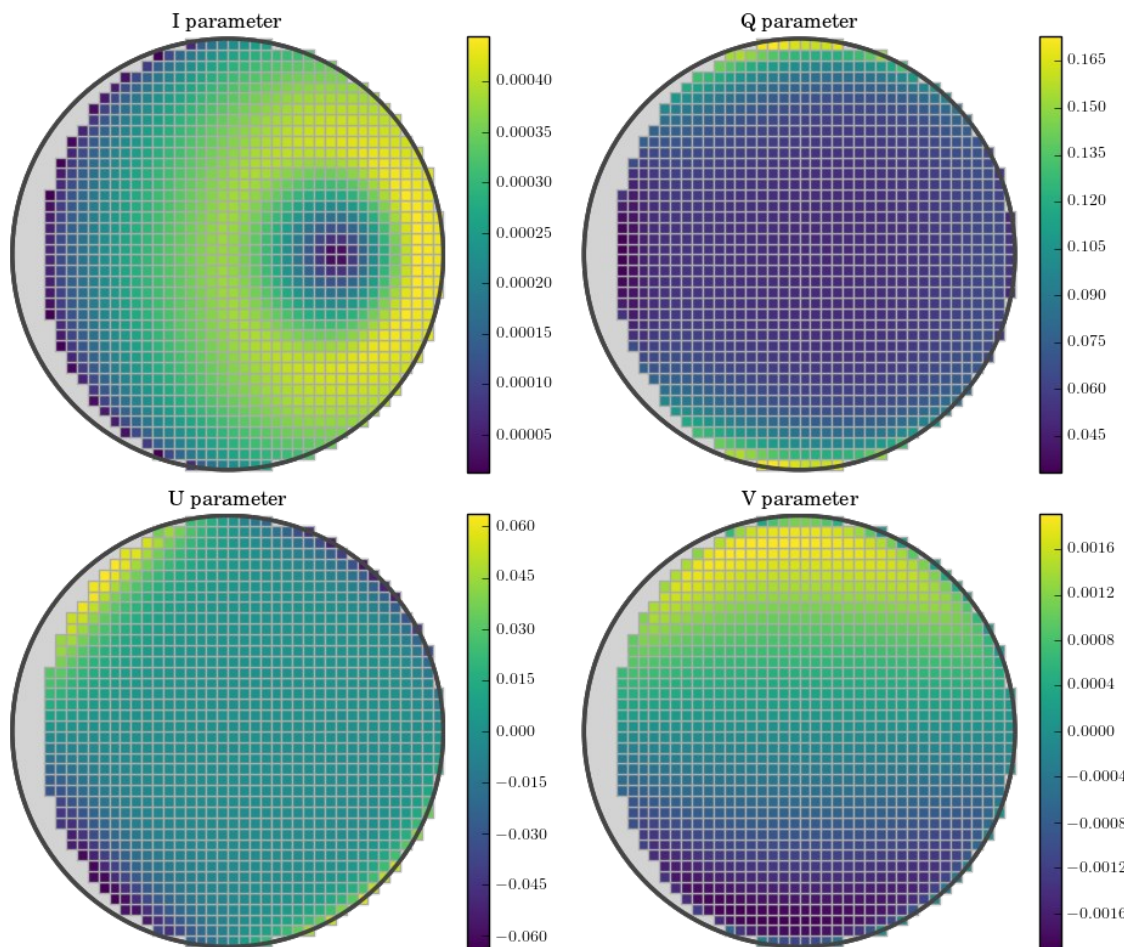
341 out of 365
342 out of 365
343 out of 365
344 out of 365
345 out of 365
346 out of 365
347 out of 365
348 out of 365
349 out of 365
350 out of 365
351 out of 365
352 out of 365
353 out of 365
354 out of 365
355 out of 365
356 out of 365
357 out of 365
358 out of 365
359 out of 365
360 out of 365
361 out of 365
362 out of 365
363 out of 365
364 out of 365
365 out of 365
1.87932401498 mins

```

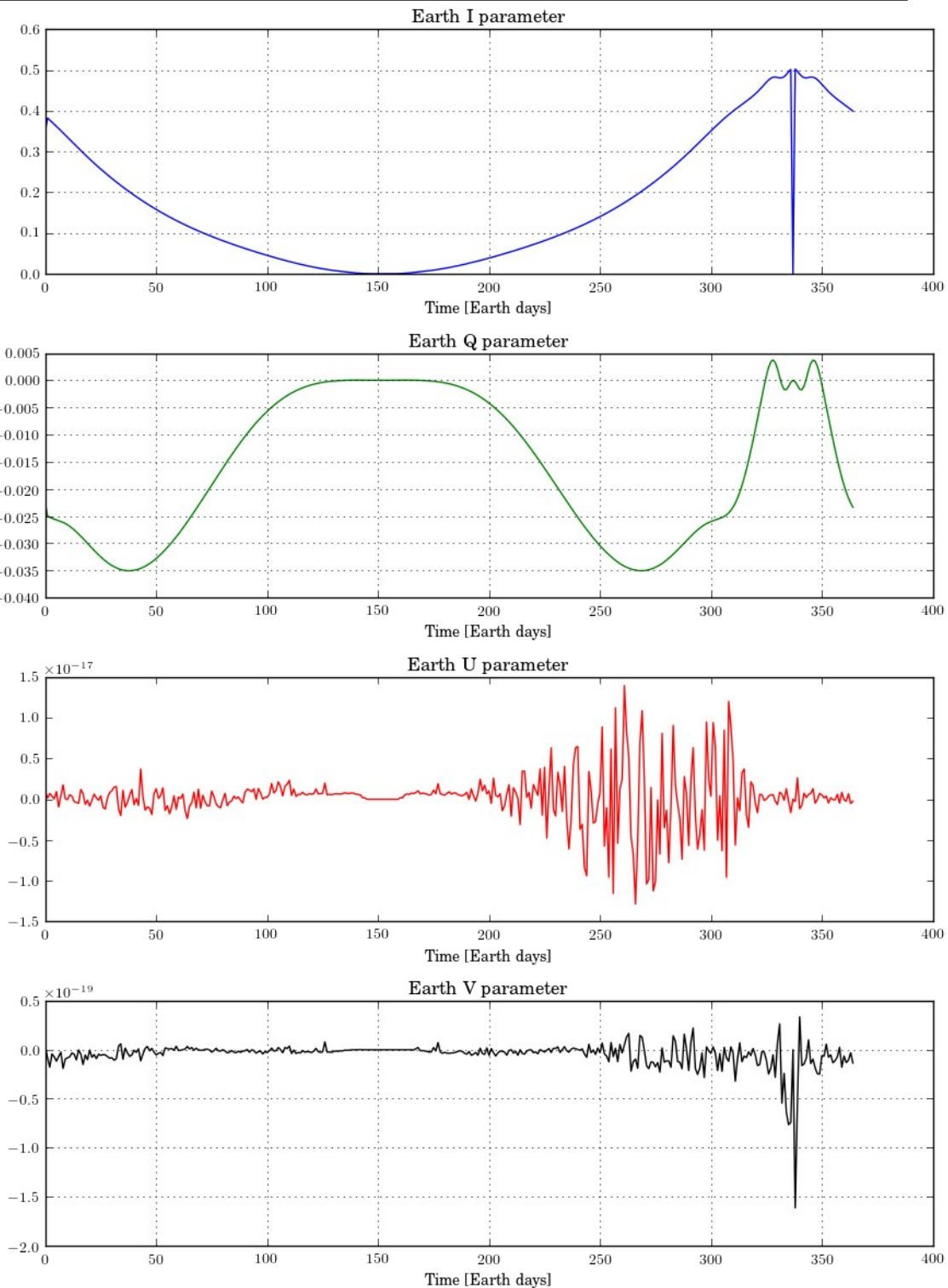
As output, the discretized reflected signals as well as the integrated signals are obtained. These can be easily plotted through some of the pre-defined display functions as follows:

In [43]: `exopy.plot.radiance_d(Earth)`

⇒ Plotting stokes parameters of planet Earth at t = 0.0 seconds



In [44]: `exopy.plot.radiance(Earth)`

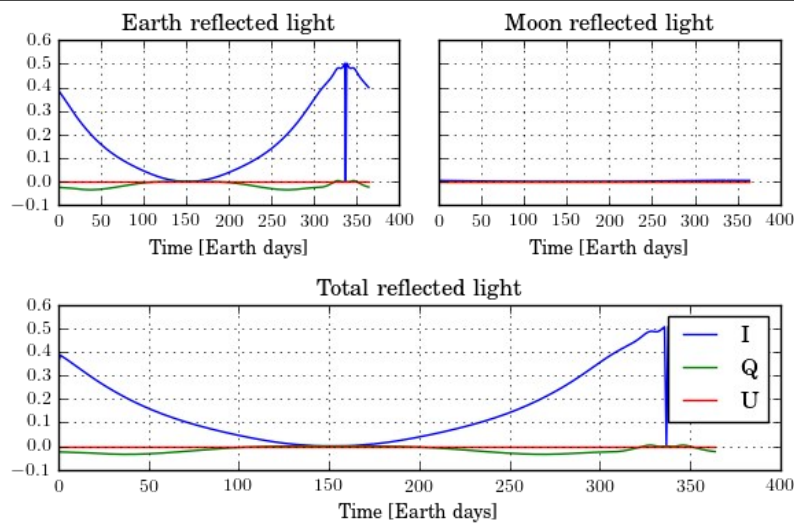


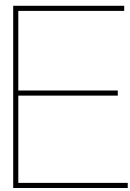
Finally, the individual signals are combined taking one particular body and one particular scattering plane as reference through the `exopy.compute.combine` function.

```
In [47]: I,Q,U,V,P,Chi = exopy.compute.combine([Earth, Moon])
... combining radiance results
```

The final results can be displayed for the overall planetary system:

```
In [48]: exopy.plot.detail_radiance([Earth,Moon], I, Q, U, V)
```





Reproduction of EPSC 2017 abstract

Reproduction of the European Planetary Science Congress (EPSC) 2017 submitted abstract on the work carried out during this Master's Thesis, accepted for poster presentation (19 September 2017 – 20 September 2017).

Traces of exomoons in flux and polarization signals of starlight reflected by exoplanets

J. Berzosa-Molina, D. M. Stam, and L. Rossi
 Faculty of Aerospace Engineering, Delft University of Technology, Delft, The Netherlands (j.berzosamolina@gmail.com)

Abstract

The detection of moons around extrasolar planets is one of the main focuses of current and future observatories. These silent companions contribute to the planets' observed signals but are barely detectable with current methods. Numerous gaseous exoplanets are known to orbit in the habitable zones of stars, and the expected abundance of natural satellites and their diversity in composition make them ideal targets when looking for habitable celestial bodies. And moons are suspected to play key roles in stabilizing a planet's rotational axis and hence its climate. We show that an exomoon orbiting an Earth-like exoplanet could be identified by measuring the flux and polarization of starlight reflected by the planet-moon system, allowing the characterization of their orbital motions and physical properties.

1. Introduction

Current instruments such as Spectro-Polarimetric High-contrast Exoplanet Research (SPHERE) on the Very Large Telescope (VLT) and Gemini Planet Imager (GPI) on the Gemini North telescope, together with the Exoplanet Imaging Camera and Spectrograph (EPICS) on the future European Extremely Large Telescope (E-ELT), have capabilities to perform high-contrast, direct imaging and characterization of exoplanets, both through spectroscopy and polarimetry.

Previous modelling of light curves and polarization signals [3, 9, 10, 8] shows that polarimetry not only increases the contrast between the exoplanet and its star, but can also unveil the structure and composition of the atmosphere and surface. Here, we take one step further by analysing how the presence of an exomoon influences the flux and polarization signals of an Earth-like exoplanet. The influence is two-fold: 1. the flux reflected by the planet-moon system increases according to the moon's reflection properties, and 2. the transits and eclipses between the moon, planet, and star modulate the observable signal (see Fig. 1).

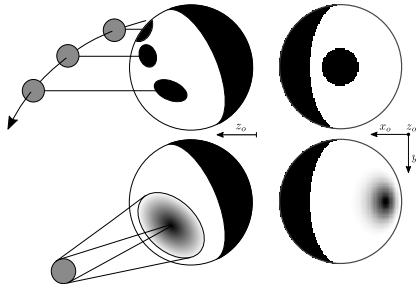


Figure 1: Sketches of a lunar transit of the planet (top left), an eclipse (bottom left), the discretization during a lunar transit (top right), and during a planetary eclipse (bottom-right). The z_o -axis points towards the observer.

2. Numerical model and results

We describe the flux and polarization of starlight that is reflected by a spatially unresolved planet-moon system by a Stokes vector [2] computed using an adding-doubling radiative transfer model [1], assuming the starlight is unpolarized [5]. Our model planet has a Lambertian surfaces with horizontally homogeneous atmospheric layers filled with gas and/or aerosol particles on top, and our model moon has a Lambertian surface without atmosphere.

The observable Stokes vectors at a certain epoch are a function of the illumination and viewing geometries of each body, which depend on the bodies' phase angle α (the angle between the direction to the star and the observer measured from the centre of the body), and on the orbital geometry of the bodies involved, as that can lead to situations in which they interfere with each other. In particular, we have modelled the following interferences (see Fig. 1):

- A transit: the interposition of a body between the observed target and the observer, partially (or to-

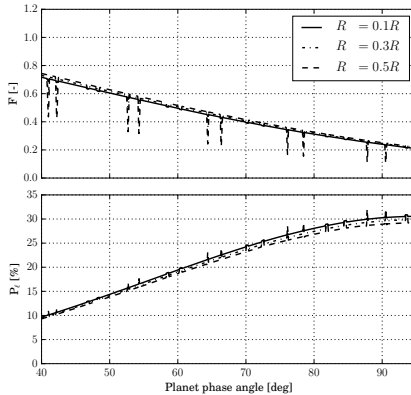


Figure 2: Flux (top) and degree of linear polarization (bottom) of an edge-on system consisting of an Earth-like planet and an exomoon with surface albedo 0.1, for different moon radii R_m expressed in the planet radius R_p .

tally) blocking the light that is reflected by the target while adding reflected light from the body.

- An eclipse: the interposition of a body between the star and the observed target, casting a shadow on (part of) the reflecting target.

We compute the orbital dynamics and geometries using the 'nested two-body' model introduced in [7, 6], that is based on the assumption that the motion of the planet and moon around the planet–moon system barycentre, as well as the motion of this barycentre around the star, can be described by Keplerian orbits.

Fig. 2 shows the flux and degree of linear polarization obtained as the exoplanet and moon transit and eclipse each other in a zero-eccentricity, system that is viewed edge-on, for different moon radii R_m .

3. Discussion

The traces of exomoons that we find in our numerical simulations (see Fig. 2), show up as remarkable signatures in the signal of the spatially unresolved planetary system. The flux and polarization variations due to eclipses and transits are of the same order of magnitude as the overall signal and can span several hours (depending on the moon radius with respect to the planet and the orbital periods). The observable signals appear similar to those obtainable with the well-

known transit photometry technique applied on stars except for delivering enhanced contrast between bodies and a greater frequency of observation, although with much less photons and thus requiring much larger telescopes.

4. Conclusion

We aim to investigate the correlation between the flux and degree of polarization of the reflected starlight and the orbital characteristics of the planet-moon system. The results obtained for an Earth-like planet will be compared to those for a giant Jupiter-like planet, analysing the impact of using varying atmospheric models. We also aim at estimating the required instrument radiometric and polarimetric accuracy, assessing the feasibility of exomoon discoveries through polarimetry with current and future technology [4].

References

- [1] de Haan, J. F., Bosma, P. B. and Hovenier, J. W.: The adding method for multiple scattering calculations of polarized light, *A&A* 183, 371-391, 1987.
- [2] Hansen, J. E. and Travis, L. D.: Light scattering in planetary atmospheres, *Space Sci. Rev.* 16, 527-610, 1974.
- [3] Karalidi, T., Stam, D. M. and Hovenier, J. W.: Looking for the rainbow on exoplanets covered by liquid and icy water clouds, *A&A* 548, A90, 2012.
- [4] Keller, C. U., Schmid, H. M., Venema, L. B., et al.: EPOL: the exoplanet polarimeter for EPICs at the E-ELT, *Proc. SPIE*, 2010.
- [5] Kemp, J. C., Henson, G. D., Steiner, C. T. and Powell, E. R.: The optical polarization of the Sun measured at a sensitivity of parts in ten million, *Nature*, 326, 270-273, 1987.
- [6] Kipping, D. M.: How to weigh a star using a moon, *MNRAS: Letters*, Oxford University Press, 409, L119-L123, 2010.
- [7] Kipping, D. M.: Transit Timing Effects Due to an Exomoon (in *The Transits of Extrasolar Planets with Moons*), Springer Berlin Heidelberg, 2011.
- [8] Seager, S., Whitney, B. A. and Sasselov, D. D.: Photometric Light Curves and Polarization of Close-in Extrasolar Giant Planets, *ApJ* 540, 504, 2000.
- [9] Stam, D. M.: Spectropolarimetric signatures of Earth-like extrasolar planets, *A&A*, 482, 989-1007, 2008.
- [10] Stam, D. M., Hovenier, J. W. and Waters, L. B. F. M.: Using polarimetry to detect and characterize Jupiter-like extrasolar planets, *A&A*, 428, 663-672, 2004.

Bibliography

- C. B. Agnor and D. P. Hamilton. Neptune's capture of its moon triton in a binary–planet gravitational encounter. *Nature*, 441(7090):192–194, 2006.
- J. W. Barnes and J. J. Fortney. Measuring the oblateness and rotation of transiting extrasolar giant planets. *The Astrophysical Journal*, 588(1):545, 2003.
- L. Ben-Jaffel and G. E. Ballester. Transit of exomoon plasma tori: new diagnosis. *The Astrophysical Journal Letters*, 785(2):L30, 2014.
- D. P. Bennett, V. Batista, I. Bond, C. Bennett, D. Suzuki, J.-P. Beaulieu, A. Udalski, J. Donatowicz, V. Bozza, F. Abe, et al. Moa-2011-blg-262lb: a sub-earth-mass moon orbiting a gas giant primary or a high velocity planetary system in the galactic bulge. *The Astrophysical Journal*, 785(2):155, 2014.
- J.-L. Beuzit, M. Feldt, K. Dohlen, D. Mouillet, P. Puget, J. Antichi, A. Baruffolo, P. Baudoz, A. Berton, A. Boccaletti, M. Carbillet, J. Charton, R. Claudi, M. Downing, P. Feautrier, E. Fedrigo, T. Fusco, R. Gratton, N. Hubin, M. Kasper, M. Langlois, C. Moutou, L. Mugnier, J. Pragt, P. Rabou, M. Saisse, H. M. Schmid, E. Stadler, M. Turrato, S. Udry, R. Waters, and F. Wildi. SPHERE: A 'Planet Finder' Instrument for the VLT. *The Messenger*, 125, September 2006.
- W. J. Borucki. Kepler mission: development and overview. *Reports on Progress in Physics*, 79(3):036901, 2016.
- K. Bott, J. Bailey, L. Kedziora-Chudczer, D. V. Cotton, P. Lucas, J. P. Marshall, and J. Hough. The polarization of hd 189733. *Monthly Notices of the Royal Astronomical Society: Letters*, 459(1):L109–L113, 2016.
- A. Burrows, L. Ibgui, and I. Hubeny. Optical albedo theory of strongly irradiated giant planets: The case of hd 209458b. *The Astrophysical Journal*, 682(2):1277, 2008.
- J. Cabrera and J. Schneider. Detecting companions to extrasolar planets using mutual events. *Astronomy & Astrophysics*, 464(3):1133–1138, 2007.
- K. L. Cahoy, M. S. Marley, and J. J. Fortney. Exoplanet albedo spectra and colors as a function of planet phase, separation, and metallicity. *The Astrophysical Journal*, 724(1):189, 2010.
- B. Campbell, G. A. Walker, and S. Yang. A search for substellar companions to solar-type stars. *The Astrophysical Journal*, 331:902–921, 1988.
- R. M. Canup and W. R. Ward. A common mass scaling for satellite systems of gaseous planets. *Nature*, 441(7095):834–839, 2006.
- A. Cassan, D. Kubas, J.-P. Beaulieu, M. Dominik, K. Horne, J. Greenhill, J. Wambsganss, J. Menzies, A. Williams, U. G. Jørgensen, et al. One or more bound planets per milky way star from microlensing observations. *Nature*, 481(7380):167–169, 2012.
- S. Chandrasekhar. Radiative transfer. clarendon, 1950.
- D. Charbonneau, T. M. Brown, R. W. Noyes, and R. L. Gilliland. Detection of an extrasolar planet atmosphere. *The Astrophysical Journal*, 568(1):377, 2002. URL <http://stacks.iop.org/0004-637X/568/i=1/a=377>.
- G. Chauvin, A.-M. Lagrange, C. Dumas, B. Zuckerman, D. Mouillet, I. Song, J.-L. Beuzit, and P. Lowrance. A giant planet candidate near a young brown dwarf-direct vlt/naco observations using ir wavefront sensing. *Astronomy & Astrophysics*, 425(2):L29–L32, 2004.

- C. J. Conselice, A. Wilkinson, K. Duncan, and A. Mortlock. The evolution of galaxy number density at $z < 8$ and its implications. *The Astrophysical Journal*, 830(2):83, 2016.
- N. B. Cowan, V. Chayes, É. Bouffard, M. Meynig, and H. M. Haggard. Odd harmonics in exoplanet photometry: weather or artefact? *Monthly Notices of the Royal Astronomical Society*, 467(1):747–757, 2017.
- David R. Williams. Nasa planetary fact sheet - metric, 2017. URL <https://nssdc.gsfc.nasa.gov/planetary/factsheet/>. Retrieved on 10/01/2017 from <https://nssdc.gsfc.nasa.gov/planetary/factsheet/>.
- J. F. de Haan, P. B. Bosma, and J. W. Hovenier. The adding method for multiple scattering calculations of polarized light. *AAP*, 183:371–391, September 1987.
- R. De Kok, D. Stam, and T. Karalidi. Characterizing exoplanetary atmospheres through infrared polarimetry. *The Astrophysical Journal*, 741(1):59, 2011.
- I. De Pater and J. J. Lissauer. *Planetary sciences*, chapter Dynamics, pages 22–55. Cambridge University Press, 2015.
- R. C. Domingos, O. C. Winter, and T. Yokoyama. Stable satellites around extrasolar giant planets. *Monthly Notices of the Royal Astronomical Society*, 373(3):1227–1234, 2006. doi: 10.1111/j.1365-2966.2006.11104.x.
- D. Forgan and V. Yotov. The effect of planetary illumination on climate modelling of earth-like exomoons. *Monthly Notices of the Royal Astronomical Society*, 441(4):3513–3523, 2014.
- T. Fusco, G. Rousset, J.-F. Sauvage, C. Petit, J.-L. Beuzit, K. Dohlen, D. Mouillet, J. Charton, M. Nicolle, M. Kasper, et al. High-order adaptive optics requirements for direct detection of extrasolar planets: Application to the sphere instrument. *Optics Express*, 14(17):7515–7534, 2006.
- Georgia State University. Inverse square law, Nov 2016. URL <http://cnx.org/contents/0119fe7d-4d1a-42de-b580-aa46659f8228@4>. Retrieved at June 20, 2017, from the website <http://hyperphysics.phy-astr.gsu.edu>.
- R. L. Gilliland, W. J. Chaplin, E. W. Dunham, V. S. Argabright, W. J. Borucki, G. Basri, S. T. Bryson, D. L. Buzasi, D. A. Caldwell, Y. P. Elsworth, et al. Kepler mission stellar and instrument noise properties. *The Astrophysical Journal Supplement Series*, 197(1):6, 2011.
- J. Girard, C. Dumas, and A. Kaufer. Very large telescope naco user manual, 2011.
- R. Gratton, M. Kasper, C. Vérinaud, M. Bonavita, and H. M. Schmid. Science with epics, the e-elt planet finder. *Proceedings of the International Astronomical Union*, 6(S276):343–348, Oct 2010. doi: 10.1017/S1743921311020412. URL <https://www.cambridge.org/core/article/div-class-title-science-with-epics-the-e-elt-planet-finder-div/AA94C98367F33EF35BB4846DE751ECDB>.
- C. Han and W. Han. On the feasibility of detecting satellites of extrasolar planets via microlensing. *The Astrophysical Journal*, 580(1):490, 2002.
- E. Han, S. X. Wang, J. T. Wright, Y. K. Feng, M. Zhao, O. Fakhouri, J. I. Brown, and C. Hancock. Exoplanet orbit database. ii. updates to exoplanets.org. *Publications of the Astronomical Society of the Pacific*, 126(943):827, 2014.
- J. E. Hansen and L. D. Travis. Light scattering in planetary atmospheres. *Space Science Reviews*, 16(4):527–610, 1974. ISSN 1572-9672. doi: 10.1007/BF00168069. URL <http://dx.doi.org/10.1007/BF00168069>.
- R. Heller. Exomoon habitability constrained by energy flux and orbital stability. *Astronomy & Astrophysics*, 545:L8, 2012.
- R. Heller. Detecting extrasolar moons akin to solar system satellites with an orbital sampling effect. *The Astrophysical Journal*, 787(1):14, 2014.

- R. Heller. On the detection of extrasolar moons and rings. *arXiv preprint arXiv:1701.04706*, 2017.
- R. Heller and R. Barnes. Exomoon habitability constrained by illumination and tidal heating. *Astrobiology*, 13(1):18–46, 2013.
- R. Heller and R. Barnes. Runaway greenhouse effect on exomoons due to irradiation from hot, young giant planets. *International Journal of Astrobiology*, 14(02):335–343, 2015.
- R. Heller, D. Williams, D. Kipping, M. A. Limbach, E. Turner, R. Greenberg, T. Sasaki, É. Bolmont, O. Grasset, K. Lewis, et al. Formation, habitability, and detection of extrasolar moons. *Astrobiology*, 14(9):798–835, 2014.
- R. Heller, M. Hippke, and B. Jackson. Modeling the orbital sampling effect of extrasolar moons. *The Astrophysical Journal*, 820(2):88, 2016a.
- R. Heller, M. Hippke, B. Placek, D. Angerhausen, and E. Agol. Predictable patterns in planetary transit timing variations and transit duration variations due to exomoons. *Astronomy & Astrophysics*, 591:A67, 2016b.
- C. Henry, O. P. Lay, M. Aung, S. M. Gunter, S. Dubovitsky, and G. H. Blackwood. Terrestrial planet finder interferometer: architecture, mission design, and technology development. In *SPIE Astronomical Telescopes+ Instrumentation*, pages 265–274. International Society for Optics and Photonics, 2004.
- N. R. Hinkel and S. R. Kane. Habitability of exomoons at the hill or tidal locking radius. *The Astrophysical Journal*, 774(1):27, 2013.
- M. Hippke. On the detection of exomoons: A search in kepler data for the orbital sampling effect and the scatter peak. *The Astrophysical Journal*, 806(1):51, 2015.
- J. H. Hough and P. W. Lucas. Polarimetry as an aid to the detection of extra-solar planets. In M. Fridlund, T. Henning, and H. Lacoste, editors, *Earths: DARWIN/TPF and the Search for Extrasolar Terrestrial Planets*, volume 539 of *ESA Special Publication*, pages 11–17, October 2003.
- J. H. Hough, P. W. Lucas, J. A. Bailey, and M. Tamura. A high-sensitivity polarimeter for the direct detection and characterization of extra-solar planets, 2003. URL <http://dx.doi.org/10.1111/12.458222>.
- J. W. Hovenier and C. V. M. van der Mee. Fundamental relationships relevant to the transfer of polarized light in a scattering atmosphere. *AAP*, 128:1–16, November 1983.
- J. W. Hovenier, C. V. van der Mee, and H. Domke. *Transfer of polarized light in planetary atmospheres: basic concepts and practical methods*, volume 318. Springer Science & Business Media, 2004.
- E. Hugot, M. Ferrari, K. El Hadi, A. Costille, K. Dohlen, P. Rabou, P. Puget, and J. Beuzit. Active optics methods for exoplanet direct imaging-stress polishing of supersmooth aspherics for vlt-sphere planet finder. *Astronomy & Astrophysics*, 538:A139, 2012.
- P. Kalas, J. R. Graham, E. Chiang, M. P. Fitzgerald, M. Clampin, E. S. Kite, K. Stapelfeldt, C. Marois, and J. Krist. Optical images of an exosolar planet 25 light-years from earth. *Science*, 322(5906):1345–1348, 2008.
- L. Kaltenegger and M. Fridlund. The darwin mission: Search for extra-solar planets. *Advances in Space Research*, 36(6):1114–1122, 2005.
- Karalidi, T., Stam, D. M., and Hovenier, J. W. Looking for the rainbow on exoplanets covered by liquid and icy water clouds. *A&A*, 548:A90, 2012. doi: 10.1051/0004-6361/201220245. URL <https://doi.org/10.1051/0004-6361/201220245>.
- Y. Kawata. Circular polarization of sunlight reflected by planetary atmospheres. *Icarus*, 33(1):217 – 232, 1978. ISSN 0019-1035. doi: [http://dx.doi.org/10.1016/0019-1035\(78\)90035-0](http://dx.doi.org/10.1016/0019-1035(78)90035-0). URL <http://www.sciencedirect.com/science/article/pii/0019103578900350>.

- C. U. Keller, H. M. Schmid, L. B. Venema, H. Hanenburg, R. Jager, M. Kasper, P. Martinez, F. Rigal, M. Rodenhuis, R. Roelfsema, F. Snik, C. Verinaud, and N. Yaitskova. Epol: the exoplanet polarimeter for epics at the e-elt, 2010. URL <http://dx.doi.org/10.1117/12.857626>.
- J. C. Kemp, G. D. Henson, C. T. Steiner, and E. R. Powell. The optical polarization of the sun measured at a sensitivity of parts in ten million. *Nature*, 326(6110):270–273, March 1987. URL <http://dx.doi.org/10.1038/326270a0>.
- M. A. Kenworthy and E. E. Mamajek. Modeling giant extrasolar ring systems in eclipse and the case of j1407b: sculpting by exomoons? *The Astrophysical Journal*, 800(2):126, 2015.
- D. M. Kipping, S. J. Fossey, G. Campanella, J. Schneider, and G. Tinetti. Pathways Towards Habitable Moons. *ArXiv e-prints*, November 2009. URL <http://arxiv.org/abs/0911.5170>.
- D. M. Kipping. Transit timing effects due to an exomoon. *Monthly Notices of the Royal Astronomical Society*, 392(1):181–189, 2009a.
- D. M. Kipping. Transit timing effects due to an exomoon–ii. *Monthly Notices of the Royal Astronomical Society*, 396(3):1797–1804, 2009b.
- D. M. Kipping. How to weigh a star using a moon. *Monthly Notices of the Royal Astronomical Society: Letters*, 409(1):L119–L123, 2010a.
- D. M. Kipping. How to weigh a star using a moon. *Monthly Notices of the Royal Astronomical Society: Letters*, 409(1):L119–L123, 2010b.
- D. M. Kipping. *The Transits of Extrasolar Planets with Moons*, chapter Transit Timing Effects Due to an Exomoon, pages 127–164. Springer Theses. Springer Berlin Heidelberg, 1 edition, 2011. doi: 10.1007/978-3-642-22269-6. URL <https://doi.org/10.1007%2F978-3-642-22269-6>.
- D. M. Kipping, G. Á. Bakos, L. Buchhave, D. Nesvorný, and A. Schmitt. The hunt for exomoons with kepler (hek). i. description of a new observational project. *The Astrophysical Journal*, 750(2):115, 2012.
- D. M. Kipping, A. R. Schmitt, X. Huang, G. Torres, D. Nesvorný, L. A. Buchhave, J. Hartman, and G. Á. Bakos. The hunt for exomoons with kepler (hek). v. a survey of 41 planetary candidates for exomoons. *The Astrophysical Journal*, 813(1):14, 2015.
- N. Kostogryz, T. Yakobchuk, O. Morozhenko, and A. Vid'Machenko. Polarimetric study of transiting extrasolar planets. *Monthly Notices of the Royal Astronomical Society*, 415(1):695–700, 2011.
- N. Kostogryz, T. Yakobchuk, and S. Berdyugina. Polarization in exoplanetary systems caused by transits, grazing transits, and starspots. *The Astrophysical Journal*, 806(1):97, 2015.
- K. Kumar, Y. Abdulkadir, P. van Barneveld, F. Belien, S. Billemont, E. Brandon, M. Dijkstra, D. Dirkx, F. Engelen, D. Gondelach, et al. Tudat: a modular and robust astrodynamics toolbox. In *Fifth ICATT, International Conference on Astrodynamics Tools and Techniques*, pages 1–8. ESA Noordwijk, 2012.
- M. Kuzuhara, M. Tamura, T. Kudo, M. Janson, R. Kandori, T. Brandt, C. Thalmann, D. Spiegel, B. Biller, J. Carson, et al. Direct imaging of a cold jovian exoplanet in orbit around the sun-like star gj 504. *The Astrophysical Journal*, 774(1):11, 2013.
- O. R. Lehmer, D. C. Catling, and K. J. Zahnle. The longevity of water ice on ganymedes and europas around migrated giant planets. *The Astrophysical Journal*, 839(1):32, 2017.
- K. M. Lewis, P. D. Sackett, and R. A. Mardling. Possibility of detecting moons of pulsar planets through time-of-arrival analysis. *The Astrophysical Journal Letters*, 685(2):L153, 2008.
- F. Link. *Eclipse Phenomena in Astronomy*. Springer Berlin Heidelberg, 1969. ISBN 9783642864759. URL <https://books.google.nl/books?id=y-31CAAAQBAJ>.

- N. R. Lomb. Least-squares frequency analysis of unequally spaced data. *Astrophysics and space science*, 39(2):447–462, 1976.
- B. Macintosh, Gemini Planet Imager instrument Team, G. Planet Imager Exoplanet Survey, and G. Observatory. The Gemini Planet Imager. In *American Astronomical Society Meeting Abstracts #223*, volume 223 of *American Astronomical Society Meeting Abstracts*, page 229.02, January 2014.
- B. Macintosh, J. R. Graham, T. Barman, R. J. De Rosa, Q. Konopacky, M. S. Marley, C. Marois, E. L. Nielsen, L. Pueyo, A. Rajan, J. Rameau, D. Saumon, J. J. Wang, M. Ammons, P. Arriaga, E. Artigau, S. Beckwith, J. Brewster, S. Bruzzone, J. Bulger, B. Burningham, A. S. Burrows, C. Chen, E. Chiang, J. K. Chilcote, R. I. Dawson, R. Dong, R. Doyon, Z. H. Draper, G. Duchêne, T. M. Esposito, D. Fabrycky, M. P. Fitzgerald, K. B. Follette, J. J. Fortney, B. Gerard, S. Goodsell, A. Z. Greenbaum, P. Hibon, S. Hinkley, T. H. Cotton, L.-W. Hung, P. Ingraham, M. Johnson-Groh, P. Kalas, D. Lafreniere, J. E. Larkin, J. Lee, M. Line, D. Long, J. Maire, F. Marchis, B. C. Matthews, C. E. Max, S. Metchev, M. A. Millar-Blanchaer, T. Mittal, C. V. Morley, K. M. Morzinski, R. Murray-Clay, R. Oppenheimer, D. W. Palmer, R. Patel, J. Patience, M. D. Perrin, L. A. Poyneer, R. R. Rafikov, F. T. Rantakyrö, E. Rice, P. Rojo, A. Rudy, J.-B. Ruffio, M. T. Ruiz, N. Sadakuni, L. Sadlemyer, M. Salama, D. Savransky, A. C. Schneider, A. Sivaramakrishnan, I. Song, R. Soummer, S. Thomas, G. Vasishth, J. K. Wallace, K. Ward-Duong, S. J. Wiktorowicz, S. G. Wolff, and B. Zuckerman. Discovery and spectroscopy of the young jovian planet 51 eri b with the gemini planet imager. *Science*, 2015. ISSN 0036-8075. doi: 10.1126/science.aac5891. URL <http://science.sciencemag.org/content/early/2015/08/12/science.aac5891>.
- N. Madhusudhan and A. Burrows. Analytic models for albedos, phase curves, and polarization of reflected light from exoplanets. *The Astrophysical Journal*, 747(1):25, 2012.
- G. Mahapatra, D. Stam, L. Rossi, M. Rodenhuis, and F. Snik. Investigating circular patterns in linear polarization observations of venus. In *EGU General Assembly Conference Abstracts*, volume 19, page 15926, 2017.
- M. S. Marley, C. Gelino, D. Stephens, J. I. Lunine, and R. Freedman. Reflected spectra and albedos of extrasolar giant planets. i. clear and cloudy atmospheres. *The Astrophysical Journal*, 513(2):879, 1999.
- C. Marois, B. Macintosh, T. Barman, B. Zuckerman, I. Song, J. Patience, D. Lafrenière, and R. Doyon. Direct imaging of multiple planets orbiting the star hr 8799. *Science*, 322(5906):1348–1352, 2008.
- C. Marois, B. Zuckerman, Q. M. Konopacky, B. Macintosh, and T. Barman. Images of a fourth planet orbiting hr 8799. *Nature*, 468(7327):1080–1083, 2010.
- A. Morbidelli, K. Tsiganis, K. Batygin, A. Crida, and R. Gomes. Explaining why the uranian satellites have equatorial prograde orbits despite the large planetary obliquity. *Icarus*, 219(2):737–740, 2012.
- C. D. Murray and A. C. M. Correia. *Keplerian Orbits and Dynamics of Exoplanets*, pages 15–23. December 2010.
- NASA’s Jet Propulsion Laboratory. Exoplanet exploration: Planets beyond our solar system. <https://exoplanets.nasa.gov/>. Accessed: 2017-06-15.
- J.-P. Nelk and D. Stam. Flux and polarization signals of starlight reflected by exoplanets with dusty rings. *Astrophysical Journal*, 2017.
- OpenStax College. Polarization, Sep 2013. URL <http://cnx.org/contents/0119fe7d-4d1a-42de-b580-aa46659f8228@4>.
- A. Pál. Light-curve modelling for mutual transits. *Monthly Notices of the Royal Astronomical Society*, 420(2):1630–1635, 2012.
- E. Palle, M. R. Z. Osorio, R. Barrena, P. Montanes-Rodriguez, and E. L. Martin. Earth’s transmission spectrum from lunar eclipse observations. *Nature*, 459(7248):814–816, June 2009. ISSN 0028-0836. URL <http://dx.doi.org/10.1038/nature08050>.

- R. T. Reynolds, C. P. McKay, and J. F. Kasting. Europa, tidally heated oceans, and habitable zones around giant planets. *Advances in Space Research*, 7(5):125–132, 1987.
- F. Roddier and C. Roddier. Stellar coronograph with phase mask. *Publications of the Astronomical Society of the Pacific*, 109(737):815, 1997.
- P. Rosenblatt, S. Charnoz, K. M. Dunseath, M. Terao-Dunseath, A. Trinh, R. Hyodo, H. Genda, and S. Toupin. Accretion of phobos and deimos in an extended debris disc stirred by transient moons. *Nature Geoscience*, 2016.
- L. Rossi and D. Stam. Using polarimetry to retrieve the cloud coverage of earth-like exoplanets. *Astronomy & Astrophysics*, 2017.
- L. Rossi and D. Stam. Using polarimetry to retrieve the cloud coverage of earth-like exoplanets. In *EGU General Assembly Conference Abstracts*, volume 19, page 8095, 2017.
- L. Rossi and D. M. Stam. Determination of cloud coverage of earth-like exoplanets by polarimetry. In *AAS/Division for Planetary Sciences Meeting Abstracts*, volume 48, 2016.
- L. Rossi, E. Marcq, F. Montmessin, A. Fedorova, D. Stam, J.-L. Bertaux, and O. Koralev. Preliminary study of venus cloud layers with polarimetric data from spicav/vex. *Planetary and Space Science*, 113:159–168, 2015a.
- L. Rossi, E. Marcq, F. Montmessin, A. Fedorova, D. Stam, J.-L. Bertaux, and O. Koralev. Retrieval of venus' clouds parameters with polarization using spicav-ir onboard venus express. In *EGU General Assembly Conference Abstracts*, volume 17, 2015b.
- L. Rossi, E. Marcq, F. Montmessin, J.-L. Bertaux, A. Fedorova, O. Koralev, and D. Stam. Latitudinal and temporal variability of venus clouds and hazes observed by polarimetry with spicav-ir. In *International Venus Conference 2016*, 2016a.
- L. Rossi, D. Stam, and M. Hogenboom. Pymiedap: a versatile radiative transfer code with polarization for terrestrial (exo) planets. In *EGU General Assembly Conference Abstracts*, volume 18, page 4712, 2016b.
- R. Rufu, O. Aharonson, and H. B. Perets. A multiple-impact origin for the moon. *Nature Geoscience*, 2017.
- H. N. Russell. On the albedo of the planets and their satellites. *Proceedings of the National Academy of Sciences*, 2(2):74–77, 1916.
- S. Saar and S. Seager. Uses of linear polarization as a probe of extrasolar planet atmospheres. *ASP Conf. Ser.*, 294:529, 2003.
- P. Sartoretti and J. Schneider. On the detection of satellites of extrasolar planets with the method of transits. *Astronomy and Astrophysics Supplement Series*, 134(3):553–560, 1999.
- M. Sato and H. Asada. Effects of mutual transits by extrasolar planet–companion systems on light curves. *Publications of the Astronomical Society of Japan*, 61(4):L29–L34, 2009.
- J. D. Scargle. Studies in astronomical time series analysis. ii-statistical aspects of spectral analysis of unevenly spaced data. *The Astrophysical Journal*, 263:835–853, 1982.
- C. A. Scharf. The potential for tidally heated icy and temperate moons around exoplanets. *The Astrophysical Journal*, 648(2):1196, 2006.
- J. Schneider, V. Lainey, and J. Cabrera. A next step in exoplanetology: exo-moons. *International Journal of Astrobiology*, 14(02):191–199, 2015.
- J. Schneider, A. Léger, M. Fridlund, G. J. White, C. Eiroa, T. Henning, T. Herbst, H. Lammer, R. Liseau, F. Paresce, et al. The far future of exoplanet direct characterization. *Astrobiology*, 10(1):121–126, 2010.

- J. Schneider, C. Dedieu, P. Le Sidaner, R. Savalle, and I. Zolotukhin. Defining and cataloging exoplanets: the exoplanet.eu database. *Astronomy & Astrophysics*, 532:A79, 2011.
- S. Seager and D. Sasselov. Extrasolar giant planets under strong stellar irradiation. *The Astrophysical Journal Letters*, 502(2):L157, 1998.
- S. Seager, B. A. Whitney, and D. D. Sasselov. Photometric light curves and polarization of close-in extrasolar giant planets. *The Astrophysical Journal*, 540(1):504, 2000. URL <http://stacks.iop.org/0004-637X/540/i=1/a=504>.
- S. Sengupta. Polarimetric detection of exoplanets transiting t and l brown dwarfs. *The Astronomical Journal*, 152(4):98, 2016.
- S. Sengupta and M. S. Marley. Detecting exomoons around self-luminous giant exoplanets through polarization. *The Astrophysical Journal*, 824(2):76, 2016.
- A. Simon, K. Szatmáry, and G. M. Szabó. Determination of the size, mass, and density of “exomoons” from photometric transit timing variations. *Astronomy & Astrophysics*, 470(2):727–731, 2007.
- A. Simon, G. M. Szabó, K. Szatmáry, and L. Kiss. Methods for exomoon characterization: combining transit photometry and the rossiter-mclaughlin effect. *Monthly Notices of the Royal Astronomical Society*, 406(3):2038–2046, 2010.
- A. Simon, G. M. Szabó, L. Kiss, and K. Szatmáry. Signals of exomoons in averaged light curves of exoplanets. *Monthly Notices of the Royal Astronomical Society*, 419(1):164–171, 2012.
- A. Simon, G. M. Szabó, L. Kiss, A. Fortier, and W. Benz. Cheops performance for exomoons: The detectability of exomoons by using optimal decision algorithm. *Publications of the Astronomical Society of the Pacific*, 127(956):1084, 2015.
- I. A. Snellen, E. J. de Mooij, and S. Albrecht. The changing phases of extrasolar planet corot-1b. *Nature*, 459(7246):543–545, 2009.
- F. Snik. Astronomical polarimetry: new concepts, new instruments, new measurements & observations, 2009. URL <http://dspace.library.uu.nl/handle/1874/36157>.
- F. Snik and C. U. Keller. *Astronomical Polarimetry: Polarized Views of Stars and Planets*, pages 175–221. Springer Netherlands, Dordrecht, 2013. ISBN 978-94-007-5618-2. doi: 10.1007/978-94-007-5618-2_4. URL http://dx.doi.org/10.1007/978-94-007-5618-2_4.
- D. M. Stam. Polarization spectra of extrasolar planets. In M. Fridlund, T. Henning, and H. Lacoste, editors, *Earths: DARWIN/TPF and the Search for Extrasolar Terrestrial Planets*, volume 539 of *ESA Special Publication*, pages 615–619, October 2003.
- D. M. Stam. Spectropolarimetric signatures of earth-like extrasolar planets. *A&A*, 482(3):989–1007, 2008. doi: 10.1051/0004-6361:20078358. URL <https://doi.org/10.1051/0004-6361:20078358>.
- D. M. Stam and J. W. Hovenier. Errors in calculated planetary phase functions and albedos due to neglecting polarization. *A&A*, 444(1):275–286, 2005. doi: 10.1051/0004-6361:20053698. URL <https://doi.org/10.1051/0004-6361:20053698>.
- D. M. Stam, J. W. Hovenier, and L. B. F. M. Waters. Using polarimetry to detect and characterize jupiter-like extrasolar planets. *A&A*, 428(2):663–672, 2004. doi: 10.1051/0004-6361:20041578. URL <https://doi.org/10.1051/0004-6361:20041578>.
- D. Stam and T. Karalidi. Polarimetry for rocky exoplanet characterization. In *EGU General Assembly Conference Abstracts*, volume 15, page 12850, 2013.
- D. Stam, W. De Rooij, G. Cornet, and J. Hovenier. Integrating polarized light over a planetary disk applied to starlight reflected by extrasolar planets. *Astronomy & Astrophysics*, 452(2):669–683, 2006.

- D. Sudarsky, A. Burrows, and P. Pinto. Albedo and reflection spectra of extrasolar giant planets. *The Astrophysical Journal*, 538(2):885, 2000.
- D. Sudarsky, A. Burrows, I. Hubeny, and A. Li. Phase functions and light curves of wide-separation extrasolar giant planets. *The Astrophysical Journal*, 627(1):520, 2005.
- G. M. Szabó, K. Szatmáry, Z. Divéki, and A. Simon. Possibility of a photometric detection of “exo-moons”. *Astronomy & Astrophysics*, 450(1):395–398, 2006.
- W. A. Traub and B. R. Oppenheimer. Direct imaging of exoplanets. In *Exoplanets*, pages 111–156. University of Arizona Press, 2010a.
- W. A. Traub and B. R. Oppenheimer. Direct imaging of exoplanets. *Exoplanets*, 1:111–156, 2010b.
- W. A. Traub, M. Levine, S. Shaklan, J. Kasting, J. R. Angel, M. E. Brown, R. A. Brown, C. Burrows, M. Clampin, A. Dressler, et al. Tpf-c: status and recent progress. In *SPIE Astronomical Telescopes+ Instrumentation*, pages 62680T–62680T. International Society for Optics and Photonics, 2006.
- J. T. Trauger and W. A. Traub. A laboratory demonstration of the capability to image an earth-like extrasolar planet. *Nature*, 446(7137):771–773, 2007.
- L. R. M. Tusnski and A. Valio. Transit model of planets with moon and ring systems. *The Astrophysical Journal*, 743(1):97, 2011.
- H. C. Van de Hulst. *Multiple light scattering: tables, formulas and applications*. Academic Press, 1980.
- R. van Holstein. Accurate high-contrast imaging polarimetry of exoplanets with sphere/irdis. Master’s thesis, Delft University of Technology, 2016.
- K. Wagner, D. Apai, M. Kasper, K. Kratter, M. McClure, M. Robberto, and J.-L. Beuzit. Direct imaging discovery of a jovian exoplanet within a triple-star system. *Science*, 353(6300):673–678, 2016a. ISSN 0036-8075. doi: 10.1126/science.aaf9671. URL <http://science.sciencemag.org/content/353/6300/673>.
- K. Wagner, D. Apai, M. Kasper, K. Kratter, M. McClure, M. Robberto, and J.-L. Beuzit. Direct imaging discovery of a jovian exoplanet within a triple-star system. *Science*, 353(6300):673–678, 2016b.
- K. F. Wakker. Fundamentals of astrodynamics, 2015.
- J. Wertz and N. C. for Space Technology (U.S.). *Mission Geometry: Orbit and Constellation Design and Management : Spacecraft Orbit and Attitude Systems*. Space technology library. Microcosm Press, 2001. ISBN 9781881883074. URL <https://books.google.nl/books?id=aQWPPwAACAAJ>.
- S. J. Wiktorowicz and G. P. Laughlin. Toward the detection of exoplanet transits with polarimetry. *The Astrophysical Journal*, 795(1):12, 2014.
- D. Williams and R. Knacke. Looking for planetary moons in the spectra of distant jupiters. *Astrobiology*, 4(3):400–403, 2004.
- J. N. Winn. Exoplanet transits and occultations. In *Exoplanets*, pages 55–77. University of Arizona Press, 2010a.
- J. N. Winn. *Exoplanets*, chapter Exoplanet Transits and Occultations. Space Science Series. University of Arizona Press, 2010b. ISBN 9780816529452. URL <https://books.google.nl/books?id=V1SVMxgPgGYC>.
- A. Wolszczan and D. A. Frail. A planetary system around the millisecond pulsar psr1257 + 12. *Nature*, 355(6356):145–147, January 1992. URL <http://dx.doi.org/10.1038/355145a0>.
- Q. Zhuang, X. Gao, and Q. Yu. The rossiter–mclaughlin effect for exomoons or binary planets. *The Astrophysical Journal*, 758(2):111, 2012.